Experimental Investigations of the Mechanics of Gassy Sands – Testing Methodology, Shear Tests, and Imaging

Vom Promotionsausschuss der
Technischen Universität Hamburg

zur Erlangung des akademischen Grades

Doktor-Ingenieurin (Dr.-Ing.)

genehmigte Dissertation (Monografie)

von
Pauline Kaminski

aus
Langenhagen

2024

1. Gutachter: Univ.-Prof. Dr.-Ing. Jürgen Grabe
2. Gutachter: Univ.-Prof. Dr.-Ing. Tim Pucker
3. Gutachter: Prof. Dr. Norbert Hoffmann

Tag der mündlichen Prüfung: 14.08.2024

Experimental Investigations of the Mechanics of Gassy Sands – Testing Methodology, Shear Tests, and Imaging

von

Pauline Kaminski

Herausgegeben von

J. Grabe

Technische Universität Hamburg
Institut für Geotechnik und Baubetrieb

Veröffentlichungen des Instituts für Geotechnik und Baubetrieb

62

Herausgeber:

Univ.-Prof. Dr.-Ing. Jürgen Grabe
Technische Universität Hamburg
Institut für Geotechnik und Baubetrieb
Harburger Schloßstraße 20
D – 21079 Hamburg
e-mail: *grabe@tuhh.de*

ISBN-13: 978-3-936310-64-1 (Erstausgabe)

DOI: 10.15480/882.13225

Druckerei

Druckzentrum Neumünster GmbH
Rungestraße 4
24537 Neumünster

In derselben Reihe erschienen:

1. J. Grabe (Hrsg.), 2000: Verbrennungsrückstände. Tagungsband, ISBN 3-936310-00-9

2. J. Grabe (Hrsg.), 2001: Schaden- und Risikomanagement im Tiefbau. Tagungsband, ISBN 3-936310-01-7

3. J. Grabe, 2003. Bodenmechanik und Grundbau. ISBN 3-936310-03-3

4. J. Grabe (Hrsg.), 2003: Euronormen in der Geotechnik – Was ändert sich? Tagungsband, ISBN 3-936310-04-1

5. J. Grabe (Hrsg.), 2003: Bodenverdichtung, Experimente - Modellierung - Geräteentwicklung - Baustellenberichte - F+E-Bedarf. Tagungsband, ISBN 3-936310-05-X

6. M. Kelm, 2004: Nummerische Simulation der Verdichtung rolliger Böden mittels Vibrationswalzen. Dissertation, ISBN 3-936310-06-8

7. J. Grabe (Hrsg.), 2004: Kaimauern - Messungen und Numerik. Tagungsband, ISBN 3-936310-07-6

8. J. Stein, 2005. Experimentelle und numerische Untersuchungen zum Düsenstrahlverfahren. Dissertation, ISBN 3-936310-09-2

9. J. Grabe (Hrsg.), 2005: Grenzschicht Wasser und Boden - Phänomene und Ansätze. Tagungsband, ISBN 3-936310-10-6

10. J. Grabe (Hrsg.), 2005: FEM in der Geotechnik - Qualität, Prüfung, Fallbeispiele. Tagungsband, ISBN 3-936310-11-4

11. B. Mardfeldt, 2006: Zum Tragverhalten von Kaikonstruktionen im Gebrauchszustand. Dissertation, ISBN 3-936310-12-2

12. J. Grabe (Hrsg.), 2006: Optimierung in der Geotechnik - Strategien und Fallbeispiele. Tagungsband, ISBN-13 978-3-936310-13-9

13. T. Bierer, 2007: Bodenschwingungen aus Straßenverkehr auf unebener Fahrbahn im Zeitbereich - experimentelle und theoretische Untersuchungen. Dissertation, ISBN-13 978-3-936310-14-6

14. J. Grabe (Hrsg.), 2007: Bemessen mit Finite-Elemente-Methoden. Tagungsband, ISBN-13 978-3-936310-15-3

15. K.-P. Mahutka, 2008: Zur Verdichtung von rolligen Böden infolge dynamischer Pfahleinbringung und durch Oberflächenrüttler. Dissertation, ISBN-13 978-3-936310-16-0

16. J. Grabe (Hrsg.), 2008: Seehäfen für Containerschiffe zukünftiger Generationen. Tagungsband, ISBN-13 978-3-936310-17-7

17. F. König, 2008: Zur zeitlichen Traglastentwicklung von Pfählen und der nachträglichen Erweiterung bestehender Pfahlgründungen. Dissertation, ISBN-13 978-3-936310-18-4

18. S. Henke, 2008: Herstellungseinflüsse aus Pfahlrammung im Kaimauerbau. Dissertation, ISBN-13 978-3-936310-19-1

19. J. Grabe (Hrsg.), 2009: Spundwände – Profile, Tragverhalten, Bemessung, Einbringung und Wiedergewinnung. Tagungsband, ISBN-13 978-3-936310-20-7

20. J. Dührkop, 2009: Zum Einfluss von Aufweitungen und zyklischen Lasten auf das Verformungsverhalten lateral beanspruchter Pfähle in Sand. Dissertation, ISBN-13 978-3-936310-21-4

21. O. Möller, 2009: Zum Langzeit-Kompressionsverhalten weicher organischer Sedimente. Dissertation, ISBN-13 978-3-936310-22-1

22. J. Grabe (Hrsg.), 2011: Ports of container ships of future generations. Tagungsband, ISBN-13 978-3-936310-23-8

23. S. Kinzler, 2011: Zur Parameteridentifikation, Entwurfs- und Strukturoptimierung in der Geotechnik mittels numerischer Verfahren. Dissertation, ISBN-13 978-3-936310-24-5

24. G. Qiu, 2012: Coupled Eulerian Lagrangian Simulations of Selected Soil-Structure Problems. Dissertation, ISBN-13 978-3-936310-25-2

25. X. Ma, 2013: Nutzung der oberflächennahen Geothermie mittels Energiepfählen und Erdwärmesonden. Dissertation, ISBN-13 978-3-936310-26-9

26. J. Grabe (Hrsg.), 2013: Proceedings of the Conference on Maritime Energy COME 2013. Tagungsband, ISBN-13 978-3-936310-28-3

27. J. Grabe (Hrsg.), 2013: Bemessen mit numerischen Methoden. Tagungsband, ISBN-13 978-3-936310-29-0

28. T. Pucker, 2013: Stoffmodell zur Modellierung von stetigen Materialübergängen im Rahmen der Optimierung geotechnischer Strukturen. Dissertation, ISBN-13 978-3-936310-30-6

29. S. Henke, 2013: Untersuchungen zur Pfropfenbildung infolge der Installation offener Profile in granularen Böden. Habilitation, ISBN-13 978-3-936310-31-3

30. J. Grabe (Hrsg.), 2014: Ports for Container Ships of Future Generations. Tagungsband, ISBN-13: 978-3-936310-32-0

31. J. Grabe (Hrsg.), 2014: Offshore Basishäfen. Tagungsband, ISBN-13: 978-3-936310-33-7

32. C. Rudolph, 2015. Untersuchungen zur Drift von Pfählen unter zyklischer, lateraler Last aus veränderlicher Richtung. Dissertation, ISBN-13: 978-3-936310-34-4

33. J. Grabe (Hrsg.), 2015: Morphodynamics 2015. Tagungsband, ISBN-13: 978-3-936310-35-1

34. T. Hamann, 2015: Zur Modellierung wassergesättigter Böden unter dynamischer Belastung und großen Bodenverformungen am Beispiel der Pfahleinbringung. Dissertation, ISBN-13: 978-3-936310-36-8

35. B. Schümann, 2015: Beitrag zum dynamischen Dreiphasenmodell für Boden auf Basis der Finite-Elemente-Methode. Dissertation, ISBN-13: 978-3-936310-37-5

36. M. Milatz, 2015: Untersuchungen zum Einfluss der Kapillarität auf das hydraulisch-mechanische Verhalten von granularer Tragschichten für Verkehrswege. Dissertation, ISBN-13: 978-3-936310-38-2

37. H. Kaya, 2016: Bodenverschleppung und Spaltbildung infolge der Einbringung von Profilen in Dichtungsschichten aus Ton. Dissertation, ISBN-13: 978-3-936310-39-9

38. J. Grabe (Hrsg.), 2017: Proceedings of the Conference on Maritime Energy COME 2017. Tagungsband, ISBN-13: 978-3-936310-40-5

39. B. Kocak, 2017: Zur numerischen Modellierung von hydraulisch-mechanisch gekoppelten Prozessen in gesättigten granularen Böden mittels Smoothed Particle Hydrodynamics. Dissertation, ISBN-13: 978-3-936310-41-2

40. K. Siegl, 2017: Zur Pfahldynamik von gerammten Großrohrpfählen und der daraus resultierenden Wellenausbreitung in Wasser und im Meeresboden. Dissertation, ISBN-13: 978-3-936310-42-9

41. J. Grabe (Hrsg.), 2017: Conference Proceedings of Workshop on Numerical Methods in Geotechnics 2017. Tagungsband, ISBN-13: 978-3-936310-43-6

42. J. Grabe (Hrsg.), 2018: Digitale Infrastruktur und Geotechnik (DIG 2018). Tagungsband, ISBN-13: 978-3-936310-44-3

43. D. Osthoff, 2018: Zur Ursache von Schlosssprengungen und zu einbringbedingten Lageabweichungen von Spundwänden. Dissertation, ISBN-13: 978-3-936310-45-0

44. E. Heins, 2018: Numerical based identification of the pile-soil interaction in terms of the axial pile bearing capacity. Dissertation, ISBN-13: 978-3-936310-46-7

45. K.-F. Seitz, 2021: Zur Topologieoptimierung von geotechnischen Strukturen und zur Tragfähigkeitssteigerung des Baugrunds durch Scherfugenverfestigung. Dissertation, ISBN-13: 978-3-936310-47-4

46. D. Plenker, 2021: Physical and numerical investigations of the dynamic interaction of saturated granulates and fluid. Dissertation, ISBN-13: 978-3-936310-48-1

47. J. Grabe, J. O. Backhaus, P. Vogel, 2021: Bauprojektmanagement. Skriptum, ISBN-13: 978-3-936310-49-8

48. M. Kanitz, 2021: Experimental and numerical investigations of particle-fluid systems in geotechnical engineering. Dissertation, ISBN-13: 978-3-936310-50-4

49. J. O. Backhaus, 2021: A methodology for the numeric time-cost forecast and paretro optimization of large injection projects in tunneling. Dissertation, ISBN-13: 978-3-936310-51-1

50. S. N. Sinduri, 2021: Optimisation of deep compaction as liquefaction mitigation measure. Dissertation, ISBN-13: 978-3-936310-52-8

51. J. Bubel, 2022: Zum Versagen von Unterwasserböschungen im Seegang. ISBN-13: 978-3-936310-53-5

52. J. Grabe (Hrsg.), 2022: Adaptive Structures At Shore 2022. ISBN-13: 978-3-936310-54-2

53. J. Grabe (Hrsg.), 2022: Numerische Methoden in der Geotechnik. ISBN-13: 978-3-936310-55-9

54. J. Grabe (Hrsg.), 2022: Processes in natural and technical Particle-Fluid Systems (PintPFS). DOI 10.15480/882.4640, ISBN-13: 978-3-936310-56-6

55. T. Törzs, 2022: Zum hydraulisch-mechanisch gekoppelten Verhalten teilgesättigter granularer Geomaterialien infolge hydraulischer und mechanischer Beanspruchungen. Dissertation, ISBN-13: 978-3-936310-57-3

56. M. Milatz, 2023: Investigation of capillary effects on the grain scale by means of in situ experiments, imaging and numerical simulations. Habilitation, ISBN-13: 978-3-936310-58-0

57. A. Chmelnizkij, 2023: Regularized MPM for porous media. Dissertation, ISBN-13: 978-3-936310-59-7

58. J. Grabe (Hrsg.), 2023: Herausforderungen in der Geotechnik - 25 Jahre Institut für Geotechnik und Baubetrieb, Technische Universität Hamburg. Tagungsband, ISBN-13: 978-3-936310-60-3

59. J. Beuße, 2023: Zur Einbringung und zum Tragverhalten von kombinierten Spundwänden von Ufereinfassungen. Dissertation, ISBN-13: 978-3-936310-61-0

60. D. Zobel, 2023: Zur Implementierung höherwertiger Stoffmodelle für Böden am Beispiel der Hypoplastizität. Dissertation, ISBN-13: 978-3-936310-62-7

61. A. Hagemann, 2024: On cyclic and dynamic pile-bearing behaviour. Dissertation, ISBN-13: 978-3-936310-63-4

„The sea is everything! It covers seven-tenths of the world's surface. Its breath is pure and salubrious. It is a vast desert where you are never alone because you feel the constant beat of life all around you. The sea is merely the embodiment of a supernatural and wonderful existence. It is nothing other than motion and love, it is infinity in action.“

Captain Nemo

Editor's Preface

Es ist bekannt, dass marine Böden bedingt durch anaerobe mikrobiologische Umsetzungsprozesse oder aus tieferen Schichten aufsteigende Gase nicht vollständig gesättigt sind. Diese Gase liegen in Abhängigkeit des Drucks und der Temperatur im Porenwasser gelöst oder als verteilte oder zusammenhängende Gasblasen vor. Es ist naheliegend, dass vorhandene oder sich bildende Gasblasen Einfluss auf das bodenmechanische Verhalten der Sedimente haben. Bei schnellen Druckänderungen führt die reduzierte Kompressibilität des Porenwassers zudem zu einem verzögerten Druckausgleichung mit resultierenden Porenwasserüberdrücken. Zum anderen reduzieren die Gasblasen die Scherfestigkeit der Böden, was als ursächlich für Rutschungen von submarinen Unterwasserböschungen angesehen wird. Komplex wird es, wenn dicht gelagerte Böden geschert werden, sich dabei dilatant verhalten, was den Porenwasserdruck in der Scherfuge reduziert und eine Gasblasenbildung initiiert. Bisher ist das komplexe bodenmechanische Verhalten von gashaltigen Böden (*gassy soils*) wenig erforscht. Allein die versuchstechnische Untersuchung gashaltiger Böden und die Interpretation der erhaltenen Versuchsergebnisse ist herausfordernd. Die Arbeit ist zu wesentlichen Teilen im Rahmen des von der DFG geförderten Projektes GR 1024/35-1 „*Investigation of gas migration as a TRIggering mechanism for Submarine land¬slides on COntinental slopes (TRISCO)*“, anfänglich in Kooperation mit dem GEOMAR Helmholtz-Zentrum für Ozeanforschung Kiel, Prof. Dr. Morelia Urlaub, bearbeitet worden. Die Erforschung des mechanischen Verhaltens von gashaltigen Böden bekommt vor dem Hintergrund der Vorhaben zur unterirdischen Verbringung und Lagerung von Kohlendioxid (CCS) eine zusätzliche aktuelle Bedeutung. Die Thematik der Dissertation von Frau Kaminski ist daher für die Bodenmechanik und die Marine Geotechnik von großer Relevanz.
Zielsetzung der Arbeit von Frau Kaminski ist gemäß Kapitel 3, Seite 18 und 19, ist:

1. *Development of a Sample Preparation Methodology*
2. *Analysis of the Macroscopic Behaviour of Gassy Soils*
3. *Analysis of the Microstructure of Gassy Soils*
4. *Assessment of the Microstructural Impact on the Continuum Stress-Strain Behaviour of Gassy Soils*

Frau Kaminski entwickelt einen Versuchsaufbau, um eine gashaltige Sandprobe reproduzierbar herzustellen. An diesen Proben führt sie Triaxialversuche durch, um das makroskopische Verhalten zu untersuchen. Mittels bildgebender Verfahren im Computertomographen untersucht sie die Mikrostruktur zweier Sande mit unterschiedlicher Korngrößenverteilung, um Einblick in die Mikrostruktur zu bekommen. Schließlich verbindet sie die mikromechanischen Beobachtungen mit den makromechanischen Messungen, um Thesen zum bodenmechanischen Verhalten gashaltiger Sande aufzustellen. Die Wahl der Methoden und ihre Vorgehensweise sind nachvollziehbar und zielführend.
In Kapitel 1 führt sie zielstrebig in die Thematik ein. Der Stand der Technik und Wissenschaft ist in Kapitel 2 auf wenigen Seiten dargestellt. Es folgt in Kapitel 3 die Ableitung ihrer Zielsetzung.

Das Kapitel 4 behandelt die von ihr entwickelte Versuchstechnik zur Herstellung von gashaltigen Böden. Tab. 4.1 gibt einen Überblick möglicher Prozeduren. Sie entscheidet sich für die sogenannte „*axis-translation method (pressure)*“. Als Modellböden wählt sie zwei Sande, nämlich sogenannten Hamburger Sand und ISS0-Sand. Deren Kornverteilungen sind in Abb. 4.1 gegeben. Eine mikroskopische Aufnahme davon ist in Abb. 4.2 zu sehen. Sie verwendet Kohlendioxid als Gas. Das Prinzip des experimentellen Aufbaus ist in Abb. 4.2 abgebildet. Das Porenwasser wird durch Wasser mit unter Druck gelöstem Kohlendioxid ausgetauscht und danach der Druck reduziert, sodass eine definierte Menge Gas in den Poren freigesetzt wird. Das Diagramm 4.9 zeigt den genutzten physikalischen Zusammenhang. Das Funktionsprinzip lässt sich an einer Sektflasche anschaulich zeigen.

In Kapitel 5 untersucht sie das makroskopische Verhalten der gashaltigen Sande in einem Triaxialversuchsstand, siehe Abb. 5.1. Die Versuchsreihen mit Variation des Sättigungsgrades für die beiden Versuchssande sind in Tab. 5.1 gegeben. Zur Bestimmung des Sättigungsgrades nutzt sie den Zusammenhang zwischen der Kompressionswellengeschwindigkeit und dem Sättigungsgrad aus, siehe Abb. 5.5 und 5.6. Für die Versuche wird eine Butylmembran verwendet. Deren Einfluss auf die radiale Spannung wird gemäß Gl. 5.9 ff berücksichtigt. Abb. 5.12 zeigt die Änderung des gemessenen Porenwasserdrucks in Abhängigkeit der Zeit zu Beginn der Gasblasenbildung. Warum der Porenwasserdruck ansteigt, ist zunächst verwunderlich. Möglicherweise führt die volumenmäßig wachsende Gasblase zu einer lokalen Verdrängung des Porenwassers, was mit einer Erhöhung des Porenwasserdrucks einhergeht. Neuerdings haben wir an der TUHH einen Magnetresonanztomografen (MRT) mit dem das vielleicht untersucht werden könnte. Abb. 5.13 zeigt die erwartete erhebliche Reduktion der Deviatorspannung mit abnehmender Sättigung für beide Sande, siehe auch Tab. 5.3. In den Abb. 5.18 sind die gemessenen Spannungspfade, Deviatorspannung s als Funktion der isotropen Spannung t, dargestellt. Auffällig sind die veränderten Verläufe bei Erreichen des Grenzzustandes gegenüber der vollständig gesättigten Probe. Dies ist in Abb. 5.20 schematisch verdeutlicht.

In Kapitel 6 stellt Frau Kaminski ihre Untersuchungen im Computertomografen vor. Hierzu konnte sie den CT an der TU Braunschweig nutzen, siehe Abb. 6.2. Sie musste ihren Versuchsaufbau auf die dortigen Verhältnisse umbauen. Erfahrungen liegen in unserem Institut insbesondere durch die Pionierarbeiten von Marius Milatz vielfältig vor. Tab. 6.2 listet die durchgeführten Versuche. Die Abb. 6.4 ff geben einen ersten Eindruck. Sie zeigen, dass die Verteilungen der Gasblasen sich bei beiden Sanden deutlich unterscheiden. Im gröberen Sand sind die Gasblasen in einzelnen Poren verteilt, während im feineren ISS0 Sand es zu zusammenhängenden Gebieten mit Gas kommt. Die weitere Segmentierung führt zu den Abb. 6.12 ff.

In Kapitel 7 führt sie ihre makromechanischen Untersuchungen mit den mikromechanischen Bildern zusammen. Abschnitt 7.2 fasst das Wesentliche zusammen. In Abschnitt 7.3 und Abschnitt 7.4 stellt sie nachvollziehbar verschiedene Thesen zur Erklärung der Beobachtungen auf. Ihre Ausarbeitungen bilden eine hervorragende Grundlage für nachfolgende Forschungsarbeiten. Die Arbeit schließt mit einem Fazit und einem Ausblick in Kapitel 8.

Die von Frau Kaminski vorgelegte Arbeit besticht durch ihre systematische Vorgehensweise und methodische Breite. Ihre Ergebnisse liefern einen wesentlichen Beitrag zum besseren Verständnis des mikro- und makromechanischen Verhaltens von gashaltigen Sanden. Frau

Kaminski hat vier in der Fachwelt sehr beachtete Veröffentlichungen in qualitätsgesicherten Fachzeitschriften und sechs Beiträge auf internationalen und nationalen Tagungen vorzuweisen. Frau Kaminski hat mit ihren Untersuchungen einen wesentlichen Beitrag zum Stand der Wissenschaft in der Bodenmechanik und in der Marinen Geotechnik geleistet. Ich danke Frau Kaminski für ihre Neugier und ihr enormes Engagement. Es wäre toll, wenn sie auch weiterhin der Wissenschaft erhalten bleibt und in Forschung und Lehre die nächsten Schritte geht.

Hamburg, August 2024

Jürgen Grabe

Author's Preface

During the last five years at the Institute of Geotechnical Engineering and Construction Management at Hamburg University of Technology I was given the opportunity to dive into research and follow my interests. And even though it is said that completing a dissertation is a rather lonely endeavour, this thesis would not have been written without the support and involvement of a noteworthy amount of people. Therefore, I would like to express my most sincere gratitude and appreciation to all those who have accompanied me along the way.

In particular, I would like to acknowledge the support of my doctoral supervisor Jürgen Grabe who pointed me towards investigating gassy soils and encouraged me to pursue my ideas. Further, I would like to thank Norbert Hoffmann and Tim Pucker for reviewing my thesis and participating in the examination committee, as well as Peter Fröhle for taking over the chair of the examination committee.

The investigations on gassy sands presented on the following pages of this thesis would not have been possible without the research conducted within the scope of the DFG project GR 1024/35-1 entitled „*investigation of gas migration as a TRIggering mechanism for Submarine landslides on COntinental slopes (TRISCO)*". I therefore thank the German Research Foundation for funding this project. The cooperation with Morelia Urlaub, Christian Berndt, and Thore Sager from GEOMAR Helmholtz Centre for Ocean Research Kiel within the TRISCO project was very cordial and fruitful. Thank you for broadening my understanding of scientific practice in general and soils in particular. Moreover, I would like to acknowledge the contribution of Madhusudhan B. N. Murthy and Antonis Zervos from University of Southampton in the initial stages of the experimental design. In this context, I explicitly do NOT wish to thank the Covid-19 virus for making it impossible to put plans into action.

Moreover, the people I shared my everyday life with have played a big part in this work. I would therefore like to thank all my colleagues, and especially the laboratory staff, for their support. Particularly, the valuable technical discussions with Marius Milatz have helped me immensely to grow with my research. Further, Anne Hagemann and Jannik Beuße have enriched my time at the institute in both, a professional and amicable way, and have been the most wonderful office mates. A very special thanks goes to Corinna Kraft for teaching me English punctuation and to Tobias Engel for showing up.

Finally, I thank my parents for their unconditional support that has given me the confidence to begin and the strength to finish this doctoral project. I thank my partner for being my source of serenity in the midst of the daily madness. And I thank my daughter for giving my life a new perspective.

Hamburg, August 2024

Pauline Kaminski

Schlagwörter:

gashaltiger Sand, partielle Sättigung, granulare Böden, Triaxialversuche, Kapillareffekte, Rissbildung, Bildgebung, Computertomografie (CT)

Keywords:

gassy sand, partial saturation, granular soils, triaxial tests, capillary effects, fracturing, imaging, computed tomography (CT)

Abstract

Most soils in the offshore area contain small amounts of gas; either originating from bacterial metabolistic processes or from thermogenic gas production in deeper layers and subsequent upward migration. For a variety of research questions, for example in the fields of submarine slope stability and carbon capture and storage, the interaction of soil grains, pore water, and gas becomes a relevant aspect. However, the impact of occluded gas bubbles on the soil's stress-strain behaviour has not been thoroughly investigated to date, with the existing studies focusing only on very specific boundary conditions. Particularly the characteristics of the gas phase in the pore space and how they influence the macroscopic stress-strain behaviour remain a matter of theoretical assumptions not validated to date. A holistic assessment of the implications of marine gas occurrence is therefore not possible with the existing knowledge and a requirement for further laboratory investigations can be derived.

The overarching objective of this thesis is to forward the general understanding of gassy soil mechanics to allow for a holistic understanding of geological systems such as the continental slopes. A micro-to-macro approach was chosen for the experimental investigations. This approach allows for the analysis of microstructural controls for the macroscopic stress-strain behaviour of gassy soils and therefore offers the potential for a more fundamental understanding of the soil mechanical processes. To this end, a sample preparation methodology is developed which is subsequently employed in macroscopic CU triaxial tests as well as in microscopic μCT experiments. Finally, all experimental results are combined in a joint interpretation.

The conclusions drawn from the investigations conducted within the scope of this thesis can be summarised as follows:

The advancement of the axis-translation method for gassy soils, as introduced in this thesis, is suitable for a reliable preparation of gassy soil samples under different experimental boundary conditions. The application of the method on two poorly graded model sands was successful in the triaxial as well as μCT experiments. Within the test series two different gas morphologies can be identified in the two investigated gradations: gas clusters that grow by capillary invasion of a stationary grain skeleton in medium sand and macropores within a saturated soil matrix that grow by fracturing in fine sand. Therefore, the grain size is the governing factor for the pore habit of the gas phase. The basic soil mechanical assumptions regarding the distribution of the gas phase within the pore space differ from the observations in this thesis; e. g. in contrast to the literature assumptions capillary forces play a great role in gassy sands. Consequently, the mechanical implications are likewise diverging. The shearing behaviour is impacted differently in the two gradations. The friction angle is slightly elevated in the gassy medium sand compared to its saturated equivalent. In the gassy fine sand, a substantial capillary cohesion is induced by the gas phase. Both model sands fail at significantly lower stress levels than the saturated baseline tests. Thus, a general negative impact of the gas can be deduced.

Contents

1 Introduction

The oceans cover 70 % of the earth's surface (Bosch et al., 2010). Besides offering extraordinary habitats to a diversity of marine life, they supply humankind with a variety of so-called ecosystem services. These include the exploitation of resources, such as renewable energies, food, fossil fuels, and other raw materials, but also the use of the oceans for logistical and recreational purposes or as a disposal site (Ramirez-Llodra et al., 2011). However, nowadays one of the most important ecosystem services provided by the oceans is to buffer the consequences of global climate change (Bindoff et al., 2019). As only an intact ecosystem can offer the said services, a growing demand has brought the ecosystems beyond the ability to sustainably provide these resources. In addition, global climate change has an adverse effect on the condition of the oceans (Bosch et al., 2010; Bindoff et al., 2019). Even measures for mitigating and adapting to the accelerating climate change exert further pressure (Ramirez-Llodra et al., 2011). A prominent example is the necessity to extensively employ negative emission technologies in the second half of the 21st century in order to meet the climate goals set by the international community, since there are no remaining (1.5°C by 2100) or no probable (2.0°C by 2100) alternative courses of action left (Rogelj et al., 2015).

Carbon capture and storage (CCS) is one feasible negative emission technology (Ringrose and Meckel, 2019). CCS describes the removal of carbon dioxide (CO_2) from the atmosphere and the subsequent injection of its supercritical form together with brine into a geological formation for permanent storage (Bui et al., 2018). Much of the required technology for the industrial-scale implementation of CCS, e. g. the construction of injection wells, is already being applied in oil and gas production (Bui et al., 2018). Leakage control, an aspect with a high impact on greenhouse gas budgets, however, has not been in the focus of the petroleum industry. Well integrity issues with resulting methane (CH_4) escape were reported for active and decommissioned petroleum wells (Dusseault and Jackson, 2014; Böttner et al., 2020; Soares et al., 2021). Besides the release of greenhouse gases to the water or the atmosphere, the charging of shallow soil layers with gas is a side effect of poor well integrity (Dusseault and Jackson, 2014; Van De Ven and Mumford, 2020a). Due to the corrosive nature of CO_2, long-term well integrity will potentially become a greater challenge in CCS applications than for hydrocarbon production (Watson and Bachu, 2009). Since dissolution of CO_2 in the formation water is the dominating trapping mechanism, groundwater movement can also lead to gas escape from the reservoir (Gilfillan et al., 2009; Van De Ven and Mumford, 2020a; Connelly et al., 2022). While leakage has not been reported from the existing industrial-scale CCS projects for the time being (Blackford et al., 2015), studies from natural CO_2 reservoirs by Gilfillan et al. (2009) show losses of $50-90$ % of the initial CO_2 predominantly to dissolution at the testing sites over millenial time scales. Additionally, leakage detection for CO_2 escape remains a challenge, particularly since diffusive low flux leaks spread over larger areas (Gilfillan et al.,

2011; Blackford et al., 2015). Nonetheless, some monitoring strategies and maximum CO_2 leakage rates processible by the marine ecosystem have been proposed by the research community (Blackford et al., 2015; Connelly et al., 2022).

Current research efforts have thus targeted gas migration as well as geobiological and geochemical effects of the gas phase in the host soil as well as implications for the groundwater chemistry and, for onshore applications, consequently the quality of the public water supply. However, in this context, soil mechanical implications of a spreading gas phase in shallow soil layers were neglected to date.

For an efficient storage of the required amount of CO_2 to meet the climate goals, the continental margins provide the most promising boundary conditions (Ringrose and Meckel, 2019). The continental margins are part of the most dynamic regions of the seafloor, which is reflected, amongst others, in sediment transport processes. While the sediment is moved by suspension or bed load transport in the shallow shelf seas, the continental slopes are characterised by slope failures (Locat and Lee, 2002; Masson et al., 2006). Submarine landslides are the most important sediment transport process to the deep sea and differ in their characteristics from typical terrestrial landslides. The soil masses put in motion are substantially larger than those of previously reported failure events on land (Masson et al., 2006). The largest known submarine landslide, the Storegga slide, involved approximately $3{,}000\,km^3$ of soil (Haflidason et al., 2004). In addition, most submarine landslides occur at very low slope inclinations of $\leq 2°$ and, therefore, on slopes that are almost always stable on land (Hühnerbach and Masson, 2004; Twichell et al., 2009). The displacement of water occuring during the movement of such large soil masses can generate tsunamis with catastrophic effects for coastal communities (Locat and Lee, 2002; Wendlinger et al., 2008). During its movement, the sliding soil mass takes up water and can develop into a turbidity current. These turbidity currents travel long distances with high velocities and have a high destructive potential for offshore infrastructure (Masson et al., 2006; Hsu et al., 2008). Even though a large number of submarine landslide events has been identified and analysed already, the trigger mechanisms are not yet conclusively clarified (Locat and Lee, 2002; Mountjoy et al., 2020). Amongst others, submarine gas occurrence is under consideration as a trigger mechanism for submarine landsliding (Bünz et al., 2005; Berndt et al., 2012; Elger et al., 2018). It has already been demonstrated that a gas-induced increase in pore pressures with subsequent soil liquefaction can trigger failure and that gas-disturbed soils can precondition slopes for failure under specific circumstances (Chillarige et al., 1997; Clare et al., 2016; Kaminski et al., 2021). Nevertheless, the current state of knowledge on the mechanical properties of gassy soil is insufficient to allow for meaningful conclusions to be drawn beyond the limited conditions that have been specifically investigated.

To enable further research on the matter, knowledge of the basic properties of marine gas is crucial: The majority of the naturally occuring gas in the seafloor is biogenic CH_4 produced by anaerobic methanogenesis in shallow soil layers. Additionally, thermogenic CH_4 from abionic, chemical processes in exceptionally deep sediment layers, i. e. petroleum gas, plays a role (Archer, 2007). Gas occurrence at the continental margins has been linked to phenomena like pockmarks, subsurface pipe structures which result from fluid flow and migration processes, and gas seeps (Judd and Hovland, 2009; Skarke et al., 2014). The presence of naturally occurring free gas in the sediment could be proven for continental margins all around the world (Fleischer et al., 2001; Judd and Hovland, 2009). A holistic

understanding of the repercussions of marine gas occurrence is therefore fundamental to comprehend the systemical processes.
Furthermore, the gas can also be bound in hydrates: water molecules form a cage structure that contains a gas molecule and results in an ice-like substance. Hydrates are only stable at sufficiently high pressures and low temperatures (Kvenvolden, 1993; Archer, 2007). A link between hydrate dissociation and accompanying gas production rates with global climate change could be substantiated for specific local boundary conditions (Ruppel and Kessler, 2016). As the mobility of the gas phase in the soil is controlled by the soil properties (Fauria and Rempel, 2011; Stranne et al., 2016), there is a need for a better understanding of the interplay between gas phase and soil mechanics.
It is clear from the examples above that naturally formed and anthropogenically produced gas deposits on continental slopes are relevant for both natural systemic processes (e. g. sediment transport) and industrial use. Regarding the latter, it is well known that marine gas occurrence can have a negative impact on the integrity of offshore infrastructure (Kong et al., 2005; Tjelta et al., 2007; Mabrouk and Rowe, 2011). Many questions regarding the interaction of soil and gas are still unresolved, interdisciplinary analyses on the correlation of different aspects – such as gas migration mechanisms and the soil's stress-strain response – are lacking, and fundamental soil mechanical studies on gassy soils exist only in a limited number, each with very specific testing conditions. However, a broad understanding of the entire continental slope system is required to derive measures to ensure that the initially described ecosystem services remain accessible for society in a long-lasting and sustainable manner.
Therefore, the primary objective of this thesis is to advance the fundamental understanding of the mechanical properties of gassy soils. The following chapter summarises the current state of research in the field of gassy soils. On this basis, the specific objectives for this study are identified and appropriate research methods are selected in chapter 3. Further information on the employed notation is provided in appendix A.

2 State of Research

The mechanical behaviour of gassy soils is a complex interaction of three phases: solids (soil particles), fluid (water) and gas. In order to exclude salinity-induced effects on the soil behaviour, hereinafter, the water phase is assumed to exhibit 0 % salinity. In the following, the current state of knowledge regarding different aspects of gassy soils is summarised. In this thesis, the terms degree of saturation and saturation are used interchangeably. The results of the literature review presented in this chapter have partly been published in Kaminski et al. (2020).

2.1 Definition and General Aspects of Gassy Soil

Gas in soil can occur dissolved in the pore water, as free gas, or in the form of gas hydrates (Kvenvolden, 1993). Given no exsolution takes place, dissolved gas does not influence the mechanical behaviour of the soil (Sills and Wheeler, 1992). Free gas, however, has a substantial impact on the soil mechanics and will therefore be discussed further in the following. Gas hydrates and hydrate-cemented soils are a broad research field of its own that adjoins the topic of gassy soils but will not be further explored within the scope of this thesis.

2.1.1 Definition of Gassy Soil

All partially saturated soils contain the three phases solid, water and gas. However, the characteristics of partially saturated soils vary, and, thus, the term gassy soils describe a particular set of boundary conditions to be encountered in the field of partially saturated soils. A necessary prerequisite for gassy soils is a degree of saturation S_r of $\geq$ 85 % (Nageswaran, 1983; Fredlund and Rahardjo, 1993; Grozic et al., 1999). Generally, at this saturation, the gas phase is discontinuous, i.e. appears as gas bubbles, while the water phase is continuous. Consequently, capillary effects, such as capillary cohesion, are not attributed a significant role in the mechanical behaviour of the soil (Sobkowicz and Morgenstern, 1984; Wheeler, 1986). Often, a distinctive feature of gassy soil is that the gas phase does not consist of air and is not under atmospheric pressure and temperature conditions. This results from the gas production mechanism, e.g. bacterial decomposition of organic matter, migration from a deeper soil layer, or others (Judd and Hovland, 2009). Thus, geobiological or geochemical processes are often implicated. However, this thesis addresses only the geomechanical component.

2.1.2 General Properties of a Gas Phase in Soil

The thermodynamic condition of a gas is defined entirely by its pressure and temperature. The material properties of the gas therefore crucially rely on these two parameters (Rist, 1996). For geomechanical applications, gases at standard ambient conditions (101,325 kPa and 298,15 K ≙ 25°C) can approximately be considered to behave like ideal gases (Atkins et al., 2018). This assumption implies that the distance between the gas molecules is large compared to the size of the molecules. Additionally, collisions between gas molecules are assumed to lead to entirely elastic behaviour, and inter-molecular forces are neglectable (Atkins et al., 2018). The thermodynamical behaviour of gases can then be described by the ideal gas law

$$p \cdot V_g = n \cdot R_s \cdot T. \tag{2.1}$$

It expresses the proportional relation of pressure p, gas volume V_g and temperature T depending on the amount of gas n in mol and the specific gas constant R_s equal to 8.314 J/(mol·K), (Rist, 1996).
In contrast to gas, the material properties of the other two phases in geomaterials – water and soil grains – are not as strongly dependent on the pressure and temperature. This is reflected in a considerable difference in the compression, respectively bulk moduli K of the three phases, see fig. 2.1. For geomechanical investigations, water is usually considered incompressible. The properties of the solid particles only become relevant when grain crushing is considered a significant process. Thus, generally the compressibility of granular packings with dry or water-filled pore spaces is decisive. The high compressibility of the gas phase therefore introduces a significantly different component to the mechanical response of partially saturated soils.
Mixtures of water and gas can be characterised as miscible and/or immiscible (Fredlund and Rahardjo, 1993). For gassy soils, features of both characteristics become relevant. In miscible mixtures, solubility and phase change processes occur, i.e. the gas dissolves in the liquid phase and water vapour mixes with the gas phase (Fredlund and Rahardjo, 1993). However, for gassy soils, dis- and exsolution processes are particularly important. The solubility of the gas depends on the acting temperature and pressure and can differ significantly with the gas species. Fig. 2.2 shows the solubility boundary c_g of CO_2 and CH_4 in water with 0 % salinity at 24.85° C, based on data by Carroll et al. (1991), Duan et al. (1992), Valtz et al. (2004), and Hou et al. (2012). Thereby, the boundary indicates the amount of gas that can be taken up by the water. If a condition located above the solubility curve in fig. 2.2 is reached, the liquid is called *supersaturated*. In this case, all excess gas will exsolve and be present as a free gas phase for the respective pressure and temperature combination. Thus, in gassy soils, the pore water generally is fully saturated with the respective gas and any change in the acting boundary conditions will lead to dis- and exsolution processes. In the following, minor water density changes due to the dissolution of gas will be neglected.
For immiscible mixtures, the interface between the two phases becomes the characterising feature. Thus, with the existence of a gas phase, the behaviour of the soil is further influenced by the properties of the gas-water interface – the contractile skin or meniscus, when curved, – which has substantially different properties than the gas or water phase alone. In equilibrium, a surface tension T_s (pulling force) acts tangential to the contractile skin because the attractive forces between water molecules are not in balance at an interface,

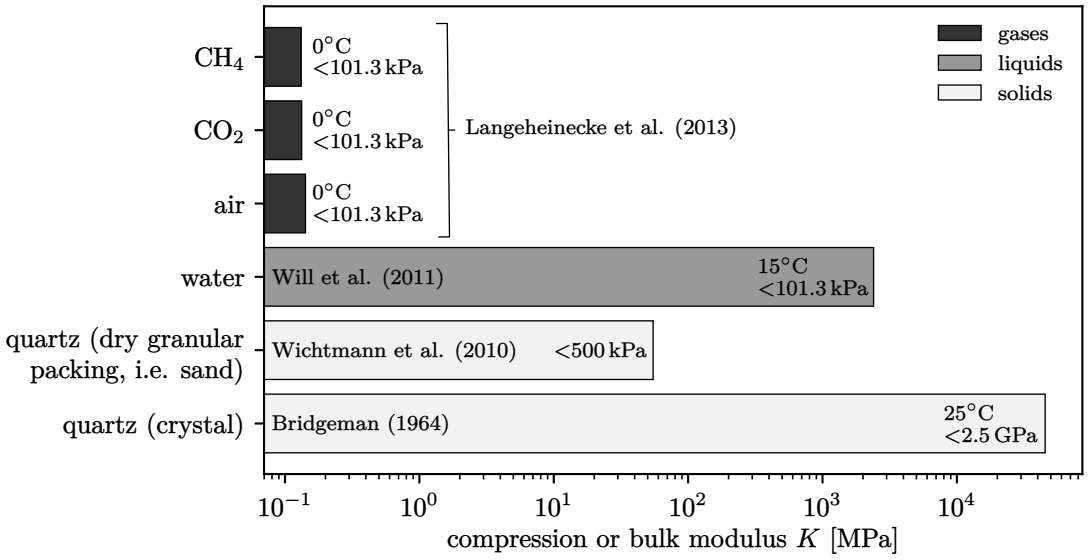

Figure 2.1: compression or bulk moduli of frequently encountered substances in geomechanics according to Bridgeman (1964), Wichtmann et al. (2010), Will et al. (2011), and Langeheinecke et al. (2013); the annotated pressure and temperature values correspond to the respective testing conditions at which K was determined

with the resulting force directed towards the water phase. Therefore, the contractile skin behaves like an elastic membrane between the gas and water phase (Fredlund et al., 2012). The gas pressure inside a gas bubble can thus always be slightly elevated compared to the surrounding water phase; like the gas pressure inside a balloon compared to the surrounding atmosphere. However, the acting tensile force in the contractile skin is also the cause for capillary effects. The capillary pressure or matric suction, i.e. the pressure difference between gas and water phase ($u_g - u_w$), leads to a rise of water in small capillary tubes and, in contrast, determines the required gas pressure to invade the capillary and displace the water in the process. Since, according to Sobkowicz and Morgenstern (1984), Sills and Wheeler (1992), and Finno et al. (2017), the gas entry into the pore space has greater importance for gassy soils than capillary effects, the latter are not further discussed. Assuming the soil particles are perfect spheres and based on the YOUNG-LAPLACE equation, Fredlund et al. (2012) approximate the required capillary pressure for air invasion into the pore space in kPa with

$$u_g - u_w = \frac{0.3513 \left[\frac{\text{kPa}}{\text{mm}}\right]}{r}, \tag{2.2}$$

where r represents the particle radius in mm. Equ. 2.2 implies $T_{\text{s,air}} = 72.75\,\text{mN/m}$ for an air-water interface. The surface tension of a CO_2-water interface is $T_{\text{s,CO}_2} = 72\,\text{mN/m}$ (measured at 25°C and 0.1 MPa; Espinoza and Santamarina, 2010), and for a CH_4-water interface $T_{\text{s,CH}_4} = 72.76\,\text{mN/m}$ (measured at 25°C and 1 MPa; Sun et al., 2004). Hence, in the given pressure range, the introduced relationship can not only be applied for air-water interfaces but in approximation also for other gases.

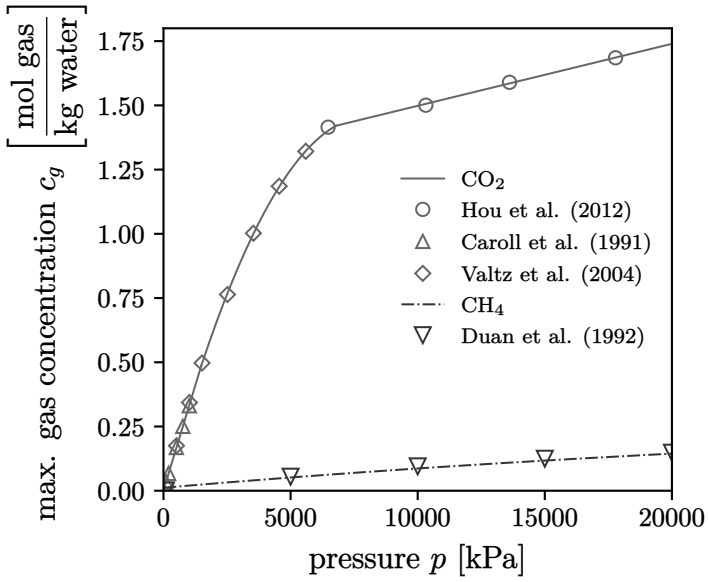

Figure 2.2: solubility of CO_2 and CH_4 in water with 0 % salinity at 24.85°C (Carroll et al., 1991; Duan et al., 1992; Valtz et al., 2004; Hou et al., 2012)

2.1.3 Characteristics of Gassy Soil

The characteristics of a gassy soil are always determined by the interaction of the three phases. The gradation of the solid particles, which determines the properties of the pore space available for the gas and water phases, conclusively dominates the appearance of gassy soils. Most studies on gassy soils classified the gradation by ASTM D2487-17e1 (2020), according to which a grain diameter of 0.075 mm marks the transition from sand (coarse-grained soil) to silt and clay (fine-grained soils). It thereby serves as a distinguishing criterion for gassy soil characteristics (Sills and Wheeler, 1992). Fig. 2.3 summarises relevant characteristics of partially saturated soils.

Coarse-Grained Soil

Corresponding to the larger grain size of sands compared to silt and clay, the pore spaces in the soil are respectively larger. It is therefore assumed that the diameter of the gas bubbles is smaller than the dimensions of the voids, as depicted in fig. 2.3a. The gas bubbles, thus, do not induce structural changes in the grain skeleton (Sills and Wheeler, 1992; Grozic et al., 1999). The appearance of the gas phase as singular bubbles within the pore space presupposes a lack of bridging menisci between soil grains, see fig. 2.3b compared to fig. 2.3a. Furthermore, for geomechanical investigations, it is sufficiently specific to assume the pressure inside the gas bubbles to equal the pore water pressure ($u_g = u_w$).
According to Fredlund and Rahardjo (1993), the effective stress (σ') in partially saturated soils can be described by BISHOP's equation

$$\sigma' = (\sigma - u_g) + \chi \cdot (u_g - u_w) \ , \tag{2.3}$$

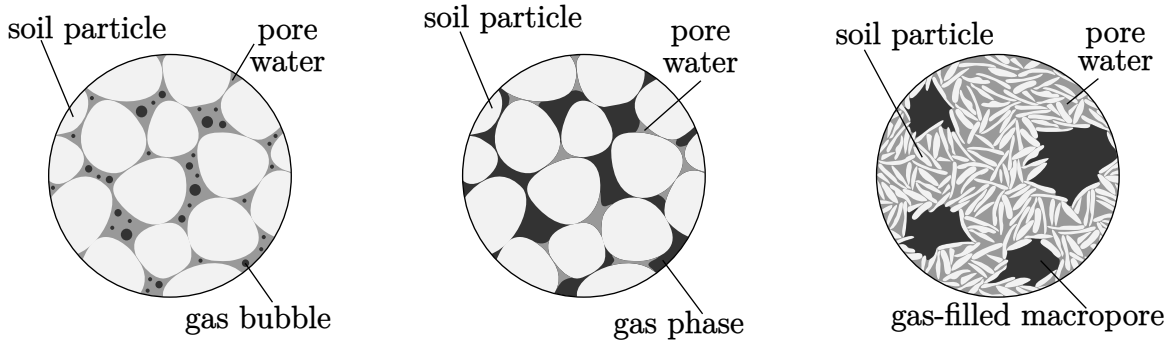

(a) gassy sand (b) unsaturated sand (c) gassy clay

Figure 2.3: characteristics of partially saturated soils

in which σ is the total stress and χ is a factor to take the degree of saturation into account. If $u_g = u_w$, equ. 2.3 degenerates to TERZAGHI's principle of effective stress

$$\sigma' = \sigma - u\,, \tag{2.4}$$

where u is the pore pressure. Finno et al. (2017) experimentally verified the validity of TERZAGHI's principle of effective stress for gassy sands for saturations of $S_r \geq 92\,\%$. However, the validation relies only on two singular triaxial tests on gassy sand. Nonetheless, the general conclusion is that in coarse-grained soil, gas mostly impacts the compressibility of the pore fluid mixture (Grozic et al., 1999; Finno et al., 2017).

Fine-Grained Soil

Analogously to coarse-grained soil, in fine-grained soil, the pore space is accordingly small. Gas bubbles cannot be accommodated in the pore space, and in order for the gas phase to enter a pore through the pore throat, the pore water has to be displaced. The capillary entry pressure required for this process (see equ. 2.2) generally exceeds the strength of the soil. Thus, the formation of gas bubbles leads to local damage in the soil skeleton, creating isolated and randomly distibuted gas voids of $0.1 - 1\,\text{mm}$ diameter within the saturated soil matrix – magnitudes larger than the mean particle diameter (Wheeler, 1988a). The resulting appearance of a gassy fine-grained soil is depicted in fig. 2.3c. The *Large Bubble Model*, a theoretical concept developed by Wheeler (1986) and Wheeler (1988a), and later enhanced by Wheeler et al. (1990), Sills et al. (1991), and Sills and Wheeler (1992), describes the associated features of such soils:
Due to their confinement by the adjacent soil particles, the gas voids are immobile and feature individual shapes and sizes. Their inner gas pressure does not necessarily correlate with the void volume or the gas pressures in neighbouring voids because it is further dependent on the overall stress and loading state of the soil as well as on the diagenetic process of the gas and the gas properties. At the interface between gas void and saturated soil matrix, menisci bridge the pore spaces between the adjacent soil particles. The menisci adjust individually according to the positioning of the particles and the local gas and water pressures. When $u_g > u_w$, the menisci show a concave shape towards the water phase. If the pressure difference increases further, the gas invades the capillaries surrounding the

void until the capillary entry pressure is in equilibrium with the gas pressure inside the void. This process is accompanied by a local pore water pressure build-up. When $u_g < u_w$, the menisci show a convex shape towards the gas phase. In the event of an ongoing rise of the pressure difference, local consolidation processes occur, i.e. the pore water enters the gas void. As the menisci supporting the cavity roof disappear in case of bubble flooding, the now water-filled void potentially loses its structural integrity, resulting in considerable structural changes in the entire soil structure.
The complex interaction between the gas and water pressures as well as their spatial variation lead to a highly non-uniform stress state of the soil on the micro-scale. In consequence, TERZAGHI's principle of effective stress can only be applied to gassy fine-grained soils if the gas-induced local pore water pressure variations and the gas voids are neglected. To elucidate the significance of the simplifications, Wheeler (1986) introduced the operational stress σ'' as

$$\sigma'' = \sigma - u_w \,, \tag{2.5}$$

which is equivalent to the effective stress for the saturated soil matrix, neglecting the gas and its impact on the stress state.
In contrast to coarse-grained soils, the water and gas phases are spatially separated in fine-grained soils. For further soil mechanical considerations the water phase can therefore be considered incompressible. Thus, the mechanical behaviour of a gassy fine-grained soil is presumably incomparable to granular soils.

2.2 Mechanical Properties of Gassy Soil

The mechanical behaviour of a gassy soil is influenced by a great variety of factors; amongst the soil properties (soil type, density, diagenesis and loading history, permeability, and others), gas properties (gas species, solubility, amount, and others), and loading properties (loading direction, velocity, and others). Additionally, the chosen experimental method to investigate the stress-strain relation still bears ambiguities. Thus, only a comprehensive analysis of the combination and interaction of the respective influencing factors can yield a reliable interpretation of the soil's stress-strain behaviour. Here, the emphasis is placed on the static undrained shearing behaviour of gassy soils.

2.2.1 Coarse-Grained Soil

Assuming the mechanical behaviour in gassy sands is predominantly influenced by a gas-induced compressibility of the pore fluid, the tendency for volumetric deformation under drained loading conditions or respectively for the development of excess pore pressures under undrained loading conditions indicate the gassy soil response in contrast to a saturated equivalent. As elaborated in section 2.1.2, with free gas present in the pore space, it can be presupposed that the pore water surrounding the gas bubbles is fully saturated with the respective gas. Therefore, a load-induced change in pore pressure alters the degree of saturation of the soil.
For pore pressure increase under undrained loading conditions, the gas dissolves in the pore water increasing the degree of saturation of the soil. Depending on the initial gas

content, the soil can reach a resaturated state ($S_r = 100\,\%$) in which it exhibits the same mechanical properties as before the gas exsolution (Grozic et al., 1999).
For pore pressure decrease under undrained loading conditions, additional gas is forced out of solution. Based on the proportional relation of pressure, volume and gas amount expressed in equ. 2.1, this exsolution process leads to a rise in gas and thus pore pressure to the equilibrium pressure of the solubility limit. In the case of an ongoing undercutting of the solubility limit, the pore pressure is held constant by the continuous gas exsolution (Sobkowicz and Morgenstern, 1984; Amaratunga and Grozic, 2009).
The described loading and unloading behaviour also governs the shearing behaviour of gassy sands. During undrained triaxial shearing of a loose sand, the development of excess pore pressures is mitigated by the presence of gas. The higher the degree of saturation, the stronger the mitigation effect (Vega-Posada et al., 2014). Therefore, for loose gassy sands, the risk of flow liquefaction is only given for high degrees of saturation (Grozic et al., 1999). Medium dense to dense samples with the tendency for a dilative volumetric response under drained conditions show a pore pressure development similar to the unloading concept of Sobkowicz and Morgenstern (1984) during undrained shearing. The consequently less intense pore pressure reduction compared to the saturated equivalent leads to a reduced shear strength (Rad et al., 1994; Vega-Posada et al., 2014; Finno et al., 2017). This effect is more pronounced with a highly soluble gas, such as CO_2 (Rad et al., 1994). Even if undrained conditions prevail, saturation-dependent volume changes of the sample can occur as a consequence of partial internal drainage (Rad et al., 1994; Grozic et al., 1999; Vega-Posada et al., 2014). Generally, the response of gassy samples to triaxial shearing is bounded by the drained and undrained stress paths of an equivalent saturated sample. Thereby, samples with a high saturation behave similarly to the undrained saturated response, and samples with a low saturation show stress paths close to those of saturated samples under drained conditions (Rad et al., 1994; Vega-Posada et al., 2014; Grozic et al., 1999; Finno et al., 2017).

2.2.2 Fine-Grained Soil

In fine-grained soils, the soil structure is significantly altered by the presence of a gas phase. The manner in which the architecture of the gas-filled pore space develops can influence the mechanical behaviour of the respective soil (Sultan et al., 2012; Jommi et al., 2019). Consequently – and due to the limited number of studies, the current state of research does not allow for any definitive, general conclusions to be drawn regarding the impacts of gas occurrence on different aspects of a fine-grained soil's response to loading. For operative stress levels as low as $\sigma'' \leq 10\,\mathrm{kPa}$, vane shear tests showed no significant changes in peak and residual shear strengths (Sills and Gonzalez, 2001). The underlying reason is the already low magnitude of shear strength at this stress level and the dominance of the saturated soil matrix over the gas inclusions on the overall soil response. If the operative stress level is higher and a larger difference between pore gas pressure and pore water pressure is possible, the influence of the gas inclusions on the shear strength increases (Wheeler, 1988b). In this case, the coupling of the gas pressure in large, enclosed bubbles and the deformation of the saturated soil matrix during shearing triggers several partly counteractive processes. Nageswaran (1983), Wheeler (1986), and Wheeler (1988b)

investigated these processes in a large test series on gassy kaolin clay. If gassy clay is compressed and the cavities shrink, the gas pressure in the cavities rises according to equ. 2.1. On the one hand, the shrinkage of gas cavities leads to a gain in overall soil stiffness and thereby favours a strain-hardening effect. On the other hand, the increasing gas pressure triggers the solution of gas in the surrounding pore water. A process which then decreases the gas pressure and counteracts the strain-hardening. For dilation and cavity growth, an analogue process with a resulting strain-softening behaviour can be observed. The relative in- or decrease of the gas pressure in the voids additionally alters the stress state around the voids and drives local consolidation processes in the surrounding saturated soil matrix. Thus, the pressure difference between the gas in the large voids and the pore water in the surrounding saturated soil matrix ($u_g - u_w$) is decisive for the detrimental or beneficial impact of the enclosed gas bubbles. Although the pressure in the gas bubbles is believed to be solely dependent on the total stress conditions, the pore water pressure in the saturated soil matrix is expected to rise in the event of undrained shearing. Thus, the critical pressure difference $u_g - u_w$ for bubble flooding can be reached during shearing. Since the cavities lose the roof support when the menisci disappear during bubble flooding, the resaturated soil structure becomes instable (Wheeler, 1988a; Wheeler, 1988b). In consequence, remarkable discontinuities show in the stress paths when the cavities collapse under shear loading (Sultan et al., 2012). Therefore, soils with a gas-disturbed soil structure show significantly lower shearing resistance when they are in a resaturated state (Wheeler, 1988b; Sultan et al., 2012).

In addition, other processes and boundary conditions can affect the shearing behaviour of gassy fine-grained soils. For instance, occluded gas bubbles inhibit natural self-weight consolidation processes and thereby favour underconsolidated states in which the loading capacity of a soil is reduced compared to normally consolidated states (Sills and Gonzalez, 2001).

Finally, peat is not the traditionally considered fine-grained soil, but prone to naturally occur in a gassy state due to its high organic content. While the enclosed gas amounts are low enough to be accomodated in the pore spaces, the soil's pore fluid can be considered compressible to describe the mechanical behaviour suitably (Jommi et al., 2019). Once the gas fractured the soil structure to enlargen the pores, a considerable reduction of operative stress sets in. This is accompanied by noteable straining of the saturated soil structure, which becomes relevant for the assessment of the peat's bearing capacity. Overall, the resulting friction angles of gassy peat are reduced by $30 - 40\,\%$ compared to saturated peat (Jommi et al., 2019).

2.3 Gas Flow and Migration Processes

Usually spherical bubbles surrounded by pore water (fig. 2.3a) or approximately spherical gas voids enclosed in a saturated soil matrix (fig. 2.3c) are presupposed for idealised geotechnical considerations. However, naturally occuring gas in the pore space of a soil often shows different characteristics (Jones et al., 1999; L. Liu et al., 2016). These are governed by the gas formation and migration processes unique to the properties of the porous medium, i. e. the soil (L. Liu et al., 2018; Terzariol et al., 2021). Since a feedback

loop with the mechanical behaviour of the soil and the properties described in section 2.2 exists (Sills and Gonzalez, 2001; Sultan et al., 2012; Ben-Noah et al., 2023), these processes are of relevance to geotechnical analyses of gassy soil.

Therefore, this section aims to give an overview on different multi-phase flow mechanisms relevant in the context of geotechnical considerations. For a more in-depth analysis of different micro- and macro-scale flow patterns in porous media and their governing factors, the reader is referred to the relevant literature (e. g. Ben-Noah et al., 2023).

2.3.1 Bubble Nucleation

As elaborated in section 2.1.2, a free gas phase is only stable in a fluid when the solubility limit of the gas species in the respective fluid is exceeded for the acting pressure and temperature combination. Therefore, gas generating processes, e. g. microbial activity, only successfully produce a gassy soil after generating enough gas to fully saturate the pore fluid (Sills and Gonzalez, 2001; Rebata-Landa and Santamarina, 2012). If a supersaturated state is reached by ongoing gas production or changes in temperature and/or pressure, in porous media, gas bubbles preferably nucleate on the surface of solids as the nucleation energy barrier is lower compared to that within the liquid bulk (Li and Yortsos, 1995; Jones et al., 1999). For homogeneous bubble nucleation in a liquid, high levels of supersaturation are required to provide sufficient energy in order to overcome the tensile forces of the liquid. A solid surface decreases the interfacial free energy and is thus a thermodynamically favourable nucleation site (Jones et al., 1999). A contributing factor is the beneficiary effect that mineralogy can have on the nucleation process (Deutscher and Fletcher, 1990). Furthermore, imperfections on the solid surface regularly lead to the trapping of smallest amounts of air during the initial contact of liquid and solid that can remain meta-stable even upon pressurisation. Pre-existing micro-bubbles lower the nucleation energy barrier substantially and thereby pose ideal nucleation sites for new gas bubbles (Jones et al., 1999).

2.3.2 Bubble Growth and Gas Migration

After nucleation, the gas bubble grows. The growth mechanism depends on the boundary conditions: Under constant temperature and pressure conditions and without ongoing gas production, the gas bubble grows by molecular diffusion (Jones et al., 1999). Implicitly, a persistant gas production process, like chemical reactions, microbial activity or else, can also induce increasing bubble volumes. A pressure or temperature change leads to an adjustment of the bubble volume according to equ. 2.1. When the bubble size reaches the size of the hosting pore, the subsequent growing behaviour is governed by the pore topology and the mechanical properties of the hosting soil (L. Liu et al., 2018). Additionally, with continuing growth, the mobility threshold of gas bubbles is exceeded and coalescence with other bubbles is possible.

Capillary Invasion

Once the pore body is occupied by the gas bubble, the required gas pressure to further intrude into a pore throat is given by equ. 2.2 and is depicted in fig. 2.4a in dependence of the grain diameter d. In this context, a rigid grain skeleton is presupposed. In geotechnical analyses of gassy soils this is presumed to exist in sands (L. Liu et al., 2016). On the micro-scale, capillary forces dominate over buoyancy, viscous drag, or inertial forces (C. Wang et al., 2021; Ben-Noah et al., 2023). Here, percolation is the significant migration process (Hu et al., 2020). The term percolation describes the successive, one-by-one capillary invasion of neighbouring pores (Li and Yortsos, 1995). In this process, the largest pore throat with the lowest capillary entry pressure provides the least resistance. A single gas bubble can grow to a gas cluster spanning several pores. As the growth of the gas cluster and the accompanying invasion of further pores leaves the one-by-one scheme and creates preferential pathways for single-phase gas flow, the migration pattern is called viscous fingering (Li and Yortsos, 1995; Hu et al., 2020). However, depending on the pore structure, snap-off of smaller gas clusters and their trapping within pores is also possible (Hu et al., 2020; Ben-Noah et al., 2023). As equ. 2.2 shows, this pore invasion process requires an imbalance of the acting gas and water pressures, which depend on the local pore geometry. Striving for equilibrium, local dissolution processes and molecular diffusion can transfer mass from gas clusters with high capillary pressure to gas clusters with lower capillary pressure (Mehmani and Xu, 2022). On the meso-scale, this process – known as Ostwald ripening – can lead to a stable equilibrium between several gas clusters of diverse characteristics (Mehmani and Xu, 2022).

Zooming out to a macro-scale perspective, the capillary gas migration mechanisms typically result in an incoherent flow pattern of gas clusters in which buoyancy competes with capillary pressure (Geistlinger et al., 2006; Ben-Noah et al., 2023). Van De Ven and Mumford (2020b) show that the migration pathway is not influenced by groundwater flow, but dominantly controlled by heterogeneties in the pore geometry. Gas migration in the field even takes place against the groundwater flow direction (Soares et al., 2021). Nonetheless, the migration velocity is much higher if the direction of groundwater flow and the migration direction of the gas phase coincide (Cahill et al., 2017). For that reason, the bubble distribution within a soil is difficult to predict and in consequence an upscaling of pore-scale processes to the macro-scale bears significant shortcomings (Ben-Noah et al., 2023). Nonetheless, continuum parameters, for instance effective permeabilities, are able to approximatly describe macro-scale migration characteristics. A further aspect of gas bubble migration on a larger scale is the change of pressure and temperature boundary conditions along an ascending migration pathway with a respective impact on the bubble's volume (Ben-Noah et al., 2023). As a result, the growing bubble can get trapped. The entrapment of gas during migration through a soil layer is another viable process for the formation of gassy soils (Fauria and Rempel, 2011). Additionally, soil layers of different grain sizes hinder gas bubble mobility (Plampin et al., 2014; Van De Ven and Mumford, 2020b). If gas bubbles get stuck below a soil layer, coalescence leads to significant gas saturations, potentially accompanied by gas pressure build-up. The migration direction will then change to a lateral spreading of the gas cloud (Plampin et al., 2014; Cahill et al., 2017).

Soil Fracturing

If the gas-entry pressure to a pore throat rises to a magnitude that does not allow the grain structure to remain rigid under the acting stress field, the soil fractures. Generally, this is the case for soils containing a large fraction of fines (L. Liu et al., 2016; Daigle et al., 2020; Terzariol et al., 2021). Under these circumstances, even small amounts of gas can induce fracturing and macro-pores filled with gas, as shown in fig. 2.3c, are formed in a saturated soil matrix. However, the boundary between capillary invasion and fracturing does not only depend on grain size but also on the effective stress (Fauria and Rempel, 2011; Daigle et al., 2020; Terzariol et al., 2021). Therefore, gas-pressure-induced rearrangement of soil particles and fracturing can also be a viable mechanism for soils of larger grain sizes, if the effective stress level is sufficiently low (Fauria and Rempel, 2011). To quantify the onset of fracturing, a variety of fracture criteria exist in the literature. The criteria by Stranne et al. (2016), Daigle et al. (2020), and Terzariol et al. (2021) are depicted in fig. 2.4b in dependence of the vertical effective stress σ'_v where stress states above the lines lead to fracturing. While Terzariol et al. (2021) assume the onset of fracture when the gas pressure equals the total stress, the criteria by Stranne et al. (2016) and Daigle et al. (2020) assume that the gas pressure exceeds the minor principal stress and, thus, expect lower pressures to suffice for fracture initiation. The depicted plot of the fracture criterion by Stranne et al. (2016) is based on the premise that the pore water pressure is hydrostatic and excess pressures are induced by the gas phase. The criterion introduced by Daigle et al. (2020) depends on the friction angle φ and the cohesion c of a soil. Therefore, a range spanning from a typical clay ($\varphi = 25°$, $c = 10\,\mathrm{kPa}$) on the upper boundary and a typical sand ($\varphi = 35°$, $c = 0\,\mathrm{kPa}$) on the lower boundary is plotted in fig. 2.4b. Additionally, the concept of linear elastic fracture mechanics (LEFM) is suggested for a mathematical description of the fracturing process (Daigle et al., 2020). Hereby, the soil is described as a linear-elastic continuum that exhibits a brittle fracture behaviour and is thus far from the common soil mechanical assumptions (Gross and Seelig, 2018).

The orientation of the emerged macro-pores as well as the direction of crack propagation is also governed by the effective stress state (L. Liu et al., 2018; Daigle et al., 2020). With increasing effective stress, the macro-pore shape deviates from a sphere towards an ellipsoid with a horizontal orientation of its longest principal axis (L. Liu et al., 2018; Blouin et al., 2019). When the macro-pore grows into a fracture, according to LEFM, the fracture propagates perpendicular to the minor principal stress axis (Gross and Seelig, 2018). In natural soil structures, the minor principal stress is usually oriented in horizontal direction; i. e. fractures propagate in vertical direction. This is in line with the observations by Ortiz et al. (2002), Daigle et al. (2020), and Falcon-Suarez et al. (2021). If the stress field is isotropic, e.g. at very shallow depths, there is no preferential direction of fracture propagation and local heterogeneities control the process (Daigle et al., 2020). In consequence, the macro-pores in the experiments by L. Liu et al. (2018) and Blouin et al. (2019) are oriented horizontally.

When the buoyancy exceeds the overburden pressure, macro-pores have the potential to mobilise in shallow, soft sediment (L. Liu et al., 2018). However, mostly macro-pores remain immobile with respect to the saturated soil matrix. Only the growth of the fracture can lead to a mobilisation of the gas phase. Thereby, an internal, single-phase gas flow

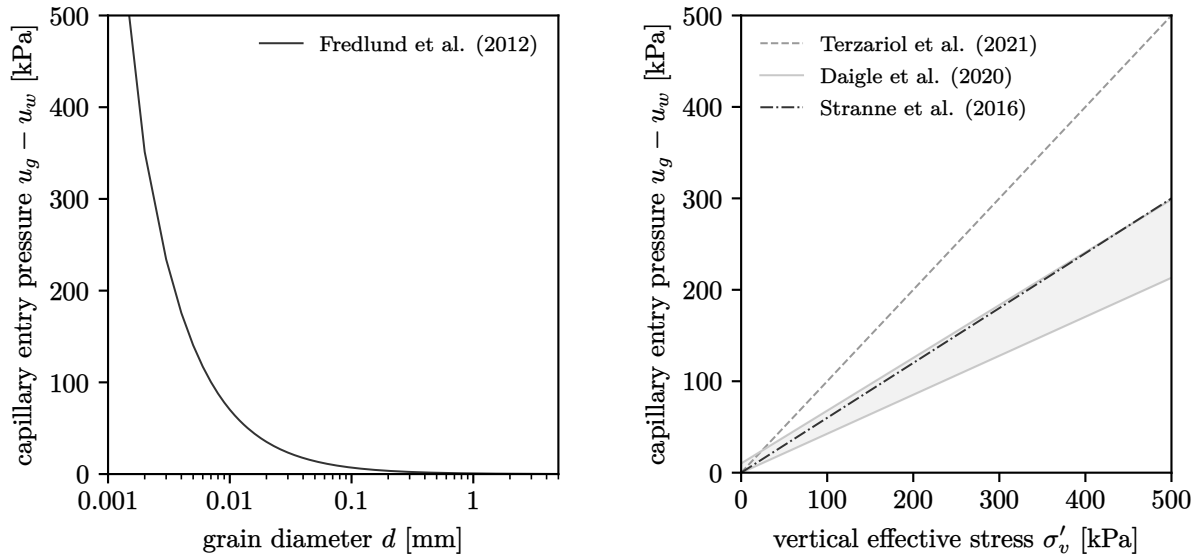

(a) capillary invasion according to equ. 2.2

(b) fracture criteria for soil

Figure 2.4: initiation criteria for gas migration

can be established along the fracture (Ben-Noah et al., 2023). Sills and Gonzalez (2001) observe a mobilisation of the gas phase at $9-12\,\%$ gas content in the soil. The gas mobility threshold Daigle et al. (2020) summarise from literature lies between $2-10\,\%$ gas content. If the fractures connect to the atmosphere or another soil layer, they allow gas escape from the host soil. Fractures thus present a very effective migration pathway. Overall, fracturing results in a higher gas mobility in fines than capillary invasion does in sands (Fauria and Rempel, 2011; L. Liu et al., 2018).

Gas migration along fractures often occurs episodically (Steelman et al., 2017; Soares et al., 2021): once the fracture opens, the gas escapes and the pressure is relieved. Thereafter, the fracture closes and gas accumulation again leads to pressure build-up and subsequent fracturing. The location of the fracture often remains the same, i. e. former fractures are reopened. The required pressure for reopening of fractures has been reported to be decreased (Falcon-Suarez et al., 2021) as well as unchanged (Ortiz et al., 2002) compared to the initial fracturing pressure.

The principles of fracture initiation and propagation as described above are generally transferable to fracture processes induced by other fluids, such as water, cement suspensions, or brine.

3 Objectives

The mechanical behaviour of multi-phase granular materials, such as gassy soil, is difficult to describe due to the multitude of influencing factors (see chapter 2). Not only the characteristics of the solid particles and the grain skeleton impact the stress-strain response, also the chemical properties of the gas and its interplay with the water phase exert a significant influence on it. Additionally, the loading, drainage, and pore flow conditions affect the overall soil behaviour. Thus, a variety of different influencing factors have to be understood in order to achieve an integrated view on the general mechanical properties of gassy soils. Consequently, the primary objective of this thesis is to perform a profound analysis of the stress-strain behaviour of gassy soils in order to foster a comprehensive understanding of gassy soil mechanics.

The summary of the current state of research in the previous chapter shows that the modest number of existing studies only provides insights into the mode of action of a limited range of influencing factors. Among these factors, there are grain size and soil type, the packing density for granular soils, gas species, and static and cyclic loading conditions. Conclusively, parameters such as the distribution of the gas phase within the sample, the impact of the pore space structure in granular soils, and the over-consolidation ratio for fine-grained soils have yet to be investigated. Moreover, the state of research reveals the lack of a consistent testing methodology. While the focus of past research consistently lies on triaxial testing, every method employed so far to prepare gassy soil samples bears significant shortcomings with respect to the sample quality. Hence, the comparability of different studies is not guaranteed. Therefore, existing sample preparation methods need to be reviewed and further developed to facilitate repeatable and comparable laboratory investigations of all relevant influencing factors in the stress-strain behaviour of gassy soils. Furthermore, existing knowledge of multi-phase flow problems in porous media has not yet been considered in soil mechanical analyses despite strong indications for mutual interference. This includes the nucleation behaviour of gas bubbles and the migration behaviour of a non-wetting gas phase in a pore network. All relevant soil mechanical investigations and interpretations rely on theoretical models of the gas phase distribution in the pore space initially developed in the 1980's, although nowadays more recent knowledge on the underlying processes is available in the literature. Besides, new technologies with the ability to verify their validity are emerging in the geotechnical context. It is therefore indispensable to incorporate this new knowledge into soil mechanical considerations. The theoretical models require experimental validation and the implications for the continuum properties of gassy soils need to be assessed.

Given the mentioned deficiencies in the current state of knowledge, the subordinate objectives to be described in the following have been derived for this study to address the existing shortcomings. To this end, a micro-to-macro approach is employed in this study. It emphasises both, the pore-scale features (micro) and the continuum behaviour (macro)

of multi-phase granular systems by combining different experimental methods. The advancement of technologies that give three-dimensional insights into the inner structure of materials, such as X-ray computed tomography (CT) and neutron imaging, but also a variety of discrete element numerical analyses, has led to their growing application in soil mechanical research with promising results (e. g. Wildenschild and Sheppard, 2013; Tengattini et al., 2021). The great potential of the micro-to-macro approach lies, thus, in the possibility to analyse micromechanical processes and extrapolate their influence to the macro-scale and thereby gain an in-depth and systematic understanding of the investigated material.

1. **Development of a Sample Preparation Methodology**
   For gassy soils, the sample preparation has a particular relevance because, generally, it is not possible to sample these soils from the field. The depressurisation accompanying the sampling process leads to gas expansion and the subsequent destruction of the soil structure. Furthermore, the applied preparation methodology has the potential to predetermine the mechanical behaviour of the resulting sample. This especially applies to the introduction of the gas phase into the soil sample. As previously outlined, particular importance is ascribed to a generally applicable, repeatable, and comparable sample preparation that reproduces the in-situ conditions as alike as possible. Additionally, for this study, the methodology has to be applicable in both, the microscopic and the macroscopic experiments, and therefore in two different test set-ups. To ensure all of the above and to create robust testing conditions, the sample preparation method has to meet the following criteria:
   - The preparation of the samples is repeatable.
   - The methodology is applicable to different soil types.
   - The properties of the soil are not altered due to the methodology of gas introduction.
   - The degree of saturation of the samples can be regulated.
   - The created gas phase is distributed homogeneously within the soil sample.
   - The introduction of the gas phase is temporally independent of the sample consolidation.

   Chapter 4 reviews existing approaches, evaluates them with regard to the aforementioned criteria, and describes further developments, improvements, and the implementation of the final sample preparation procedure.

2. **Analysis of the Macroscopic Shearing Behaviour of Gassy Soil**
   The macroscopic stress-strain behaviour of gassy soil is analysed based on triaxial testing in combination with the previously developed sample preparation methodology. Triaxial tests are commonly used to examine the shear strength in geotechnical applications and to directly infer a stress-strain relationship based on the assumed element deformation. However, the gas phase introduces a significant amount of complexity compared to the standard procedure for triaxial testing because gas diffusion, the compressibility, and the temperature dependence need to be accounted

for. Therefore, the triaxial set-up and procedure have to be adapted to the requirements of gassy soil testing. Due to the resolution of the microscopic experimental method described in the following objective, the focus of this study lies on sands. In order to investigate the effect of the characteristics and the migration behaviour of the gas phase, which depend on the morphology of the pore network, different gradations have to be tested. The triaxial set-up and procedure as well as the test results are outlined in chapter 5.

3. **Analysis of the Microstructure of Gassy Soils**
   In order to examine the microstructural processes in gassy soils, laboratory experiments were favoured over numerical analyses for the advantage of an identical sample production procedure and due to the level of development of the numerical methods available to model the fluid phases. The experimental method applied in this study is CT imaging. The method relies on the varying attenuation of X-rays in different materials based on their density. The attainable image data holds three-dimensional information and is obtained in a non-destructive manner. For this purpose, a specific test stand has to be developed that fulfills the requirements of a CT analysis in terms of space, materials transparent to X-rays, and available infrastructure in the scanning chamber, such as electricity and water supply. The evaluation of CT imaging data alone allows to determine the applicability of the theoretical pore-scale models of gassy soils and illuminate micromechanical processes. Chapter 6 gives details on the CT methodology and summarises the development of the test stand as well as the obtained image data.

4. **Assessment of the Microstructural Impact on the Continuum Stress-Strain Behaviour of Gassy Soil**
   The final objective is the interpretation of the experimental testing data in the light of both investigated scales and the determination of their interaction to establish a connection between the micro- and macro-scales. Based on this assessment, new hypotheses on the mechanical processes in gassy soils can be derived and examined in future research activities. This quintessential discussion of the experimental results is presented in chapter 7.

4 Sample Preparation Methodology for Gassy Soils

The sample preparation methodology presented in the following aims to replicate the in-situ conditions of gassy sediment at the continental slopes. Chapter 2 outlines the relevant soil characteristics. The methodology developed within the scope of this doctoral research has been published in Kaminski and Grabe (2023a) and Kaminski and Grabe (2023b).

4.1 Available Methods for Gassy Sample Preparation

Generally, the available and approved methods to prepare gassy soil samples can be summarised in three categories based on their operating principle: biological, chemical, and physical sample preparation methods (Y. Wang et al., 2021). Additionally, other experimental methods can be employed. For example, Thomas (1987) mixed polysterene beads into soil slurry to mimic gas inclusions under oedoemetric testing conditions. These experimental methods, however, will not further be taken into account due to their very limited scope of application.

4.1.1 Biological Methods

Biological methods comprise all sample preparation methods relying on the metabolism of microorganisms to produce the gas phase. The microorganisms can either occur naturally in the given soil samples, or deliberately be mixed into a soil slurry of fine-grained material before consolidation. In bioactive samples, the gas production rate can be adjusted by controlling the temperature, the amount of biomass, or the amount of available nutrients. Since the latter two factors are usually incomparable within naturally sourced samples, they are not advantageous regarding the control of the degree of saturation and the repeatablity within a test series. For instance, Sills and Gonzalez (2001) employed this method to study the self-weight consolidation behaviour of dredged harbour sediments including naturally occuring microorganisms. In naturally sourced samples, neither the amount of biomass nor of nutrients is adjustable during the experiment. Therefore, the gas production starts before the consolidation process is concluded. Even though, the temperature can be adjusted, the metabolistic processes might only be slowed down instead of stopped. In all bioactive samples, the generated gas species depends on the species of microorganisms. Moreover, microbial activity has the potential to impact the soil properties (DeJong et al., 2013). Rebata-Landa and Santamarina (2012) and He et al. (2013) applied artificial bioactive samples with microbial denitrification, thus using nitrogen (N_2) as their gas phase. Puzrin et al. (2011) implemented the production of CH_4 by anaerobic fermentation.

4.1.2 Chemical Methods

Part of the chemical methods is causing chemical reactions whose end product is a gas within the sample. The implementation is straightforward when one of the reaction partners is the pore water. The resulting degree of saturation in the sample can be controlled by adjusting the amount of chemicals added to the sample. The reacting substance is added to a soil slurry of fines to be homogeneously distributed within the sample. In this process, it is difficult to retard the reaction. The gas production will thus start before the slurry is consolidated to the targeted stress state. Furthermore, the application of this method to different soil types is challenging. In the study of Eseller-Bayat (2009), sodium perborate was brought to react with the pore water to produce oxygen (O_2) gas. Generally, other reactions and substances can also be applied. However, care should be taken whether the end products of the reaction have the potential to either contaminate the sample or affect the soil properties in other ways.
Additionally, gas production by water electrolysis can be accounted to the chemical methods. Hereby, two electrodes are mounted to the sample and a current is applied. Subsequently, by ionisation hydrogen (H_2) gas is produced at the anode and O_2 at the cathode. Due to the strongly localised gas production, the resulting gas phase is not distributed homogeneously within the sample. Moreover, depending on the sample size, the location of the electrodes, and the intended loading of the sample, the inserted electrodes bear the potential to interfere with an unhindered sample deformation. Yegian et al. (2007) implemented water electrolysis in model tests with gassy sand. The application of this method in combination with a fine-grained soil is still pending.

4.1.3 Physical Methods

All sample preparation methods that rely on a mechanical process to introduce the gas phase are summarised under the physical methods. They include a variety of approaches with very different implications.
First to name is the direct injection of any gas species or gas mixture into the sample of any soil type at any stress state through, e. g. a syringe. The injection process is pressure-controlled and easy to implement. This approach, however, bears some significant shortcomings as the local pressurisation can lead to the formation of fractures. Fractures can predetermine shear planes and thus have a considerable effect on the mechanical behaviour of the sample. As their form is dependent on local heterogeneities, they cannot be reproduced in a comparable manner within a test series. Even without fracturing taking place, direct injection leads to a very localised accumulation of the injected gas. The amount of injected gas can be controlled by the injection pressure or by a flow meter. Direct gas injection was applied in many studies, amongst others by Boudreau et al. (2005). However, the majority of them did not have a soil mechanical research objective.
Furthermore, the zeolite sieve technique is a successfully implemented approach. Zeolites are a silicate substance with high microporosity and, thus, adsorption capacity that are commercially used as molecular sieves. Depending on the type of zeolite, specific gas molecules can be adsorbed in the micropore structure. Since zeolites have a distinct affinity to polar molecules, when in touch with water the adsorbed gas molecules are exchanged

with water molecules. Gas-charged zeolites can therefore be mixed into a soil slurry and create a gassy soil sample as a consequence of the molecule exchange. The amount of gas-charged zeolites thereby controls the achieved degree of saturation. One disadvantage of the method, however, is that as in the chemical reaction method the gas production, i. e. the molecule exchange, cannot be retarded. The timing of gas production is therefore not decoupled from the consolidation process. Furthermore, with this technique the material properties of the zeolites, which are highly thixotropic, impact the soil properties. This technique was applied by Nageswaran (1983), Wheeler (1986), and Thomas (1987) with CH_4 and by Hong et al. (2018) with N_2.
Finally, the gas phase can be introduced to the sample by provoking an exsolution process from the pore water. To do so, the pore water has to be saturated with the chosen gas species. This can be implemented by dissolving gas in water in a pressure-controlled vessel outside the test stand and subsequently circulating the gas-saturated water into the soil sample by applying a pressure gradient. In order for the exsolution process to take place, the solubility limit of the gas in water at the acting temperature and pressure has to be undershot. This can be achieved either by increasing the temperature or by decreasing the pressure. Unloading offers the advantage of an instantaneous reaction, while the temperature increase relies on heat transport and therefore acts with a time lag. Possibly a strongly heterogeneous temperature and consequently gas distribution is created within the sample. Changes in temperature can also impact the soil mechanics in certain soil types (Cekerevac and Laloui, 2004). Additionally, gas exsolution can be triggered by an impact force (Rodríguez-Rodríguez et al., 2014). However, the reaction is highly dynamic which makes the control of the targeted degree of saturation difficult. Moreover, the disadvantages of a change in the soil properties caused by the impact force are evident. Both, gas exsolution by impact force or temperature increase, have never been applied in geotechnical testing.
In the pressure-driven exsolution process, an unloading step can be included in the experimental procedure to create a gassy specimen. In several studies, this approach was employed with CO_2 due to its high solubility for different types of soil (Sobkowicz and Morgenstern, 1984; Grozic et al., 1999; Amaratunga and Grozic, 2009; Sultan et al., 2012; Vega-Posada et al., 2014; Jommi et al., 2019). Rad et al. (1994) also proved the method valid with CH_4. The studies applied a trial and error procedure to determine the correct magnitude of unloading without reasonable control of the achieved degree of saturation in the sample. The exsolution process in this method is independent from the sample consolidation. In analogy to the axis-translation technique for unsaturated soils, this approach has been named the axis-translation technique for gassy soils by T. Liu et al. (2022). The comparability of the two methods arises from shifting the sample's pressure level to a range where the relevant soil properties can be observed. For unsaturated soils, this is a pressure level that avoids cavitation, while for gassy soils, it is a pressure level at which the target degree of saturation is the equilibrium condition.

4.1.4 Method Evaluation

Depending on the specific application case, all of the introduced methods can be viable. However, the objective of this study is the development of a generally applicable sample

preparation method that fulfills the criteria defined in chapter 3. In tab. 4.1, a comparison of all successfully implemented methods with respect to the defined criteria is given. None of the methods described above meets all the requirements. In conclusion, new approaches need to be developed to overcome the indicated shortcomings.
The axis-translation method for gassy soil with pressure-driven gas exsolution is most compliant with the defined criteria. A precise control of the induced sample saturation has never been implemented successfully, though. Therefore, the target of this thesis is to address this deficiency. The newly developed implementation approach relies on the precise alignment of the amount of dissolved gas and the magnitude of unloading depending on the solubility limit at the acting temperature and pressure conditions and is described in detail in the following section.

Table 4.1: overview of sample preparation methods for gassy soil and the requirements

	repeatability	homogeneous gas phase distribution	applicable to different soil types	no changes of soil properties	control of saturation	independence from consolidation process
artficial bioactive samples	✓	✓		(✓)	✓	
natural bioactive samples				✓		
chemical reactions	✓	✓		(✓)	✓	
water electrolysis	✓		(✓)	(✓)	✓	✓
direct gas injection			✓	(✓)	✓	✓
zeolite sieve technique	✓	✓			✓	
axis-translation method (pressure)	✓	✓	✓	✓		✓
axis-translation method (temperature)	(✓)	(✓)	✓	(✓)		✓
axis-translation method (impact)	✓	✓	✓			✓

notation: ✓= requirement fulfilled, (✓) = requirement possibly fulfilled

4.2 Enhancement and Implementation of the Axis-Translation Method for Gassy Soil

Even though the axis-translation method for gassy soil has successfully been put into practice by several researchers, a precise control of the sample's degree of saturation has never been implemented. Thus, the established experimental procedure is extended for this purpose and the corresponding newly developed methodology is outlined in the following. Moreover, the set-up and procedure realised in this study are described and details on the employed materials are given. All test series in this study employ the developed method with identical procedure to ensure comparability.

4.2.1 Utilised Materials

To guarantee comparability between the microscopic and the macroscopic experiments, the utilised materials are identical in both test series. To be able to account for geochemical side effects, it is important to be aware of the specific material properties.

Gas

Due to its good solubility at pressures practicable for geotechnical laboratory applications, CO_2 is chosen as the gas species in the experiments. Specifically, CO_2 with a purity of ≥ 99.95 vol-% is used because it allows to neglect partial pressures of other trace gases in the mixture in the solubility calculations. CO_2 is colour- and odourless in the gaseous state. In contrast to, e. g. CH_4, it is not flammable or explosive and, thus, easy to handle in the laboratory.
The solubility of CO_2 in water is given in fig. 2.2 for 24.85°C. Since data of solution experiments is available for a wide pressure range at this temperature, it is used as the designated temperature for all experiments. It is noteworthy that the solubility depends significantly stronger on pressure than on temperature changes.
When in touch with water, apart from solution processes, CO_2 has the potential to form hydrates. However, for 24.85°C, the required pressure for hydrate formation is ≥ 6 MPa (Fahed Qureshi et al., 2022). As the experimental pressure range is well below this value, it can be excluded that hydrate formation influences the experiments.
A small portion of CO_2 reacts with water and forms carbonic acid and the pH value of CO_2-saturated water is decreased. Therefore, a potential geochemical impact on the soil properties has to be considered when using CO_2. Some additional relevant properties of CO_2 as provided by the product supplier are summarised in tab. 4.2.

Table 4.2: properties of CO_2 (GPG Gase Partner GmbH, 2023)

molar mass	44.01 g/mol
gas density at 15°C & 100 kPa (to compare: 24.85°C)	1.85 kg/m^3 (1.79 kg/m^3)
relative density (air = 1)	1.53
sublimation point	−78.5°C
triple point	−56.5°C & 518 kPa
critical point	31°C & 7 380 kPa

Model Soils

For the experiments two model sands are employed: ISS0 sand and Hamburg (HH) sand. According to the Unified Soil Classification System (USCS) given in ASTM D2487-17e1, both sands are classified as clean, poorly-graded sands (class SP). ISS0 sand is a fine sand, while Hamburg sand classifies as a medium sand. The corresponding grain size distributions of both sands are depicted in fig. 4.1.
Hamburg sand exhibits well-rounded grain shapes with smooth surfaces. The grains of ISS0 sand show a slightly higher, but overall moderate angularity and roughness, as observable in fig. 4.2.

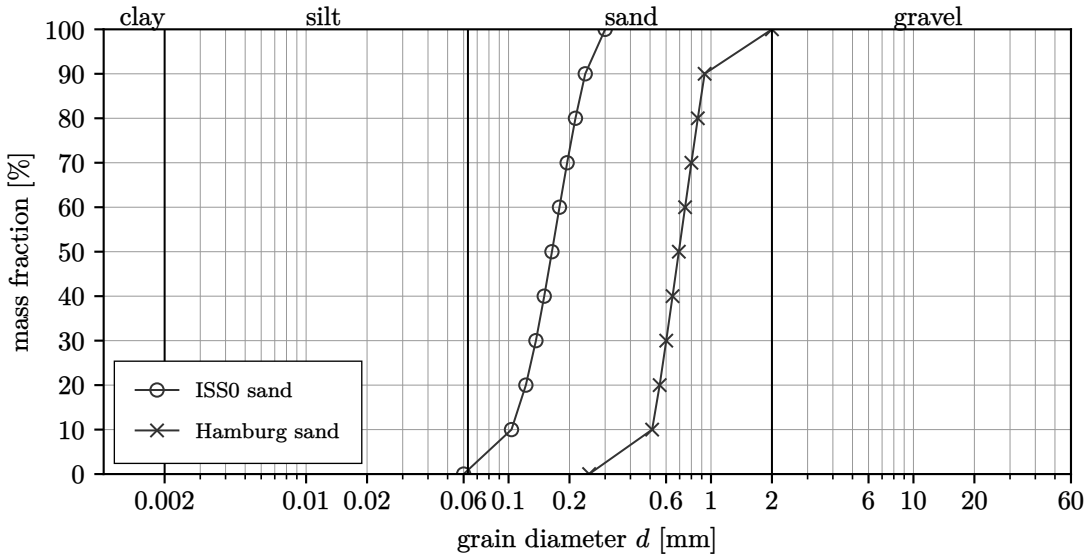

Figure 4.1: grain size distribution of the model sands

The mineralogy of both sands consists predominantly of quartz. Quartz is an inert material that is not involved in geochemical reactions with the CO_2 gas introduced during the experiments. While ISS0 sand is composed almost entirely of quartz, Hamburg sand also contains small fractions of other minerals such as feldspar. Nonetheless, $\rho_s = 2\,650\,\mathrm{kg/m^3}$ is assumed as the grain density for both soils. Several additional key parameters are given in tab. 4.3.

Table 4.3: properties of the utilised model sands

			ISS0 sand	Hamburg sand
permeability (at medium density)	k_f	[m/s]	$1.49 \cdot 10^{-4}$	$7.22 \cdot 10^{-4}$
mean grain diameter	d_{50}	[mm]	0.164	0.694
coefficient of uniformity	C_u	[-]	1.7	1.5
coefficient of curvature	C_c	[-]	1.0	0.9
maximum void ratio	e_{max}	[-]	1.020	0.813
minimum void ratio	e_{min}	[-]	0.599	0.526

4.2.2 Experimental Set-Up and Procedure

As described in section 4.1, in the axis-translation method for gassy soils, the pore water in the sample is exchanged with gas-saturated water before a pressure relief triggers the exsolution process of gas from the water. Broken down, the experimental realisation requires the steps illustrated in fig. 4.3. In order to put the described procedure into practice, the set-up shown in fig. 4.4 and fig. 4.5 was designed. The components and processes are outlined below.

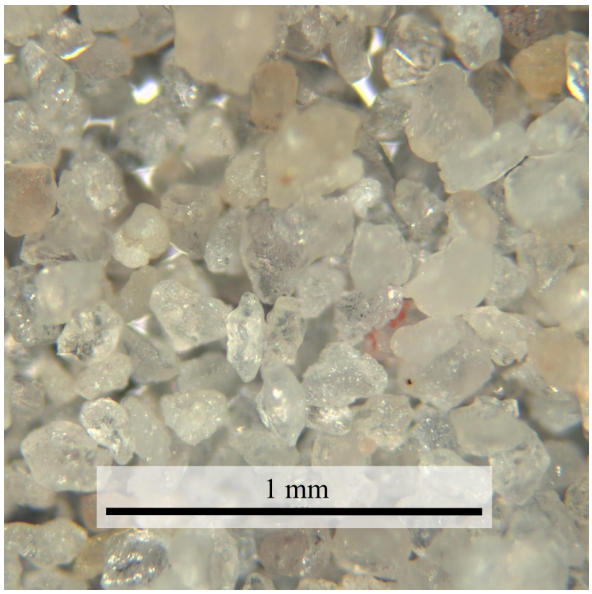

(a) ISS0 sand

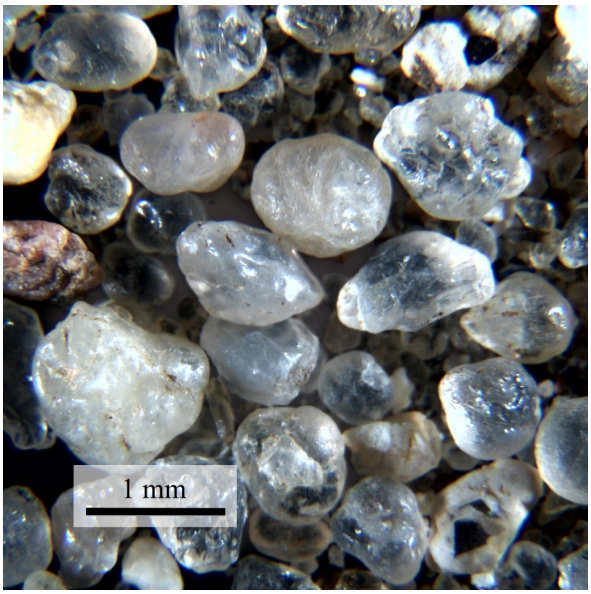

(b) Hamburg sand

Figure 4.2: microscope pictures of the employed model sands

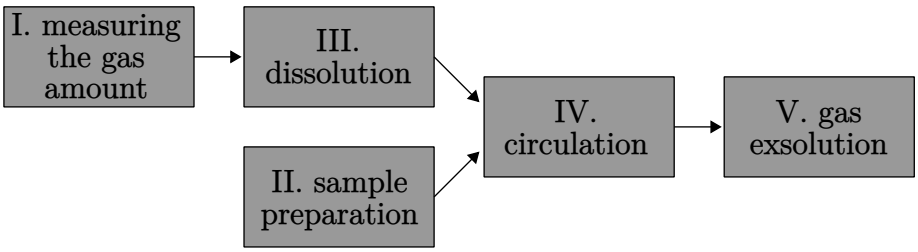

Figure 4.3: experimental procedure of the axis-translation method for gassy soils

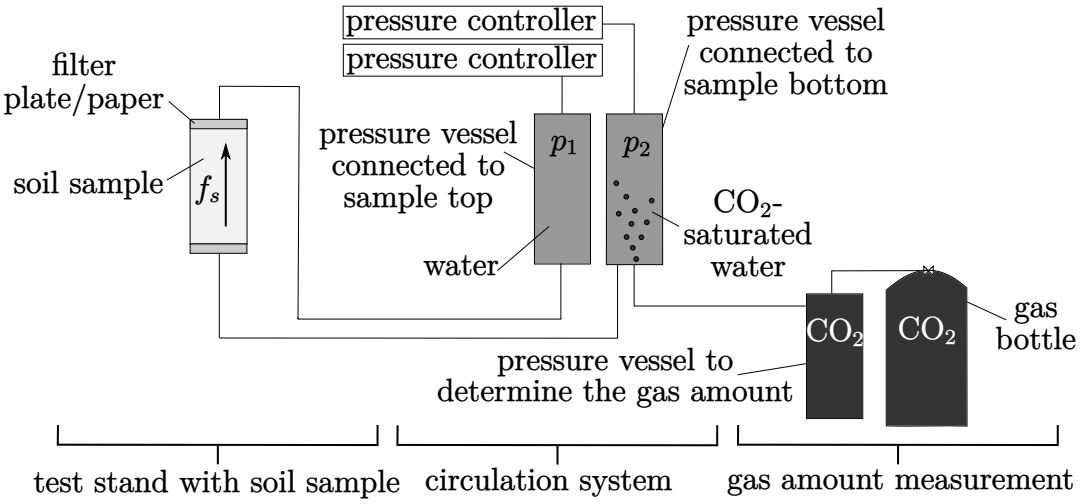

Figure 4.4: experimental set-up for gassy sample preparation

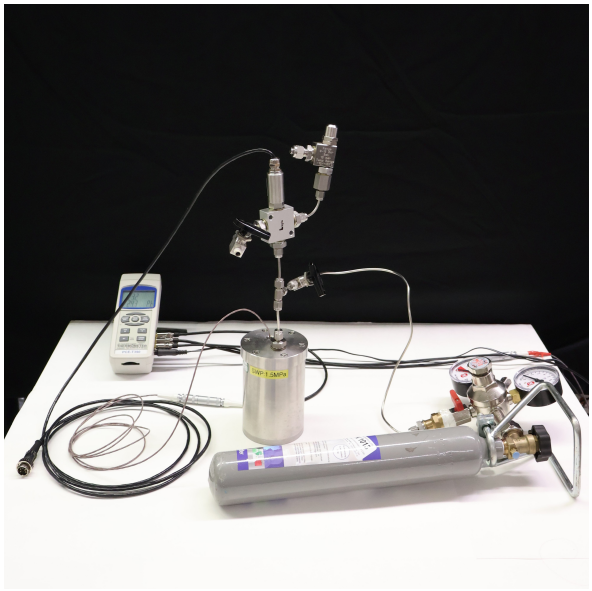

(a) set-up to measure the injected amount of gas

(b) set-up of the FTVs in the circulation system

Figure 4.5: implementation of the gas amount measurement and the circulation system

Step I: Measuring the Amounts of Gas (Solute) and Water (Solvent)

An experiment begins with the measurement of the gas amount to be dissolved and the water working as the solvent. Measuring the mass of an amount of water (m_{H_2O}) is standard laboratory procedure and is conducted under consideration of the temperature-density relation (Wagner and Pruß, 2002). The measured water is filled into the pressure vessel of the circulation system (fluid transfer vessel, FTV) that is connected to the bottom of the soil sample, i. e. the bottom FTV. Deionised water is used in this study.
In order to measure the amount of gas, the ideal gas law (see equ. 2.1) is employed: knowing the temperature, pressure, and volume, the amount of gas can be calculated. Therefore, the gas from the gas bottle is firstly fed into a stainless-steel pressure vessel of known volume. This metering vessel is equipped with a temperature and a pressure sensor. The system is depicted in fig. 4.5a.
Secondly, the valves are closed and the data is logged. Subsequently, the valves towards the water-filled bottom FTV of the circulation system are opened for the gas to escape the metering vessel. The pressures in the two vessels equilibriate. In the moment the gas enters the water, the dissolution process begins. When gas is dissolved, the pressure in the FTV decreases, allowing more gas from the metering vessel to flow into the water. Dissolution is not an instantaneous process. The process of feeding the gas from the metering vessel to the FTV, thus, requires time. The valves of the metering vessel are closed when the pressure has decreased significantly and temperature and pressure data is logged again. The difference between the initial and second measurement gives the amount of gas fed into the FTV by

$$n = \frac{p_1 \cdot V_g}{R_s \cdot T_1} - \frac{p_2 \cdot V_g}{R_s \cdot T_2}. \tag{4.1}$$

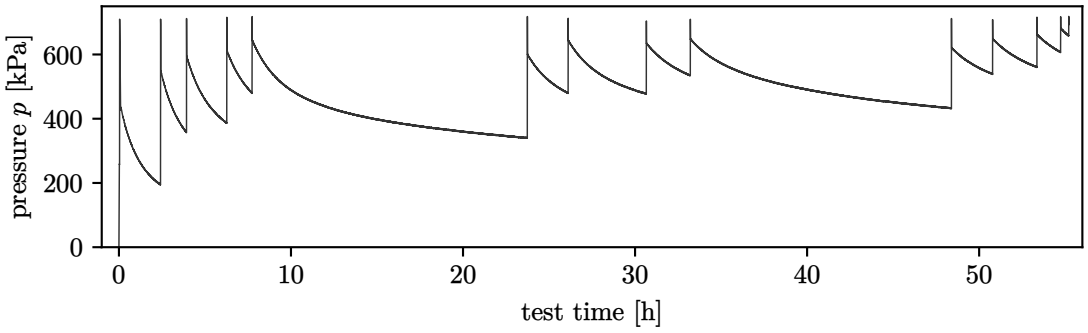

(a) pressure development

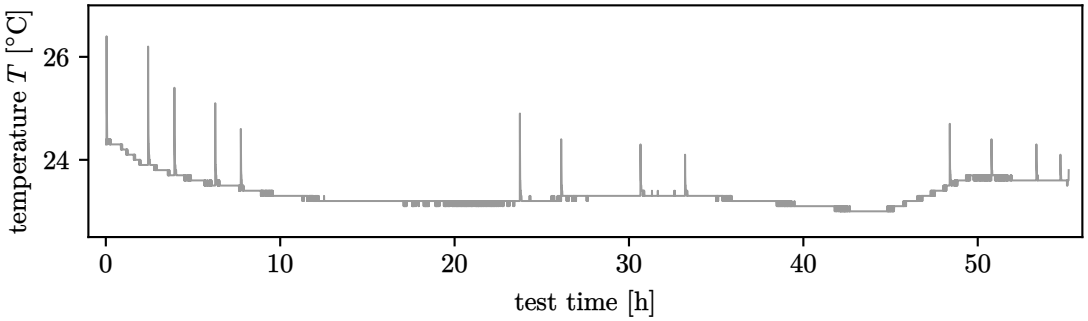

(b) temperature development

Figure 4.6: data log from an exemplary gas metering process

The process is then repeated several times until the targeted amount of gas has been fed into the FTV. The logged pressure and temperature data from a measuring process is exemplarily shown in fig. 4.6. After the measuring process, the resulting gas concentration in the bottom FTV is determined by

$$c_g = \frac{\sum n_i}{m_{\mathrm{H_2O}}} \tag{4.2}$$

from which the required unloading magnitude is derived in the later stages of the experiment.

For the macroscopic experiments, a mean gas concentration of c_g=0.18 mol/kg with a standard derivation of 0.014 mol/kg has been achieved. The microscopic experiments have been conducted at a lower pressure level with a resulting concentration of c_g=0.13 mol/kg.

The components for the gas amount measurement do not require a precise, external temperature control because the depressurisation of the gas when escaping the gas bottle and the subsequent pressurisation when entering the measuring vessel lead to inevitable temperature changes of the gas (see fig. 4.6b).

Step II: Sample Preparation

Water pluviation is chosen as the sample preparation method because it mimics natural alluvial soil diagenesis. By sedimentation through the water column, the soil can be segregated by grain size. Since the employed model soils are poorly-graded, however, the estimated impact is low. Lagioia et al. (2006) found water pluviation to be independent of depositional intensity and fall height and in consequence less operator-dependent compared to other preparation techniques. Furthermore, in the context of the axis-translation method for gassy soils, it bears the strong advantage of ensuring full saturation before the circulation and gas exsolution stages of the experiments.
In practice, the sample mould is filled with deionised water to mid-height. Subsequently, the sand is trickled into the mould with a spoon so that the content of one spoon covers the entire sample area. After five rounds of pluviation, the sample is compacted four times with light intensity by means of a tamper. The procedure is continued until the sample surface has reached the intended sample height. To ensure comparability between all experiments conducted in this study, the soil samples are prepared with identical procedures for all tests. The implementation is shown in fig. 4.7. In this study, the soil samples have been prepared with medium initial density ($0.333 < I_{D,0} < 0.667$).

Steps III & IV: Dissolution and Exchange of Pore Water (Circulation System)

The circulation system consists of two identical, water-filled pressure vessels made of Perspex cylinders (FTVs, see fig. 4.5b). Both FTVs have an individual pressure control put into practice by means of GDS Instruments pressure controllers ($200\,\mathrm{cm}^3$ standard pressure controllers for the microscopic experiments and $1\,000\,\mathrm{cm}^3$ advanced pressure controllers for the macroscopic experiments). The pressure control is connected to a nitrile bladder inside the pressure vessel. The bladder serves as a water-water interface to separate the pressure control from the free gas phase as it might interfere with a proper functioning of the controller. The two FTVs are connected to the sample bottom and sample top, respectively. As outlined in the previous section, the gas is fed into the vessel connected to the sample bottom for dissolution. The implementation is shown in fig. 4.5. Once the gas injection process is finished, the bottom FTV is pressurised to force the gas into solution. The plot of the controller volume in fig. 4.8b shows an abrupt increase upon pressurisation in the beginning when the gas is compressed according to equ. 2.1. Subsequently, a smooth increase over several hours indicates the dissolution process. The circulation system is positioned in a temperature-controlled room (room temperature of $24^\circ\mathrm{C} \pm 1.5^\circ\mathrm{C}$ in the macroscopic experiments and below $25^\circ\mathrm{C}$ in the microscopic experiments). Additionally, the FTV is pressurised to a pressure above the solubility limit to ensure a successful and complete dissolution process.
When the soil sample in the connected test stand has completed a saturation stage, a circulation stage follows (see fig. 4.8). For the circulation, the two FTVs are brought to their targeted pressures (p_1 and p_2 in fig. 4.4). When the valves towards the sample are opened, the pressure gradient induces a flow force (f_s in fig. 4.4). In the macroscopic experiments, the pressures are set to $p_1 = 950\,\mathrm{kPa}$ and $p_2 = 1\,000\,\mathrm{kPa}$, and in the microscopic experiments to $p_1 = 490\,\mathrm{kPa}$ and $p_2 = 500\,\mathrm{kPa}$. Because $p_1 < p_2$, the direction of flow within the sample is against gravity. The incipient flow transports the gas-saturated

(a) sample preparation tools

(b) sample preparation mould

Figure 4.7: implementation of the water pluviation technique for sample preparation in the triaxial test series

water into the sample. The circulation is conducted in three stages with intermittent breaks to avoid the formation of preferential flow paths (see fig. 4.8a). The duration of the circulation steps generally depends on the soil's permeability and the sample size. In the macroscopic experiments, the circulation has been conducted in 15-minutes intervals, and in the microscopic experiments in 5-minutes intervals.

Step V: Control of the Sample's Degree of Saturation

Once the pore water in the soil sample is saturated with gas, the relation of acting pore pressure and solubility limit becomes important for the proceeding experiment. This is of particular importance for the generation of a targeted saturation within the sample. S_r is defined as a volumetric relation of liquid volume V_l and pore volume V_p by

$$S_r = \frac{V_l}{V_p} = \frac{V_{tot} - V_s - V_g}{V_{tot} - V_s}. \tag{4.3}$$

and is therefore variable with pressure and temperature. S_r can also be expressed by means of the total sample volume V_{tot}, the volume of solids V_s, and the volume of gas

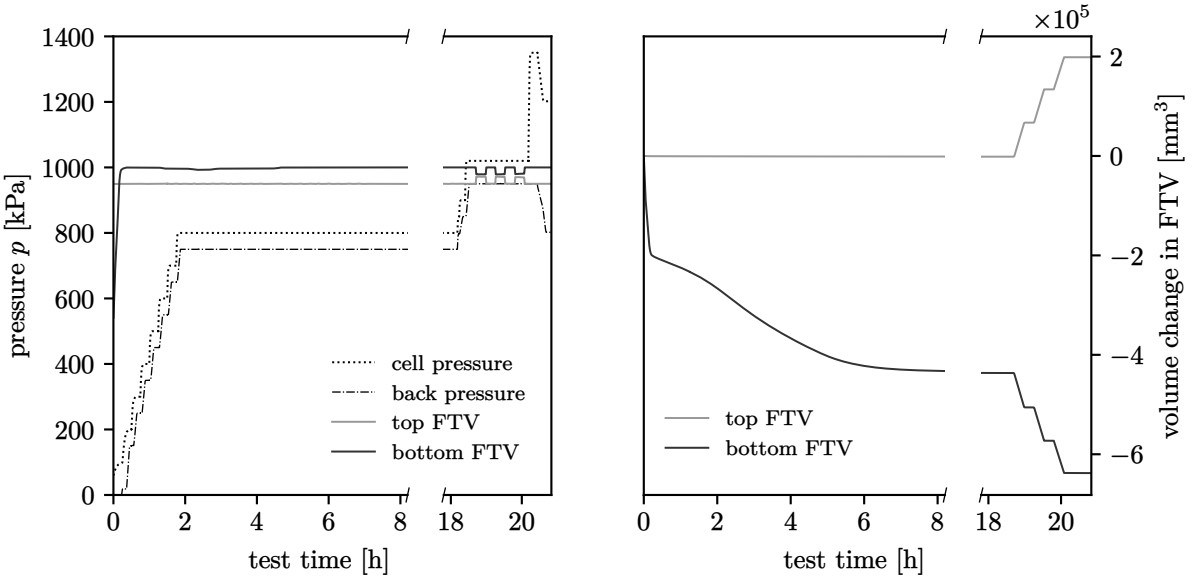

(a) pressures in the triaxial test stand and the circulation system

(b) controller volumes in the circulation system

Figure 4.8: overview of the testing procedure before the shear phase in the macroscopic laboratory experiments

V_g. The first two parameters are easy to measure precisely in the laboratory and not dependent on external parameters. They are therefore practicable for further use in the calculations. For constant temperature and pressure conditions, V_g can thus be inferred from equ. 4.3 as

$$V_g = (V_{tot} - V_s) \cdot (1 - S_r)\,. \tag{4.4}$$

To account for the pressure and temperature dependence, equ. 4.4 can be brought together with the ideal gas law (equ. 2.1), quantifying V_g as moles of free gas n_{free}:

$$n_{\text{free}} = \frac{(V_{tot} - V_s) \cdot (1 - S_r) \cdot p}{R_s \cdot T}. \tag{4.5}$$

Because under equilibrium conditions free gas only exists in a soil when the solubility limit of the pore water is exceeded, an additional quantity of gas n_{dis} has to be dissolved in the pore water. n_{dis} is related to the solubility limit via

$$n_{dis} = c_g \cdot [V_{tot} - V_s - (V_{tot} - V_s) \cdot (1 - S_r)] \cdot \rho_l\,, \tag{4.6}$$

where ρ_l is the density of the liquid. Therefore, the total amount of gas n_{tot} required to produce a specific degree of saturation is

$$n_{tot} = n_{\text{free}} + n_{dis}. \tag{4.7}$$

The maximum concentration of gas c_g is shown in fig. 2.2 for CO_2 and CH_4 at 24.85°C. The regression curve for CO_2 fitted by minimising the sum of the squared residuals is given by the function

$$c_g = 3.261 \cdot 10^{-4} \cdot p + 1.702 \cdot 10^{-3} \tag{4.8}$$

for the pressure range $0\,\text{kPa} < p \leq 1\,492\,\text{kPa}$. As shown in fig. 4.9, the pressure difference between n_{free} and n_{dis}, i. e. the required magnitude of unloading to produce the designated degree of saturation, can also be inferred from equ. 4.8. The calculation scheme presented above presumes equilibrium between the phases and is imprecise in the case of supersaturation.

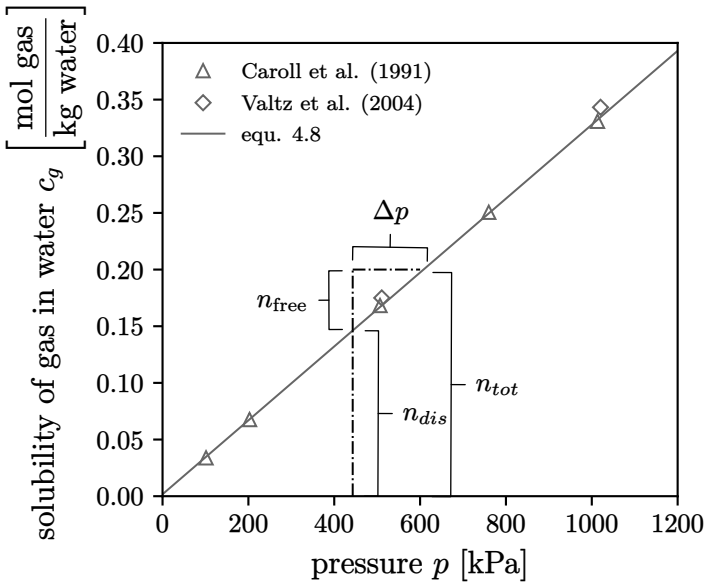

Figure 4.9: determination of the unloading magnitude based on the solubility curve in an exemplary case

5 Macroscopic Shearing Behaviour of Gassy Soil

In order to analyse the continuum stress-strain behaviour of gassy sands, consolidated undrained (CU) triaxial tests are conducted. Triaxial compression tests are assumed to evoke element deformation in the sheared samples. Thereby, a direct relation between stress and strain can be deduced. Even though triaxial testing is state of the art, the investigation of gassy soils requires more elaborate equipment and testing procedures. This chapter therefore discusses the experimental set-up as well as the particularities of gassy soil testing compared to the standardised procedures before presenting the test results. The implementation of the test set-up and the procedure employed in this study is also described in Kaminski and Grabe (2023b).

5.1 Triaxial Routine

In order to investigate gassy soil in the triaxial apparatus, the circulation system described in chapter 4 needs to be implemented in the apparatus and the accompanying procedures have to be incorporated in the testing routine. Besides the experiments on gassy samples, saturated baseline tests are conducted for all investigated parameters to facilitate comparable test results.

5.1.1 Experimental Set-Up and Procedure

To conduct triaxial tests on gassy soil samples, a triaxial apparatus is supplemented with the testing equipment required to put the axis-translation method for gassy soils into practice. An overview of the entire experimental set-up for the triaxial tests is depicted in fig. 5.1.
The employed triaxial apparatus is an advanced dynamic triaxial system which is generally fit to apply static as well as cyclic triaxial loading conditions. The system is designed for a maximum pressure of 2 000 kPa and can sustain a maximum axial load of 10 kN in the implemented configuration. The cell pressure control is realised by means of a 1 000 cm^3 advanced pressure controller. The large controller volume is necessary due to the large cell volume. In consequence, the pressure regulation of the cell is slow compared to the remaining equipment which has to be accounted for during the execution of the experiments. The back pressure control is put into practice with the help of a 200 cm^3 standard pressure controller. Both controllers also supply pressure data to the data acquisition system. For logging the pore pressure in the sample, the back pressure controller is supplemented with a pore pressure sensor. This sensor is implemented in the drainage pipe on the sample's

side of a shut off valve which protects the pressure controller from excessive gas migration into the controller during undrained shearing. The pore pressure sensor records one pressure value representative for the entire sample. Thus, no distinction between pore gas and pore water pressure can be made.
The base pedestal and top cap enclosing the soil sample are both equipped with vertical bender elements. Due to the utilisation of the bender elements, filter stones made of sintered bronze and manufactured with an opening allowing the bender elements to reach into the soil specimen are employed. Filter papers are not used and the sample ends are not lubricated to ensure proper interlocking of bender element and grain skeleton in the experiments. The base pedestal provides two drainage lines for the sample. The drainage lines are connected to the back pressure control and the bottom FTV of the circulation system, respectively. The top cap is outfitted with one drainage line which is connected to the top FTV of the circulation system. Moreover, two axial and one radial HALL effect displacement transducers are implemented in order to measure the local strains of the sample. The triaxial cell is further equipped with one PT100 temperature sensor.
The apparatus itself, all implemented sensors, and other equipment is manufactured by GDS INSTRUMENTS. Therefore, the data acquisition is put into practice by means of a proprietary acquisition pad in combination with the software GDSLAB. The system logs all data generated in the experiments, including for the axis-translation method equipment. The data acquisition for the bender element testing is realised with the software GDSBES.

The experimental procedure involved with the axis-translation method for gassy soils is combined with the standardised triaxial testing procedure. The resulting experimental steps are summarised in fig. 5.2. In the following, only deviations from or additional information to the procedure described in chapter 4 are outlined.
The sand samples prepared for triaxial testing are slender samples with a height-to-diameter ratio of 2:1. The initial height H_0 is 100 mm and the initial diameter D_0 is 50 mm. Employing the previously described water pluviation technique, samples of medium density are prepared. All samples are prepared with the identical procedure. Consequently, the samples of ISS0 sand show a mean initial specific density $I_{D,0}$ of 0.583 with a standard deviation of 0.039. Hamburg sand specimens exhibit a mean initial specific density of 0.500 with a standard deviation of 0.024. After the sample preparation, the sample is subjected to a suction pressure of -20 kPa while the local strain sensors are mounted and the triaxial cell is assembled and filled with water. The test begins with a saturation stage. The cell and back pressures are increased to 800 kPa and 750 kPa, respectively. The pressure increase is implemented in a stepwise manner due to the different response speeds of the two pressure controllers. Subsequently, a B-check with a target cell pressure of 850 kPa is conducted to verify full saturation.
During the simultaneously occuring dissolution stage, the pressure of the bottom FTV is set to 1 000 kPa in order to decrease the dissolution time frame and to ensure that all injected gas is in solution. Therefore, after the B-check, the sample's pressure state is increased to this pressure in preparation of the circulation stage. In the subsequent circulation stage, the cell pressure is 1 020 kPa and the back pressure is initially regulated to 950 kPa before the back pressure controller is shut off and the valves towards the circulation system are opened. An overview of the acting pressures during the preparatory

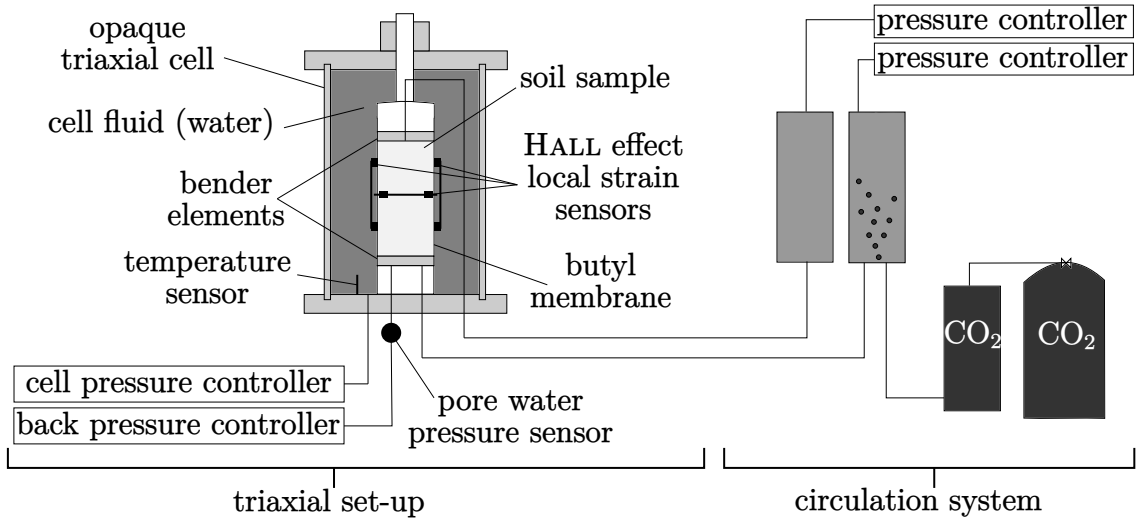

(a) schematic illustration

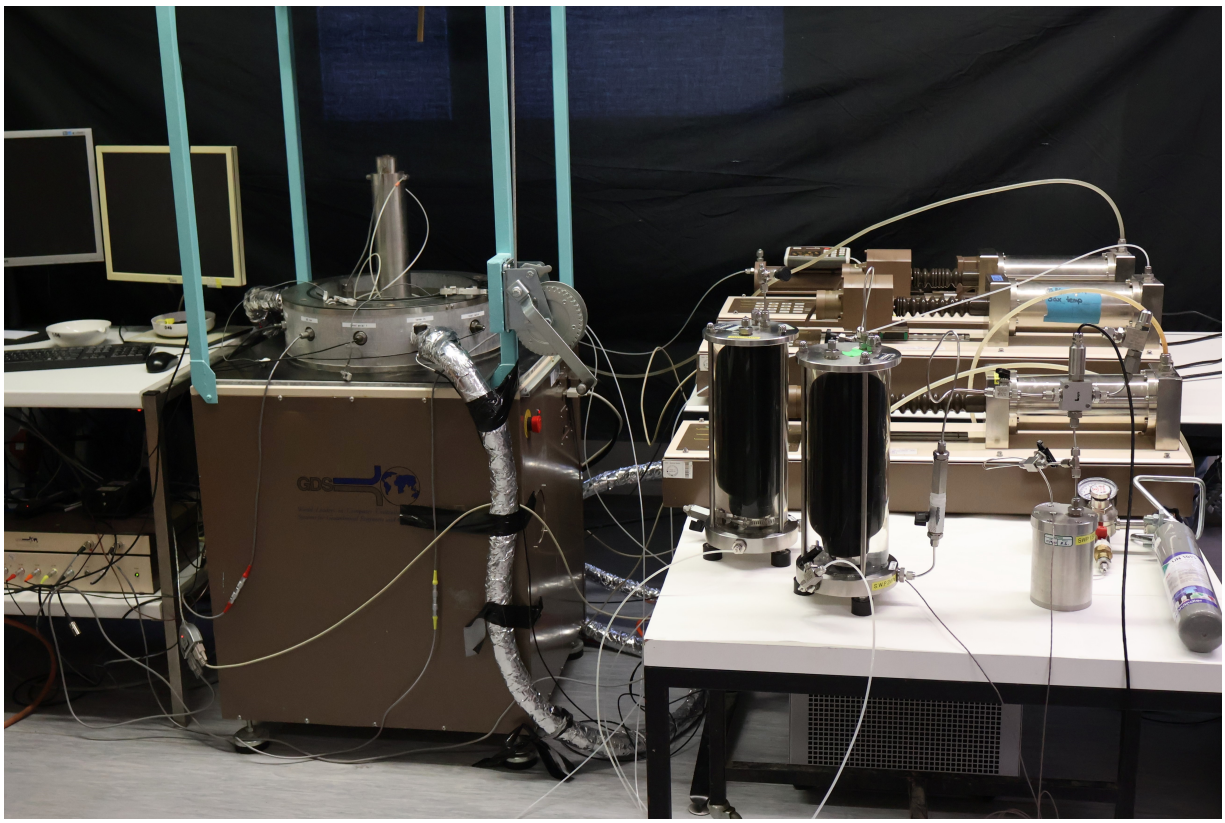

(b) implementation in the laboratory

Figure 5.1: experimental set-up for the macroscopic triaxial tests

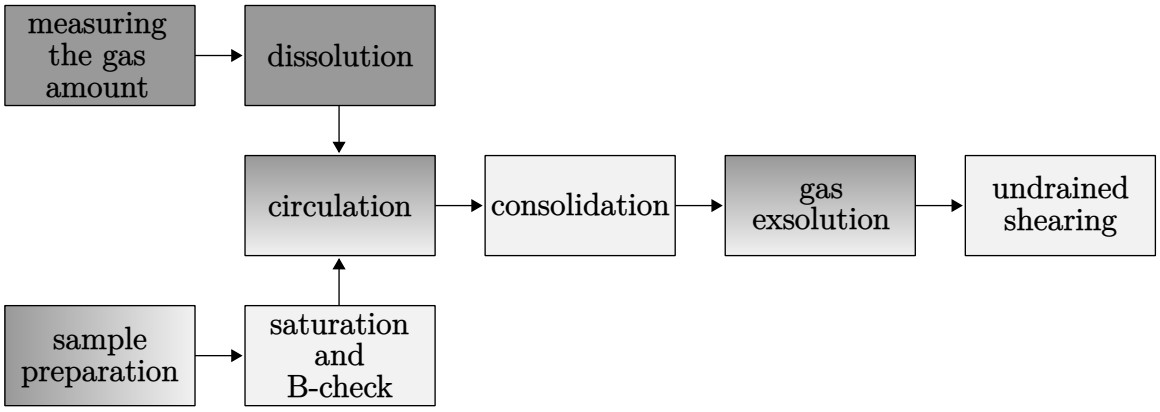

Figure 5.2: experimental procedure of the triaxial tests (*light grey*) in combination with the axis-translation method for gassy soils (*dark grey*, compare fig. 4.3)

phases of an experiment is given in fig. 4.8. The sample's pore water is then exchanged according to the circulation procedure described in section 4.2.2. The induced flow force can impact the specimen geometry and void ratio. Therefore, the saturated specimens are circulated with deaired water for better comparability. The ensuing consolidation stage applies an isotropic consolidation stress σ'_c.

To induce the gas exsolution, the designated gassy samples are unloaded isotropically in a subsequent test stage. During the unloading, the applied effective stress state is maintained. The target cell and back pressures are adjusted individually in each experiment based on the dissolved amount of gas, the target saturation, and the sample's initial void ratio. Subsequent to the gas exsolution, the drainage valve is closed to avoid gas loss from the sample. All further stages are thus executed under undrained conditions. Afterwards, the sample is docked to ensure direct loading with the subsequent beginning of the shear phase. The saturated samples lack the unloading phase but contain a docking phase before the shear phase.

The samples are sheared under monotonic loading. Since the shearing is conducted in a displacement-controlled manner, the induced stress path is governed by an increase in axial load while the confining pressure is kept constant. The shearing velocity is 0.1 mm/min and the samples are sheared to a minimum of 20 % axial strain.

The experimental procedure as described above has a time requirement of five days for a singular experiment including the preparatory gas amount measurement and dissolution as well as the subsequent sample decommissioning.

5.1.2 Overview of the Conducted Test Series

Within the scope of this study two triaxial test series were conducted: one test series for each of the introduced model soils. Besides the gradation of the investigated soil the consolidation stress as well as the target initial degree of saturation are varied. All other influencing parameters are kept constant. Thus, nine experiments per model soil are presented hereafter. Tab. 5.1 contains a summary of all performed triaxial tests.

Table 5.1: overview of the triaxial test series

denotation	test type	soil type	consolidation stress σ_c' [kPa]	target saturation S_r^* [-]	target temperature T [°C]
I200-100	CU	ISS0	200	1.00	24.85
I300-100	CU	ISS0	300	1.00	24.85
I400-100	CU	ISS0	400	1.00	24.85
I200-095	CU	ISS0	200	0.95	24.85
I300-095	CU	ISS0	300	0.95	24.85
I400-095	CU	ISS0	400	0.95	24.85
I200-090	CU	ISS0	200	0.90	24.85
I300-090	CU	ISS0	300	0.90	24.85
I400-090	CU	ISS0	400	0.90	24.85
H200-100	CU	HH	200	1.00	24.85
H300-100	CU	HH	300	1.00	24.85
H400-100	CU	HH	400	1.00	24.85
H200-095	CU	HH	200	0.95	24.85
H300-095	CU	HH	300	0.95	24.85
H400-095	CU	HH	400	0.95	24.85
H200-090	CU	HH	200	0.90	24.85
H300-090	CU	HH	300	0.90	24.85
H400-090	CU	HH	400	0.90	24.85

5.2 Specificities of Gassy Soils in the Triaxial Apparatus

The triaxial boundary conditions are altered due to the compressible nature of the gas phase as well as its chemical properties. The described triaxial set-up and procedure take several particularities into account. These are discussed in detail as follows.

5.2.1 Temperature Control

The triaxial test series are conducted in a temperature-controlled laboratory room. The room temperature is set to 24°C and is regulated with a precision of ±1.5°C. In the pressure range between 0 and 1 000 kPa the temperature dependency of the CO_2 solubility in water is minor compared to the pressure dependency (Diamond and Akinfiev, 2003). Therefore, the major objective of the experimental temperature control is to keep the cell temperature constant to avoid temperature-induced gas expansion or compression during the test and a consequent impact on the stress-strain behaviour instead of a precise match of the test and target temperatures. The utilisation of the room temperature control for the experimental temperature control is successful in achieving a constant temperature over the course of an experiment. The averaged temperature difference between begining and end of the shear phase amounts to an absolute value of 0.54°C for all gassy experiments. A general evaluation of the cell temperature in dependence of the axial strain ε_1 applied within the conducted test series is illustrated in fig. 5.3. Further data is given in appendix B.

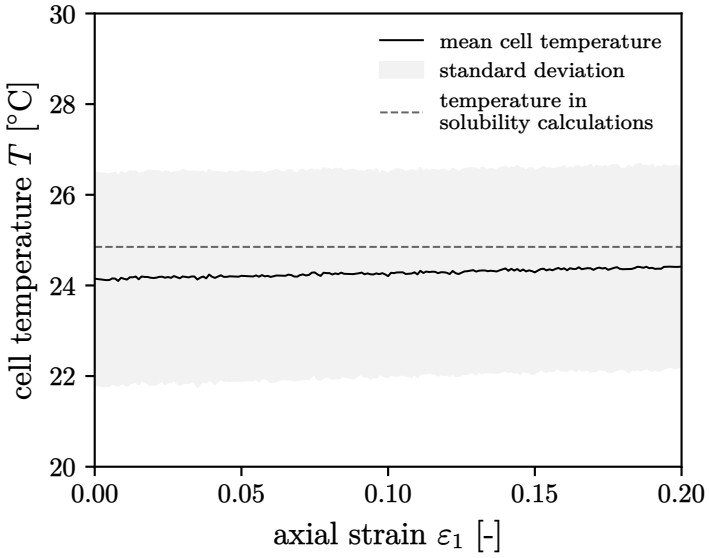

Figure 5.3: mean cell temperature and the standard deviation for all gassy experiments

5.2.2 Monitoring the Degree of Saturation

A precise control of the sample saturation, which is an explicit objective of this study, requires a reliable monitoring of the degree of saturation. Furthermore, a continuous measurement of the sample saturation allows for a broader interpretation of the data set. However, the degree of saturation cannot be measured directly but only be deduced with the help of a proxy parameter. The velocity of pressure waves (P-waves) was often used as an indicator for the saturation in past studies, though only for qualitative analyses; amongst Amaratunga and Grozic (2009) and Sultan et al. (2012).

Governing factors for the velocity of the P-wave v_p are the density as well as the shear and bulk moduli of the soil. As illustrated in fig. 2.1, the bulk moduli of the materials composing a multi-phase medium like gassy sand show significant differences. Therefore, the P-wave velocity through gassy sand strongly depends on the relative proportion of the three media, i. e. the amount of gas present in the pore space (Tamura et al., 2002; Kumar and Madhusudhan, 2012). In a more detailed consideration, the characteristics (e. g. microbubbles vs. gas-filled macropores or gas type) and the distribution of the gas phase in the sample also impact the P-wave velocity (Tamura et al., 2002; Astuto et al., 2023). However, the state of research on this matter is not sufficient to consider it in the evaluations. Regarding the other parameters varied in the test series, no impact on the P-wave velocity can be assumed for the varying consolidation stress (Ferreira et al., 2021; Molina-Gómez et al., 2023), and only a minor interference is expected to be caused by the soil type since both model soils are quartz sands with similar densities.

The P-wave velocity can be recorded by means of bender elements during triaxial testing. Bender elements are piezoceramic transducers that deform when a voltage is applied. The transducers are implemented in the pedestal and top cap of the triaxial apparatus (see fig. 5.4a) and cantilever into the soil sample. The transmitting bender element excites the sample upon deformation and thereby emits a P-wave. In this study, a sinusoidal

(a) bender elements in pedestal and top cap

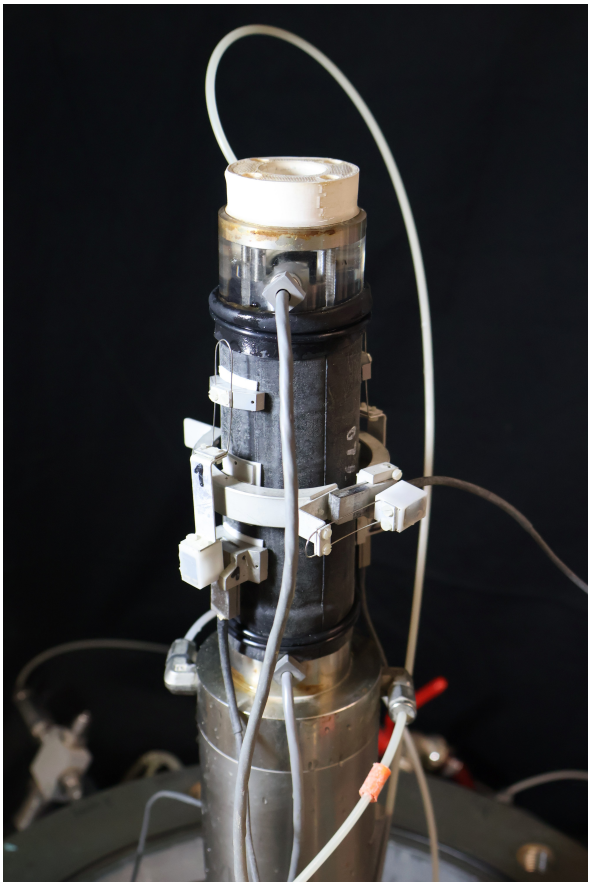

(b) HALL effect sensors on a soil specimen

Figure 5.4: sensor equipment of the triaxial specimens

excitation is applied because it was established to provide the most reliable travel time data (Ferreira et al., 2021). The amplitude of the sine pulse is 14 V and the period 0.1 ms. The opposing and receiving bender element detects the incoming wave. By comparison of the emitted and recorded signal the velocity of the wave can be inferred. To this end, multiple approaches exist – either in the time or in the frequency domain. Particularly for the specification of P-wave velocities, the difference in travel times yielded by the different approaches is insignificant (Kumar and Madhusudhan, 2012). ASTM D8295-19 suggests the peak-to-peak method for the evaluation of bender element measurements. Thus, in the following, the peak-to-peak method is employed. It is a straightforward approach relying on the identification of the first peaks respectively of the induced and recorded signal in the time domain. The interim equals the travel time of the wave. Further, the travel distance is required to calculate the velocity. Generally, the tip-to-tip distance between the bender elements, which directly depends on the sample height, is used (Ferreira et al., 2021). To determine the tip-to-tip distance it has to be taken into account that the implemented bender elements each cantilever 1.5 mm into the sample, and that the sample height during a triaxial test continuously decreases with increasing axial strain.
In order to translate the P-wave velocities into degrees of saturation, several studies are consulted. Fig. 5.5 gives the data of Gardner (1988), Eseller-Bayat (2009), Y. Wang et

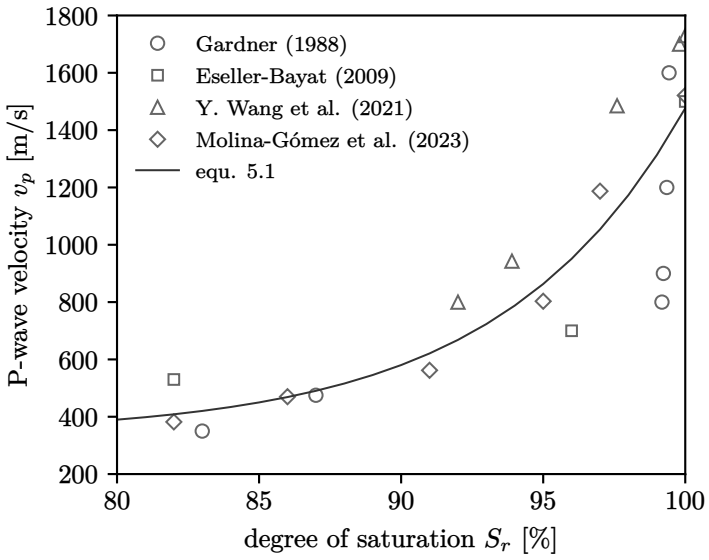

Figure 5.5: correlation between S_r and v_p based on literature data

al. (2021), and Molina-Gómez et al. (2023), who investigated the impact of enclosed gas bubbles in gassy soils on the P-wave velocity. The corresponding regression curve is given by

$$v_p \left[\frac{\mathrm{m}}{\mathrm{s}}\right] = 2.149 \cdot 10^{-4} \cdot \mathrm{e}^{0.158 \cdot S_r\,[\%]} + 338.387\,. \tag{5.1}$$

The scatter of the data plotted in fig. 5.5 is significant. This is based on the diverse testing and soil conditions, and on the dependency of the P-wave velocity on those. Consequently, an unconditional application of equ. 5.1 is inadvisable. Therefore, an exsolution experiment was conducted to verify the application within the scope of this thesis.
For the exsolution experiment, a sample was prepared analogue to the procedure illustrated in fig. 5.2. However, the gas exsolution stage was designed differently and the shear stage was omitted entirely. After the consolidation stage ($\sigma_c' = 300\,\mathrm{kPa}$), several unloading stages were executed and P-wave measurements were conducted for each unloading stage. Additionally, the theoretically expected degree of saturation based on the calculation procedure introduced in section 4.2.2 and the measurement of pore pressures and cell temperature as well as the knowledge about the sample dimensions, thus porosity, and the dissolved amount of gas is determined. However, this value can be somewhat vague because the phases in the sample are not necessarily in equilibrium directly after the exsolution process. Both values are compared in fig. 5.6 and the bender element data is presented in detail. Despite the existing shortcomings in both approaches, the fit between the P-wave evaluation and the theroretical degrees of saturation is satisfactory. Hence, P-wave velocity measurements and the introduced correlation are considered suitable for the further course of this study.
In the experiments, bender element tests are conducted in increments of 1 % axial strain. Every test implies ten single measurements at intervals of one second that are subsequently stacked and averaged to provide a more reliable reading.

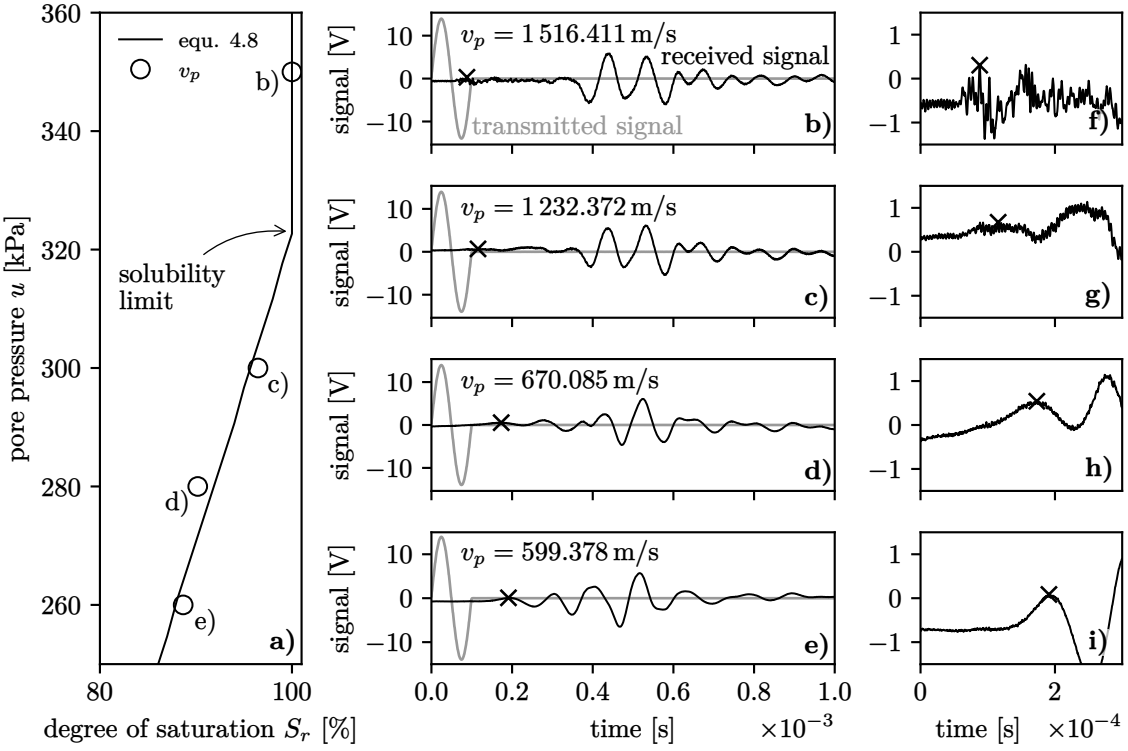

Figure 5.6: results of the exsolution experiment
a) comparison of the sample saturations derived from P-wave velocity measurements and the theoretical calculations
b) – e) results of the bender element tests
f) – i) peak identification for the peak-to-peak approach

5.2.3 Non-Isochoric Sample Deformation

Soil samples experience volume change upon triaxial compression, even under undrained conditions. The causes for volume change are the membrane penetration effect and the compressibility of the pore fluid induced by small gas inclusions (Garga and Zhang, 1997). The former can be neglected for the investigated grain sizes (Nicholson et al., 1993). The latter, however, is of particular relevance for gassy samples as the included amount of gas is substantial to the point that the assumption of isochoric sample behaviour becomes invalid. Several techniques to measure the change in sample volume exist; amongst the application of local strain sensors (Clayton and Khatrush, 1986; Garga and Zhang, 1997). Local strain measurement equipment is easy to implement in standard triaxial devices. However, it bears the disadvantage of measuring the deformation of only one section of the sample and of being designed only for small strains. In contrast to more sophisticated methods, like the application of a double cell, imperfect volumetric deformation of the entire sample thus has to be inferred from singular strain readings and can consequently be imprecise. Nonetheless, local strain measurement was opted for in this study, since the employed triaxial device is not fit to be retrofitted with a double cell.
One kind of suitable local strain sensor is the HALL effect displacement transducer. As the name implies, the operating principle of the sensor relies on the HALL effect: A magnetic

field generates a voltage in a conductor supplied by electric current. The sensor consists of a semiconductor plate and a magnetic counterpart, both installed on two independent mounting blocks. The two sensor parts are glued to the membrane and displace relative to each other upon sample deformation. When the magnet slides over the semiconductor plate, the change in voltage is recorded and translated into a displacement. The radial HALL effect sensor is constructed as an open ring enclosing the sample at mid-height. The horizontally oriented magnet and semiconductor plate thus measure the increase in mid-height sample circumference when the ring opens up during sample bulging. The HALL effect sensors and their application on a soil specimen is presented in fig. 5.4b. Compared to other frequently used sensor types (e. g. linear variable differential transducers, LVDTs), HALL effect sensors offer the advantages of being applicable in different cell fluids independent of their electrical conductivity as well as their light-weight design and easy handling. Furthermore, the measurements are not sensitive to temperature changes or vibrations. However, the linear range of the sensor is limited to $\pm 3\,\mathrm{mm}$ and is therefore too small to account for the expected radial expansion during the triaxial shear phase. For the application in this study, calibration tests were conducted to additionally exploit the non-linear regime of the sensor. Details on the calibration testing is given in appendix B.

The HALL effect displacement transducers are more sensitive than all other sensors installed in the triaxial apparatus. Additionally, the sensor accuracy is only guaranteed for the linear range and despite the calibration curves for the non-linear regime the method cannot compete in accuracy with more sophisticated sample volume monitoring methods. The measurement data can therefore be subjected to inaccuracies. Since the data directly impacts the stress calculations, the data are smoothed to avoid strong singular impacts on the stress state that are possibly artefacts caused by the method and are not representative of the sample's stress state. In case the radial expansion exceeds even the non-linear range of the sensor, the smoothed data are extrapolated based on the preceding evolution of the deformations. The smoothed measurement data are depicted in fig. 5.7a. The given sample diameters are normalised by the sample diameter at the beginning of the shear phase D_0 to support direct comparability among each other. The data show a significant deviation of the mid-height diameter from the theoretical diameter in element deformation, also in the saturated experiments. In combination with observations from the laboratory this points to a barrel-type deformation behaviour. Furthermore, the gassy samples generally show larger diameters than saturated samples. From the scatter of the data plots it can be deduced that each individual sample shows a unique bulging behaviour.

As described above, local radial strain measurement captures the radial expansion at the respective height but not the volumetric deformation of the sample. This has to be inferred from the approximated shape of the deformed sample. Even though element deformation is a prerequisite for the triaxial testing principle, it is consensus that the sample shape deviates from a perfect cylinder with increasing axial compression. Typically, slender samples adopt a barrel-type shape with its maximum diameter at medium sample height (Bishop and Green, 1965). The discussed sample deformation mechanisms are depicted in fig. 5.8. In this study, the bulging behaviour of the gassy samples during shear cannot be observed because the triaxial cell is opaque. Furthermore, the dissolved gas creates an additional obstacle. When decreasing the cell pressure to the atmospheric pressure level for sample decommissioning after the shear phase is completed, the excess gas exsolves from the pore

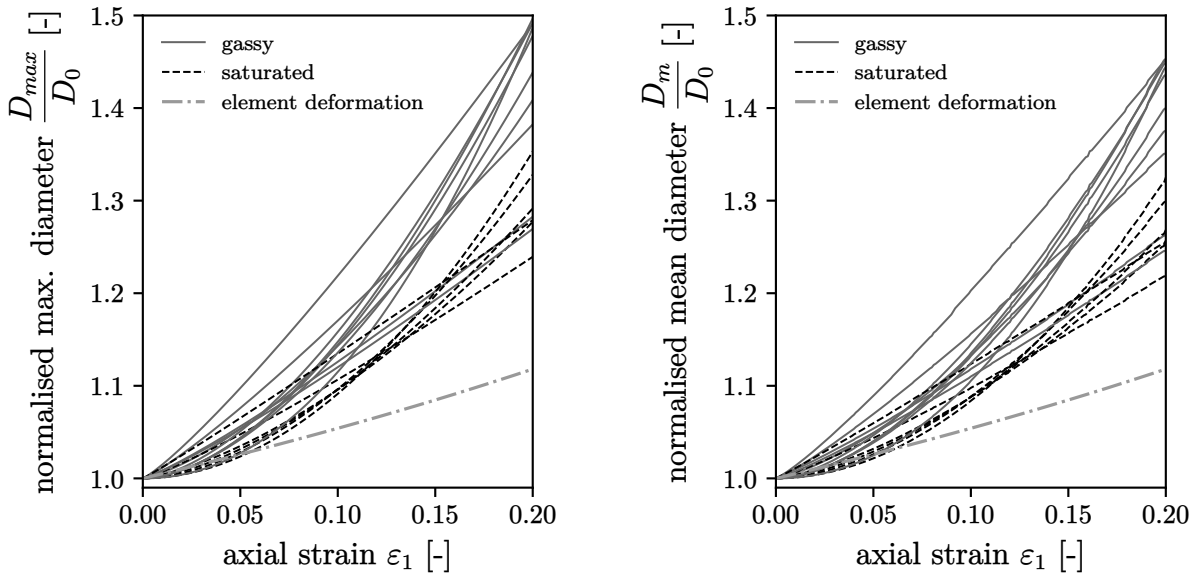

(a) maximum diameter D_{max} equivalent to the measurement data at mid-height

(b) mean diameter D_m averaged over the middle half of the sample based on equ. 5.2

Figure 5.7: sample diameter normalised with respect to the initial diameter for gassy and saturated tests compared to element deformation

water. This process leads to a severe disturbance of the sample structure. Additionally, the membrane enclosing the sample inflates and thereby conceals any remaining shear features the sample might still exhibit despite the disturbing exsolution process (see fig. 5.9).

To infer the sample's shape, the barrelling behaviour observed in the saturated baseline tests is referred to. Bishop and Green (1965) suggest to describe the barrelled sample by means of a parabolic function. In order to express the sample diameter D as a function of the sample height, the following parabolic function is therefore derived:

$$D = \frac{4 \cdot (D_0 - D_{max})}{H^2} \cdot H_{rel}^2 + D_{max} \tag{5.2}$$

in which H_{rel} is the sample height relative to the location of the radial strain sensor at medium sample height. The total sample height H can be expressed by means of

$$H = H_0 \cdot (1 - \varepsilon_1) \tag{5.3}$$

where H_0 is the initial sample height, and ε_1 is the axial strain. The initial sample diameter D_0 is assumed to describe the sample diameter at the bottom and top of the deformed sample due to the non-lubricated ends. D_{max} gives the maximum sample diameter which is assumed to occur at mid-height and thus equals the diameter measured by the radial strain sensor. All relevant variables are additionally indicated in the schematic illustration provided in fig. 5.8. The development of the sample diameter over the sample height at different axial strains is illustrated in fig. 5.10.

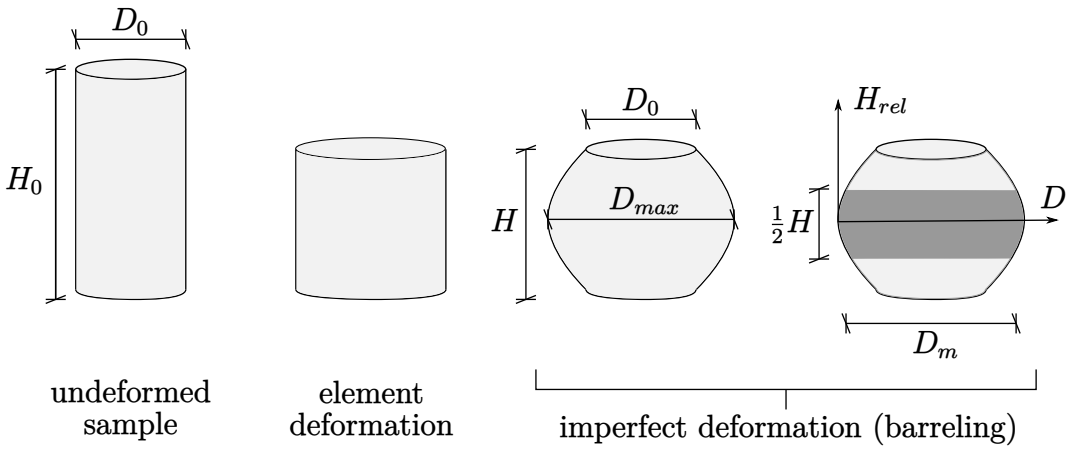

Figure 5.8: sample deformation mechanisms

(a) gassy sample at atmospheric pressure conditions

(b) sample after releasing the exsolved excess gas

Figure 5.9: sheared gassy sample after relieving the cell pressure with subsequent exsolution of the dissolved excess gas

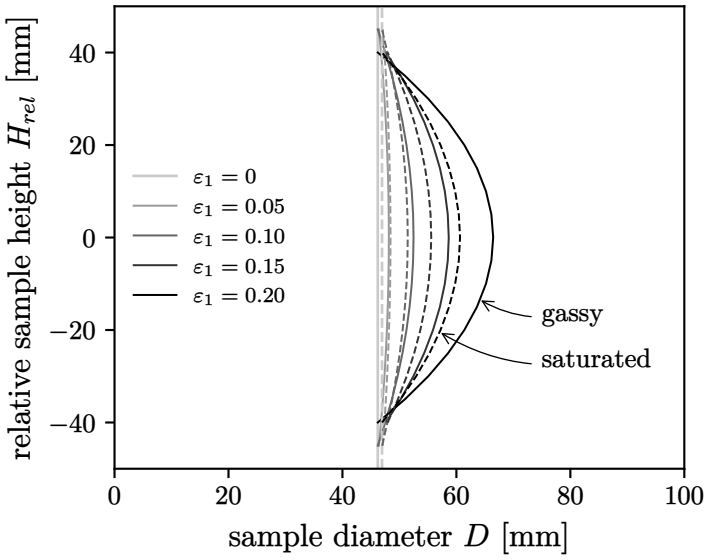

Figure 5.10: sample diameter D over the height of the sample according to equ. 5.2; exemplarily for tests H400-100 and H400-090

Being able to describe the shape and volumetric deformation of the entire sample, the averaged sample area entering into the stress calculations can be derived. For this purpose, several approaches are suggested in the literature (e. g. Bishop and Green, 1965; Zhang and Garga, 1997; Omar and Sadrekarimi, 2014). While Bishop and Green (1965) showed that the effect on the resulting friction angle is marginal, Omar and Sadrekarimi (2014) demonstrate a noteworthy impact of area correction on the shear strength. In this study, the average cross-sectional area of the middle half of the sample derived by means of the mean diameter in this sample section D_m is used for the stress calculations (as indicated in dark grey in fig. 5.8). This approach ranks in the intermediate range of the approaches proposed by Bishop and Green (1965), Zhang and Garga (1997), and Omar and Sadrekarimi (2014) in terms of its influence on the shear stresses. The normalised mean diameter derived thereby is shown in fig. 5.7b. In comparison to the measured maximum diameter no substantial convergence towards the diameter in the ideal case of element deformation occurs. It can therefore be concluded that this approach results in smaller shear stresses due to the larger mean sample area compared to the element deformation assumption. Nonetheless, it depicts the stress state more realistically and is hence considered adequate for further calculations.

5.2.4 Prevention of Gas Diffusion from the Sample

Striving to create equilibrium, molecules of the dissolved gas diffuse along the chemical gradient to areas of lower gas saturation. The tendency for diffusion is often more pronounced for gases with a high solubility because the acting concentration gradients in the solvent are generally higher. The impact of diffusion should thus be considered for applications with CO_2. In the given set-up for triaxial testing, gas diffusion is of particular relevance since the specimen is surrounded by the cell water, which exhibits a signifi-

cantly lower CO_2-saturation than the pore water of the sample after the circulation stage. Hence, the diffusive forces are large enough to cause substantial gas loss from the sample. Consequently, measures have to be employed to prevent diffusion from the sample's pore water to the cell water as well as the resulting inaccuracy of the unloading magnitude and produced degree of saturation. In previous studies, this challenge was tackled by using multiple latex membranes with an intermediate grease layer and even by additionally attaching aluminium foil sheets on the outer membrane (Amaratunga and Grozic, 2009; Sultan et al., 2012). However, the handling in the laboratory is cumbersome. Therefore, butyl membranes are employed in this study. Butyl is a gas-tight material that allows for the use of a singular membrane and is thereby comparably easy to process in the laboratory. The butyl membranes exhibit a thickness of $t_m = 0.4\,\text{mm}$ which is twice the thickness of conventional latex membranes. Additionally, the material is stiffer. Therefore, membrane effects have to be accounted for.
In triaxial testing the term "membrane effects" generally summarises membrane penetration and the influence on the sample's stress state due to the restriction of the radial expansion. As already established in the previous section, membrane penetration can be neglected. To incorporate the membrane's hoop tension in the stress calculations all relevant standards offer validated approaches. However, these approaches are designed for the use of a single and conventional latex membrane. Therefore, the material properties of the butyl membranes need to be assessed in order to apply the standardised stress correction approaches. The ASTM D4767-11 suggests a straightforward testing procedure to evaluate the Young's modulus of the membrane material in which a circumferential strip of 15 mm width is stretched while measuring the tensile force and the displacement. The implemented experimental set-up according to ASTM D4767-11 is depicted in fig. 5.11a. The application of HOOKE's law yields the Young's modulus of the membrane E_m as shown in fig. 5.11b. The plotted mean E_m is evaluated based on four tests and can be approximated in dependence of the dimensionless radial strain ε_{rad} by

$$E_m\ [\text{kPa}] = 1\,509.265 \cdot |\varepsilon_{rad}\ [-]\,|^2 - 1\,628.715 \cdot |\varepsilon_{rad}\ [-]\,| + 1\,427.167 \tag{5.4}$$

to be incorporated into the evaluation scheme for the triaxial tests. ε_{rad} depends on the change in sample diameter:

$$\varepsilon_{rad} = \frac{D_0 - D}{D_0}\,. \tag{5.5}$$

All strain parameters are defined positive for compression and negative for expansion in line with the triaxial testing conventions. Equivalent to the calculation of the relevant sample cross section for the stress calculations, the mean diameter D_m averaged over the middle half of the sample's height and inferred from equ. 5.2 is consulted to implement the membrane correction.

5.3 Evaluation Scheme

A standardised evaluation scheme for undrained triaxial testing is suggested in ASTM D4767-11 and DIN EN ISO 17892-9, which are widely identical. The suggested procedure is partly adapted to account for the particularities of gassy soils and to make the best

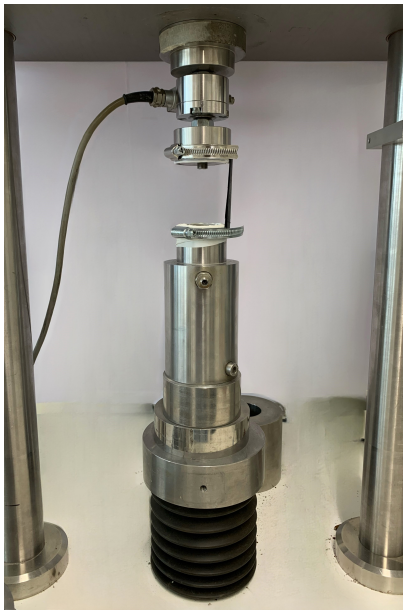

(a) experimental set-up

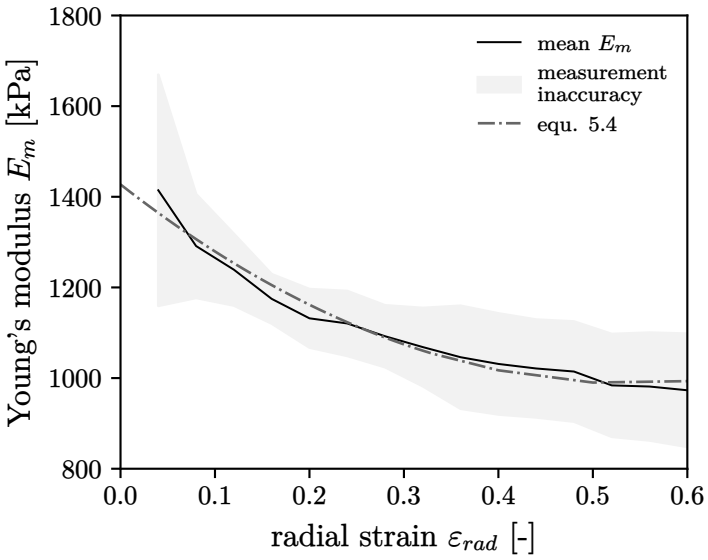

(b) resulting Young's modulus

Figure 5.11: examination and evaluation of the Young's modulus of butyl membranes according to ASTM D4767-11

use of the additional sensor equipment. In the following, the data evaluation procedure applied for all triaxial tests is outlined. Individual changes in the procedure in case of sensor failure or other disturbances are marked in tab. 5.2.

5.3.1 Specimen Properties

The standards stipulate to determine several basic specimen properties before the beginning of each experiment. All relevant parameters at the beginning of an experiment are summarised in tab. 5.2 for all specimens. Here, all parameters at the beginning of the shear phase are indicated with the index 0.
Due to the application of the water pluviation method for the sample preparation, the degree of saturation after preparation is assumed to be $S_r = 100\,\%$ for all tested specimens. This assumption is verified by conducting a B-check after the saturation stage. The B-check is considered successful, and hence the sample saturated, when the B value is

$$B = \frac{\Delta u}{\Delta \sigma_3} \geq 0.9\,. \tag{5.6}$$

Δu and $\Delta \sigma_3$ are the changes in pore and cell pressure, respectively. B is allowed to assume smaller values than in the standard because the technically conditioned slow regulation of the cell pressure leads to a lower precision in B.
Furthermore, the sample properties after the consolidation phase play a role. In gassy soil triaxial testing, this state is equivalent to the sample conditions after the gas exsolution and docking of the sample, i. e. at the beginning of the shear phase.

The specimen height at the beginning of shear is derived from the local axial HALL effect sensor data as well as from the axial displacement data of the pedestal. Since the local axial strain sensors only measure the deformation of the sample between the two mounting blocks of the sensor, the displacement of the entire sample cannot be inferred directly. A combination of the two measurements results in a reliable procedure.
The cross-sectional area of the sample is inferred from the sample diameter at the beginning of the shear phase recorded by the local radial HALL effect sensor together with the approach described in section 5.2.3.

5.3.2 Shear Data

The basic shear parameters are determined according to the approaches in the standards for the entire length of the shear phase. Thus, the axial strain of the sample ε_1 is calculated by

$$\varepsilon_1 = \frac{H_0 - H}{H_0} \tag{5.7}$$

and the deviator stress according to

$$\sigma_1 - \sigma_3 = \frac{F}{A}\,. \tag{5.8}$$

σ_1 and σ_3 are the principal stresses in axial and radial direction, respectively. F is the force measured by the load cell. The sample's cross-sectional area A is continuously derived from the diameter given by the radial strain sensor data which is then averaged over the middle half of the sample, as described above.
The correction for filter paper is not employed because no filter papers are used in the experiments. The correction for the rubber membrane, however, is important. As elaborated in section 5.2.4, the Young's modulus of the membrane is determined according to equ. 5.4. Based on this, the membrane specific correction value for the principle stress difference $\Delta\left(\sigma_1 - \sigma_3\right)_m$ is given by

$$\Delta\left(\sigma_1 - \sigma_3\right)_m = \frac{4 \cdot E_m \cdot t_m \cdot \varepsilon_1}{D_0}\,, \tag{5.9}$$

which is subsequently taken into account in the corrected deviator stress $\left(\sigma_1 - \sigma_3\right)_c$ by

$$\left(\sigma_1 - \sigma_3\right)_c = \frac{F}{A} - \Delta\left(\sigma_1 - \sigma_3\right)_m\,. \tag{5.10}$$

The membrane correction is employed for the entire test length independent of the magnitude of the correction value compared to the minimum threshold value in the standard.
The effective minor principle stress σ_3' is determined by

$$\sigma_3' = \sigma_3 - u \tag{5.11}$$

and the effective major principle stress σ_1' by

$$\sigma_1' = \sigma_1 - u \tag{5.12}$$

according to TERZAGHI's principle of effective stress in equ. 2.4. Thereby, the assumptions proposed in the geotechnical literature on gassy granular soils are adopted (see chapter 2). u is the pore pressure recorded by the pore pressure transducer as the back pressure controller is shut off during the shear phase. The induced pore pressure Δu is determined by

$$\Delta u = u - u_0 \tag{5.13}$$

where u_0 is the pore pressure in the beginning of the shear phase.
Finally, the volumetric strain ε_{vol} of the sample is derived by means of

$$\varepsilon_{vol} = \frac{V_0 - V}{V_0} = \frac{D_0^2 \cdot H_0 - D^2 \cdot H}{D_0^2 \cdot H_0} \tag{5.14}$$

and thereby relies on the local radial strain sensor data in combination with equ. 5.2. Here, V describes the sample volume and V_0 the initial sample volume at the beginning of the shear phase. In contrast to the calculation of the sample's cross-sectional area the entire sample height is consulted to derive the sample volume. H is determined by equ. 5.3.

5.3.3 Advanced Parameters

For the graphical representation of the data and the determination of the effective friction angle φ' and cohesion c', the parameters

$$t = \frac{(\sigma_1 - \sigma_3)_c + 2 \cdot \sigma_3'}{2} = \frac{(\sigma_1' + \sigma_3')}{2} \tag{5.15}$$

and

$$s = \frac{(\sigma_1 - \sigma_3)_c}{2} \tag{5.16}$$

are required. The shear parameters can be determined by deriving the gradient of the failure plane α' as well as the intercept with the ordinate axis k in the t-s diagram of three tests at different consolidation stresses. For the construction of the failure plane the maximum shear stresses are defined as the failure criterion. The effective friction angle is then given by

$$\sin(\varphi') = \tan(\alpha') \tag{5.17}$$

and the effective cohesion by

$$c' = \frac{k}{\cos(\varphi')}\,. \tag{5.18}$$

Further advanced parameters are based on data from the additional sensor equipment in the triaxial cell. This refers, for example, to the degree of saturation S_r which is derived according to the P-wave velocity evaluation procedure outlined in section 5.2.2 and from equ. 5.1.

5.4 Triaxial Testing Results

The triaxial testing results achieved with the methodology described above are outlined hereafter. However, not only the shear stage but all stages of an experiment impact the soil sample. Thus, a brief overview of the stages before shearing is provided first. Thereafter,

the shear data is presented. Supplementary to the compilation of information on the experimental test series above (tab. 5.1), tab. 5.2 summarises the relevant properties of the samples after the sample preparation as well as at the beginning and the end of the shear phase. In the following, the designated target degree of saturation of an experiment is indicated by S_r^* while S_r refers to the measured and variable saturation during the experiment.

5.4.1 Overview of the Sample Properties Before Shearing

For every sample, a B-check is conducted after the saturation phase. In all experiments, the B-checks fulfill the criterion defined in equ. 5.6 and, thus, confirm the initial assumption of full saturation based on the employed water pluviation method.
In all gassy experiments, the samples experience a significant increase in pore pressure compared to the cell pressure during the unloading and exsolution stage of the testing procedure; exemplarily shown in fig. 5.12. This pore pressure increase is caused by the exsolution process itself and is based on the spatial requirements involved with the formation of a third phase. As a result, a substantial derivation between the consolidation stresses and the effective stresses at the beginning of the shear stage occurs (compare tab. 5.2). Additionally, in combination with the constant development of the sample geometry in this stage, it can be concluded that a relevant part of the induced supersaturation is expressed by creating a pressure equilibrium instead of putting the gas exsolution into effect by volumetric expansion. Possibly, the reason is an obstruction of the volumetric expansion by the grain structure of the soil. Although both mechanisms – pressure or volume increase – can involve the same amount of exsolved gas in terms of moles, it will impact the degree of saturation as it is a volumetric measure. This is a potential reason why the degrees of saturation at the beginning of the shear stage do not match the target saturations.

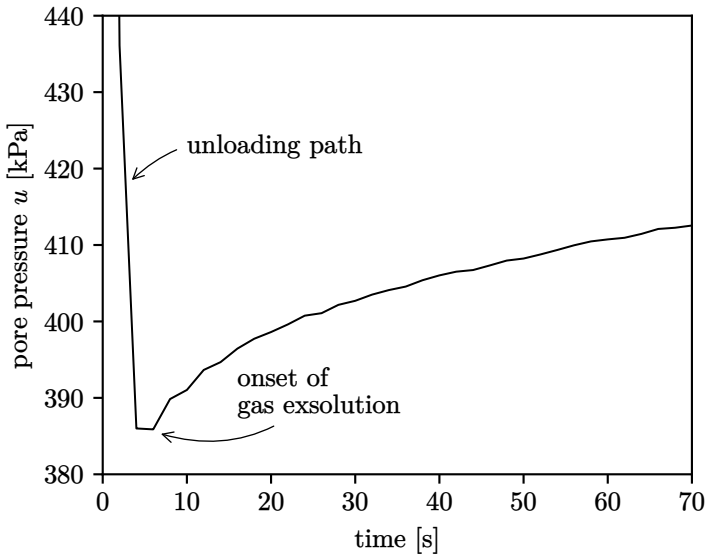

Figure 5.12: pore pressure increase as a consequence of gas exsolution after unloading; exemplarily shown for the unloading stage in test H400-090

Table 5.2: overview of the sample properties of the triaxial test series after preparation as well as in the beginning and end of the shear phase

denotation	sample properties after preparation			initial	initial	final	temperature
	void ratio	density	dry unit weight	effective stress	saturation	saturation	change
	e_{prep} [-]	$I_{\text{D,prep}}$ [-]	γ_d [kN/m^3]	$\sigma'_{1,0}$ [kPa]	$S_{r,0}$ [-]	$S_{\text{r},\varepsilon_1=0.2}$ [-]	ΔT [°C]
I200-100	0.770	0.593	14.683	204.749	–	–	–
I300-100	0.775	0.582	14.645	300.945	–	–	–
I400-100	0.770	0.594	14.688	416.666	–	–	–
I200-095*	0.807	0.507	14.390	107.919	0.982	0.914	0.136
I300-095	0.792	0.541	14.504	210.269	0.992	0.921	1.254
I400-095	0.763	0.610	14.742	312.183	0.988	0.922	0.602
I200-090	0.759	0.620	14.780	48.295	0.912	0.909	−0.105
I300-090	0.778	0.575	14.621	177.609	0.984	0.919	1.454
I400-090†	0.755	0.630	14.816	209.375	0.939	0.921	−0.312
H200-100	0.659	0.492	15.673	235.589	–	–	–
H300-100*	0.659	0.490	15.668	255.986	–	–	–
H400-100	0.655	0.507	15.712	409.540	–	–	–
H200-095	0.658	0.494	15.679	143.882	0.994	0.919	−0.776
H300-095	0.671	0.449	15.561	241.120	0.937	0.934	−0.006
H400-095	0.653	0.512	15.726	352.305	1.000	0.942	−0.025
H200-090	0.653	0.512	15.725	179.830	0.938	0.914	1.284
H300-090	0.655	0.507	15.712	277.606	0.936	0.925	0.166
H400-090	0.645	0.540	15.799	370.049	0.948	0.938	−0.330

* failure of local radial strain transducer: averaged circumference data of tests with identical soil type and saturation are used

† local radial strain transducer gives implausible values

5.4.2 Shear Data and Interpretation

After the gas exsolution and the docking of the top cap to the load cell, the sample is sheared to a minimal axial strain of $\varepsilon_1 = 0.2$ with a shearing velocity of 0.1 mm/min. The data recorded during the shear phase is presented and interpreted as follows.

Deviator Stress

The acting deviator stress during shear is depicted in fig. 5.13. The saturated samples reach a distinctive maximum before showing a decrease in deviator stress, which is an expected response for medium dense sands. ISS0 sand exhibits higher shear stresses than Hamburg sand in the saturated state. In tendency, the peak stress is lower for samples with lower consolidation stresses. This feature can also be observed in the gassy experiments. Generally, the gassy experiments show significantly lower shear stresses compared to the saturated baseline tests. Also, the expression of the peak in the stress path is not as distinct. Nonetheless, the maximum deviator stresses are reached in a similar range of axial strains. In contrast to the saturated state, Hamburg sand tends to show higher shear stresses in the gassy state than ISS0 sand. Thus, the negative impact of the gas on the stress-strain behaviour is less pronounced for the coarser gradation. Regarding the difference between the experiments with varying target saturations, an antithetical effect can be identified for the two gradations. For gassy ISS0 sand, lower maximum deviator stresses are reached in experiments with lower initial saturations. In contrast, for gassy Hamburg sand, samples with higher initial saturations show the lowest peaks in deviator stress. All maximum deviator stresses and their corresponding axial strains are summarised in tab. 5.3.

Induced Pore Pressures

The explanation for the profound gas-induced changes in the deviator stress can be sourced in the development of the pore pressures during the shear process; see fig. 5.14. Under drained conditions, saturated medium dense samples would initially compact until reaching the maximum density and subsequently dilate under shear loading. Under undrained and saturated conditions, the specimens exhibit an identical response, which is, however, prohibited by the incompressibility of the water and the resulting constant volume deformation. Hence, the pore pressure adjusts accordingly: Initially, an increase in induced pore pressure can be recorded which is followed by a decrease. Here, the peak of the induced pore pressure curve indicates the transition from contractive to dilative deformation behaviour in the drained equivalent. When negative pore pressures below the atmospheric pressure level are reached, the pressure remains constant. This behaviour is probably caused by small air inclusions in the sample, which occur despite the preparation procedure and become relevant due to the induced suction pressures.
A fundamentally different behaviour can be observed in the experiments on gassy samples. Here, the induced pore pressures remain largly constant during the entire shearing process, thus resulting in significantly lower effective stress. The constant path of the induced pore pressure curve settles at an absolute pressure around the solubility limit. In a detailed analysis, it has to be noted that, like in the saturated tests, some experiments on gassy

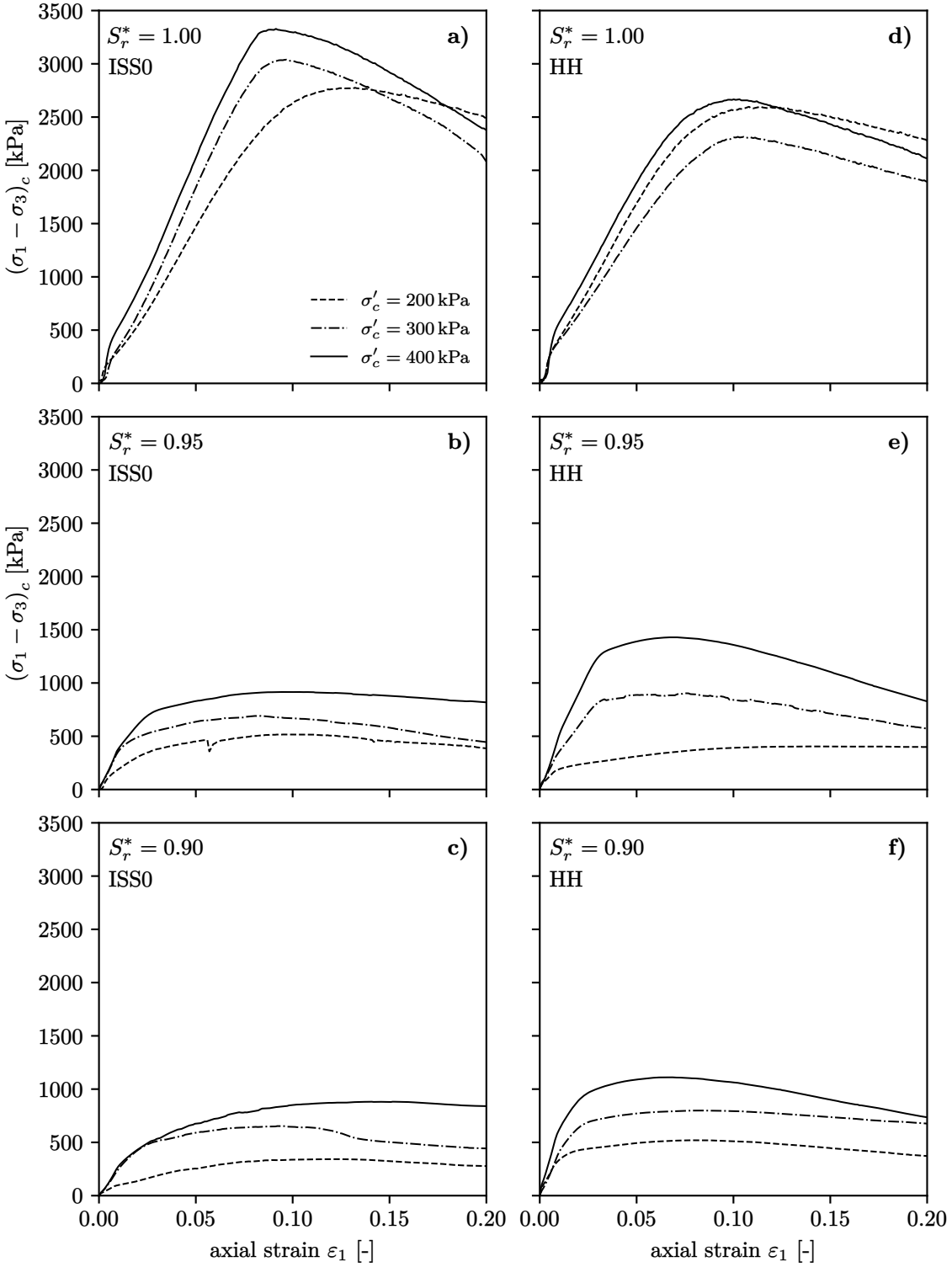

Figure 5.13: development of the deviator stress $(\sigma_1 - \sigma_3)_c$ versus the axial strain ε_1

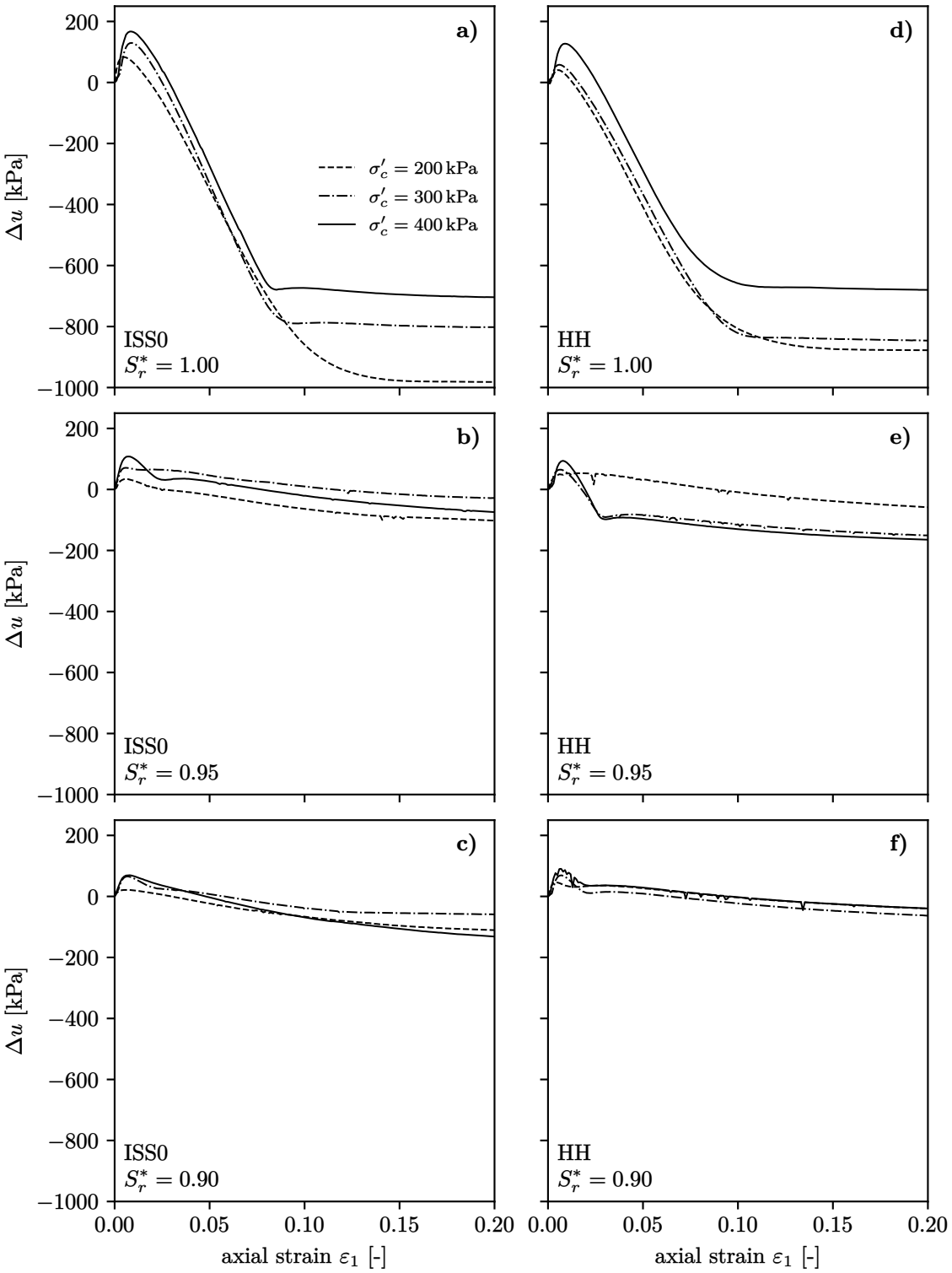

Figure 5.14: development of the induced pore water pressure Δu versus the axial strain ε_1

Table 5.3: maxima of shear stress and pore pressure change during triaxial shear

denotation	max. deviator stress $(\sigma_1 - \sigma_3)_{c,max}$ [kPa]	corresponding axial strain $\varepsilon_{1,(\sigma_1-\sigma_3)_{c,max}}$ [-]	max. induced pore pressure Δu_{max} [kPa]	corresponding axial strain $\varepsilon_{1,\Delta u_{max}}$ [-]
I200-100	2 775.631	0.132	83.286	0.005
I300-100	3 039.119	0.097	129.721	0.009
I400-100	3 328.623	0.091	167.036	0.008
I200-095	516.741	0.098	34.081	0.006
I300-095	690.862	0.084	70.929	0.006
I400-095	915.308	0.094	107.899	0.007
I200-090	343.002	0.121	21.296	0.006
I300-090	652.976	0.092	65.471	0.007
I400-090	881.888	0.152	69.447	0.008
H200-100	2 598.094	0.114	40.490	0.005
H300-100	2 314.585	0.102	58.152	0.006
H400-100	2 666.816	0.103	127.256	0.009
H200-095	404.838	0.146	53.200	0.018
H300-095	903.775	0.075	64.824	0.006
H400-095	1 428.910	0.070	93.967	0.008
H200-090	520.354	0.082	46.328	0.004
H300-090	799.149	0.081	69.176	0.007
H400-090	1 110.844	0.066	90.481	0.007

samples also show the distinctive initial peak in the induced pore pressure. However, at a certain point, the following decrease is inhibited by the gas. This peak formation is more pronounced in Hamburg sand than in ISS0 sand, i. e. in coarser sand, and principally occurs in samples with higher consolidation pressures. The peak values and the axial strains at which they occur are given in tab. 5.3.
Furthermore, the pore water pressure values incorporate the pore gas pressure in the gassy experiments. According to the basic soil mechanical assumptions for gassy sands as discussed in chapter 2, the pore gas pressure is expected to equal the pore water pressure since the gas bubbles are presumably fully surrounded by the pore water. Both parameters mutually interact. In the gassy experiments, the given pore pressures thus represent the pressure in the water phase and imply the gas pressure.

Volumetric Sample Deformation

Under the assumption that the soil retains its tendency for dilative deformation in the presence of a gas phase, it can be concluded that in gassy samples this tendency manifests itself in fact in a volumetric deformation of the sample instead of exclusively in the pore pressure response. Conditionally supporting this conclusion, fig. 5.15 shows a volumetric expansion for the majority of the gassy experiments compared to the saturated baseline tests. A quasi-drained soil behaviour exhibiting features of both, drained and undrained

conditions, can be deduced from this observation. However, in which proportions the volumetric deformation and the pore pressure reduction participate in the overall soil response cannot be quantified.
The volumetric strains have to be interpreted with caution as the impact of the employed approach to consider the barrel-type sample deformation is substantial. This is clearly illustrated by the data of the saturated experiments in fig. 5.15 a) and d) for which the volumetric strain should be zero due to the undrained conditions. Thus, the resulting volumetric strains for the gassy tests are also larger than expected. Furthermore, the measurement of the local radial strain proved difficult during the application, resulting in three experiments suffering from lacking or implausible data, as indicated in tab. 5.2. For example, test I400-090 depicted in fig. 5.15 c) shows a principally unexpected contractive deformation behaviour. It is assumed that the maximum diameter evolved at a different sample height than where the sensor was mounted and that, thus, all further geometric assumptions are not representative of the sample deformation. A further interpretation of the volumetric strain is therefore only conducted in a qualitative manner. Nonetheless, a basic conclusion can be drawn from the volumetric strain data in fig. 5.15 by comparing the gassy tests to their saturated equivalents: Generally, the gassy samples exhibit more straining than the saturated samples. The larger volume expansion is probably caused by the expansion of the gas phase within the sample and a dilative deformation of the grain skeleton.

An Equilibrium State of Saturation

As previously established, gassy samples show a quasi-drained soil behaviour. To clarify the underlying mechanisms of the quasi-drained soil behaviour, the development of the sample saturation during the shear phase can be consulted. Fig. 5.16 depicts the degree of saturation in dependence of the axial strain. Initially, the sample saturation increases before it decreases again. This peak formation in the beginning of the shear phase coincides with the peaks in the pore pressure development. Subsequently, the degree of saturation remains constant in all gassy experiments. It can be assumed that the value, at which the degree of saturation settles, represents an equilibrium state. Simultaneously, this equilibrium state illustrates the maximum gas content the sample encounters under the given shearing conditions. In the following, the saturation at the end of the shear phase is adopted as a representative equilibrium degree of saturation $S_{\mathrm{r,equ}}$. The corresponding saturation values are outlined in tab. 5.4 together with the axial strains and deviator stresses at which the onset of the equilibrium condition is identified based on the development of the saturation. Furthermore, the point, at which an equilibrium is reached, is indicated in fig. 5.16 by diamond markers. For test I200-090, no equilibrium condition is identified because the saturation data is ambiguous. The equilibrium condition is located at lower saturations for samples consolidated to a lower stress level. Therefore, the equilibrium between pore water and pore gas is most likely governed by the rigidity of the grain skeleton and the interplay of the three phases.
Looking at the dependencies between saturation and deviator stress (fig. 5.17), it can be determined that higher degrees of saturation occur at low deviator stresses. This phenomenon is a consequence of the interrelations between stress and pore pressure as well

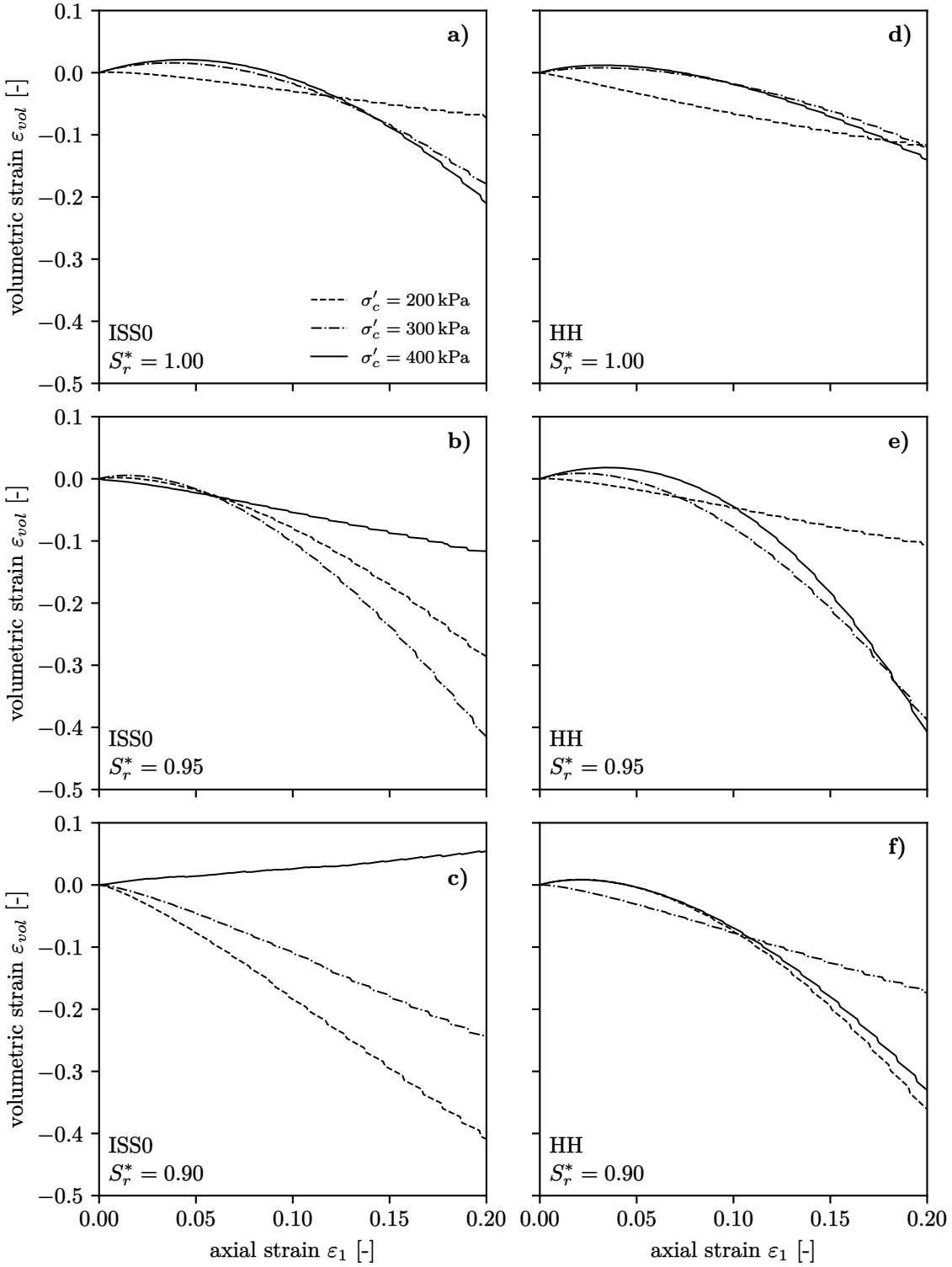

Figure 5.15: development of the volumetric strain ε_{vol} versus the axial strain ε_1

Table 5.4: equilibrium conditions of the degree of saturation in gassy samples during triaxial shear

denotation	equilibrium saturation $S_{r,equ}$ [-]	axial strain at onset of equilibrium $\varepsilon_{1,S_{r,equ}}$	deviator stress at onset of equilibrium $(\sigma_1 - \sigma_3)_{c,S_{r,equ}}$ [kPa]
I200-095	0.914	0.022	323.257
I300-095	0.921	0.021	496.047
I400-095	0.922	0.043	803.119
I200-090*	–	–	–
I300-090	0.919	0.029	507.401
I400-090	0.921	0.013	330.077
H200-095	0.919	0.021	237.045
H300-095	0.934	0.0	61.716
H400-095	0.942	0.010	502.250
H200-090	0.914	0.031	454.484
H300-090	0.925	0.072	794.211
H400-090	0.938	0.012	684.483

* no distinct identification of equilibrium onset possible (see fig. 5.16b))

as pore pressure and saturation. Thus, a dominant impact of the beginning of the shear path on the sample saturation can be established, also supported by the knowledge from the previously introduced data in fig. 5.14, fig. 5.16, and tab. 5.3. Analysing the change in pore pressure before the establishment of a saturation equilibrium, it is noteworthy, that the sample's deformation behaviour changes from contractive to dilative within this period. Therefore, the quasi-drained behaviour in dilative deformation possibly is a prerequisite for the existence of an equilibrium as it allows the pore pressures and the gas volume to find a balance instead of forcing one of the parameters to adjust to the other. Moreover, fig. 5.17 shows that the equilibrium is reached before the deviator stress is at its maximum. The general shear parameters of the soil are therefore influenced by the adopted equilibrium state.

Shear Parameters and Stress Path Habits in the t-s diagram

According to the evaluation scheme described in section 5.3, the overall shear strength of the soil, represented by the friction angle and the cohesion, is determined based on the parameters t and s. The t-s diagrams given in fig. 5.18 show the stress paths together with the respective failure planes. The resulting shear parameters are summarised in tab. 5.5. The stress paths of the saturated samples distinctively follow the failure plane before reaching the maximum shear stress. A slight scattering of the failure plane inclinations can be observed. However, due to the heterogeneity of the material this can be expected in geomechanical testing. The parameters α' and k of the failure planes are optimised to depict the stress paths of all three tested consolidation stresses for the respective soils. As a result, an effective friction angle of $\varphi' = 35.442°$ is determined for saturated ISS0 sand

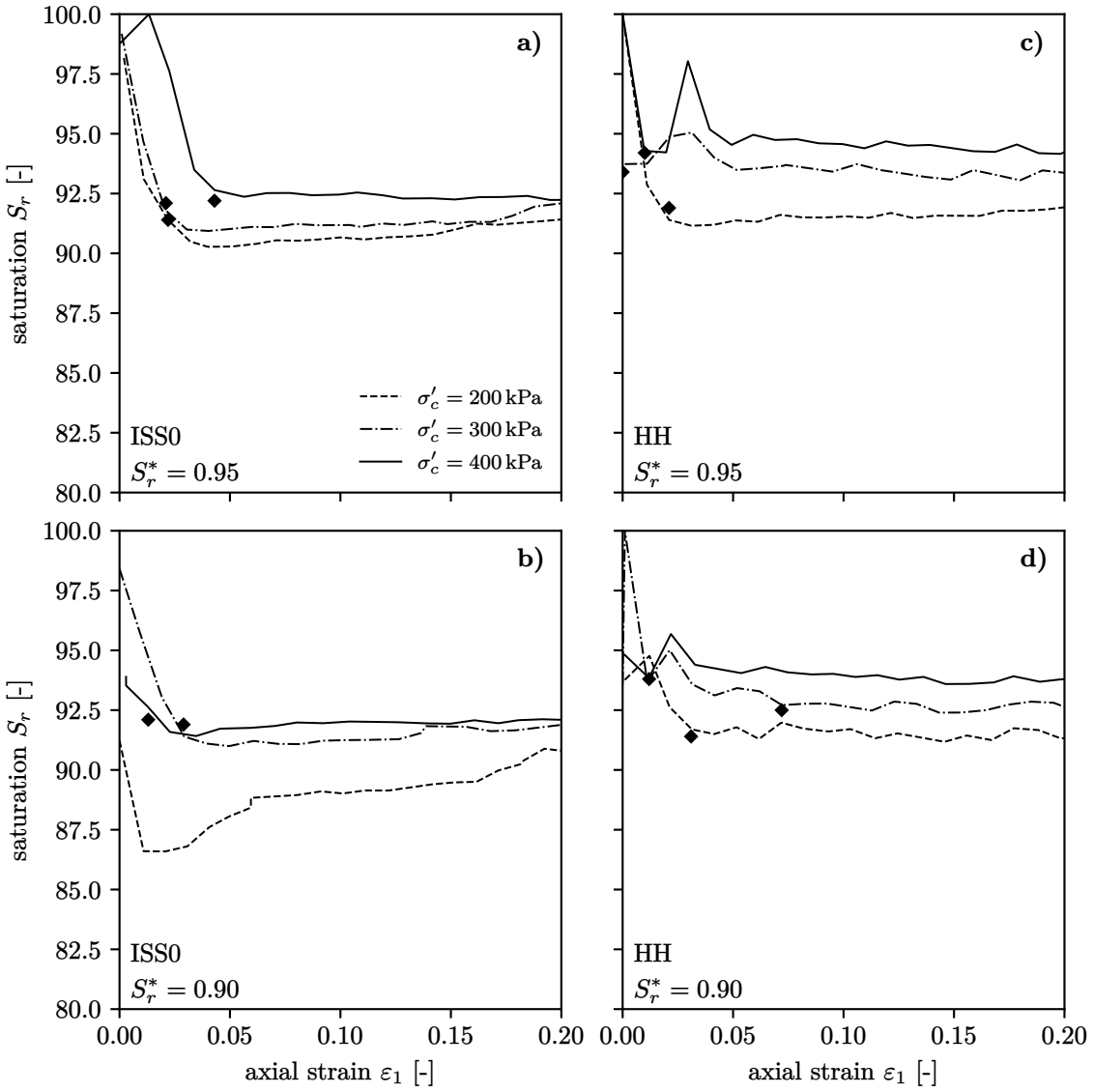

Figure 5.16: development of the degree of saturation S_r versus the axial strain ε_1 (the annotated S_r^* refers to the target saturation)

and of $\varphi' = 32.937°$ for saturated Hamburg sand. Both parameters are in the expected magnitude for the tested soils.

The experiments on gassy samples show a different behaviour. On the one hand, the maximum stresses are significantly lower. On the other hand, the gassy stress paths are not as smooth as the saturated ones and exhibit changes in their gradient (see also fig. 5.19). For gassy ISS0 sand, this results in a lower effective friction angle, but also in a significant cohesion component of the shear strength. Since both sands do not exhibit cohesive forces in their saturated state, this cohesion is most likely of capillary origin. Gassy Hamburg sand presents other consequences for the shear parameters: the effective friction angle is increased compared to the saturated state, but no capillary cohesion is determined.

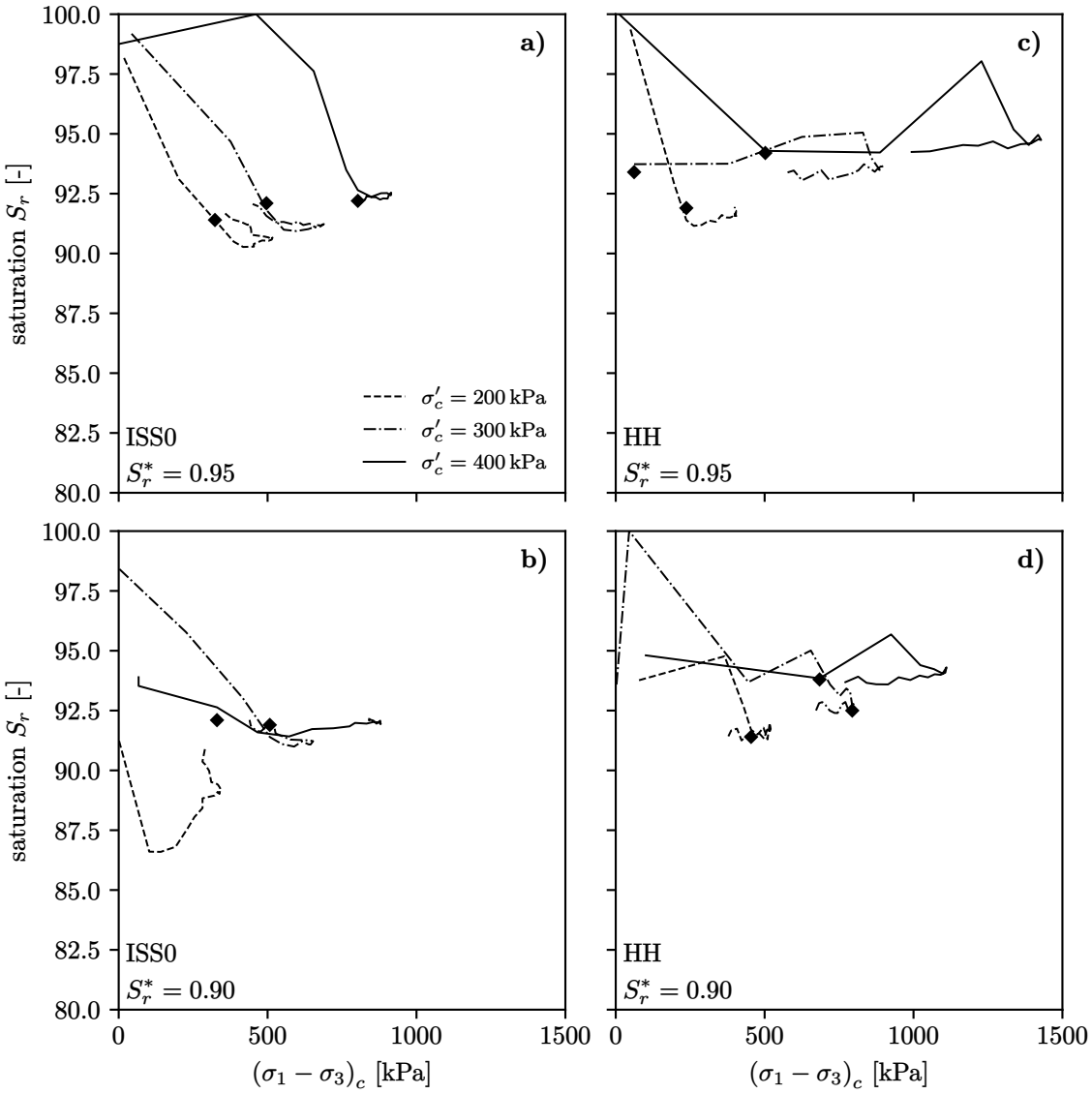

Figure 5.17: development of the degree of saturation S_r versus the deviator stress $(\sigma_1 - \sigma_3)_c$ (the annotated S_r^* refers to the target saturation)

The different results for the two gradations lead to the question of how the shearing process is influenced differently as a consequence of the gas presence in the differently shaped pore spaces of the two gradations. In order to investigate this, a more detailed analysis of the gassy stress paths compared to the respective saturated baseline tests is conducted; see fig. 5.19. Several observations can be made based on this comparison. In ISS0 sand, the majority of the gassy stress paths are shifted parallelly above the saturated stress paths. This includes the initial stress state, which is shifted towards the origin as a consequence of the pore pressure increase during exsolution as illustrated in fig. 5.12. In Hamburg sand, the initial stress state is located closer to the saturated baseline test than it is the case for the ISS0 sand. Subsequently, the majority of the gassy stress paths follow the saturated stress path until an apparent critical point is reached at which the gassy stress

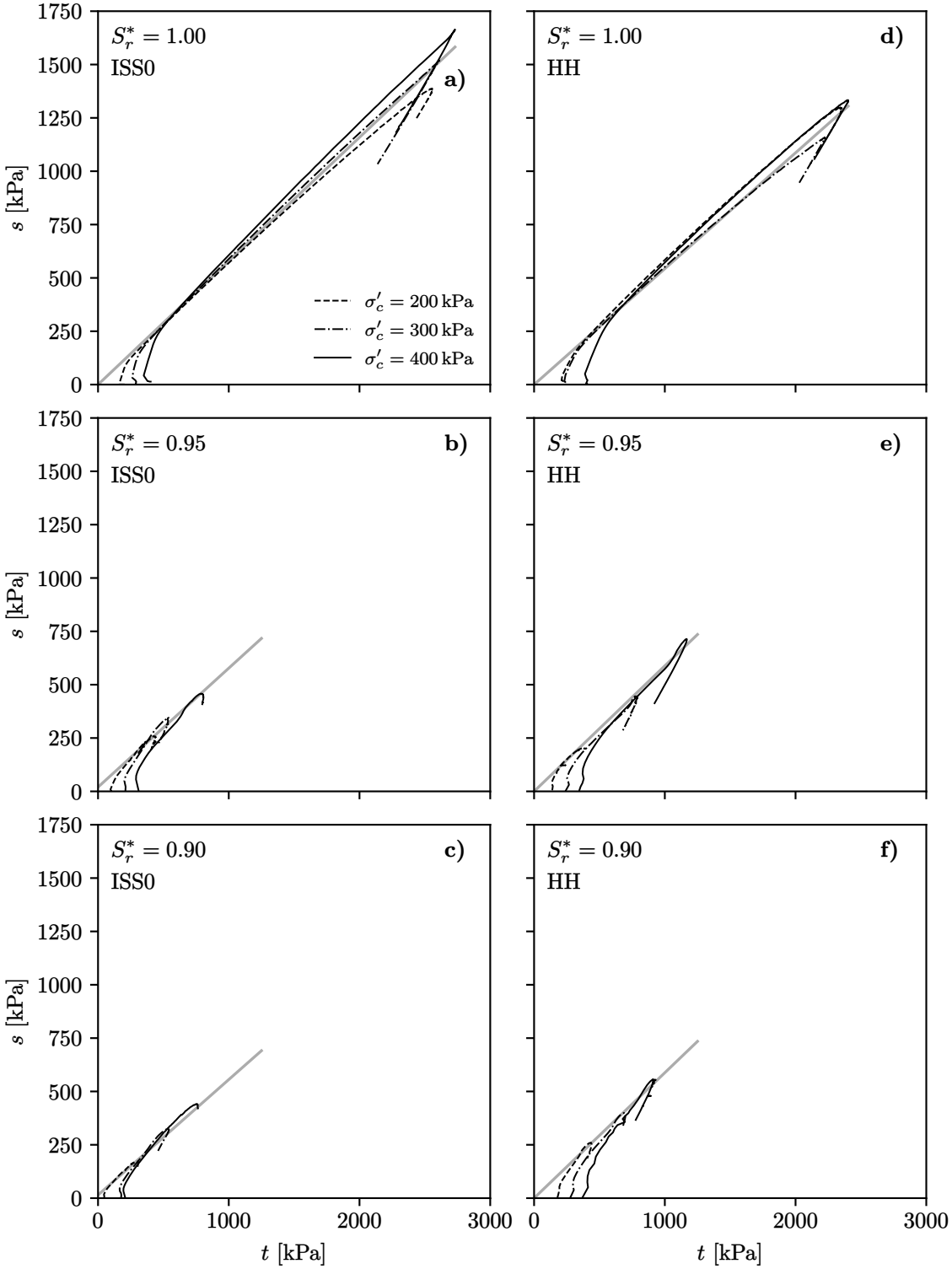

Figure 5.18: *t*-*s* diagram for the evaluation of the shear parameters; the failure planes are indicated in grey

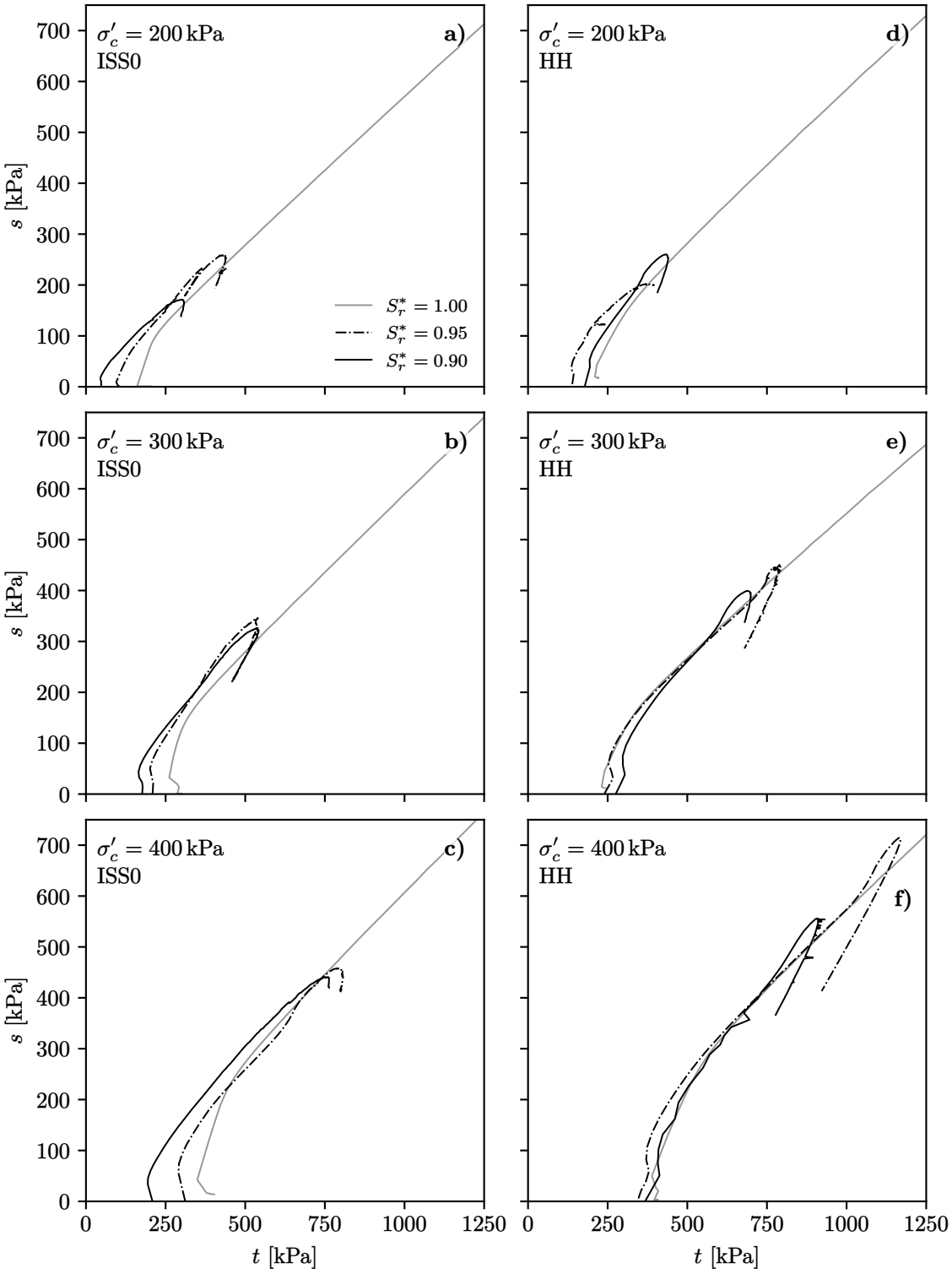

Figure 5.19: comparison of the stress paths of gassy and saturated experiments in the t-s diagram

Table 5.5: shear parameters derived from the triaxial tests for gassy and saturated conditions

soil type	saturation S_r^* [-]	friction angle φ' [°]	cohesion c' [kPa]
ISS0	1.00	35.442	0.0
ISS0	0.95	34.017	24.129
ISS0	0.90	32.994	17.319
HH	1.00	32.937	0.0
HH	0.95	36.143	0.0
HH	0.90	36.111	0.0

path develops into the domain above the saturated stress path. This critical point is denoted the point of capillary relevance (PCR).

These two types of stress path habit are very distinct and are labelled as types I and II in the following. A schematic illustration is provided in fig. 5.20. Additionally, tab. 5.6 allocates the single experiments to their respective stress path type. Based on these observations, each type can be accounted to one of the employed soils. Therefore, the schematic illustration in fig. 5.20 also contains the predominant characteristics of the failure planes as observed in the introduced triaxial test series to demonstrate the impact of the stress path habit on the resulting shear parameters.

The development of the stress path into the region above the saturated equivalent's critical state usually is an indicator for an enactment of capillary forces within an unsaturated sample. In the ISS0 sand samples behaving according to type I, the relevance of capillary forces is substantiated by the resulting cohesion, i. e. the parallel shift of the failure plane. Theoretically, this mechanism is also conceivable for the stress path shape of type II. However, it was not observable in the experiments conducted within the scope of this study. Instead, the upward shift of the stress path is compensated by an increased inclination of the failure plane. Consequently, a capillary cohesion is not identified in gassy Hamburg sand. Nonetheless, it is likely that the deviation from the saturated stress path in type II is caused by the surface tension acting at the gas-water-interface. The point at which this deviation occurs is the PCR, as hypothetically only from this point forward the soil behaviour is impacted by the enclosed gas. The development of the induced pore pressures in the experiments behaving according to stress path type II mimics its path: The formation of the peak in the initial part of the shear phase corresponds to the behaviour of the saturated baseline test. The relative minimum, which forms when the pore pressure development in the gassy experiments deviates from that in the saturated tests, corresponds to the PCR. The relevant parameters at the point of capillary relevance for every sample behaving according to type II are further summarised in tab. 5.6.

A valid hypothesis regarding the PCR is that it coincides with the onset of the saturation equilibrium as it marks the maximum gas content and might thus be accompanied by strong enough capillary forces to impact the stress path development. To test this hypothesis, fig. 5.21 depicts the PCRs and onset points of the saturation equilibrium for

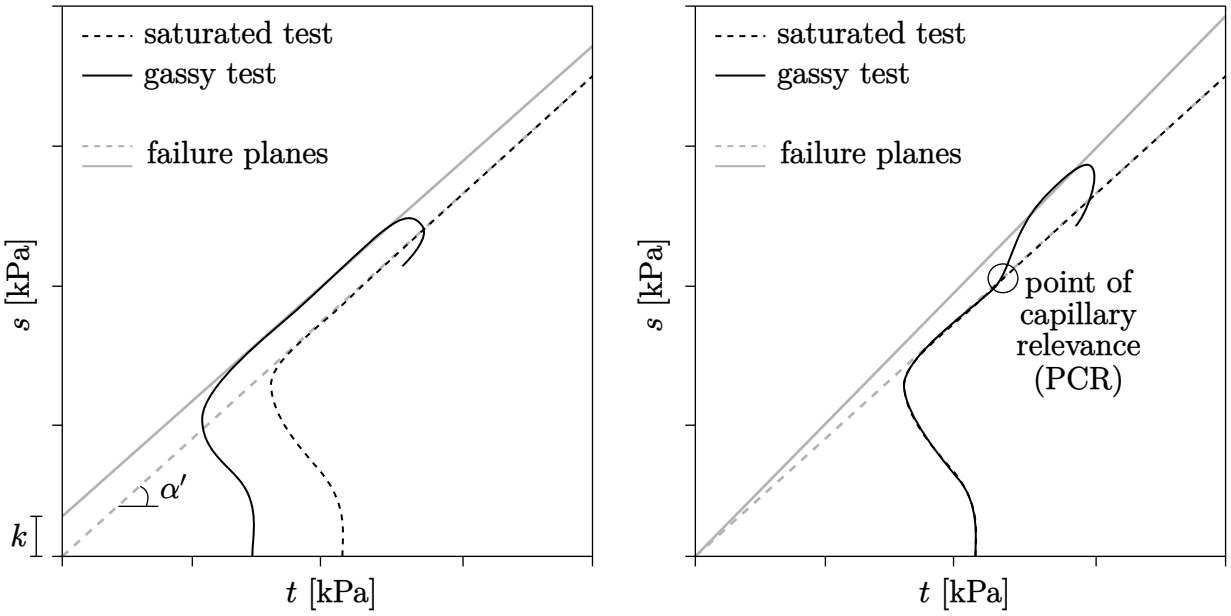

(a) type I (b) type II

Figure 5.20: schematic illustration of the two types of stress paths in medium dense gassy sands

Table 5.6: stress path behaviour of the gassy experiments

denotation	behaviour type	for type II: properties at point of capillary relevance			
		saturation $S_{\mathrm{r,PCR}}$ [-]	axial strain $\varepsilon_{1,\mathrm{PCR}}$ [-]	deviator stress $(\sigma_1 - \sigma_3)_{\mathrm{c,PCR}}$ [kPa]	pore pressure Δu_{PCR} [kPa]
I200-095	I	–	–	–	–
I300-095	I	–	–	–	–
I400-095	II	0.976	0.026	700.789	31.515
I200-090	I	–	–	–	–
I300-090	I	–	–	–	–
I400-090	I	–	–	–	–
H200-095	I	–	–	–	–
H300-095	II	0.951	0.030	818.345	-90.752
H400-095	II	0.980	0.028	1 175.747	-92.273
H200-090	II	0.926	0.019	422.634	33.009
H300-090	II	0.950	0.019	625.715	13.685
H400-090	II	0.957	0.018	845.870	42.595

all tests with a stress path behaviour of type II. No significant correlation can be identified. While the equilibrium condition is reached at comparable saturations but at different axial strains, the PCR is encountered at different saturations, however at a similar strain range. The saturation at the point of capillary relevance $S_{r,PCR}$ is generally located above the equilibrium saturation. In conclusion, the point of capillary relevance occurs before the sample settles in the saturation equilibrium and comparably low degrees of saturation suffice to impact the overall soil behaviour.

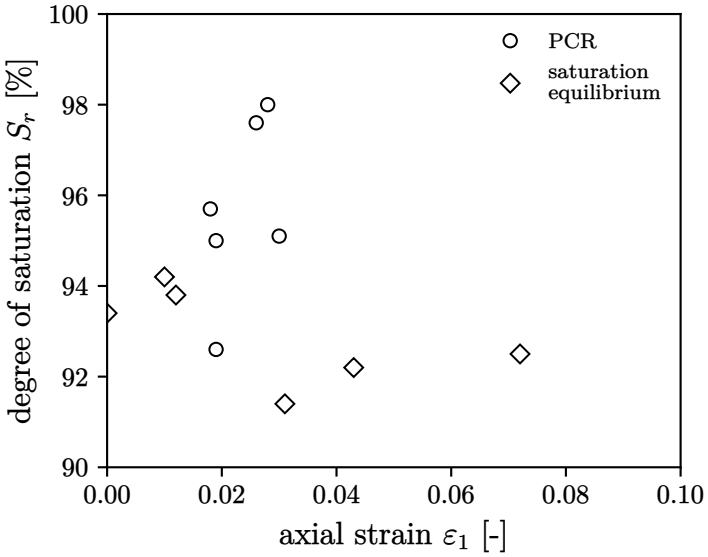

Figure 5.21: comparison of the point of capillary relevance with the onset of the saturation equilibrium

6 Microstructure of Gassy Sands

Many processes governing the constitutive behaviour of soils are rooted in the micro-scale. However, the term *micro* is a somewhat ambiguous expression as the actual size scale often depends on the specific application. In this study, the processes of interest occur on the pore-level of granular soils. Therefore, the scale of observation is in millimetres and the scale of resolution is in microns. The analysis of these micro-scale processes is conducted by means of the imaging method X-ray computed tomography.

6.1 The X-Ray Computed Tomography Method

Imaging is a well-established and popular method to obtain information during experiments in various disciplines due to its non-destructive nature. The use of X-radiation is particularly beneficial because it enables the collection of internal data of opaque objects and materials. In the context of CT scanning, the acquired data provide three-dimensional (3D) information, and is consequently superior to traditional two-dimensional (2D) imaging methods.

6.1.1 Technical Functionality

The underlying operating principle of computed tomography is X-radiation, also referred to as RÖNTGEN radiation, which is an electromagnetic radiation located beyond the ultraviolet light on the electromagnetic spectrum. X-rays are capable to penetrate matter. However, their energy decays in the process depending on the material's density. Computed tomography exploits this density-dependent attenuation to visualise the penetrated object. For this purpose, a CT scanner consists of an X-ray source, the scanned object, and a detector (see fig. 6.1; Buzug, 2008).
Within the vacuum of an X-ray tube, X-rays are generated by accelerating and decelerating electrons: Free electrons are generated at a hot cathode and accelerated towards the anode by an applied acceleration voltage. When the electrons collide with the anode, usually manufactured from metal, they are decelerated abruptly. This deceleration generates a so-called *bremsstrahlung*, i. e. a continuous radiation spectrum (Buzug, 2008). Additionally, the characteristic RÖNTGEN radiation is generated when the collision of arriving electrons with an atom of the anode leads to the emission of an orbital electron from the atom. This characteristic RÖNTGEN radiation depends on the material of the anode (Ketcham and Carlson, 2001). The overall radiation spectrum emitted by the vast majority of industrial CT devices is polychromatic and, thus, consists of a spectrum of energies – analogous to white light being composed of a spectrum of wavelengths (Wildenschild and Sheppard, 2013). The magnitude of the emitted energy spectrum influences the quality of

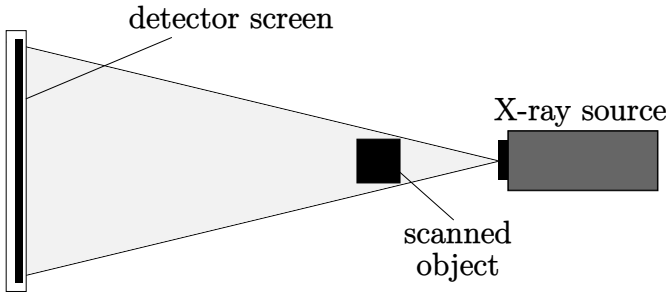

Figure 6.1: general set-up of a computed tomography scanner

the resulting image data, as high-energy X-ray spectra show better penetrative capabilities but are less sensitive to density changes in the scanned object; vice versa for low-energy X-ray spectra. The X-ray tube emits a beam of conical shape. The opening angle of this conical X-ray beam is governed by the focal spot size and thereby impacts the achievable spatial resolution of the resulting image (Ketcham and Carlson, 2001). With the focal spot size the X-ray flux or intensity changes. Small focal spot sizes involve a low X-ray flux. In consequence, it is challenging as well as time-consuming to obtain a very high scanning resolution (Cnudde and Boone, 2013).
The X-rays emitted by the X-ray source traverse the scanned object. While penetrating the material, the X-ray is attenuated due to primarily three effects: photoelectric absorption, Compton scattering, and pair production (Buzug, 2008). Photoelectric absorption is relevant at low X-ray energies and is therefore the dominant effect in geoscientific applications (Ketcham and Carlson, 2001). It describes the physical process occuring when an incoming X-ray photon leads to the ejection of electrons from an atom. Compared to the other two processes, photoelectric absorption shows a strong dependency on the number of protons in the atom's nucleus, i. e. the atomic number, and, thus, a strong dependency on the element which makes up the material in question (Buzug, 2008). For this reason, the attenuation of low-energy X-rays is more sensitive to the properties of the penetrated material. The attenuation can be described by BEER's law:

$$I = I_0 \cdot \exp\left(-\mu_a \cdot x\right) , \tag{6.1}$$

where I and I_0 are the attenuated and initial X-ray intensity, respectively. x is the thickness of the scanned object and μ_a describes the linear attenuation coefficient of the penetrated material. This relation is only valid for monochromatic beams in which the radiation spectrum is of uniform energy and wavelength. Thus, for polychromatic beams, the energy-dependent attenuation coefficient would need to be evaluated for the entire energy spectrum (Ketcham and Carlson, 2001; Buzug, 2008; Wildenschild and Sheppard, 2013).
After the X-rays pass through the scanned object and are attenuated in the process, they impinge on the detector screen where they are recorded as a digital data set. Most detector screens combine a scintillating material with a CCD (charge-coupled-device) camera (Wildenschild and Sheppard, 2013). Scintillating material is excited by X-rays and other short-wave radiation and emits the absorbed energy in the form of light, i. e. long-wave ra-

diation (Buzug, 2008). The generated light flashes are recorded by the CCD camera. The quality of the recorded image is strongly influenced by the number of detection points on the detector screen, its size, and the energy spectrum detectable by the respective screen (Ketcham and Carlson, 2001).
Image acquisition put into practice with the method described above yields a two-dimensional sinogram. Computed tomography, as developed by Hounsfield (1973), Ambrose (1973), and Ommaya et al. (1976), requires the object of interest to be scanned from different angles in order to reconstruct a three-dimensional image from the two-dimensional scanning results. Therefore, either the combination of source and detector needs to rotate around the scanned object, as implemented in medical applications, or the scanned object has to be placed on a rotating stage, as implemented in the majority of industrial CT applications. The latter allows for a more precise positioning of the scanned object in the beam. Considering the rotational movement, the optimum shape of the scanned object is a cylinder due to its rotational symmetry. Besides the rotational movement, several other characteristics distinguish industrial CT scanning from the more commonly known medical application of the method. Amongst is the obvious factor of the scanned object being inanimate and hence motionless during the scan as well as unconcerned with the absorbed radiation dose. Therefore, higher X-ray energies and longer exposure durations can be implemented in industrial applications or material scientific investigations, which enable higher quality scans with higher spatial resolutions (Ketcham and Carlson, 2001). However, standardised procedures mostly only exist for medical applications. Therefore, the choice of scanning parameters in industrial and scientific CT applications strongly depends on the operator, which limits comparability (Cnudde and Boone, 2013).
For a given X-ray tube with its specific capabilities, the obtainable voxel size is a result of the geometric relation between source, object, and detector as given by the intercept theorem. Besides the number of detection points on the detector screen, the resolution is limited by the field of view, which corresponds to the detector size. It is advisable to align the scanned volume with the actual volume of the sample as the scanning of subsamples can lead to significant shortcomings in the scanning results. Furthermore, an interdependency between the volume of the sample and the lowest possible voxel size exists due to computational limits during the reconstruction process. Frequently, the term spatial resolution is used as a synonym for the achieved voxel size. However, it can also refer to the number of voxels per data cube or, more colloquially, to the smallest resolvable feature of the material in question (Cnudde and Boone, 2013). Generally, the achievable resolutions of modern CT applications vary strongly. Typical medical CT scanners record voxel sizes in the millimetre domain. For industrical applications micro-CT (μCT) or nano-CT devices, that acquire image data with voxel sizes in the (sub-)micron range, are available as well (Ketcham and Carlson, 2001).

6.1.2 Processing of Image Data

Typically, the acquisition of image data involves the physical scanning of the sample as described above, which is followed by several steps to generate and process the digital data set. These processing steps include the initial reconstruction of a 3D data cube from the 2D sinograms, the removal of scanning artifacts, as well as preparatory steps for a further

analysis of the data. As follows, general information on processing procedures and their influence on the quantitative reliability of the image data is discussed. Specific information on the algorithms employed in this study is presented hereinafter as part of the evaluation scheme in section 6.3.

Reconstruction

Reconstruction describes the transformation of the acquired two-dimensional scans from different angles into a coherent compilation of three-dimensional attenuation data representing the scanned object. Prior to the reconstruction procedure, the 2D raw data can be pre-processed by means of denoising algorithms in order to enhance the image quality. These involve temporal filters for noise reduction or image domain filters for, e. g. edge enhancement. Many manufacturers of medical and industrial CT devices provide proprietary approaches in order to prepare the raw data for 3D reconstruction (Schafer and Siewerdsen, 2020).
3D reconstruction generally is a computationally expensive endeavour that has profited from advances in affordable parallel computing capacities over the last years. Additionally, new reconstruction approaches are investigated with the advent of machine learning (Greenspan et al., 2016). However, the typically employed procedure for 3D reconstruction in cone-beam CT scanning are filtered backprojection algorithms. In a backprojection the trajectory of an X-ray is traced backwards in order to infer the corresponding attenuation value. Simply put, this is achieved by relating the scanned object, its projections at different angles, and its Fourier transform by means of the Fourier slice-projection theorem. However, in a simple backprojection, each point on the image grid is influenced by the other points. The resulting attenuations are thus not exact and the obtained image appears blurred. Therefore, a high-pass filter is applied to 'sharpen' the blur in a filtered backprojection algorithm (Buzug, 2008; Schafer and Siewerdsen, 2020). As a thorough elaboration of reconstruction algorithms is beyond the scope of this thesis, the reader is referred to Buzug (2008) for further information.
The image data resulting from the reconstruction process is a three-dimensional 8-bit grey-scale image with 256 grey values, on which 0 corresponds to not dense and 255 to dense. Thus, denser materials appear in lighter shades of grey while low-density materials are represented by dark grey. Consequently, in geomaterials, the solids are shown in light grey, the pore water adopts a medium grey color, and the pore gas appears in dark grey. The three dimensions are achieved by displaying two-dimensional cross-sectional views of the scanned object (*slices*) in a data *stack*.

Artefacts

The complex process of a CT scan bears many instances at which the recorded attenuation values can be diverted from the actual attenuation value of the scanned material. This is particularly relevant for complex materials consisting of different phases and/or a variety of materials. These small errors express themselves as visible artefacts in the resulting images.
A prominent artefact in many CT applications is *beam hardening*. The visual expression of beam hardening is a brighter appearance of the scanned object's edges compared to its

centre. Thus, the edges are identified as a denser and more attenuating material. This effect is caused by a shift in the beam's energy spectrum during the passage through the object. High-energy X-rays are attenuated more difficultly than low-energy X-rays. Therefore, the less energetic (soft) part of the X-ray spectrum does not pass through the scanned object and the exiting beam consists only of the X-rays of higher energy (harder X-rays), i. e. the beam is hardened. As a consequence, the edges of the scanned object have a higher relative attenuation than the centre (Wildenschild and Sheppard, 2013). Since this artefact is continuous and inhomogeneous, a retroactive correction of the raw data is difficult and particularly challenging for complex materials (Cnudde and Boone, 2013). Therefore, care should be taken to address the issue during the set-up and scanning phases of an experiment. This can be done by chosing a high-energy X-ray spectrum or by pre-filtering the beam to exclude the low-energy rays before they enter the scanned object (Ketcham and Carlson, 2001; Wildenschild and Sheppard, 2013).

Further, *ring artefacts* are common artefacts. According to their name, ring artefacts appear as full or partial circles around the rotation axis. The cause for ring artefacts are disturbances or changes in the scanning conditions which can induce a shift in the data read out by the detector. Changes in temperature or initial beam intensity can be compensated for by an appropriate experimental design. However, as described above, changes in the beam hardness are not easily corrected. Ring artefacts occur, e. g. when the object is scanned unevenly and varying degrees of hardness are created during beam hardening. As previously outlined, the use of high-energy beams or filters can also mitigate this artefact. In contrast to beam hardening, the correction of ring artefacts in the processing stage is not as complex. However, the limitation of blurring possibly relevant circular features in the scanned object has to be considered when applying a correction (Ketcham and Carlson, 2001).

The *partial volume effect* denotes the averaging of grey values within one voxel. This effect is of relevance when multiple materials with different attenuations exist within one voxel, e. g. at a material boundary. As every voxel represents one attenuation value, an average is given for voxels enclosing more than one material. In consequence, material boundaries appear blurred in the image data and features smaller than the voxel size are not resolvable. The partial volume effect can cause difficulties in the segmentation process or in quantitative analyses when the voxel in question has to be accounted to one or the other material (Ketcham and Carlson, 2001; Cnudde and Boone, 2013). Since the partial volume effect is a shortcoming inherent to the CT methodology, no posterior correction approaches exist. It can only be remedied or reduced by aiming for smaller voxel sizes during the scan.

Phase contrast is an effect caused by the refraction of X-rays. The density of the penetrated material influences the propagation speed of the X-ray. This manifests itself in a change of wavelength, i. e. a phase shift, and consequently in a change of propagation direction. In analogy, X-rays passing through the scanned object behave like rays of light passing through a lens. Therefore, the intensity spectrum arriving at the detector is influenced by attenuation and reflection. However, the severity of the reflective part increases with growing distance between object and detector (Wildenschild and Sheppard, 2013). Phase contrast is of relevance for high-resolution scanning and for samples consisting of less attenuating materials. It further has an edge-enhancing impact on the resulting

image data, which can be beneficial, but also complicates the segmentation procedures. Hence, several options exist to remedy phase contrast in the processing stage (Cnudde and Boone, 2013). The respective approaches are based on the derivation of the attenuation and reflection components of the recorded intensities. This so-called phase retrieval is a complicated procedure for polychromatic cone beams. In geoscientific imaging, the correction of phase contrast has not played a greater role in the past because, additionally, the multitude of different components in one sample complicates phase retrieval. Moreover, the phases constituting a soil or rock generally exhibit high differences in attenuation to produce a sufficiently good contrast between the phases, which allows to neglect phase contrast (Wildenschild and Sheppard, 2013).
Furthermore, *starburst* or *streak artefacts* are produced by inclusions of a very dense and highly attenuating material. As metal inclusions are often the cause for these artefacts, they are also known as metal artefacts (Ketcham and Carlson, 2001; Cnudde and Boone, 2013).
Other artefacts involve, for instance, the *cone-beam effect*, which appears in slices located at greater distance from the cone centre. It is a result of reconstruction in circular scanning and can be avoided by using a helical scanning path. Moreover, movement of the scanned object leads to *movement artefacts*, which appear as a blur or as shadows in the image data (Cnudde and Boone, 2013).

Data Optimisation

Apart from the previously discussed artefacts, the image quality is always restricted by the existence of noise and blur. Blur is a product of the finite amount of sampling points on the detector screen and therefore not amendable at the processing stage (Buades et al., 2005). Further, image noise is an immanent part of image data acquisition because it results from measurement inaccuracies at the detector. In CT scanning, the sources of the inaccuracies are two-fold: Firstly, quantum noise is caused by fluctuations in the scattering and absorption of X-rays while passing through the scanned object. Thus, the amount and characteristics of the incoming X-rays at the detector always varies, even if the scanning conditions are kept constant. Secondly, detector noise results from changes in the surrounding conditions, such as the temperature of the detector, which influences the recorded value. In consequence, the detected value can deviate from the actual value and thus appears erroneous in the final image (Buades et al., 2005; Buzug, 2008). A common measure for the quality of an image is the signal-to-noise ratio, which relates the power of the signal to the power of the noise.
A multitude of denoising algorithms exists, all of them following the objective of improving the contrast between features of interest and, at the same time, of reducing artefacts, i. e. of increasing the signal-to-noise ratio. However, denoising does not remove the noise from the image data. It rather smoothes or diminishes it to a scale small enough to be irrelevant for further analyses. An unwelcome side effect of denoising is therefore the loss of image information as, generally, it is not possible to distinguish between small image details and noise. Thus, different algorithms were developed to address different image features, such as edge preservation or flat zone preservation (Ketcham and Carlson, 2001; Buades et al., 2005; Tengattini et al., 2021).

Data optimisation often is a necessary preliminary measure to allow for a smooth segmentation of the data, as image noise and faulty grey values can result in a faulty allocation of voxels to a defined subset.

Segmentation Procedures

In a segmentation procedure, the image data is divided (*segmented*) into subsets. These subsets usually correspond to different materials, e. g. quartz (soil grains) and water, or even to individual units, e. g. singular grains (Wildenschild and Sheppard, 2013). Nowadays, segmentation is a routine approach in different kinds of mundane image processing applications beyond CT scanning, such as text recognition. Thus, over the years, hundreds of algorithms were developed for a broad scope of applications (Sezgin and Sankur, 2004).

Based on their operating principle, the existing algorithms can be grouped into thresholding, edge detection, and iterative pixel classification (Tengattini et al., 2021). Iterative pixel classification algorithms group data points according to homogeneity criteria or probabilistic approaches. Information on neighbouring pixels or voxels is included in the iterative procedure. Amongst these approaches is the segmentation by neural networks, which is becoming increasingly popular. However, for geoscientific CT applications their use is not yet common. Edge detection approaches rely on the identification of material boundaries by analysing grey value gradients. Due to their working principle, these methods are very suitable to identify singular bodies rather than all voxels representing the same material (N. R. Pal and S. K. Pal, 1993; Tengattini et al., 2021). Threshold-based segmentation procedures are based on global or local grey value information of the respective image, and are mostly employed in geoscientific CT applications. The most popular approaches evaluate the shape of the grey value histogram or rely on manually defined thresholds. Essentially, the entire data set is classified according to grey value (N. R. Pal and S. K. Pal, 1993; Sezgin and Sankur, 2004).

The result of segmentation is a binarised image featuring only the instances foreground (object or material of interest) and background. In application with more than two subsets of interest, multi-thresholding can be applied – leading to a trinarised image in case of three subsets, and so forth (Sezgin and Sankur, 2004).

The evaluation of the quality of a segmentation procedure is generally not straightforward, since a certain degree of ambiguity is inherent to CT data. This is caused, on the one hand, by image noise and artefacts, their removal, as well as the choice of data optimisation filters and segmentation algorithm (Iassonov et al., 2009). On the other hand, the partial volume effect makes a definite allocation of a voxel to a specific material impossible. These shortcomings can be compensated by high quality scanning conditions and the choice of a material-appropriate spatial resolution to minimise the impact of the partial volume effect. Beyond that, any remaining impacts have to be considered in further analyses steps (Wildenschild and Sheppard, 2013).

Subsequent to image segmentation, the image data can be evaluated for singular phases. Therefore, segmentation is a necessary prerequisite for more sophisticated quantitative analyses based on the CT data.

Representative Elementary Volumes

In order to save computational costs, quantitative analyses on CT data of geomaterials are frequently conducted on extracted subvolumes instead of on the entirety of the scanned sample. The challenge at hand lies in the identification of a subvolume representative of the overall sample: the representative elementary volume (REV). The representativity is determined by the convergence of the parameter of interest with increasing subvolume, that indicates the parameter's independence from micro-scale heterogeneities in the grain structure. Thus, for the identification of the minimum REV a subvolume has to be placed inside the sample, which is then expanded and successively evaluated for the parameter of interest (Gitman et al., 2007).
Different REV analysis procedures are suggested in the literature. An early approach, which became popular in the geosciences and hydrology, evaluates the respective subvolumes solely for its porosity and determines the REV size for any macroscopic soil parameter at the subvolume size at which the porosity remains constant (Al-Raoush and Papadopoulos, 2010; Wiącek and Molenda, 2016). However, Al-Raoush and Papadopoulos (2010) and Milatz (2023) showed that different REV sizes are required to reliably represent different soil parameters. Typically, the REV sizes also vary with grain size and gradation. Well-sorted soils with smoother grain surface properties and rounder shapes require smaller REV than poorly-sorted soil types with angular particles (Wiącek and Molenda, 2016).
In other engineering disciplines, the REV size is commonly defined based on macroscopic parameters only, neglecting the effect of microstructural components such as porosity (Al-Raoush and Papadopoulos, 2010; Wiącek and Molenda, 2016). For heterogeneous engineering materials, Gitman et al. (2007) suggest to determine the REV size based on the mean and variance of the heterogeneity in question, e. g. inclusions. Additionally, the statistical analysis tool called χ^2-test can be applied to evaluate for statistical scatter. When applying these criteria to geomaterials, a higher reliability of the REV can be achieved (Schmidt et al., 2022).
In order to account for meso-scale heterogeneities within a sample, e. g. shear zones, Schmidt et al. (2022) stipulate to conduct REV analyses at different locations within the sample. A subvolume chosen for further analyses is then not necessarily representative of the entire specimen but only of the respective sample section. Quintessentially, the determination of a REV therefore depends on the analysed material, the parameter of interest, and the boundary conditions and objectives of the investigation.

6.1.3 Applications in the Geosciences

In recent years, the application of CT scanning in the geosciences has become increasingly popular. Initially, simple scanning of stationary samples was employed to reveal the morphological features of pore structures and the grain skeleton (Ketcham and Carlson, 2001). Moving forward, the research activities developed into a process-focussed direction as sequential CT scanning allows for an analysis of microstructural controls of mechanical processes or flow phenomena.
In order to obtain sequential image data, testing equipment has to be installed within the scanning chamber. For this purpose, a multitude of miniaturised testing devices has

been developed, e. g. for uniaxial shear tests (Milatz et al., 2021), triaxial shear tests (Khaddour, 2015), and multi-phase flow experiments (Garing et al., 2017). The perks of in-situ experiments with simultaneous image data acquisition are evident: processes like grain crushing (Zhao et al., 2015), the formation of heterogeneities such as shear zones (Desrues et al., 1996), as well as the size and development of phase interfaces (Singh et al., 2016) can be observed and quantified in dependence of force, strain, or time. Thus, information on processes that remain hidden and mostly unquantifiable in traditional laboratory testing is made available by means of the image data. Comprehensive reviews of the prospects and applications of imaging techniques in the geosciences have been published, amongst others, by Cnudde and Boone (2013), Wildenschild and Sheppard (2013), and Tengattini et al. (2021).
However, the combination of CT and experiment also involves several constraints with regard to the experimental set-ups. Since the sample rotates during the scanning procedure, electricity and water supply to the sample and the sensors often poses a logistical challenge. The rotational movement can further lead to changes in the sample structure that impede the comparability within a scanning sequence. Furthermore, the temperature in the scanning chamber changes due to the activity of the X-ray source. While small temperature variations generally do not impact the integrity of macroscopic laboratory tests, the effect of temperature-induced density or surface tension changes is visible, thus measurable, in microscopic CT image data (Wildenschild and Sheppard, 2013). Technical solutions can be found for the above-mentioned restrictions. The necessity of immobility during the scanning procedure, however, excludes the investigation of highly dynamic or continuous processes. Moreover, the small sample sizes required to achieve high resolutions call for a well-founded consideration of the sample's representativity and scalability.

6.2 Test Routine

In this study, performing μCT experiments requires the combination of a miniaturised test stand fit for the conditions within the scanning chamber of a μCT with the equipment crucial for the preparation of gassy soil samples with the axis-translation method for gassy soils as described in chapter 4. Here, the developed test stand and the experimental procedure, which are described in the following, are not aiming to produce triaxial shear in gassy samples fully analogously to the macroscopic experiments. The objective of this test series is rather to analyse the gas propagation behaviour within a rigid grain skeleton in order to gain fundamental insights into the interplay of the three phases. A preliminary version of the developed miniature test stand is also described in Kaminski et al. (2023).

6.2.1 Experimental Set-Up and Procedure

For the μCT experiments, a customised test stand was developed. The test stand consists of a sample tube, a height-adjustable stage, the piping, and a pore pressure sensor including a self-sufficient data logging unit. Fig. 6.2 shows a schematic overview of the experimental set-up in combination with the CT scanner as well as the implementation of the test stand in the μCT scanner.

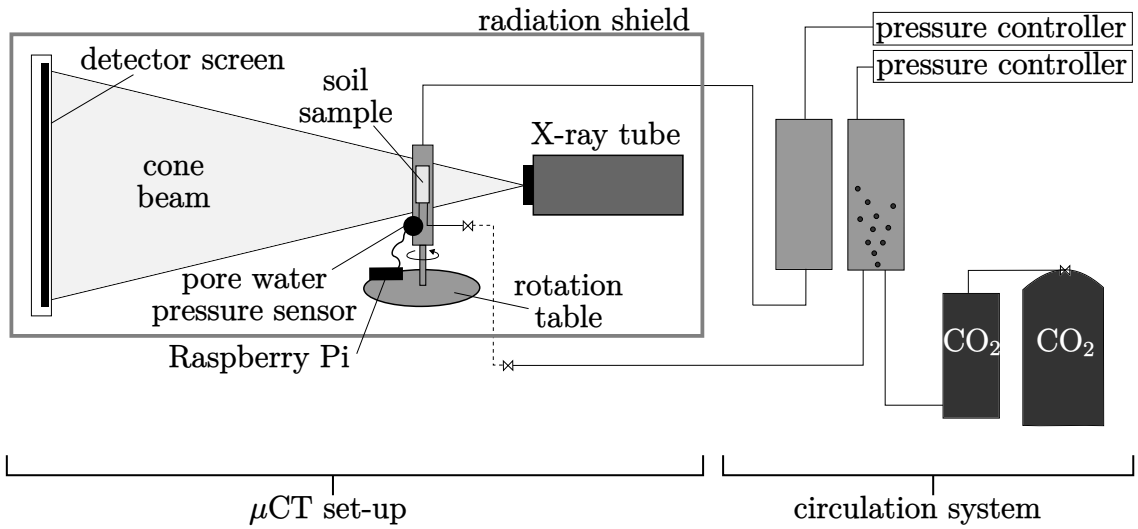

(a) schematic illustration

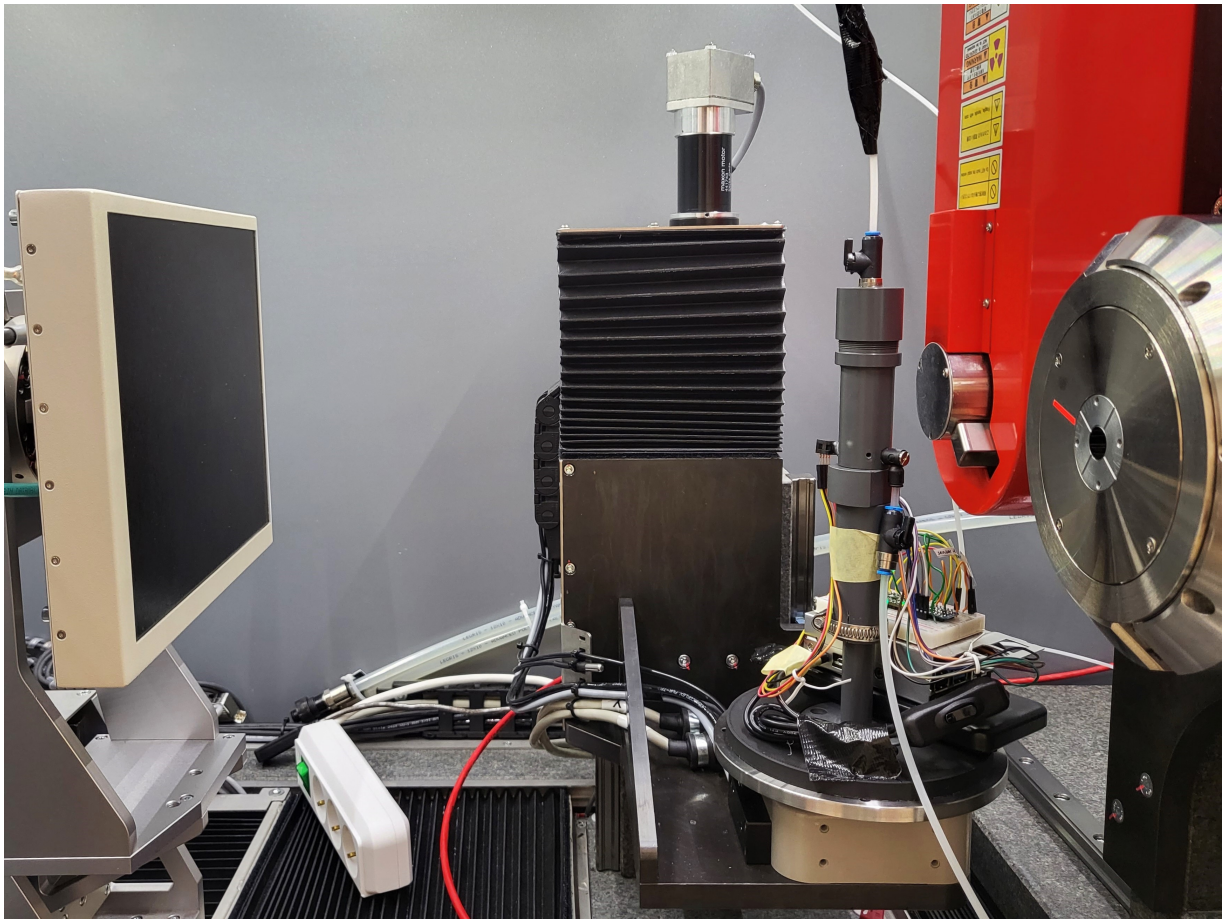

(b) implementation in the laboratory

Figure 6.2: experimental set-up for the microscopic experiments in the μCT device

The sample tube is a cylindrical tube with a screw top fabricated from the synthetic material PVC (polyvinyl chloride). Hard PVC is a robust and durable material that can be shaped by machining and is often used for industrial applications. The sample tube itself can fit a sample of 30.38 mm minimum height and 27.20 mm diameter. Within the field of view of the CT scanner, the outer walls of the tube exhibit a thickness of 1 mm. Since the test stand is supposed to contain its inner pressure during a CT scan, the tube is manufactured from one piece to limit possible weak areas at which leakage and pressure loss can occur. A tight seal of the test tube is guaranteed by a screw top, analogue to a water bottle. Here, the screw top is fabricated with an M33x1 fine thread and sealed by two rubber O-rings. Additionally, a ball valve with a push-in pipe connection towards the top FTV and the corresponding pressure control of the circulation system is integrated into the top cap. The base of the test tube incorporates two opposite inlet pipes. One of the inlet pipes is fitted with a push-in pipe connection and a second ball valve to connect the sample with the bottom FTV and the corresponding pressure control of the circulation system. The other inlet pipe connects the sample with a pore water pressure sensor.

The sensor is a Honeywell Low Pressure Sensor (type 24PCFFM6G), which is a differential pressure sensor with a measurement range between 0 and 689.5 kPa. The analogue output signal of the pore pressure sensor is converted to a digital signal by a 16-bit analogue-to digital converter of the type ADS1115 and subsequently logged via the built-in I^2C-data bus (inter-integrated circuit communication interface) of a Raspberry Pi 4 single-board computer and a simple python script. The Raspberry Pi simultaneously supplies the sensor with 5 V excitation voltage. A portable power bank is used, in turn, to supply the Raspberry Pi with electricity. Additional information on the experimental set-up is provided in appendix C.

The sample preparation in the microscopic experiments follows the procedure of the axis-translation method for gassy soils as described in chapter 4. Additionally, a summary of the necessary experimental steps in the case of the μCT experiments is illustrated in fig. 6.3. After building the sample in the test tube by water pluviation, the equipment described above is placed onto the rotation stage of the CT scanner. A height-adjustable pedestal is mounted to the centre of the rotation stage by means of a screw connection to allow an optimal positioning within the field of view of the CT scanner. In order to record a scan, the previously described test tube is fixed on top of the pedestal. The Raspberry Pi and its power supply are placed on the side of the rotation stage, allowing all the cable connections to rotate along without the hazard of entanglement (see also fig. 6.2b). Subsequently, the saturation and circulation stages follow. In this set-up, the pipe connection between the bottom FTV and the test tube is disconnected after the circulation stage so the radiation shield door can be closed for scanning. The pressure relief in the exsolution stage is induced via the top FTV. The pipe connection between the top FTV and the sample holder remains intact during the entire experiment as this pipe can be inserted in the scanning chamber through a cable duct while the equipment remains outside and accessible. To allow for meaningful sequential image acquisition, the unloading stage, thus the gas exsolution stage, is induced stepwise. The test tube is sealed after the gas exsolution to allow for the pressure within the sample to equilibriate so no movement of the phases occurs within the sample. In between the unloading stages, CT scans are conducted.

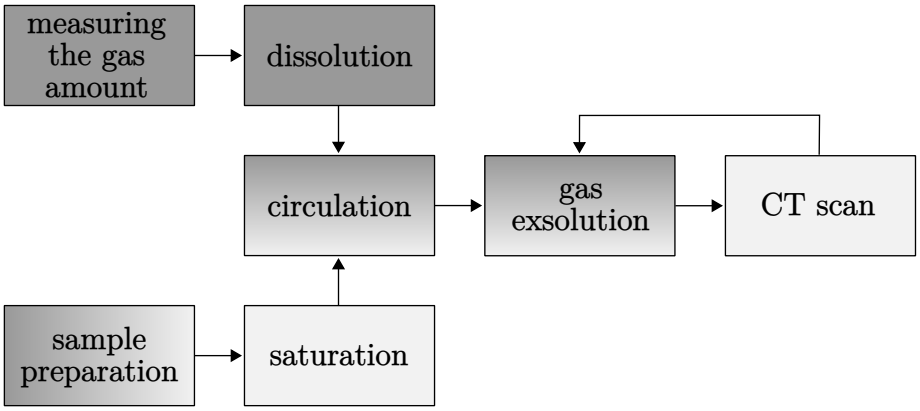

Figure 6.3: experimental procedure of the μCT experiments (*light grey*) in combination with the axis-translation method for gassy soils (*dark grey*, compare fig. 4.3)

The CT scanner itself is a nano- and μCT of the type EasyTom 160-150 fabricated by RX Solutions and located at the Institute of Applied Mechanics at Technische Universität Braunschweig. The final scanning parameters employed in this study were chosen based on experience from previous studies, e. g. by Milatz et al. (2021) and Milatz et al. (2022), as well as preliminary testing and are summarised in tab. 6.1.

The CT scanner is located in a temperature-controlled room. However, the scanning chamber itself is not temperature-controlled and is influenced by the heat production of the X-ray source during scanning. The temperature within the scanning chamber is logged during the image acquisition. Analogue to the macroscopic experiments, mainly a stable temperature development during an experiment is aimed for. This is of additional interest in the microscopic study, as the gas-water interface exhibits small-scale temperature-induced movement. Thus, it is of particular relevance to reduce the scanning times to a minimum to limit the heat production. Additionally, the radiation shield doors are opened during every unloading stage in between scans in order to air the scanning chamber.

Table 6.1: employed scanning parameters

		ISS0 sand	Hamburg sand
acceleration voltage	[kV]	150	150
X-ray source power	[W]	20	23
tube current	[μA]	130	150
images per 360° rotation	[-]	1440	1440
averaging	[-]	3	2
number of slices	[-]	1298	1298
voxel edge length	[μm]	16.09	16.09
scanning time	[min]	24	13

6.2.2 Overview of the Conducted Test Series

Similar to the macroscopic experiments, the gradation is likewise varied in the microscopic experiments. Therefore, with each of the employed model sands two experiments are conducted. In these two experiments, two different unloading magnitudes are applied in the depressurisation stages. Each experiment contains several sequential CT scans for each unloading stage. Tab. 6.2 summarises the microscopic experiments including their respective number of scans.

Table 6.2: overview of the μCT test series

denotation	test type	soil type	unloading steps / number of scans [-]	unloading magnitude per step Δp [kPa]
I10	μCT	ISS0	6	10
I5	μCT	ISS0	9	5
H10	μCT	HH	6	10
H5	μCT	HH	10	5

6.3 Evaluation Scheme

The image data resulting from the experimental procedure described above is processed and evaluated with a consistent procedure in order to ensure comparability within different scans of a sequence as well as within different experiments. Firstly, the reconstruction of each data set is conducted with the proprietary backprojection approach of the employed CT scanner's manufacturer. Its details are therefore not further discussed. The reconstructed raw data of two centre slices from two exemplary scans are depicted in fig. 6.4. Secondly, the data sets are processed, segmented, and analysed. The selection of denoising filters, segmentation algorithm, analysis procedures, and their respective configurations is outlined in the following. The data processing and analysis within the scope of this study is conducted with the software Avizo 3D 2022.1.

6.3.1 Data Optimisation and Denoising

The employed processing procedure involves an initial editing of the image volume, which is conducted to reduce the data set to the relevant parts. Hence, the test tube and the surrounding air in the scanning chamber are cut with the *Volume Edit* module. As a result, a cylindrical subvolume containing only the soil sample is obtained. Subsequently, several image optimisation filters are applied. The objective of this processing scheme is to enable a high quality image segmentation.
The applied optimisation scheme is three-fold: The first filter employed is the *Normalize Grayscale Filter*, which applies a histogram-based grey value scaling in order to increase the contrast. Subsequently, the *Median Filter* is applied to the data set. The median

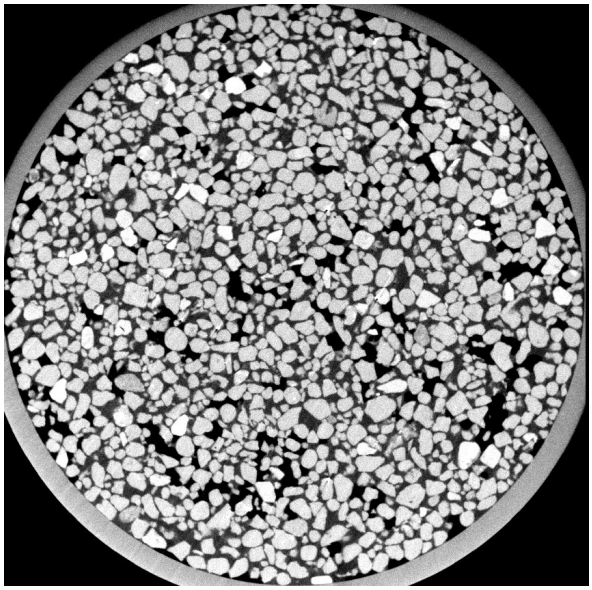

(a) Hamburg sand (H10-VI slice 649)

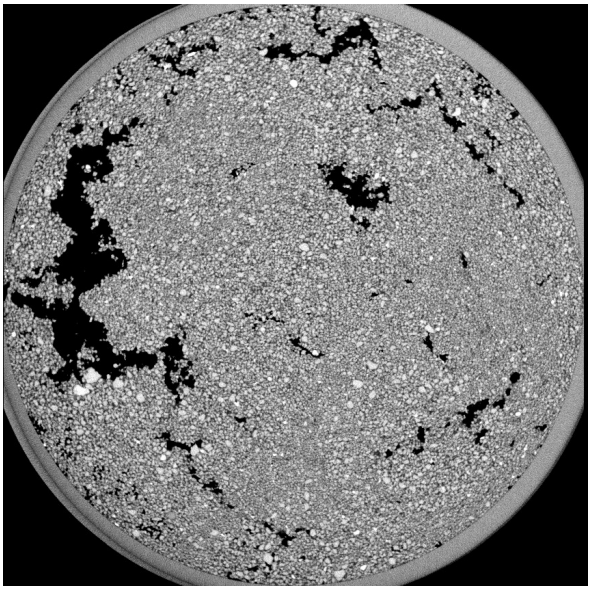

(b) ISS0 sand (I10-VI slice 670)

Figure 6.4: raw data from two exemplary CT scans

filter replaces the grey value of a voxel by the median grey value of the neighbouring voxels in an iterative procedure, and thereby reduces image noise and small artefacts. A disadvantage is that the image is defocused by this smoothing filter. Therefore, the data is further processed by means of a *Non-Local Means Filter*. This filter is an edge-preserving denoising filter based on the weighted similarity of a voxel's neighbourhood with a larger search window. The influence of the optimisation scheme on the image data is illustrated in fig. 6.5. A similar optimisation procedure is employed in Milatz et al. (2021) and Milatz (2023), as Hamburg sand was also used in these investigations.

6.3.2 Segmentation

After optimisation, the image data is passed to the segmentation phase. However, the fine ISS0 sand exhibits a gradation too fine to be resolvable at the obtained voxel size of 16.09 μm. Even though the mean grain diameter is substantially larger than the voxel size, the impact of image data processing is marginal as the influence of the partial volume effect is overwhelming. The image data shown in fig. 6.5b clearly demonstrates this predicament. A different optimisation scheme is also not able to remedy this shortcoming. It is therefore impossible to classify voxels at the water-solid material boundaries, which make up a significant percentage of the sample in fine sand. Due to the morphology of the gas phase, i. e. the gas bubbles are significantly larger than the mean grain size, a segmentation into two phases becomes possible: a gas phase and a saturated soil matrix.
In this study, a watershed segmentation algorithm is applied. The operating principle of this segmentation approach can be illustrated by means of rain falling on a mountain landscape. When the terrain is flooded, the water fills the valleys first while the mountain crests serve as watershed lines. In this analogy, the basins correspond to the image regions attributed to a phase, and the mountain crests correspond to the phase boundaries. For

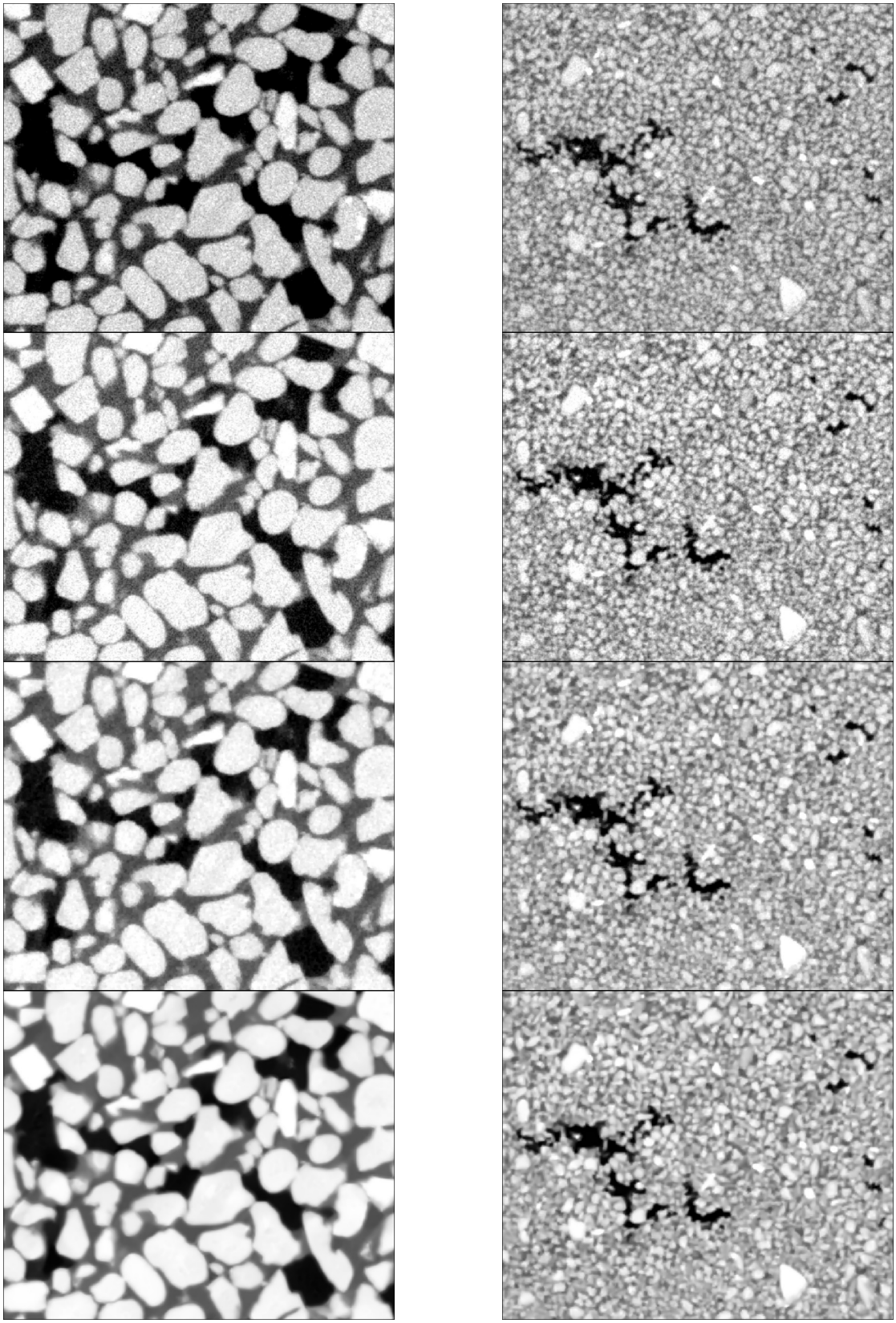

(a) Hamburg sand (H10-VI slice 649) (b) ISS0 sand (I10-VI slice 670)

Figure 6.5: influence of the optimisation scheme on the image data (from top to bottom: raw data, *Normalize Grayscale*, *Median Filter*, *Non-Local Means Filter*)

this process, the topographic relief is defined by the grey value distribution of the image (Roerdink and Meijster, 2000).
To put the image segmentation into practice the *Watershed Segmentation* module is applied to the data set. Here, the gradient magnitude of the grey values is computed, based on which the threshold markers are defined in a following step. Subsequently, the watershed algorithm implemented in AVIZO PRO, which is based on Beucher and Meyer (1992), is applied. As outlined above, the ISS0 sand image data is segmented into two phases (gas and saturated soil matrix) and the Hamburg sand image data into three phases (gas, water, and solids). Exemplary segmentation results are shown in fig. 6.6.

6.3.3 Analysis

The tri- or binarised data is further analysed in order to gain insights on the behaviour of the gas phase within the pore space. An analogue procedure is followed for both investigated sands, which is briefly outlined as follows.
Initially, the macroscopic properties of the sample are summarised. These include the measured pore pressure, the temperature in the scanning chamber, as well as measured values during the sample preparation. Furthermore, the gas content over the specimen height is analysed as it gives valuable information on the homogeneity of the gas phase within the sample. In Hamburg sand, the gas content is measured by means of the degree of saturation S_r. In ISS0 sand, S_r cannot be derived, because the solid and the water phase cannot be isolated. Therefore, the volume fraction of gas f is introduced. The parameter relates the gas volume to the total sample volume and has already been used by Wheeler (1986), Wheeler (1988a), and Wheeler (1988b) to describe the gas content in gassy clays in dependence of the void ratio e:

$$f = \frac{V_g}{V_{tot}} = \frac{(1 - S_r) \cdot e}{1 + e}. \tag{6.2}$$

For this purpose, the *Material Statistics* module is applied, which computes statistical quantities of the segmented phases in a slice-by-slice manner. In the following, parameters such as S_r, f, and e are distinguished by the terms *global* and *local*. *Global* refers to the entire CT data set, while *local* corresponds only to the sample section in question, which might be a slice or another kind of subvolume. The global parameters are assumed to equal the properties of the entire sample. However, the CT data volume is manually defined during the reconstruction process and might, thus, deviate slightly from the physical sample volume. As a consequence, the global sample properties are not necessarily constant even though the physical sample is constrained within the test tube.
In order to examine the microscopic sample properties in a following analysis step, a REV is defined for every sequence by conducting REV analyses. In these analyses a subvolume is placed in the centre of the sample and successively expanded while analysing the parameters of interest for every expansion step. Here, the parameters of interest are the volume fraction of gas in ISS0 sand and the degree of saturation as well as the void ratio in Hamburg sand. The following criteria are consulted in order to determine the REV's edge length:

- The REV is the subvolume in which the parameters of interest are not influenced by a further increase of the examined subvolume (convergence),

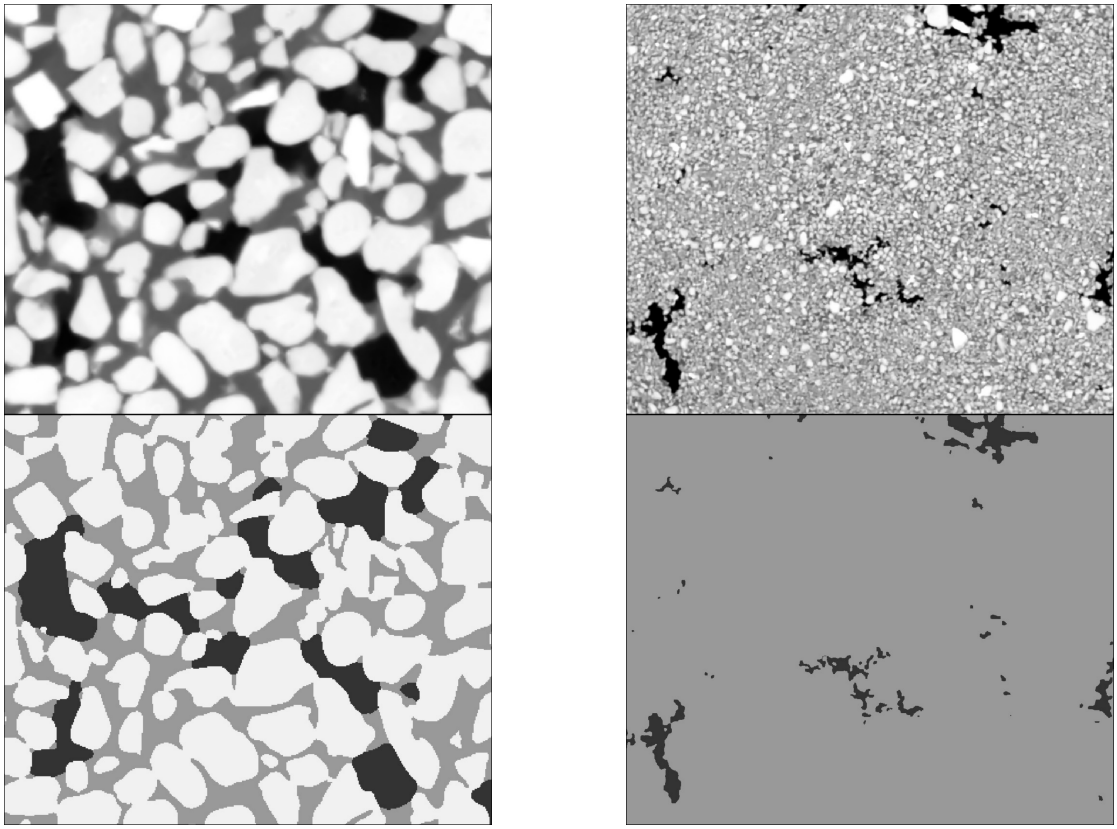

(a) Hamburg sand (H10-VI slice 649) (b) ISS0 sand (I10-VI slice 670)

Figure 6.6: segmentation of the image data (top: image after optimisation; bottom: segmented image)

- the smallest possible subvolume is chosen as the REV to exclude potential boundary effects at the test tube walls and to limit the required computational resources,
- the REV is determined on the most heterogeneous sample of a sequence and it is assumed that this REV is applicable for all scans in a sequence, and
- due to the stationary grain skeleton one centred REV is assumed to suffice for a representative description of the entire sample.

For both sands, a qualitative and phenomenological interpretation of the data is conducted before quantitative measures are derived. Based on the phenomenological assessment, basic classifications regarding the soil mechanical characteristics and the gas migration behaviour as outlined in chapter 2 are derived. The *Volume Rendering* module is employed to visualise the phases of interest.
Finally, a quantitative examination is conducted for the REV domain. To this end, the amount and size of the gas clusters as well as their development over the course of a sequence are analysed. This gives information on the exsolution behaviour as well as on the coalescence and migration behaviour of the gas phase. The *Label Analysis* module, which computes user defined quantities for coherent domains, provides the relevant information.

Besides the characteristics of the gas phase, the gas-water-interface is of relevance to the mechanical behaviour of the soil, as the surface tension acts only here. Therefore, the capillary force potential is considered by examining the development of the interface area. This is put into practice by isolating the interface with the *Generate Surface* module, which computes a triangulated surface corresponding to the interface. Subsequently, the area of this triangulated surface is calculated by the *Surface Area Volume* module.

6.4 Results and Interpretation

Two scanning sequences were acquired with the experimental set-up and procedure described above on ISS0 sand and Hamburg sand, respectively – each executed with different intermittent unloading stages between the singular scans. Test I10 and H10 were performed with an unloading magnitude of $\Delta p = 10\,\mathrm{kPa}$, and test I5 and H5 with $\Delta p = 5\,\mathrm{kPa}$ (see also tab. 6.2). These unloading magnitudes refer to the predicted pore pressure developments according to the calculated target saturations based on the solubility curve. The resulting image data and the outcomes of the analyses are described in the following. The order of analysis steps in this section follows the outline delineated in the evaluation scheme (section 6.3).

6.4.1 Specimen Properties

The properties of the scanned soil samples change with every unloading step as a consequence of the gas impact. Therefore, the initial specimen properties as well as their development during a scanning sequence are summarised before further analyses are conducted. Furthermore, constraints regarding the interpretability ensuing from the experimental procedures in single tests are discussed.

Initial Remarks

The relevant sample properties in every scan of the two sequences I10 and I5 are summarised in tab. 6.3. In line with the macroscopic experiments and the CT scans on Hamburg sand, the targeted gas contents are given as target degrees of saturation despite the inability to compute this parameter for ISS0 sand. An approximate conversion of the achieved volume fractions of gas is, thus, given for comparability. For this purpose, equ. 6.2 is applied in combination with an average void ratio of 0.774, corresponding to the mean e_{prep} from the triaxial tests on ISS0 sand.
Unfortunately, test I5 suffers from several shortcomings: a failure of the pore pressure sensor and a slightly inclined installation of the test tube on the pedestal during the scan. The former leads to a lack in data required to verify a successful testing procedure, while the latter results in a grey scale gradient in the reconstructed data set that is difficult to correct with image filters and therefore impacts the segmentation, and consequently the derived quantitative measures. For this reason, experiment I5 is mostly used for qualitative interpretations.
The specifics of all scans within the two scanning sequences on Hamburg sand, H10 and H5, are summarised in tab. 6.4. Both experiments are considered suitable for further analyses.

Table 6.3: overview of the single μCT scans on ISS0 sand conducted within the scope of experiments I10 and I5

denotation	target saturation S_r^* [-]	achieved volume fraction of gas f [-]	corresponding saturation $S_{\mathrm{r,e=0.774}}$ [-]	mean temperature T_{mean} [°C]	temperature change ΔT [°C]
I10-I	1.00	0.000	1.00	25.906	0.500
I10-II	0.98	0.007	0.984	26.286	0.500
I10-III	0.96	0.033	0.924	26.563	0.000
I10-IV	0.94	0.052	0.881	26.804	0.375
I10-V	0.92	0.067	0.847	27.173	0.188
I10-VI	0.90	0.073	0.834	27.256	0.063
I5-I	1.00	0.001	0.999	26.291	1.188
I5-II	1.00	0.001	0.999	26.561	0.250
I5-III	1.00	0.001	0.998	26.900	0.250
I5-IV	0.99	0.001	0.998	27.229	0.125
I5-V	0.98	0.001	0.998	27.344	0.188
I5-VI	0.97	0.001	0.998	27.639	0.250
I5-VII	0.96	0.001	0.998	27.754	0.125
I5-VIII	0.95	0.001	0.998	27.946	0.063
I5-IX	0.94	0.001	0.998	28.007	0.063

Sample Properties During the Scans

The success of the gas exsolution and whether the intended conditions were met during the experiment can be monitored by means of the pore pressure development, which is depicted in fig. 6.7. In the pressure curve of experiment I10 (fig. 6.7a), distinct unloading events can be identified for every scan. These are followed by an immediate rebound and the following attainment of a plateau. The pressure rebound indicates the successful exsolution of gas, in which the spatial requirements of the newly created gas phase lead to the pressure build-up. The plateau represents an equilibrium state. Therefore, the required immobility of the gas phase during a CT scan was presumably achieved in test I10. The pore pressure development in test H10 is similar to the behaviour identified in test I10 (compare fig. 6.7b). Generally, this pore pressure behaviour resembles the pore pressure development in the unloading stage of the macroscopic experiments. The rebound effect is more pronounced in the microscopic experiments I10 and H10, which possibly is a result of the smaller sample size and/or the rigid walls of the test tube compared to the flexible membrane in the triaxial test. It can therefore be concluded, that the gas exsolution proceeded similarly in the micro- and macroscopic test series. Due to the strong rebound effect, the implemented unloading magnitudes vary strongly from the intended and theoretically presumed $\Delta p = 10\,\mathrm{kPa}$ in both experiments. Additionally, no major differences with respect to the soil gradation can be identified when comparing tests I10 and H10. The pore pressure development for test H5 as shown in fig. 6.7b,

Table 6.4: overview of the single μCT scans on Hamburg sand conducted within the scope of experiments H10 and H5

denotation	target saturation S_r^* [-]	achieved saturation S_r [-]	mean temperature T_{mean} [°C]	temperature change ΔT [°C]	void ratio e [-]
H10-I	1.00	1.00	25.881	0.563	0.616
H10-II	0.98	0.970	26.215	0.250	0.622
H10-III	0.96	0.912	26.473	0.188	0.622
H10-IV	0.94	0.832	26.563	0.000	0.625
H10-V	0.92	0.778	26.571	0.063	0.634
H10-VI	0.90	0.776	26.767	0.250	0.636
H5-I	1.00	0.981	27.184	0.500	0.654
H5-II	1.00	0.986	27.516	0.438	0.657
H5-III	1.00	0.971	27.637	0.438	0.657
H5-IV	0.99	0.962	27.791	0.188	0.659
H5-V	0.98	0.953	27.944	0.063	0.661
H5-VI	0.97	0.946	27.999	0.188	0.659
H5-VII	0.96	0.937	28.138	0.125	0.659
H5-VIII	0.95	0.925	28.210	0.063	0.661
H5-IX	0.94	0.915	28.294	0.063	0.659
H5-X	0.93	0.907	28.378	0.063	0.656

however, does not allow to draw such distinct conclusions. Here, the unloading stages cannot be distinguished clearly but are within the range of the signal's noise. It appears that, with some fluctuations, the pore pressure has evened itself out at an equilibrium state around the solubility limit over the entire course of the scanning sequence. Whether the performed unloading stages still stimulated gas exsolution cannot be determined. Thus, from the pore pressure data alone the success of the exsolution process in test H5 cannot be verified.

The temperature data recorded within the scanning chamber are summarised in tab. 6.3 and 6.4 as averaged temperatures T_{mean} for the experiments on ISS0 and Hamburg sand, respectively. It shows a steady increase in temperature over the course of each scanning sequence. However, the temperature difference over the sequence is not substantial to the point that it interferes with the integrity of the acquired data. The temperature differences from the beginning to the end of every single scan are marginal and, thus, neglectable with respect to any caused movement of phase interfaces. More detailed information on the temperature development is given in appendix C.

Tab. 6.3 and 6.4 further compile the targeted and achieved degrees of saturation for every scan. For the experiments on ISS0 sand, the achieved volume fractions of gas with the corresponding conversion to degree of saturation are given. The amount of gas in the samples increases with increasing unloading step in the scanning sequences I10, H10, and H5. In experiment H5, the achieved degrees of saturation match the targeted degrees of

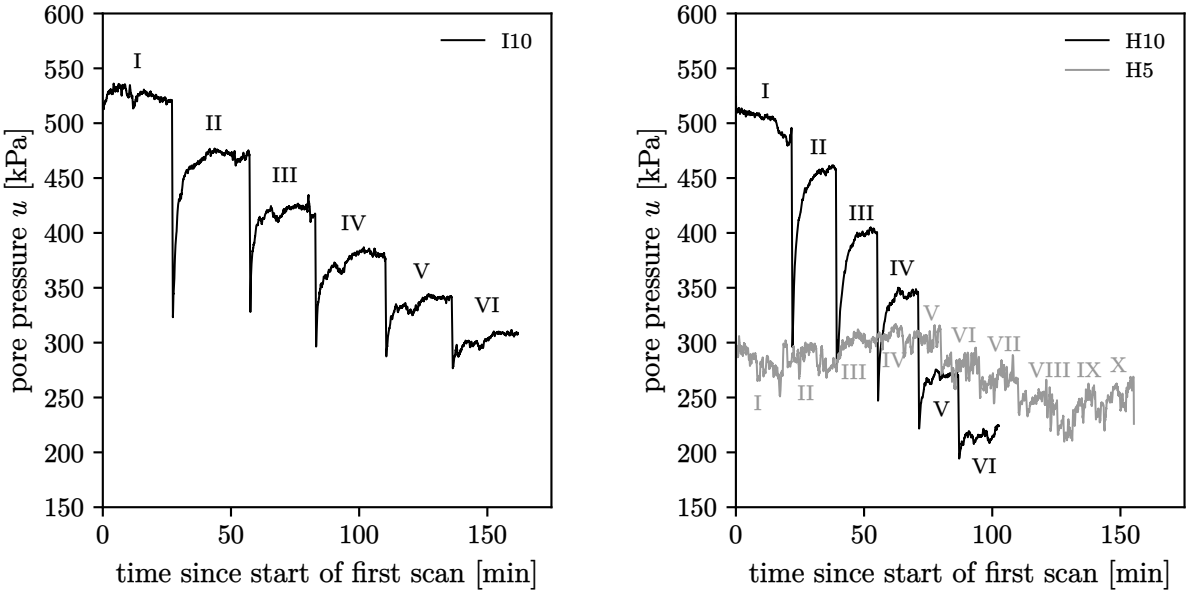

(a) ISS0 sand

(b) Hamburg sand

Figure 6.7: development of the pore pressure during the unloading and scanning sequences

saturation sufficiently well. In contrast, in tests I10 and H10, the discrepancy is significant. Assumedly, the larger unloading magnitude creates a state of supersaturation which cannot be equilibrated in the small sample volume within the rigid test tube. The strong pressure rebound after unloading in the pore pressure data supports this assumption. Since the underlying calculation scheme to identify the target pressures for specific saturations (see chapter 4) is only valid for equilibrium states, the induced saturations do not correspond to the calculated values in this case. Experiment I5 forms an exception. In this scanning sequence, the achieved saturation does not increase with decreasing pressure. Conclusively, the gas exsolution procedure was not successful in a global perspective on the sample.
Since the image data opens the opportunity to evaluate the sample's properties of interest for different height sections, the homogeneity of the sample can be assessed. Looking at the gas distribution within the ISS0 sand samples in fig. 6.8, first of all, an increase in volume fraction of gas with increasing unloading step can be identified in both scanning sequences. This points towards a successful experiment performance. However, in both scanning sequences the gas distribution exhibits a substantial heterogeneity over the sample height. Further, the heterogeneity increases with increasing unloading step. In test I10, the volume fraction of gas increases with increasing proximity to the sample surface. Furthermore, abrupt changes in gas content over a small height range are present and indicate horizontal layering of the gas phase. Test I5 exhibits a reverse behaviour with an increasing volume fraction of gas towards the bottom of the sample. Moreover, the changes in gas content are not as abrupt as in test I10 but rather continuous. Therefore, no hypotheses regarding the spatial orientation of the gas phase can be proposed. Additionally, the overall magnitude of the volume fraction of gas in test I5 is significantly lower than in test I10. Due to the lack in pore pressure data, however, it remains unclear whether this is a consequence of poor

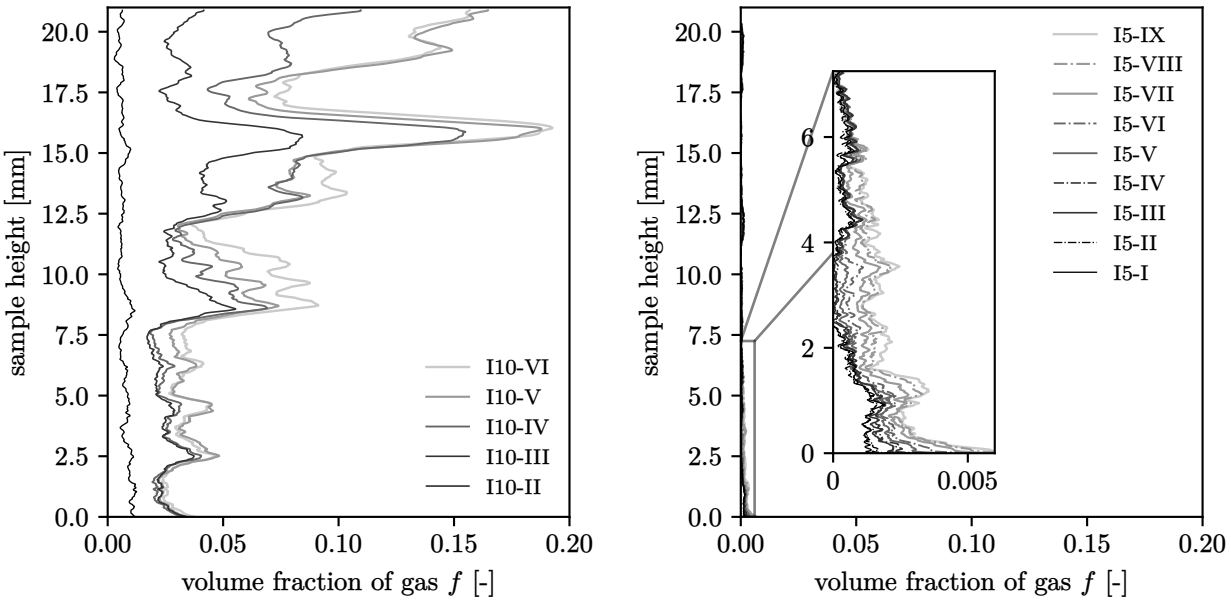

(a) I10 (b) I5

Figure 6.8: volume fraction of gas over the sample height in ISS0 sand

experiment execution or whether this is a direct effect of the lower unloading magnitudes applied in this sequence. Possibly, the lower unloading magnitude leads to an insufficiently strong exsolution reaction to initiate a fracture process. A similar analysis is conducted for the experiments on Hamburg sand. However, in this case, the degrees of saturation are derived from the image data. Fig. 6.9b and 6.10b illustrate the degree of saturation over the sample height for H10 and H5, respectively. However, no explicit dependency on the sample height can be observed for either experiment. In both tests, lower saturations are present at the bottom and the top of the sample. This suggests boundary effects, possibly induced by a preferential exsolution at the filter paper surface compared to the sand particle surface. Apart from the degree of saturation, also the heterogeneity of the gas distribution increases with increasing unloading step in both experiments. This behaviour is analogous to the experiments on ISS0 sand.

Besides the degree of saturation, the void ratio can be derived from the image data for Hamburg sand (see also tab. 6.4). In test H10, an increase of the global void ratio is observable with increasing saturation. Therefore, it can be assumed that the gas exsolution process is dynamic enough to cause changes in the structure of the grain skeleton. This observation is in line with the induced high supersaturations in the experiment with larger unloading magnitude, as higher supersaturations lead to a stronger exsolution reaction. In test H5, the variations of the void ratio are only marginal. Thus, the grain skeleton assumedly remains in its initial state when a gas phase is introduced to the sample. An analysis of the sample height dependency of the void ratio supports the described findings for test H5 over the entire sample height (see fig. 6.10a). For test H10, however, the data in fig. 6.9a shows that the increase in the sample's void ratio is only put into effect in the upper part of the sample at a low burial depth. Consequently, the grain displacing forces induced by the gas are only effective at very low effective stresses.

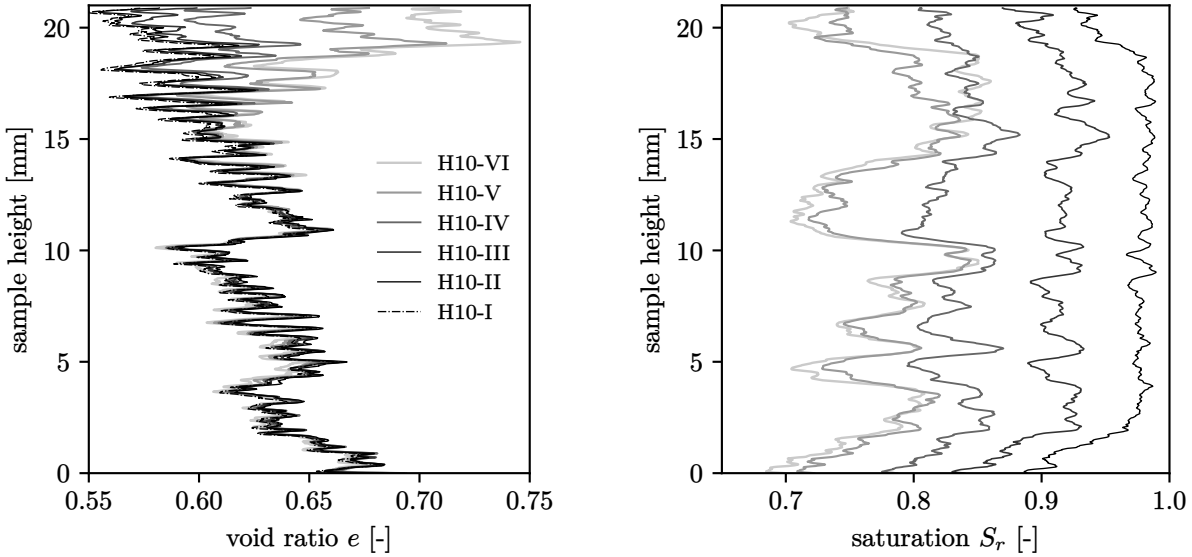

(a) void ratio (b) degree of saturation

Figure 6.9: sample properties over the sample height in Hamburg sand (H10)

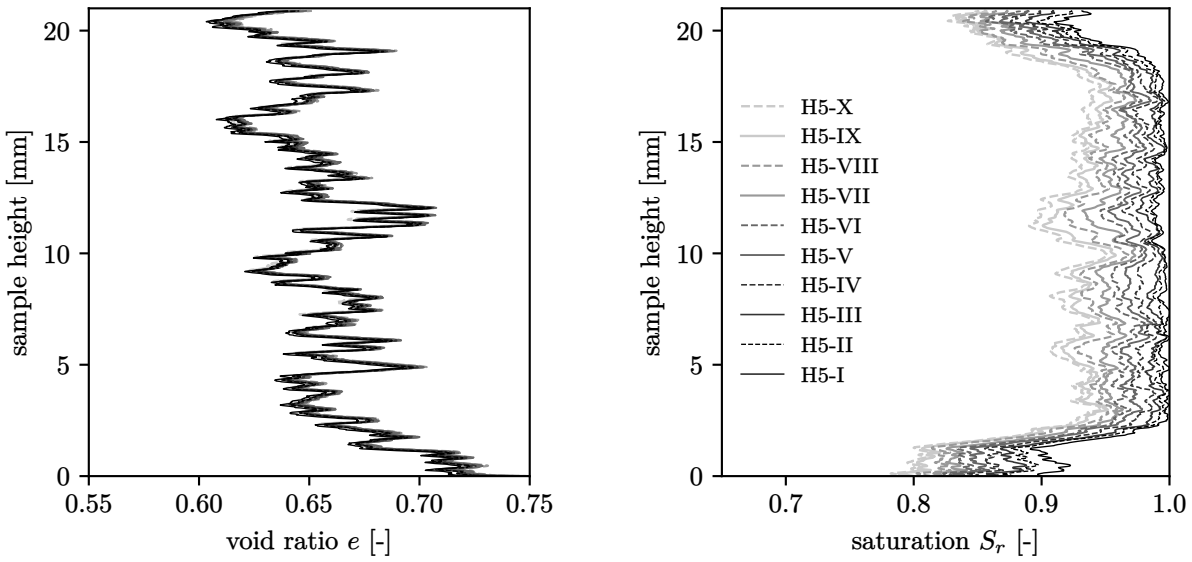

(a) void ratio (b) degree of saturation

Figure 6.10: sample properties over the sample height in Hamburg sand (H5)

6.4.2 Determination of the REV for Further Analyses

In order to determine the edge length of the REV for further analyses, the convergence of the parameters of interest with increasing subvolume size is assessed (see fig. 6.11). For ISS0 sand, the parameter of interest is f, while S_r and e are evaluated for Hamburg sand. Due to the deficiencies in test I5, the REV analysis for ISS0 sand is only conducted for test I10. Here, scan I10-VI is chosen to determine the REV, as it exhibits the highest fluctuations in the volume fraction of gas. The REV analysis scheme stipulates to place the initial subvolume in the centre of the sample. Even though the volume fraction of gas varies substantially with the sample height, the centre is considered an adequate location, as a medium volume fraction of gas can be expected in this height range. Since the analysis of the void ratio and the degree of saturation over the sample height in the experiments on Hamburg sand showed their most heterogeneous distribution for the scans with maximum unloading, scans H10-VI and H5-X are used for the REV analysis. To facilitate a coherent quantitative analysis and a comparability of both tests, identical REV sizes are chosen for both tests.
Fig. 6.11a shows the volume fraction of gas with increasing subvolume size. For small subvolume sizes below 400 px edge length, the volume fraction of gas increases from 0 and shows some fluctuations. At 600 px edge length, a value representative of larger subvolumes of ≥ 900 px sizes is reached for the first time. Since the required computational resources for the ensuing analyses are substantial, a subvolume with 600 px edge length is chosen as the REV for all scans in the sequence I10.
Fig. 6.11b presents the results of the REV analysis on Hamburg sand. For small subvolume sizes below 200 px edge length the fluctuations of both parameters are substantial. The convergence for the void ratio is reached at 400 px edge length in both scanning sequences. The degree of saturation in test H10, however, exhibits noticeable changes until an edge length of 600 px. Therefore, the latter is determined as the REV size for further analyses on Hamburg sand.

6.4.3 Phenomenological Analysis of the Gas Phase Growth

The previous sections determined the basic sample properties and elementary information for an extended analysis of the data set. Hereinafter, a qualitative analysis of the gas phase characteristics is conducted in order to identify typical features in the gas phase morphology before those are investigated in a quantitative manner in a following section. A basic assessment regarding the pore habit of the gas phase in ISS0 sand is already anticipated by the elaborations on the evaluation scheme in section 6.3: the gas appears in macrobubbles with larger diameters than the mean grain size instead of in small bubbles homogeneously dispersed in the pore space. Otherwise, neither the gas phase would be resolvable in this soil under the applied scanning conditions. In order to obtain a deeper understanding of the gas morphology in ISS0 sand, the gas phase is isolated and visualised for every applied unloading step in sequence I10; see fig. 6.12. The volume fraction of gas in the REV f_{REV} is given for every unloading step. In addition, the growth of a single gas cluster in test I5 is shown in a cross-sectional view in fig. 6.13. Both visualisations clearly support the initial presumption. Therefore, it can be concluded that the pore habit of

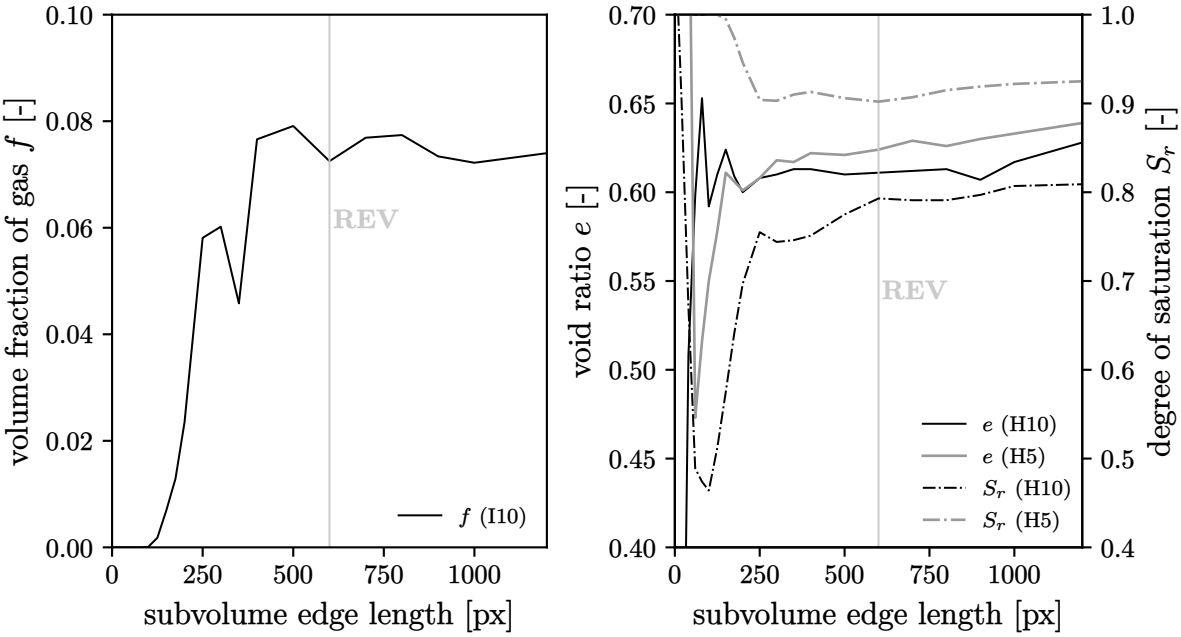

(a) ISS0 sand (I10-VI) (b) Hamburg sand (H10-VI and H5-X)

Figure 6.11: determination of the representative elementary volume

the gas rather corresponds to the characteristics expected in a fine-grained soil (compare fig. 2.3). The limiting grain size for macropore formation, thus, does not correspond to the delimiting grain size for the soil type as defined by, e. g. ASTM D2487-17e1. Instead, this mechanism is likewise feasible for granular soils. Particularly the gas phase in scan I10-II, presented in fig. 6.12b, is in accordance with the *Large Bubble Model*. Here, the gas clusters exhibit a spiky shape. A similar pore habit can also be derived from the cross-sectional views in fig. 6.13.

After identifying the fundamental morphological features of a gas phase in fine sand, the successive formation of the macropores is analysed in the following. Upon initial gas formation in test I10, the macropores are created homogeneously within the subvolume. With further unloading, i. e. increasing gas content, the gas clusters develop into horizontally bedded fractures. Therefore, the dominating gas migration mechanism is fracturing and not capillary invasion. This general morphological expression is manifested with increasing gas content, resulting in a growing thickness of the gas beds. In consequence, several large and independent gas beds separated by layers of saturated soil matrix can form in a sample. The horizontal orientation of the fractures can be a consequences of the small sample size and the resulting low effective stress level, of predetermining heterogeneities in the soil structure caused by the layerwise sample preparation, or of a heaving force induced by the unloading via the top cap. Under a different stress state, a different orientation of the fractures is conceivable as well. Accompanying the fracture formation, the gas distribution becomes rather heterogeneous within the REV, because the gas localises within the fracture planes. No prominent formation of large new gas clusters can be determined in the later unloading stages. A closer look at the cross-sectional view in fig. 6.13 reveals that the formation of small new macropores around the existing fracture is, however, a re-

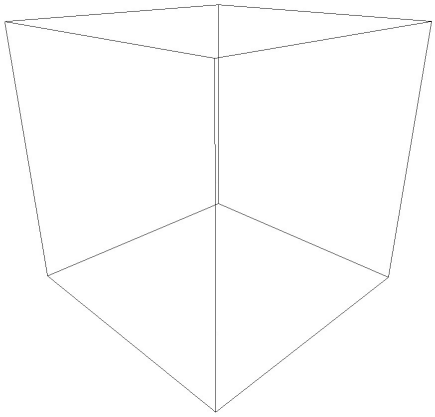

(a) I10-I ($f_{REV} = 0.00$)

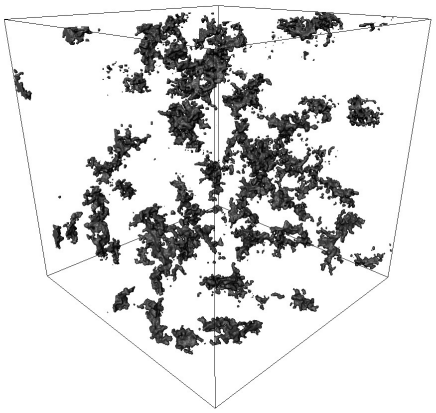

(b) I10-II ($f_{REV} = 0.008$)

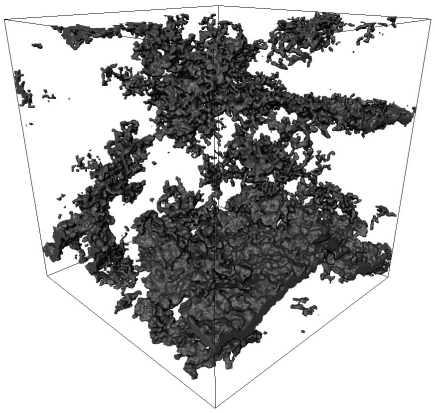

(c) I10-III ($f_{REV} = 0.040$)

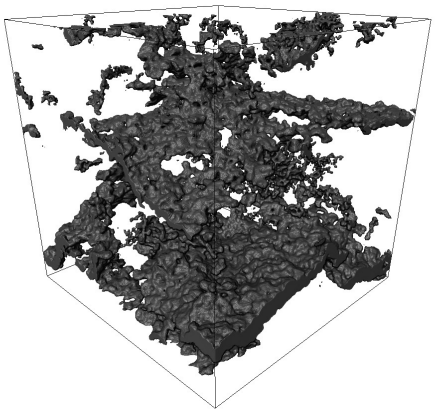

(d) I10-IV ($f_{REV} = 0.059$)

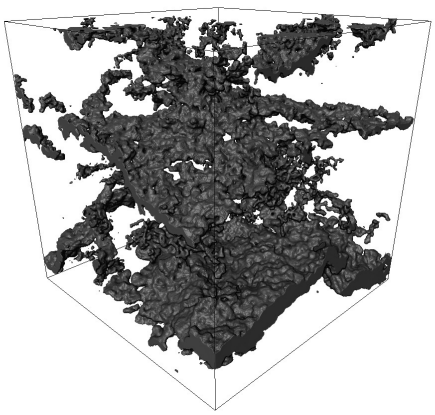

(e) I10-V ($f_{REV} = 0.062$)

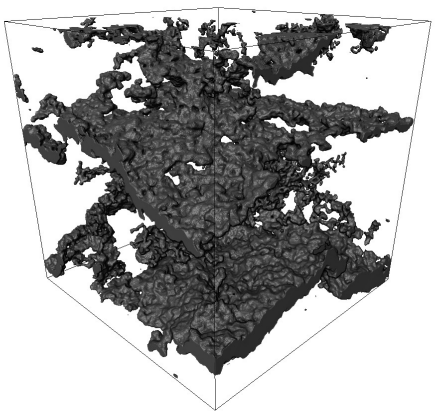

(f) I10-VI ($f_{REV} = 0.073$)

Figure 6.12: gas phase morphology in ISS0 sand (test I10)

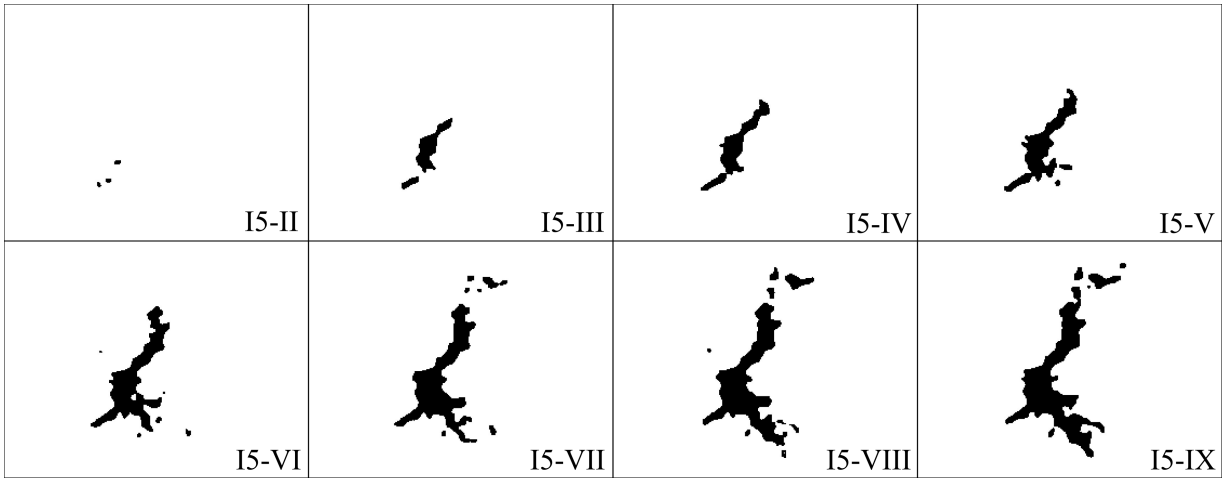

Figure 6.13: growth of a single selected gas cluster in ISS0 sand (test I5) in a cross-sectional view

peatedly occurring feature. Frequently, the smaller macropores coalesce with the fracture when it extends during the following unloading step. Conclusively, smaller macropores predetermine the fracture path of the larger fractures. Immanent to the fracturing process is a displacement of the grain skeleton. The void ratio of the sample, thus, changes with increasing gas content. To which extent the void ratio of the saturated soil matrix is impacted and how strongly this void ratio change localises in the gas-filled fractures cannot be assessed conclusively at the given image resolution. It must, however, be noted that the transferred degrees of saturation in tab. 6.3 have to be interpreted with caution as they depend on the void ratio.

Fig. 6.14 and fig. 6.15 show the gas phase isolated from the scans of tests H10 and H5, respectively. Additionally, the degree of saturation in the REV $S_{\mathrm{r,REV}}$ is indicated for the unloading steps. A complementary cross-sectional view of chosen gas clusters from test H10 is given in fig. 6.16. The gas clusters forming in Hamburg sand exhibit a fundamentally different morphology compared to those in ISS0 sand. The shape of the clusters is rounded without distinct edges or spikes. However, they have a larger size than the single pores. Hence, one pore cannot accommodate a gas bubble and it spans over several pores. Therefore, also for the coarser gradation with larger pore spaces, the gas morphology does not correspond to the theoretical model of small, dispersed bubbles without contact to the solid phase as illustrated in fig. 2.3. In test H10, the initial gas clusters are distributed rather homogeneously within the REV. In contrast, only single small gas clusters form in the initial unloading stage of test H5. Due to their small number, the gas distribution within the REV is more localised, even though – globally – test H5 appears less heterogeneous (compare fig. 6.9 and 6.10). Nonetheless, the visualised gas phase in fig. 6.15 verifies a successful experimental implementation despite the ambiguous pore pressure data. Furthermore, an evident impact of the unloading magnitude on the gas morphology can be identified from the isolated and visualised gas phase in H10 and H5. As expected, the larger supersaturations induced by the larger unloading magnitudes lead to larger amounts of gas to be exsolved. However, it appears that the higher dynamics of

the exsolution process significantly impact the homogeneity of the gas phase as well as the growth behaviour. The quantitative extent of the latter will be discussed in the following section.
Upon further unloading, the gas amount increases, thus, the degree of saturation decreases in both tests. During the process, the existing gas clusters grow. When gas clusters grow, capillary invasion is the dominant growth and migration mechanism. The cross-sectional view in fig. 6.16 elucidates this conclusion. The gas cluster highlighted with the arrow 1 extents in perfect alignment with theoretical concept of percolation along the path with the largest pore throats while displacing the water phase from the occupied pores. Furthermore, the phenomenon of gas bubble coalescence can be observed (highlighted with arrow 2). The extent of grain displacement observable in the image data of Hamburg sand is marginal. In consequence, the delimitating grain size between fracturing and capillary invasion for the implemented stress levels is located between the mean grain sizes of the chosen model sands.

6.4.4 Quantitative Analysis of the Gas Phase Growth

The growth behaviour of the gas clusters can be analysed quantitatively by comparing the development of the gas volume with the number and the size of the gas clusters. For this purpose, fig. 6.17 presents the number of all gas clusters and the sum of the gas volume in the REV $V_{\mathrm{g,REV}}$ over the volume fraction of gas, i. e. the unloading step, of test I10. The sum of the gas volume is redundant to the volume fraction of gas and is only shown to emphasize the growth mechanism. The number of the gas clusters decreases significantly from the first unloading step, in which the gas formation occurs, to the later scans. In conclusion, the initially formed macropores grow and connect to a smaller number of clusters with larger volumes each. In the later unloading steps, the number of gas clusters remains within a steady range, even though the gas volume keeps increasing. Thus, the major mechanism is the growth of the existing fractures. The phenomenological analysis of the cross-sectional view in fig. 6.13 indicates that the formation of new macropores and the rate of gas cluster coalescence are in balance during the growing process.
The findings outlined above are supported by an examination of the gas volume of the single gas clusters $V_{g,c}$ in every unloading step. The results of this analysis are shown in fig. 6.18. While the first unloading step at which a gas phase is formed (I10-II) exhibits many gas clusters of small volumes each, in later scans, the amount of gas clusters with larger volumes increases steadily. It is, however, noteworthy that the amount of gas clusters with very small volumes does not change significantly with increasing unloading step. This means, that either a large number of gas clusters exists without significant growing activity during unloading while the increase of gas volume is concentrated on very few larger fractures, or new macropores are created in every unloading step. Both mechanisms can exist in parallel, assuming that the newly created macropores are incorporated in the growing, existing fracture in a following unloading step. The feasibility of this assumption has been derived above.
Looking at the growth behaviour of the gas clusters in Hamburg sand in a quantitative manner, the conclusions derived from the previous phenomenological analysis of the gas phase can be substantiated. Fig. 6.19 shows that the number of gas clusters increases with

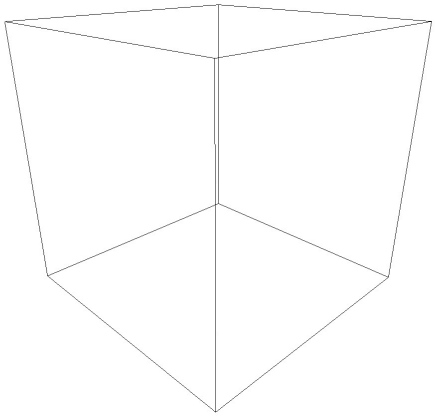

(a) $S_{\mathrm{r,REV}} = 1.00$

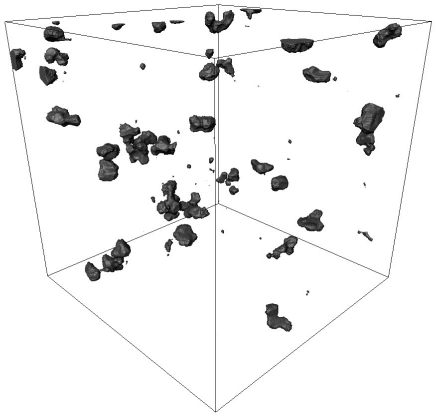

(b) $S_{\mathrm{r,REV}} = 0.986$

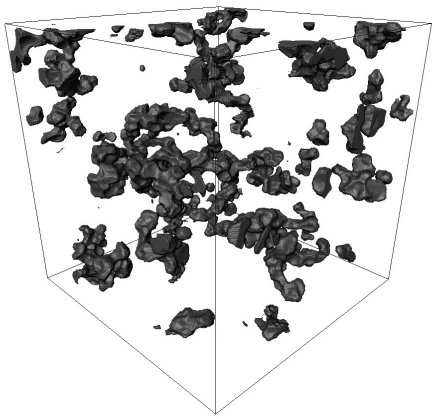

(c) $S_{\mathrm{r,REV}} = 0.923$

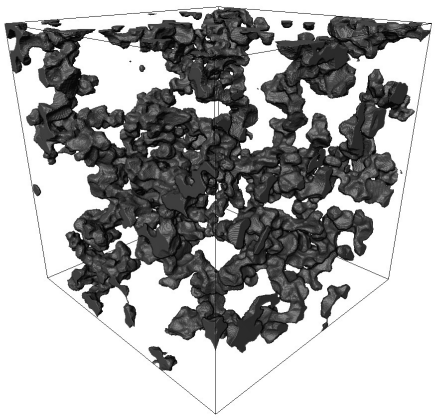

(d) $S_{\mathrm{r,REV}} = 0.833$

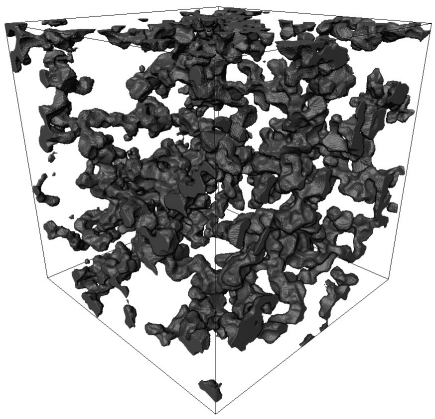

(e) $S_{\mathrm{r,REV}} = 0.814$

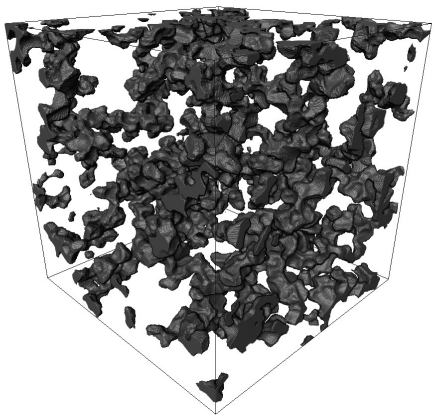

(f) $S_{\mathrm{r,REV}} = 0.793$

Figure 6.14: gas phase in Hamburg sand (test H10)

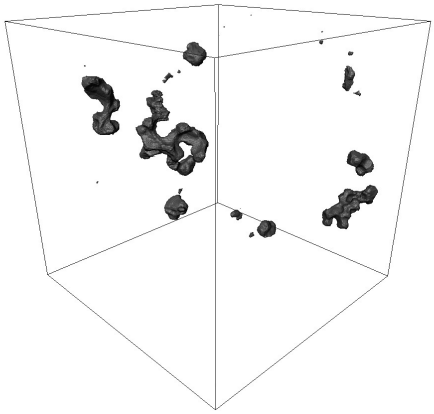

(a) H5-III ($S_{\mathrm{r,REV}} = 0.990$)

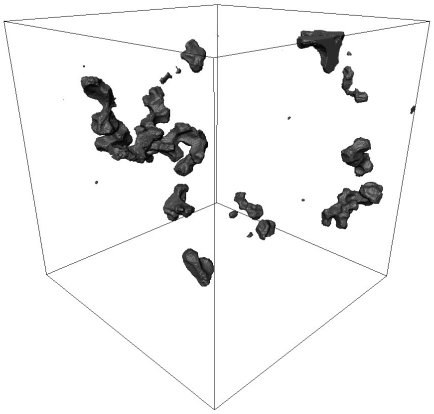

(b) H5-IV ($S_{\mathrm{r,REV}} = 0.984$)

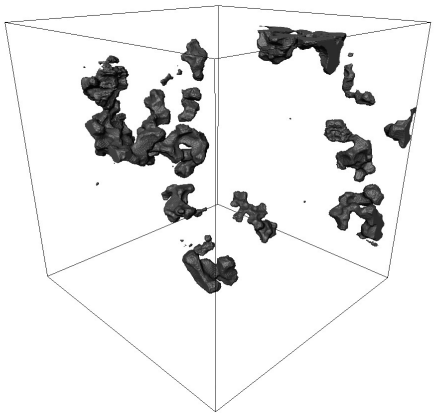

(c) H5-V ($S_{\mathrm{r,REV}} = 0.973$)

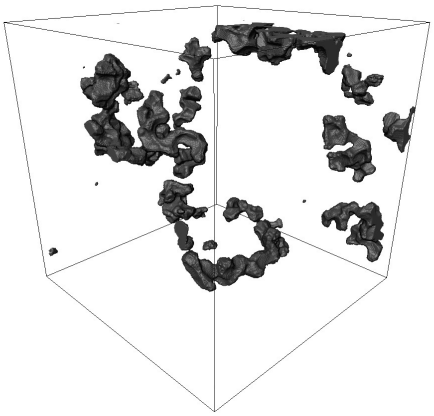

(d) H5-VI ($S_{\mathrm{r,REV}} = 0.959$)

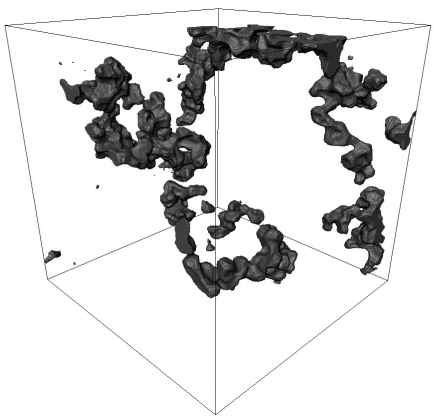

(e) H5-VII ($S_{\mathrm{r,REV}} = 0.947$)

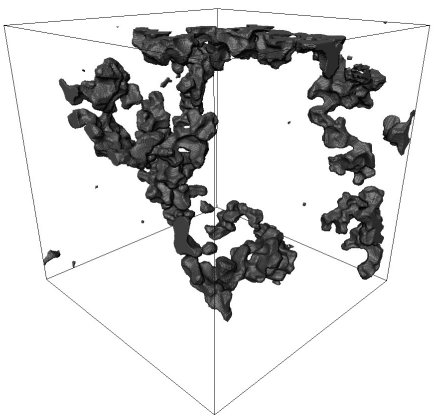

(f) H5-VIII ($S_{\mathrm{r,REV}} = 0.932$)

Figure 6.15: gas phase in Hamburg sand (excerpt from sequence H5; complete data set given in appendix C)

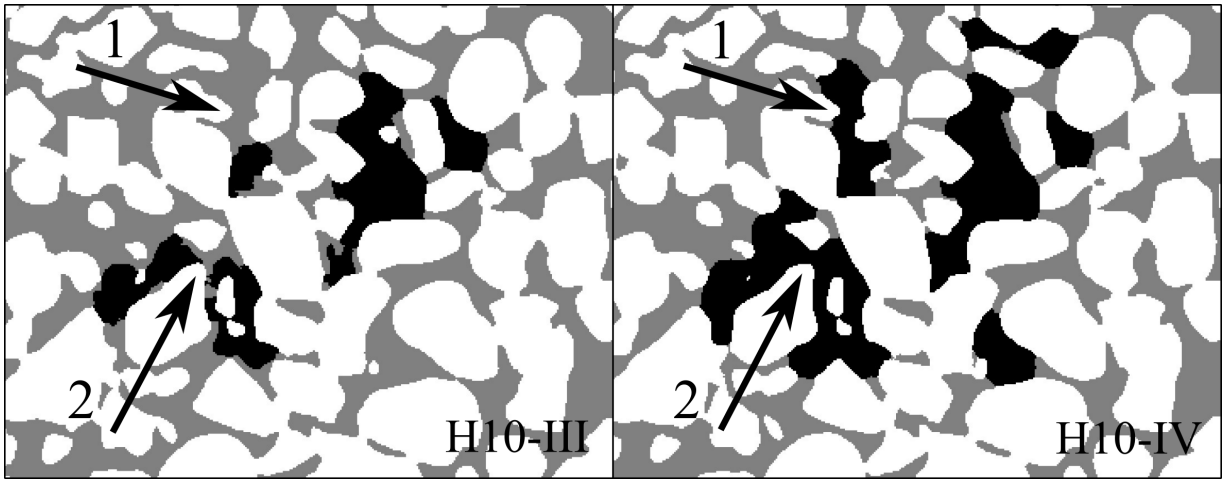

Figure 6.16: growth of selected gas clusters in Hamburg sand (test H10) in a cross-sectional view

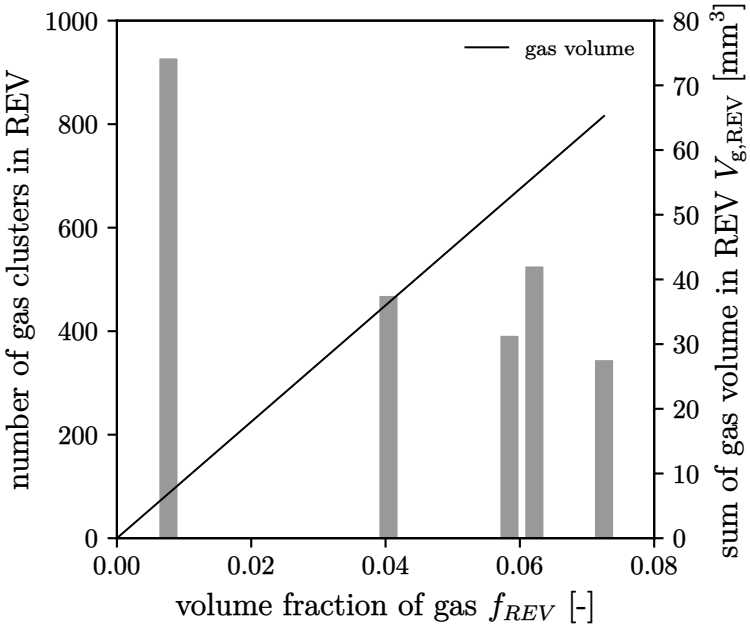

Figure 6.17: number of gas clusters and total gas volume in the REV with increasing volume fraction of gas in ISS0 sand (I10)

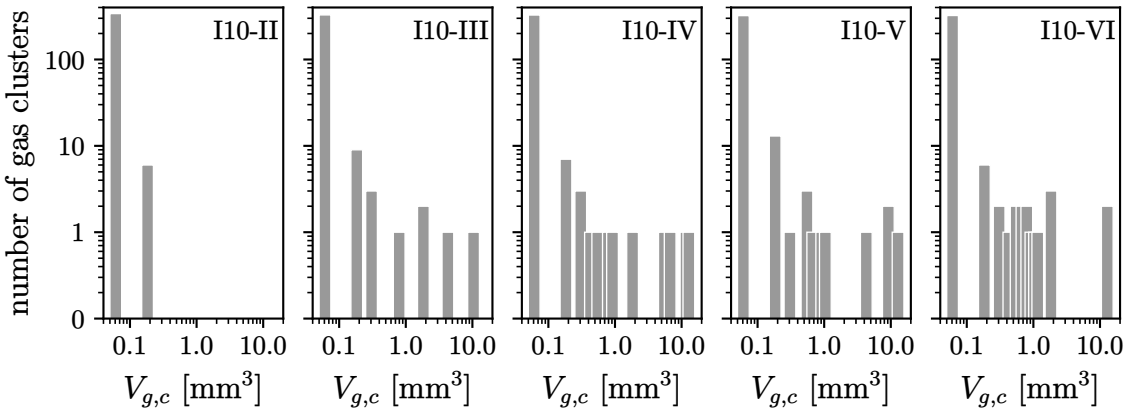

Figure 6.18: development of the single gas cluster volumes in the REV over the scanning sequence in test I10 (bar at $V_{g,c} = 10.5\,\text{mm}^3$ represents all clusters $\geq 10\,\text{mm}^3$)

increasing unloading step in both scanning sequences. Hence, new gas clusters are created with further exsolution of gas. However, the amount of gas clusters does not increase as strongly as the sum of the gas volume in the REV. Thus, the major growth mechanism must be the growth of the existing gas clusters. This mechanism is more pronounced in test H10 compared to test H5. In contrast to the finer ISS0 sand, coalescence of gas clusters appears to be less relevant in the coarser gradation. The increase of the cluster number declines with increasing gas volume. It is likely that this is attributable to the increasing gas content, since the coalescence of gas clusters becomes more likely if more gas clusters exist in the pore space. At a certain degree of saturation, gas cluster coalescence becomes unavoidable and the number of existing clusters will decrease until one large interconnected gas cluster has formed. This mechanism is only possible if capillary invasion is the governing growth mechanism. In soils that predominantly fracture, the preferential orientation of fractures will most likely prevent the formation of a fully interconnected fracture network. Despite the significantly different morphology and growth behaviour of the gas phase in ISS0 and Hamburg sand, the absolute value of the exsolved gas volume in I10 and H10 is very similar. Therefore, the parameters governing the gas phase's pore habit must be rooted in the soil behaviour and not in the gas properties.

When examining the volumes of the individual gas clusters per unloading step, as presented in fig. 6.20, the previously described gas phase behaviour of Hamburg sand is validated. A distinct shift from small volume clusters to larger clusters can be identified in both test series. Moreover, an overall increase in cluster number and gas volume is evident from the data. Therefore, both mechanisms, the formation of new gas clusters as well as the growth of existing gas clusters, play an important role in Hamburg sand. The steady increase of gas clusters with small volumes can be caused by an ongoing production of new gas bubbles with every unloading step or by a tear off of a small part of a cluster during its migration. Since the phenomenological analysis does not show substantial movement but rather expansion of stationary gas clusters with the additional appearance of new gas bubbles, the former mechanism is rated more probable. Particularly in test H5, the amount of large gas clusters increases with increasing unloading step. In direct comparison with test H10, this finding supports the hypothesis that coalescence of gas clusters plays

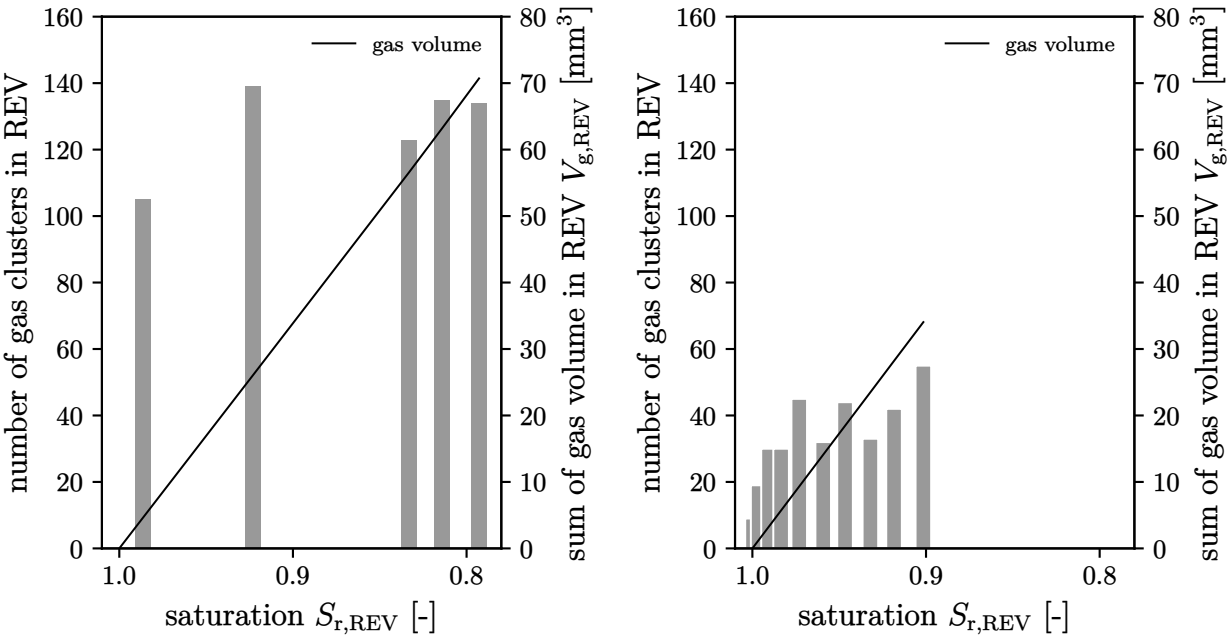

(a) test H10 (b) test H5

Figure 6.19: number of gas clusters and total gas volume in the REV with increasing degree of saturation in Hamburg sand

a greater role at higher degrees of saturation. In contrast to the analogue analysis in ISS0 sand, the amount of small gas clusters is significantly smaller in both scanning sequences on Hamburg sand. The elaborations on the bubble growth and gas migration behaviour in chapter 2 already showed that the growth of existing gas bubbles is thermodynamically preferable compared to the formation of new bubbles. However, for fracturing the difference between the fracturing for the purpose of forming a new macropore and the growth of an existing fracture seems to be less relevant.

6.4.5 Evaluation of the Capillary Force Potential

The morphology of the gas phase and its growth and migration behaviour influence the characteristics of the gas-water interface which, in turn, is relevant for the acting surface tension. Analogue to the visualisation of the gas phase in the phenomenological analysis, the interfaces are extracted from the image data and visualised in fig. 6.21 for test I10 and in fig. 6.22 for test H10. Further visualisations of the image data can be consulted in appendix C. Since in ISS0 sand the extracted interface is the interface between the saturated soil matrix and the gas phase, the overall appearance of the interface complies with the surface of the gas clusters. The actual gas-water interface exhibits a smaller and likely less coherent area. The extent of the discrepancy, however, remains unknown. The general appearance of the interface in ISS0 sand is very areal as soon as the horizontal gas beds form (I10-III and following). Thereby, the surface tension acting in the interface has a large area of impact on the saturated soil matrix. It is, however, very localised to the fracture planes. Since the morphology of the gas phase is substantially different in

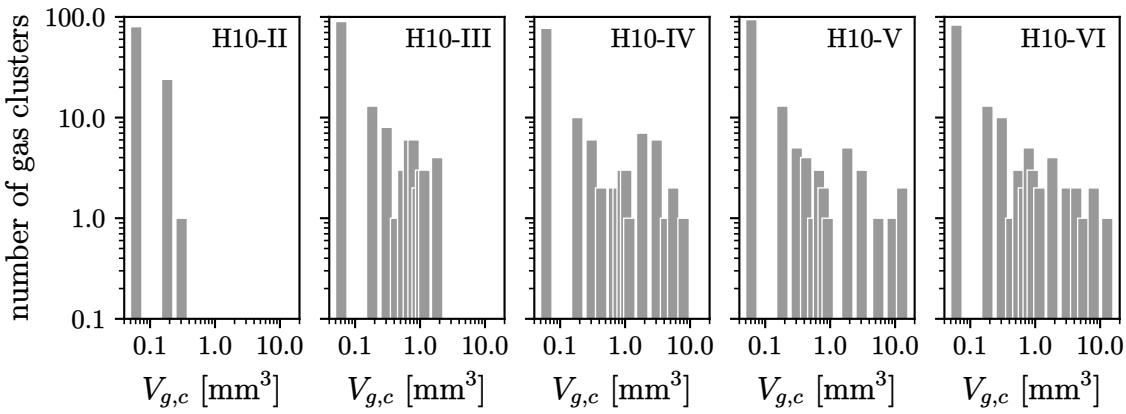

(a) test H10

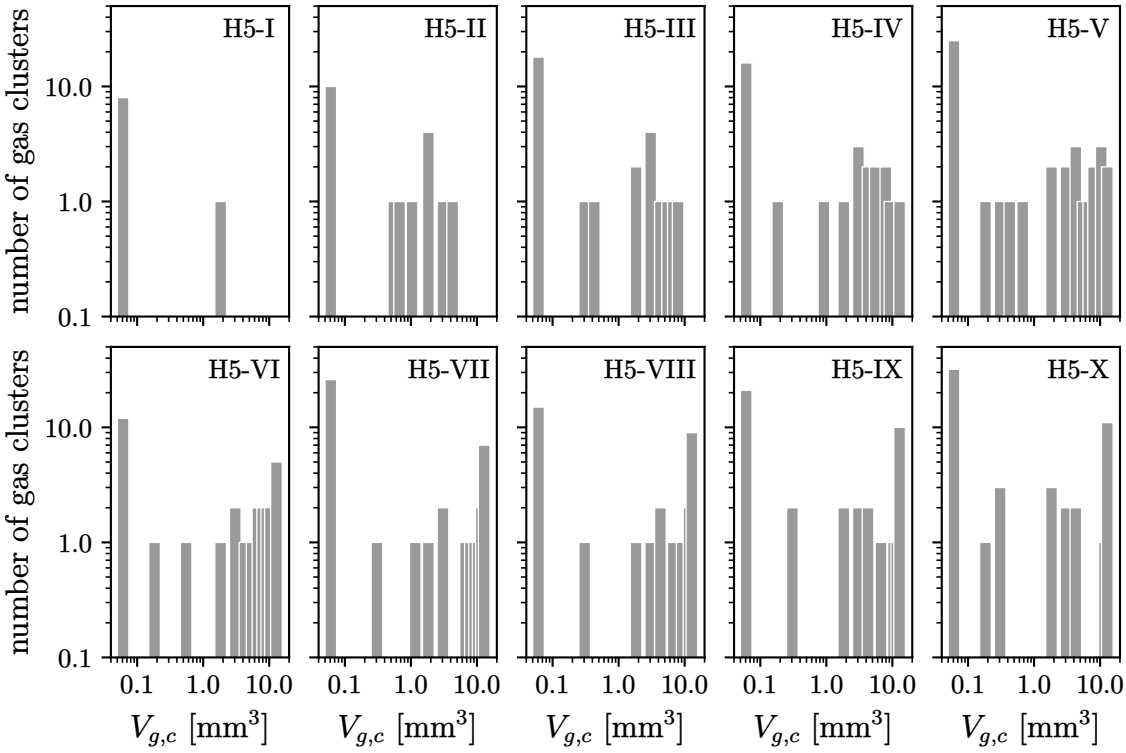

(b) test H5

Figure 6.20: development of the single gas cluster volumes in the REV over the scanning sequence in Hamburg sand (bar at $V_{g,c} = 10.5\,\text{mm}^3$ represents all clusters $\geq 10\,\text{mm}^3$)

Hamburg sand, also the appearance of the gas-water interface differs. Furthermore, in Hamburg sand the actual gas-water interface is displayed as the three phases are properly segmented for these data sets. Here, every gas cluster has contact areas with the surrounding solid as well as the surrounding pore water. Therefore, the gas-water interface appears as interconnected stripes. Consequently, the area of impact for the tensile forces is interrupted and distributed within the REV.
The interfacial area A_{if} can also be analysed in a quantitative manner. To this end, the sum of the gas-water interface area is plotted in dependence of the gas cluster count and the volume fraction of gas or degree of saturation, respectively, in fig. 6.23. In ISS0 sand (test I10), the interface shows a steady increase in its area with increasing volume fraction of gas until a threshold value is reached at which the interface stops growing. This threshold corresponds to the point at which the horizontal fractures are established and start growing in thickness instead of length. The same conclusion applies to the correlation between interfacial area and gas cluster count. In Hamburg sand, the interfacial area also increases with increasing gas content. Here, the increase is more pronounced for test H10 compared to H5. Thus, a more dynamic gas exsolution results in a larger gas-water interface. This effect is caused by the amount of gas clusters that is formed during the exsolution. Looking at the dependency between gas cluster count and gas-water interface area, a slow initial increase can be determined. It is followed by a steady growth of the interfacial area at a constant gas cluster amount. Conclusively, the growth of gas clusters has a larger effect on the interface area than the formation of new clusters. It is noteworthy, that the initial increase in tests H10 and H5 coincide for the gas cluster count. As the increment in test H10 is larger than this coinciding section, it cannot be established whether this is a substantiated correlation or coincidence.
Fig. 6.24 compares the interfacial areas in ISS0 sand and Hamburg sand based on a common and independent parameter: the volume of exsolved gas within the sample. The data clearly shows that the interfacial area in ISS0 sand is significantly lager than in Hamburg sand. In parts, this is caused by the fact that for ISS0 sand the gas-saturated soil matrix interface is displayed. Additionally, the morphology of the gas phase plays a significant role. In Hamburg sand the gas clusters strive towards a spherical shape, but are distorted by the presence of the soil grains and, thus, appear rounded. Meanwhile, the tendency for spiky macropores and fracture formation in ISS0 sand results in spiky gas cluster shapes far from spherical. As the surface-to-volume ratio is minimised in a perfect sphere, the interfacial area is naturally minimised in soils exhibiting capillary invasion as the preferential gas migration mechanism. Therefore, the impact of the acting surface tension can generally be expected to be larger in finer soils that exhibit fracturing. The impact of the very localised interfaces in ISS0 sand compared to the rather dispersed occurrence in Hamburg sand remains to be assessed.

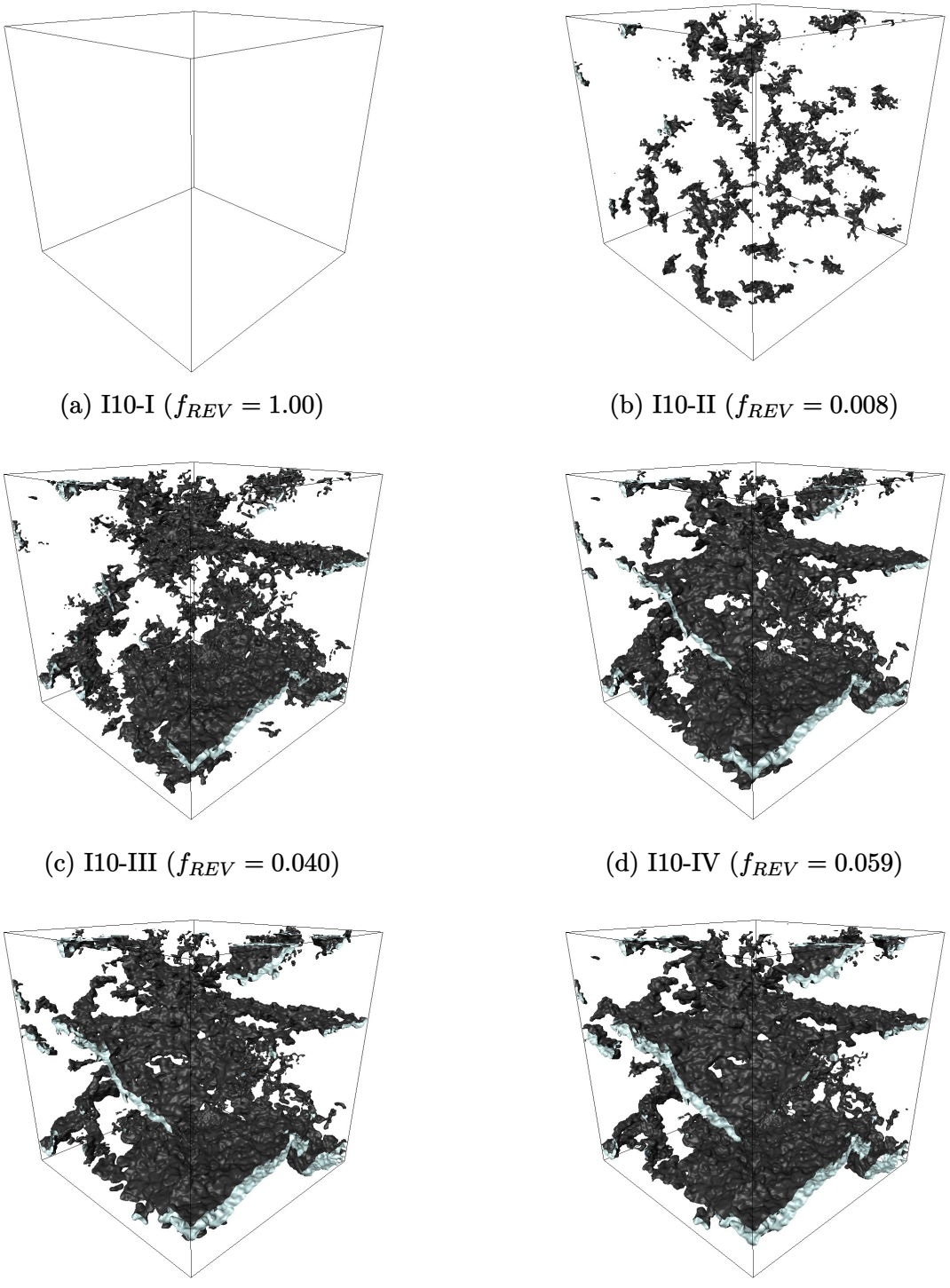

(a) I10-I ($f_{REV} = 1.00$)

(b) I10-II ($f_{REV} = 0.008$)

(c) I10-III ($f_{REV} = 0.040$)

(d) I10-IV ($f_{REV} = 0.059$)

(e) I10-V ($f_{REV} = 0.062$)

(f) I10-VI ($f_{REV} = 0.073$)

Figure 6.21: interfacial area between the gas phase and the saturated soil matrix in ISS0 sand (test I10)

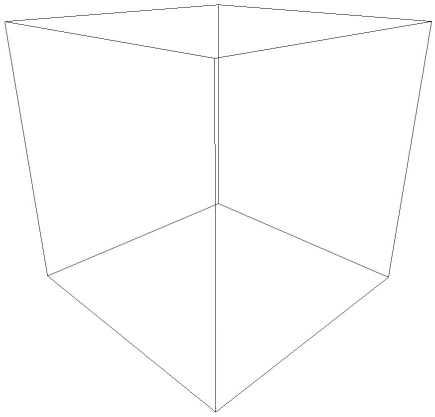

(a) H10-I ($S_{\mathrm{r,REV}} = 1.00$)

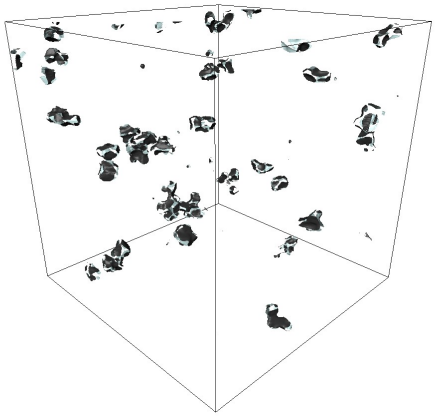

(b) H10-II ($S_{\mathrm{r,REV}} = 0.986$)

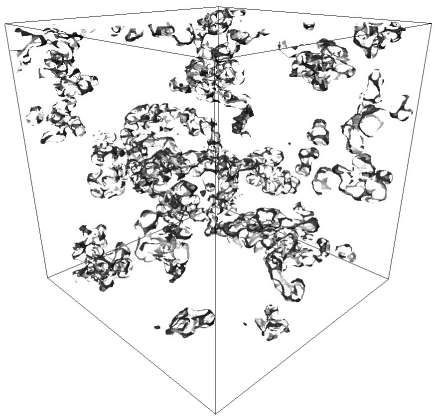

(c) H10-III ($S_{\mathrm{r,REV}} = 0.923$)

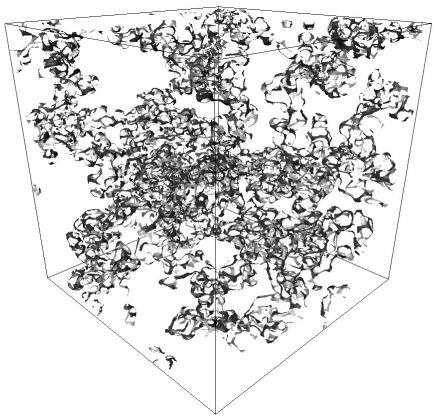

(d) H10-IV ($S_{\mathrm{r,REV}} = 0.833$)

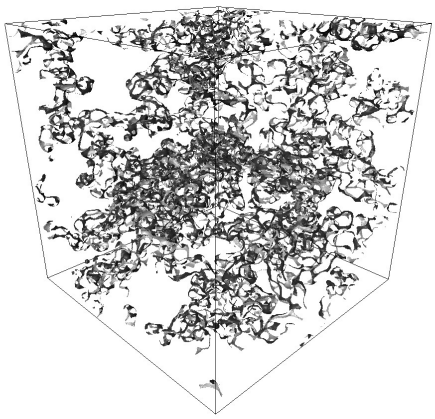

(e) H10-V ($S_{\mathrm{r,REV}} = 0.814$)

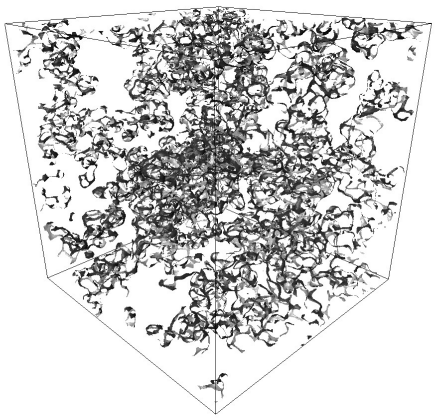

(f) H10-VI ($S_{\mathrm{r,REV}} = 0.793$)

Figure 6.22: interfacial area between the gas and water phase in Hamburg sand (test H10)

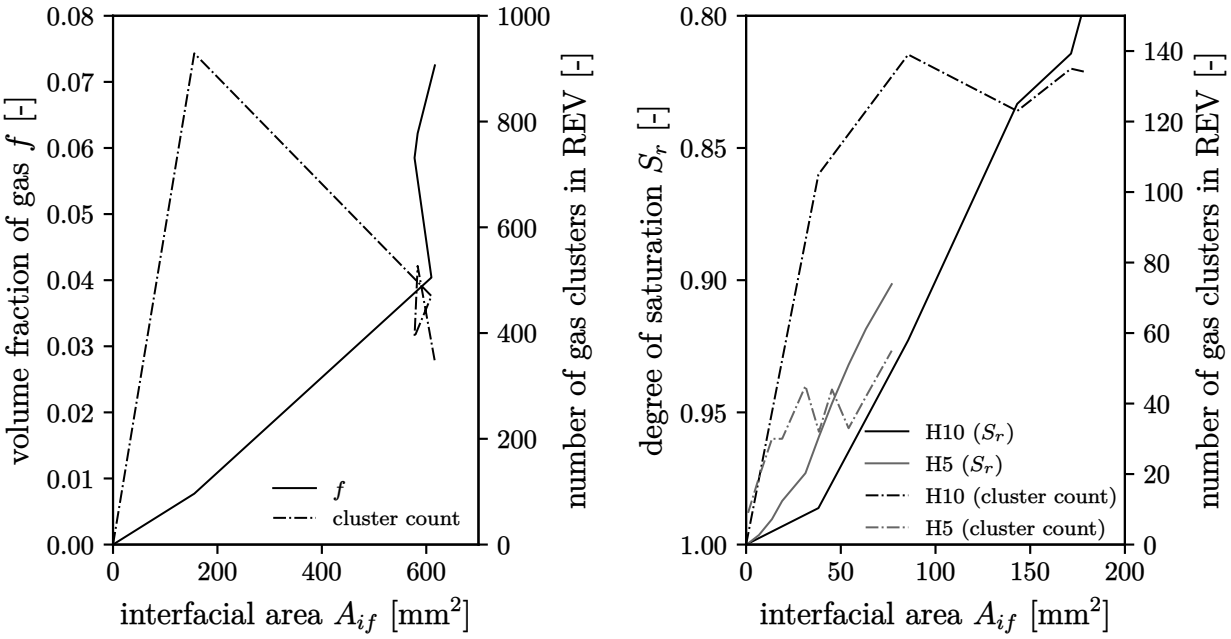

(a) ISS0 sand (only test I10) (b) Hamburg sand

Figure 6.23: development of the interfacial area (between gas phase and saturated soil matrix or gas phase and water phase) with gas content (f & S_r) and gas cluster count

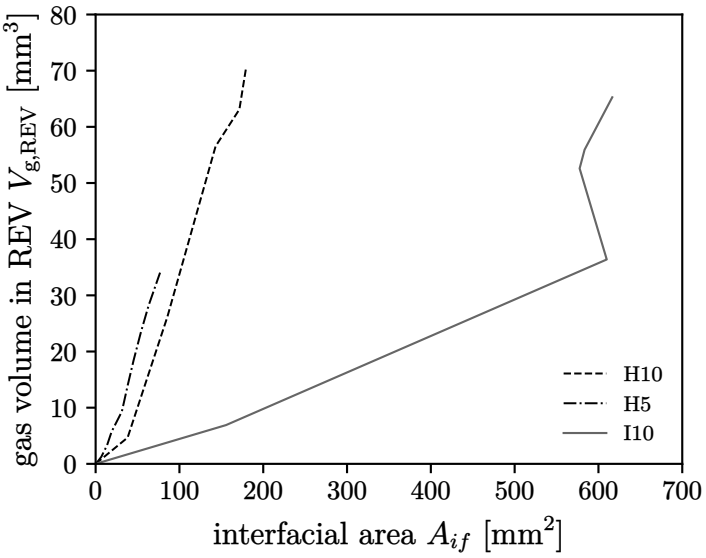

Figure 6.24: interfacial area (between gas phase and saturated soil matrix or gas phase and water phase) in ISS0 and Hamburg sand depending on the volume of free gas

7 Microstructural Impact on the Macroscopic Soil Behaviour

The previous chapters of this thesis outlined the development of a preparation methodology for gassy soil samples and its application in triaxial shear tests as well as CT imaging in order to assess the continuum behaviour and the pore-scale processes, respectively. Ensuing these research efforts, the final objective is the evaluation of the microstructural impact on the macroscopic stress-strain behaviour. Based on a summary of the main findings from the previously described test series, relations between the micro- and macro-scale can be derived and a farther reaching analysis is enabled. To this end, the following chapter first discusses the limitations and potentials of cross-scale interpretations, and subsequently identifies and interrelates the governing mechanisms on the micro- and macro-scale.

7.1 Up- and Downscaling in Micro-to-Macro Approaches

A major challenge in micro-to-macro approaches is to bring the two scales together in a joint interpretation. For this purpose, conclusions derived from the standalone, single-scale test series have to be transferred to the other scale. Oftentimes, this is complicated by different experimental procedures being applied on the different scales. Hence, the transfer of information has to occur considering likewise the features and limitations of the employed testing methods. As a consequence, several outstanding issues that require contemplation precede a combined analysis of micro- and macro-scale: Can the different scales and procedures be combined and interpreted as one? Which information is transferable across scale and method and which is not? According to which criteria can the transferability be assessed?
To this end, fig. 7.1 illustrates the scales relevant to geotechnical engineers as well as typical geotechnical testing and imaging methods on the respective scales. Initially, it has to be emphasized that the designation of the scales in the literature is ambiguous and remains somewhat subjective. The scale of observation is frequently described by the expressions *micro-*, *meso-*, and *macro-scale*, which are not unequivocally assignable to a size dimension but are rather defined by their relation to one another. In this study, the micro-scale refers to a scale of observation in the millimetre domain, which is on the pore-scale of the investigated model sands. The term *pore-scale* is defined by the size of the pore space of the respective soil under investigation and is thereby case-dependent but definite. The continuum stress-strain behaviour derivable from element testing is the designated macro-scale. In the context of scale assignment, the term *continuum* can refer to a large soil mass on the meter-scale, yet usually implies the manner of mechanical description. It therefore entails a change of perspective that becomes very relevant when

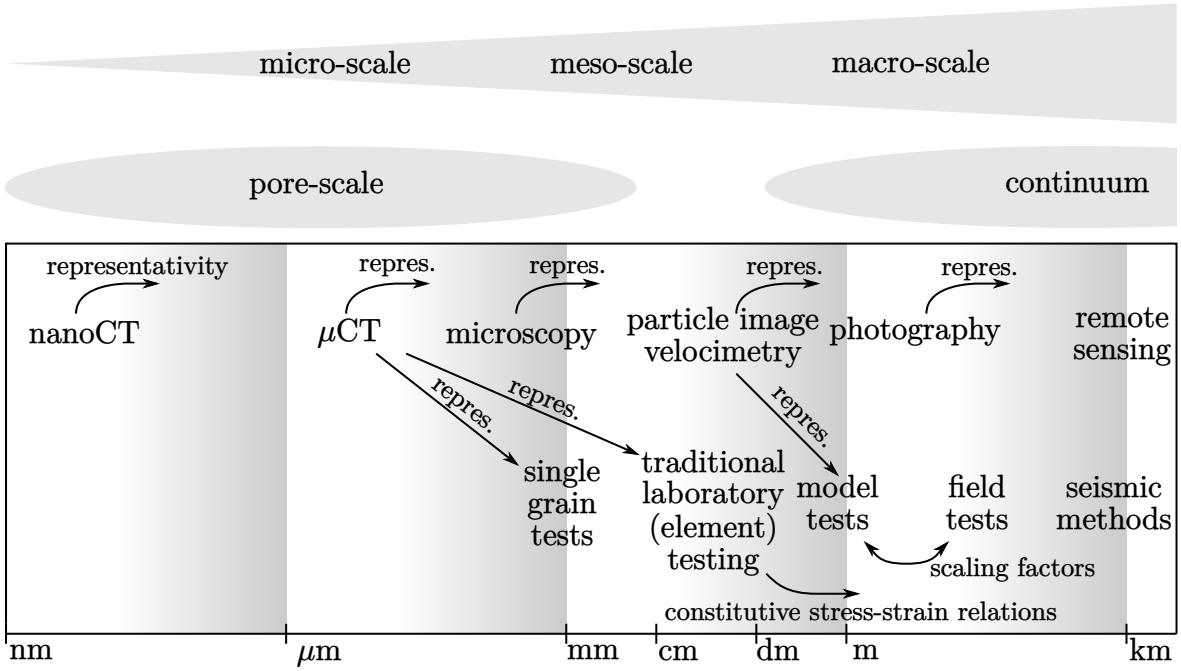

Figure 7.1: scaling in imaging methods and geotechnical testing

scaling up from the micro-scale, where particle-based processes play a superior role. For geotechnical engineering, this transition to the continuum perspective is critical, as it enables to consider the obtained information in application.

For typical geotechnical experiments such as model and field tests, the transfer of information between the scales is validated by means of scaling factors which ensure the similarity between the testing conditions. Sophisticated experimental procedures, amongst centrifuge testing, have been developed to achieve physical similarity and guarantee the transferability to the field scale. In these applications, the relevant information to be transferred frequently entails stress states, (limit) loads as well as strains and displacements. Parameters that describe the soil's mechanical behaviour in the continuum, like Young's modulus, friction angle, and Poisson ratio, can be obtained from laboratory testing. Element tests offer a direct derivation of the stress-strain relationship, which are generally applied to continuum approaches in other scales without further deliberation. On closer scrutiny, however, limitations in transferability can be recognised here. These arise, for instance, from the formation of shear zones within the test specimens which are in conflict with the homogeneous specimen deformations assumed in element tests (Desrues et al., 1996). Further, it can be presupposed that the formation of shear bands in an unconfined soil mass differs to that within a confined soil sample. Therefore, the load transmission is subject to other influences and renders the transferred stress-strain relation to a certain degree unfit (Wood, 2012). Keeping in mind the shortcomings of element testing, the premise of direct transferability is, nonetheless, assumed to be true in this study, since it is well-established in research and engineering practice.

Meanwhile, the information to be gained from imaging methods exhibits different characteristics. Certain parameters, like loads and pressures, are not directly derivable from

image data but are commonly available as meta-data from the experimental procedures. Strains and displacements as well as basic descriptive soil parameters, like density or void ratio, are immediately apparent from the data set. They might, however, not be comparable without bias to data logged with traditional displacement gauges or digital scales due to the inaccuracies immanent to the different methods. Amongst imaging methods, the image resolution and the signal-to-noise ratio are the benchmark for the quality of data, as they are the predominant influencing factors. The image resolution is linked to the scale of observation. Since the processes and features of interest occur on different scales, a finer resolution is not necessarily an equivalent to better data. There rather is an optimum for the particular applications on different scales. If the scales are to be combined in an analysis, the transferability of information is determined based on representativity. Furthermore, representativity is likewise the relevant criterion when combining different experimental methods. Therefore, it is the key to a successful joint interpretation in micro-to-macro approaches. Consequently, representativity is likewise imperative for this study.
As a corollary, the question arises as to what representativity essentially entails and how it can be assessed and measured. Wildenschild and Sheppard (2013) define a representative (sub-)sample to reflect the behaviour of the entire material. Considering the formation of heterogeneity patterns, such as the previously discussed shear bands in element tests, Schmidt et al. (2022) relativise that statement. Instead, different representatives are required for sample parts with different characteristics. This distinction allows for a more detailed analysis. However, it also introduces a case-dependency as well as a user-dependency, since the definition of the border of a shear band – to stay with this example – will always remain a matter of subjectivity. Consequently, several criteria for the representativity amongst scales and procedures are adopted within the scope of this study. These are summarised and evaluated in the following. Representativity is given when the criteria are evaluated with a similar result or comply with the respective target scale.

1. **Applied Simplifications and Basic Assumptions:** The majority of the underlying assumptions and simplifications are incorporated in the axis-translation methodology for gassys soils and therefore likewise apply to both test series. These involve the assumption of the validity of the ideal gas law, the application of the solubility limit for 24.85°C, and the prerequisite of equilibrium conditions during unloading. Moreover, in the macroscopic test series, standard assumptions regarding element testing are made. Additionally, it is presupposed that TERZAGHI's principle of effective stresses is valid for gassy sands. Since loading and stress states are not acquired in the microscopic test series, only the initial state of the experiments is considered fully representative with respect to the other scale. Intermediate or final states of the experiments are to be assessed individually.

2. **Consistency within the Standalone, Single-Scale Experimental Test Series:** Within the triaxial test series, the sample preparation followed a defined procedure that produced sufficiently similar sample properties in all experiments. Due to the simplifying assumption outlined above, the gas exsolution showed inaccuracies regarding the achieved and targeted degrees of saturations. With the results from the microscopic test series in mind, a possible reason for the inaccuracies is

the dependency of the P-wave velocity on the architecture of a gas fracture network (Blouin et al., 2019). Nonetheless, regular and repeatable patterns were created in the test series. The testing equipment applied the intended loading conditions reliably. The same applies to the μCT experiments. Therefore, both test series considered individually are generally rated repeatable and comparable as such. Based on this criterion alone, the test series can be considered representative across scales.

3. **Comparability of the Sample Properties:** In the macro- and microscopic test series, all samples were prepared with the same sample preparation methodology. The initial conditions are therefore comparable amongst scales and experimental procedures. The same applies to the (initial) unloading phase. Over the course of the experiments, however, the sample properties diverge significantly. The major driver for this is the application of shear loading in the triaxial tests versus the manually imposed pore pressure reduction on a stationary grain skeleton in the microscopic tests. Moreover, the pressure relief triggering the gas exsolution is applied from the sample bottom in the triaxial tests and from the sample top in the μCT experiments. The characteristics of the gas phase forming inside the sample can, thus, be influenced. Additionally, in the microscopic experiments the sample is not subjected to external confinement and cannot be brought to a targeted effective stress state. The representativity is therefore only given in a snapshot-like manner, possibly even only for localised parts of the samples. Unfortunately, the extent cannot be assessed based on the available data. It is therefore assumed that the initial conditions are comparable and that only cautious hypotheses can be formulated for the subsequent course of the experiments.

4. **Comparability of the Measured Parameters:** Different kinds of pressure sensors are used to log the pore pressures in the macro- and microscopic test series. However, the employed sensors are calibrated to the same pressure levels and are consequently considered comparable. The initial void ratios of the samples are derived from the weight of the soil and the sample geometry in the macroscopic tests and from the image data of the initial CT scan in the microscopic tests. They are likewise considered comparable despite the varying procedures because the procedures are both considered precise. For the further course of the experiments, however, the inaccuracies of the radial strain measurements in the triaxial tests are too large to allow a direct comparison of the values. Similarly, the degrees of saturation derived from the P-wave velocities are assumed to differ from the saturations derived from the image data due to the potential inconsistencies within the P-wave velocity measurements for the two gradations. Thus, only a qualitative transfer across the scales can be made for these parameters.

5. **Boundary Effects Imposed by the Experimental Method:** While the processes in a triaxial shear phase are of continuous nature, it is inherent to imaging methods that every image contains either the snapshot of a process or a stationary, respectively equilibrium, condition. Therefore, certain features cannot be captured in the microscopic experiments and the image data only represents single excerpts from an exsolution process.

6. **Degree of Generalisability:** Due to the employed model sands and CO_2 as the gas species, the testing conditions on both investigated scales are quite specific and the results are not directly applicable to in-situ conditions. In order to achieve direct transferability of the results to in-situ conditions, for instance, the investigation of more heterogeneous and poorly graded soil types is necessary. The results of this study do, however, offer fundamental insights on the multi-phase behaviour in porous media, which is in line with the research objectives of this thesis. Since the test series on both scales are subject to the same restrictions regarding the generalisability of their results, the mutual representativity of the the experiments is not reduced.

The elaborations above illustrate, that establishing representativity for all defined criteria via the scales and experimental procedures is a difficult endeavour. In this study, the representativity of the test series cannot be established beyond doubt for all time periods and localities. Thus, the conclusions drawn in the context of a joint evaluation remain hypotheses that should be validated in further investigations.

7.2 Governing Mechanisms in Gassy Sands

Prior to assessing the interplay between macro- and micro-scale in order to derive the governing mechanisms of the mechanics of gassy sand, the findings from chapters 5 and 6 are summarised. The results of the CU triaxial shear tests in the macroscopic test series can be aggregated as follows:

- **Deviator Stress:** The presence of gas significantly reduces the maximum deviator stress. Higher gas contents lead to lower deviatoric stresses. The overall stress reduction is less pronounced in Hamburg sand compared to ISS0 sand.

- **Induced Pore Pressure:** Hamburg sand samples show an initial peak in the induced pore pressures. In ISS0 sand samples the induced pore pressures exhibit a rather constant development with a less pronounced peak. Over the course of the shear phase, the pore pressures settle in an equilibrium condition around the solubility limit in both gradations. The pore pressure development in the gassy experiments indicate a quasi-drained behaviour.

- **Volumetric Sample Deformation:** Larger volumetric strains are recognisable in the gassy tests compared to the saturated tests.

- **Degree of Saturation:** The degree of saturation increases towards a peak in the beginning of the shear phase. This peak coincides with the peak in the pore pressures. Subsequently, an equilibrium state of saturation at the maximum gas content is reached. The equilibrium is established before the maximum deviator stress is attained. Lower saturations are achieved in samples consolidated to a lower stress level.

- **Stress Paths:** The stress paths of gassy samples are less smooth than those of saturated tests. Two distinct shapes of gassy stress paths can be identified: type

I and II (see fig. 5.20). ISS0 sand samples mostly follow stress path type I, while Hamburg sand generally behaves according to stress path type II. In stress path II, an explicit point can be determined at which capillary forces begin to influence the soil behaviour, i. e. the point of capillary relevance (PCR). The PCR occurs at similar axial strains in all experiments that follow stress path type II.

- **Shear Parameters:** The friction angle in gassy ISS0 sand is decreased compared to the saturated experiments. Additionally, gassy ISS0 sand exhibits a noticeable capillary cohesion. In Hamburg sand, the friction angle is increased in the gassy experiments compared to the saturated baseline tests. No cohesion is identified in this gradation.

The following results from the microscopic experiments are essential:

- **Gas Phase Morphology:** In ISS0 sand, macropore formation involving a displacement of the grain skeleton is the dominating mechanism. The macropores are distributed homogeneously within the sample in the inital unloading step. In Hamburg sand, homogeneously distributed gas clusters form within the existing pores.

- **Growth Mechanisms:** The macropores in ISS0 sand develop into horizontally layered gas beds by fracturing of the saturated soil matrix. Existing macropores and fractures coalesce in the process. Thus, a substantial phase heterogeneity within the sample is obtained at higher gas contents. In Hamburg sand, the gas clusters grow by means of capillary invasion of neighbouring pores, mostly without displacing the adjacent soil grains. Moreover, the rate of coalescence is lower than in ISS0 sand. Instead, new clusters are created upon further gas exsolution. In consequence, the homogeneity of the gas phase distribution is largely maintained in the process. However, for high gas contents, a certain degree of heterogeneity is unavoidable.

- **Gas-Water Interface:** In ISS0 sand, the interfacial area grows with increasing gas content until a threshold is reached at which it remains constant. At this point, the fractures only grow perpendicular to their propagation direction. In Hamburg sand, the gas-water interface area grows continuously with increasing degree of saturation. The overall area is smaller in Hamburg sand, due to the rather spherical shape of the gas clusters. Therefore, the area of impact for the acting surface tension is smaller in Hamburg sand than in ISS0 sand.

In both experimental test series, the macroscopic triaxial tests and the microscopic μCT experiments, very distinct and different types of behaviour can be identified for the two investigated model sands. As the mechanical properties of the saturated baseline tests in the macroscopic test series are largely comparable for the two sand types, it can be concluded that the discrepancies in the gassy sample's mechanical properties are caused by the varying morphology of the gas phase. This, in turn, is governed by the grain size of the model sands, as shown by the results of the microscopic test series. Namely, the medium sand is subject to capillary invasion of a rigid grain skeleton, while the fine sand exhibits fracturing. Fig. 7.2 illustrates these governing mechanisms in a vertical cross-section of the entire sample I10 and a detailed cutout of sample H5.

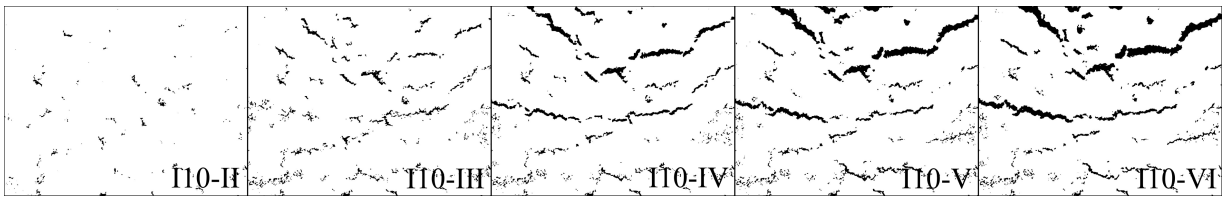

(a) fine sand (here: ISS0 sand, $d_{50} = 0.164\,\mathrm{mm}$)

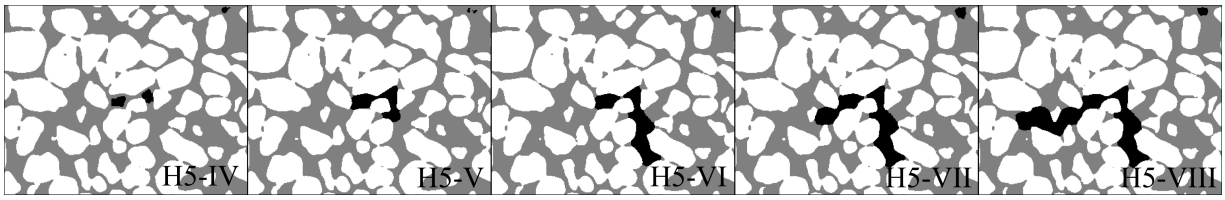

(b) medium sand (here: Hamburg sand, $d_{50} = 0.694\,\mathrm{mm}$)

Figure 7.2: micro-scale governing mechanisms for the mechanical behaviour of gassy sands

These observations are in line with the findings presented in the relevant literature on multi-phase flow in porous media (see section 2.3). The underlying assumptions in the literature on gassy soil mechanics, as presented in section 2.1 and 2.2 as well as fig. 2.3, are, however, not in accordance with the findings of this study. Since these assumptions have never been validated on a micromechanical level, the results of the investigations conducted within the scope of this study now enable valuable adjustments of underlying soil mechanical assumptions to be made for future analyses.
The mechanical implications of the described governing mechanisms can be summarised by means of the defined triaxial stress path types I and II. Fig. 7.3 displays these stress paths in combination with a farther reaching interpretation of the underlying processes derived from combining micro- and macroscopic experimental results in a joint interpretation. The following sections discuss these interpretations in detail.

7.3 Impact of Gas-Induced Fracturing on the Soil Mechanics

This section aims to derive the micromechanical controls for stress path behaviour type I based on the observations made in the micro- and macroscopic on ISS0 sand. In this fine sand, which is subjected to fracturing, the negative impact on the achieved shear stresses is higher than in the medium sand subjected to capillary invasion. This is caused by the gas-induced disturbance of the grain skeleton and manifests itself in a parallel shift of the stress path towards the origin compared to the shearing of an intact grain skeleton; see fig. 7.3a. Over the further course of the shearing process, the stress path remains on a parallel pathway and does not fall back on the course of a saturated experiment. It can therefore be concluded that the fractures remain intact during shearing. An arching effect in the roofs of the macropores or fractures possibly prevents their collapse upon loading and shields the gas inclusions, thereby impeding a formation of a prominent peak in the

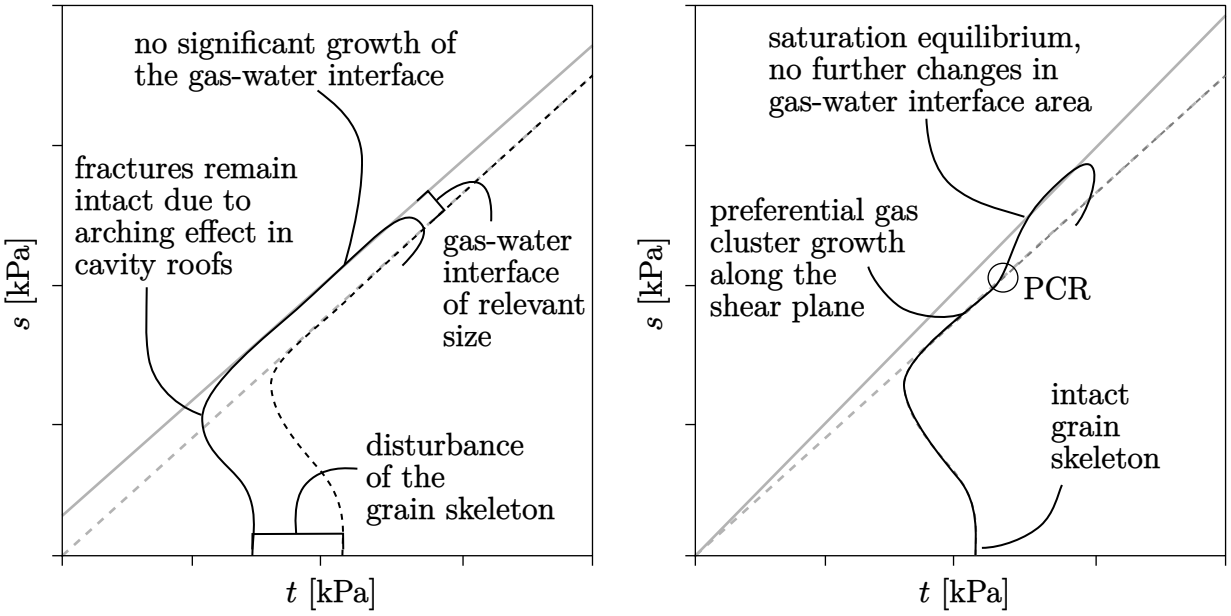

(a) type I (b) type II

Figure 7.3: interpretation of the two types of stress paths in medium dense gassy sands

pore pressure development. In consequence, the gas-water interface retains its size and the acting surface tension participates to a relevant amount in the load bearing behaviour of the initial part of the shear phase. Only this strong impact of the gas on the initial part of the shear phase, i. e. the stress path, results in a capillary cohesion being recognisable in the overall evaluation of the shear parameters.

It is plausible that the grain displacement caused by the fracturing process presupposes the location of the shear band which will unavoidably form during shearing. As the geometry of the shear band impacts the overall shearing behaviour that is deduced from an experiment, the local heterogeneities governing the details of the fracturing process thus bear superordinate implications. Conversely, the formation and spreading of a shear band can also influence the fracture propagation direction by locally changing the properties of the grain skeleton. One conceivable mechanism is an increased impact of the surface tension within the shear zone. The results of the macroscopic experiments conducted within the scope of this study suggest that a significant capillary cohesion can be introduced by a preferential fracturing within the shear zone. In contrast, the gas beds created by the fracturing process do not offer any shearing resistance. Hypothetically, the lower friction angle derived from the triaxial tests on gassy ISS0 sand is attributable to this mechanism.

The establishment of a saturation equilibrium corresponds to a halt in the fracture growth. Furthermore, it is in accordance with the constant development of the interfacial area, and thus the magnitude of the acting surface tension, after reaching a threshold value. In the context of the stress path development, the steady progression along the failure plane can be explained by this saturation equilibrium.

For all the conclusions derived above, the question of how significant the fracturing process needs to be in order to induce a stress path I-behaviour remains. The macroscopic

experiment I400-095, which is consolidated to the highest stress level and exhibits a low gas content, is the only experiment of the finer gradation not to follow stress path I. Therefore, it is possible that the boundary conditions of the experiment only sufficed to create macropores but not fully developed fractures and thereby induced a different mechanical response. Alternatively, the high stress state and the less dynamic exsolution reaction required for smaller gas contents led to a change in the micromechanical behaviour and capillary invasion is the governing mechanism in this experiment (L. Liu et al., 2018).
As already stated on previous occasions, the macropore formation and fracturing process is far from the properties expected for a gas phase in gassy sand and rather resembles the gas phase morphology expected in gassy clays. However, due to the substantially different soil properties, no conclusions for fine sand can be derived from the underlying *Large Bubble Model* by Wheeler (1986); see section 2.1. In fact, the properties of the macropores in fine sand and clay differ in their shape and consequently very probably also in their mechanical effect. The spikey shape of the macropores observable in the microscopic experiments on fine sand leads to an increased area of the gas-water interface. In consequence, the impact of the surface tension is substantial. In gassy clays, the macropores are reported to exhibit a spherical or elliptic shape depending on the loading conditions (L. Liu et al., 2018; Blouin et al., 2019). Apart from the fact that the impact of a capillary cohesion on the overall soil behaviour is to be evaluated differently in granular and cohesive soils, the extent of the grain skeleton disturbance as well as the size of the area of impact for gas pressure and surface tension differ. Therefore, macropore formation in gassy sand constitutes an additional phenomenological expression of gas that was not accounted for in previous soil mechanical considerations.

7.4 Gas Cluster Growth and Its Mechanical Implications

Analogue to the previous section, the impact of gas cluster growth by capillary invasion on the shearing behaviour of Hamburg sand is discussed in the following. Contrarily to the finer gradation exhibiting fracturing, the negative impact of the gas is less pronounced in the medium sand because with capillary invasion being the dominant micromechanical mechanism the grain skeleton is not disturbed by the gas but remains intact. Consequently, the shear load is applied to the pore fluids as well as to the grain skeleton just like in an undrained saturated experiment. In the presence of a gas phase, the pore fluid mixture reacts compressible. Therefore, the gas bubbles shrink when the pore pressure increases. This explains the concurrence of pore pressure peak and maximum degree of saturation. Furthermore, the shrinkage of the gas bubbles results in a decrease of the gas-water interface. Any relevant enactment of capillary forces is therefore retarded. For these reasons, the stress paths of type II follow the saturated stress path in the beginning of shearing; see fig. 7.3b. Since a type II stress path does not exhibit a smooth development in the later shear period, it can, however, be concluded that the morphology of the gas phase changes significantly over the course of a shear phase.
A major driver for a change in the gas phase properties is the formation of a shear band. Due to the increased void ratio within the shear band (Desrues et al., 1996; Schmidt et al., 2022), the gas cluster growth by percolation is simplified and the gas clusters perferably

extend into the shear zone. Since the onset of shear band formation occurs significantly earlier than the attainment of the peak stress (Wood, 2012), the changing gas morphology accompanying the shear band formation also impacts the stress path development before failure. Additionally, the gas-water interface is locally enlarged within the zone relevant for the shearing resistance of the entire sample. Thus, the acting tension forces are increased as well. When the tension forces, i. e. the local gas content, in the shear band are large enough to influence the stress state of the soil, the point of capillary relevance (PCR) is reached. The PCR occurs at similar axial strains in all samples following stress path type II. Therefore, the local dilation of the grain skeleton passes a threshold particularly favourable for percolation at the PCR. In consequence, the gas-influenced stress path deviates from the saturated one beyond the PCR.
The stress path deflects towards a steady development along the failure plane when the saturation equilibrium is reached and the gas-water interface retains a constant size. Consequently, also the acting capillary forces remain constant for the further course of the shear phase. The results of the triaxial tests show, that the gas volume and the pore pressures are in balance from this point forward.
Overall, the gas-water interface does not reach a size substantial enough to induce a capillary cohesion component to the general shearing behaviour of the medium sand. Nonetheless, the impact of the capillary forces is appreciable in the stress path development. It can therefore be concluded that the stress state is not accurately reflected by TERZAGHI's effective stress approach beyond the PCR. Furthermore, it is reasonable to assume that heterogeneities in element testing profoundly impact the shear parameters resulting from triaxial tests. The transfer of the derived parameters to the field scale thus has to be practiced with caution.

7.5 Applicability of Various Effective Stress Approaches for Gassy Soils

Within the scope of this thesis, the stress state of the investigated samples is described by means of TERZAGHI's effective stress approach. As elaborated in chapter 2, the relevant literature on gassy soil mechanics assumes its validity for gassy sands. However, the previous discussion regarding the micromechanical controls and the morphology of the gas phase in sands with different gradations showed that neither of the investigated model sands exhibits the properties likewise assumed by the literature. Crucial basic assumptions, such as the effective stress calculation, are therefore in need of review. Different approaches are outlined in the following and their applicability to fine and medium sands is summarised in tab. 7.1.
TERZAGHI's effective stress approach (equ. 2.4) is applicable to dry or saturated soils, since it does not take into account any interactions between the gas and water phases as well as the solid phase, namely the surface tension acting in the gas-water interface. As long as the gas phase is completely surrounded by the water phase, as assumed in previous geotechnical considerations of gassy sand (fig. 2.3a), the gas-water interface does not get in touch with the solid phase and, thus, does not excert an additional force on the grain skeleton. When the characteristics of the gas phase lead to menisci bridging the

pore spaces inbetween grains, however, the acting surface tension locally changes the stress state in the grain skeleton and TERZAGHI's effective stress becomes inaccurate. Since the effective stress is a continuum parameter, the magnitude and relevance of this inaccuracy is a matter of interfacial area as well as its distribution within the soil body in question. Conclusively, TERZAGHI's effective stress approach is only applicable to gassy sands if the gas-induced inaccuracies are neglectable or tolerable within the respective analysis. The latter remains to be assessed for the specific case at hand. Finno et al. (2017) found that TERZAGHI's approach is accurate enough for the two gassy samples with $S_r \geq 92\,\%$ and $d_{50} = 0.3\,\text{mm}$ which they investigated. In this study, the impact of capillary forces appears to be too large to be neglected in the stress calculations.

After decades of research, it is beyond doubt that capillary forces must be taken into account in the stress calculations for unsaturated soils according to fig. 2.3b. BISHOP's equation (equ. 2.3) is the prevalent approach. In contrast to gassy sand, the gas phase in the pore space of the respective sample is continuous in unsaturated sand. Therefore, most experimental procedures approved by the scientific community involve the independent measurement of the pore water as well as the pore air pressure – an endeavour nearly impossible if the gas phase presents itself in discontinuous bubbles or fractures. On the one hand, no experimental design is conceivable that measures the gas pressure inside a single bubble without significantly disturbing the sample. On the other hand, the gas pressures are not necessarily equal in all macrobubbles or gas clusters existing in a sample. This particularly applies during shear. It therefore remains an open question if a constant gas pressure can be assumed for all bubbles, and – if yes – which bubble, or respectively gas pressure, is representative for the sample. Due to the spatially varying impact of gas pressures and capillary suction in gassy sands, the pore water pressure distribution is most likely heterogenous as well. The applicability of BISHOP's effective stress to gassy sand is therefore ambiguous. Furthermore, in unsaturated sand, capillary invasion is the dominant gas migration mechanism. Thus, the application for the fine ISS0 sand is excluded. Beyond BISHOP's approach, several concepts exist in the literature that aim to further enhance BISHOP's effective stress approach, e. g. Lu et al. (2010). However, the prerequisites for unsaturated sands also apply for these approaches. As previously discussed, these prerequisites are not unequivocally transferable to gassy sands. These approaches are therefore not further elaborated.

In the experiments on Hamburg sand conducted within the scope of the present study, no gas pressure was measured in the macroscopic test series. A comparison between the effective stress approaches can therefore only be conducted in a theoretical manner. Here, test H300-090 is chosen as an exemplary test to assess the impact of the effective stress approach. The development of the effective major principle stress σ_1' calculated by means of the approaches of TERZAGHI and BISHOP is depicted in fig. 7.4. Generally, the effective stress resulting from BISHOP's approach is slighly elevated compared to TERZAGHI's approach. However, for this analysis, maximum values are chosen for the unknown parameters in order to explore a limit condition. For the application of BISHOP's effective stress approach, an upper boundary for the pore gas and water pressure difference is given by the gas entry pressure in order to invade a capillary according to equ. 2.2. Employing the grain diameter at 10 % sieve passage d_{10} as a lower boundary for the grain size, this results in $(u_g - u_w) = 1.372\,\text{kPa}$ for Hamburg sand. Any pore pressure difference greater than this

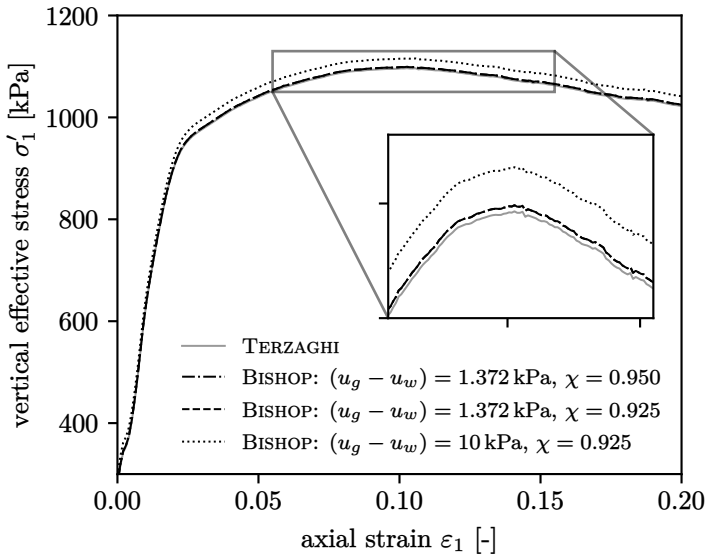

Figure 7.4: comparison of the effective stress approaches by TERZAGHI and BISHOP exemplarily for test H300-090

value implies a constant spreading of the gas phase within the pore space as the phases are not in equilibrium. In consideration of the constant development of the degree of saturation, this is an unrealistic scenario for an extensive part of the shear phase. Nonetheless, a pore pressure difference of $(u_g - u_w) = 10\,\text{kPa}$ is considered in the analysis in addition to $(u_g - u_w) = 1.372\,\text{kPa}$ in order to assess the impact on the resulting effective stress. From fig. 7.4, it becomes apparent that the pore pressure difference is a major influencing factor for the resulting effective stress. Consequently, temporary conditions during phases of gas cluster growth bear the potential to cause peaks in the effective stress curve when employing BISHOP's approach with a variable pore pressure difference.

Additionally, the choice of the saturation parameter χ is not straightforward for a stress path type II-behaviour. Within the scope of this analysis, two scenarios are assessed: $\chi = S_{\text{r,PCR}} = 0.950$ and $\chi = S_{\text{r,equ}} = 0.925$, whereby the latter represents the upper limit with respect to the gas content and impact. In both scenarios, χ is assumed constant over the development of the shear phase. However, for a more accurate analyis, the domains before and after the PCR should be treated differently, as the impact of the capillary forces becomes significant only at the PCR. Thus, the often-employed assumption $\chi = S_r$ is not valid and the correct choice of χ needs to be reassessed for a detailed analysis of gassy sands. Yet, the choice of χ does not impact the resulting effective stresses in a significant manner. Fig. 7.4 shows that the curves for the two scenarios for χ are practically congruent in case of a pore pressure difference realistic for equilibrium conditions. The difference in the maximum effective stress is 0.034 kPa. Hence, more sophisticated approaches are not considered at this point.

In conclusion, the general applicability of BISHOP's effective stress approach for gassy sands is questionable due to the basic requirements regarding the gas phase morphology and the magnitude of the pore gas pressure within different gas clusters. Furthermore,

Table 7.1: applicability of stress state approaches to gassy sand

	fine gassy sand (ISS0 sand)	medium gassy sand (Hamburg sand)
TERZAGHI effective stress	applicable, no consideration of the gas phase	applicable, no consideration of the gas phase
BISHOP effective stress and approaches beyond (e. g. Lu et al., 2010)	requirements for gas phase morphology are not met	theoretically feasible but physically impossible to realise
operative stress according to Sills et al. (1991)	feasible accepting the associated deficits	requirements for gas phase morphology are not met

the quantification of the pore gas pressure is a challenge – but necessary for a robust application of the approach since it is the major influencing factor. The determination of χ in order to consider the degree of saturation cannot rely on the same simplifications employed for unsaturated sands, but also reveals no great influence.

Sills et al. (1991) put the concept of the operative stress forward in order to account for the altered stress state in gassy clays (see equ. 2.5). As described in section 2.1, the operative stress approach assumes that the gas phase is discontinuous and appears as macropores surrounded by a saturated soil matrix. Even though the gas pressure in the macropores induces stress concentrations in the grain skeleton in their vicinity, the operative stress only describes the stresses in the saturated soil matrix that are caused by the pore water. Hence, the operative stress equals the effective stress according to TERZAGHI. By acknowledging the existence of a pore gas pressure different to the pore water pressure, the acting surface tension is implied, but neglected. The operative stress therefore is an intellectual game and a mean to point out the inadequacies of TERZAGHI's effective stress rather than a way to decrease the inaccuracies inherent to the approach. A practical application of the operative stress concept in the data evaluation conducted within the scope of this study does not involve any quantitative changes and, thus, does not bear any advantages.

Conclusively, no approach exists that considers the stress state in gassy sand accurately for either gas morphology. Furthermore, the aforementioned contingencies show that there is still a considerable need for research before gassy sands can be described without ambiguity. The changes in the grain-to-grain stresses within the soil skeleton depend on the mode of gas invasion, i. e. capillary invasion or fracturing. In turn, a significant impact on the gas morphology can be accounted to local heterogeneities in the sample. As a result, the stress distribution is also expected to vary spatially. The complexities involved with a thorough description of the stress state in gassy sands are therefore not to be underestimated.

7.6 The Gas Exsolution Process

Unloading conditions and decreasing pore pressures are integral parts of the experimental procedure of this study and the resulting soil response to shear loading observed in the conducted experiments. Hence, the implications of gas exsolution due to unloading for the experimental results are finally discussed in this section.

The undrained unloading behaviour of gassy sands was investigated by Sobkowicz and Morgenstern (1984) and Amaratunga and Grozic (2009) in order to further understand the gas-induced liquefaction potential. As a result, the analytical model describing the undrained equilibrium behaviour of gassy soil developed by Sobkowicz and Morgenstern (1984) became popular to reproduce the soil's response and is applied multiple times in attempts to formulate constitutive models for gassy soils (e. g. Grozic et al., 2005; Sultan and Garziglia, 2014).

This analytical model describes a stress path of isotropic or non-isotropic unloading for a fully saturated soil with a gas-saturated pore water. The pore pressure approaches the solubility limit from above as a result of the pressure relief. When the solubility limit is reached, gas comes out of solution and a gassy soil is created. Upon further unloading, the gas production continues and stabilises the pore pressure at a constant value equal to the solubility limit due to the volumetric expansion of the growing gas phase. Thus, the degree of saturation decreases while the pore pressure is forced to remain on a constant level. The schematics are illustrated in fig. 7.5.

In this study, isotropic unloading conditions can be encountered in the unloading phase that intends to produce a gas phase within the samples. The pressure rebound encountered in the unloading phases of the macroscopic as well as the microscopic experiments is in line with the theoretical basics of this model. As this pressure rebound is a mean to recreate equilibrium, it indicates a successful gas exsolution. However, the microscopic experiment H5 shows, that a lack in significant pore pressure decrease with subsequent rebound is no evidence for the contrary. The explanation lies in the unloading equilibrium behaviour as described by Sobkowicz and Morgenstern (1984).

This striving for an equilibrium between the phases comes along with several implications regarding a precise control of the degree of saturation. Firstly, the volumetric measure of the degree of saturation is not an adequate approach to describe a compressible medium subjected to temperature- and pressure-induced volume changes in addition to exsolution processes because it fails to reproduce the relation between in-situ conditions and thermodynamical equilibrium. Nonetheless, for the vast majority of boundary conditions typically encountered in soil mechanical applications the degree of saturation does not imply significant deficiencies. Secondly, it cannot be determined in advance to which extent the exsolved gas contributes to a volume expansion or to a pressure increase of the gas phase. Hypothetically, a controlling factor is the confinement imposed by the surrounding soil skeleton.

Further, the pore pressure decrease encountered during the shear phase of the macroscopic gassy experiments represents a phase of unloading. Since the pore pressure development during the shear phase converges towards the solubility limit, it is possible that an ongoing undercutting of the solubility limit caused by a shear loading-induced pore pressure reduction leads to a continued gas exsolution as described by the analytical model. In order

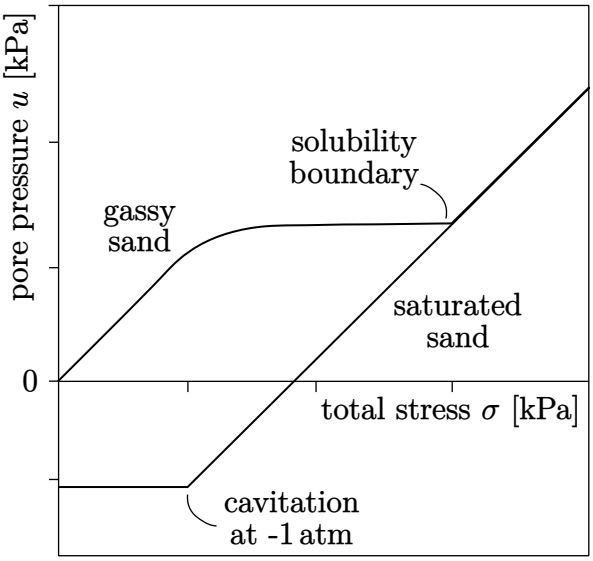

Figure 7.5: theoretical pore pressure development during unloading of a gassy and a saturated sand according to Sobkowicz and Morgenstern (1984)

to further elucidate this hypothesis, the analytical model by Sobkowicz and Morgenstern (1984) is applied to the unloading section of the shear phase. Sobkowicz and Morgenstern (1984) introduce a closed-form solution that expresses the interrelation between total stress decrease and pore pressure change as follows:

$$\alpha \cdot \Delta u^2 + \beta \cdot \Delta u + \delta = 0\,. \tag{7.1}$$

Here, the parameters α, β, and δ are adopted as

$$\alpha = C_c\,, \tag{7.2}$$

$$\beta = C_c \cdot (P_0 - C_c \cdot \Delta\sigma_1) + \frac{e_{\text{prep}}}{1 + e_{\text{prep}}} \cdot (1 - S_r + S_r \cdot H_s)\ , \tag{7.3}$$

and

$$\delta = C_c^2 \cdot \Delta\sigma_1 \cdot P_0 \tag{7.4}$$

in line with the approach for non-isotropic unloading conditions. Since under triaxial shearing conditions the horizontal total stress remains constant, only the vertical total stress changes per time step $\Delta\sigma_1$ are of relevance for the calculation. Further, the absolute pressure in the beginning of each time step P_0 is required, which is assumed to equal the pore pressure u as this pressure parameter controls the exsolution process. The solubility of the gas is described by the HENRY constant H_s, which is a dimensionless factor relating water and gas concentrations and, therefore, strictly speaking temperature- and pressure-dependent. Oftentimes, H_s is simplified to equal 0.86 for CO_2. This assumption is adopted by Sobkowicz and Morgenstern (1984) and therefore also applied in this study. While the

compressibility of the water is neglected, the compressibility of the soil is represented by the oedometric compression index C_c, likewise practiced by Sobkowicz and Morgenstern (1984). In this study, a constant value is assumed to suffice for the given stress range. For medium dense ISS0 sand C_c is 0.037, and for medium dense Hamburg sand C_c equals 0.022. A comparison of the experimental data and the modelling results is given in fig. 7.6 for ISS0 sand and in fig. 7.7 for Hamburg sand.
Looking at the experimental data depicted in fig. 7.6 and 7.7, it can be observed that the pore pressure curves do not match the theoretical development of the pore pressure during unloading illustrated in fig. 7.5. Therefore, it must first be established that the triaxial conditions are not perfectly in line with the underlying presumptions of the model. Obviously, the total stress is not solely decreasing under triaxial compression. However, even under increasing total stress conditions the pore pressures exhibit a decreasing trend over the majority of the shear phase. Since the gas dissolved in the pore water does not react to increasing grain-to-grain contact stresses but to the pore pressure development, relevant unloading phenomena can still be observed. This discrepancy represents a major shortcoming of the model, which focusses on unloading conditions in which the total stress changes always affect the (dissolved) gas phase. In order to comply with the model assumptions, only the section of the shear phase in which pore pressure and total stress decreases are present, is modelled.
The comparison between the model results and the experimental data reveals a significant mismatch. In most experiments, the pore pressure decrease is more pronounced and exhibits a reverse development of the curve's gradient compared to the modelled unloading section. It can therefore be concluded that ongoing gas exsolution is not the governing mechanism in this unloading scenario. The constant development of the degree of saturation supports this hypothesis for medium dense gassy sands under undrained triaxial shear. Even though the sample is sheared under globally undrained conditions and experiences a pore pressure decrease, the model is not fit to depict the equilibrium behaviour that manifests in this instance. This likely is a consequence of the quasi-drained (i. e. locally drained) conditions that are created by grain rearrangement during triaxial shearing in gassy sands. Conclusively, the requirements for the unloading model of Sobkowicz and Morgenstern (1984) are only met for locally undrained conditions in a stationary grain skeleton.

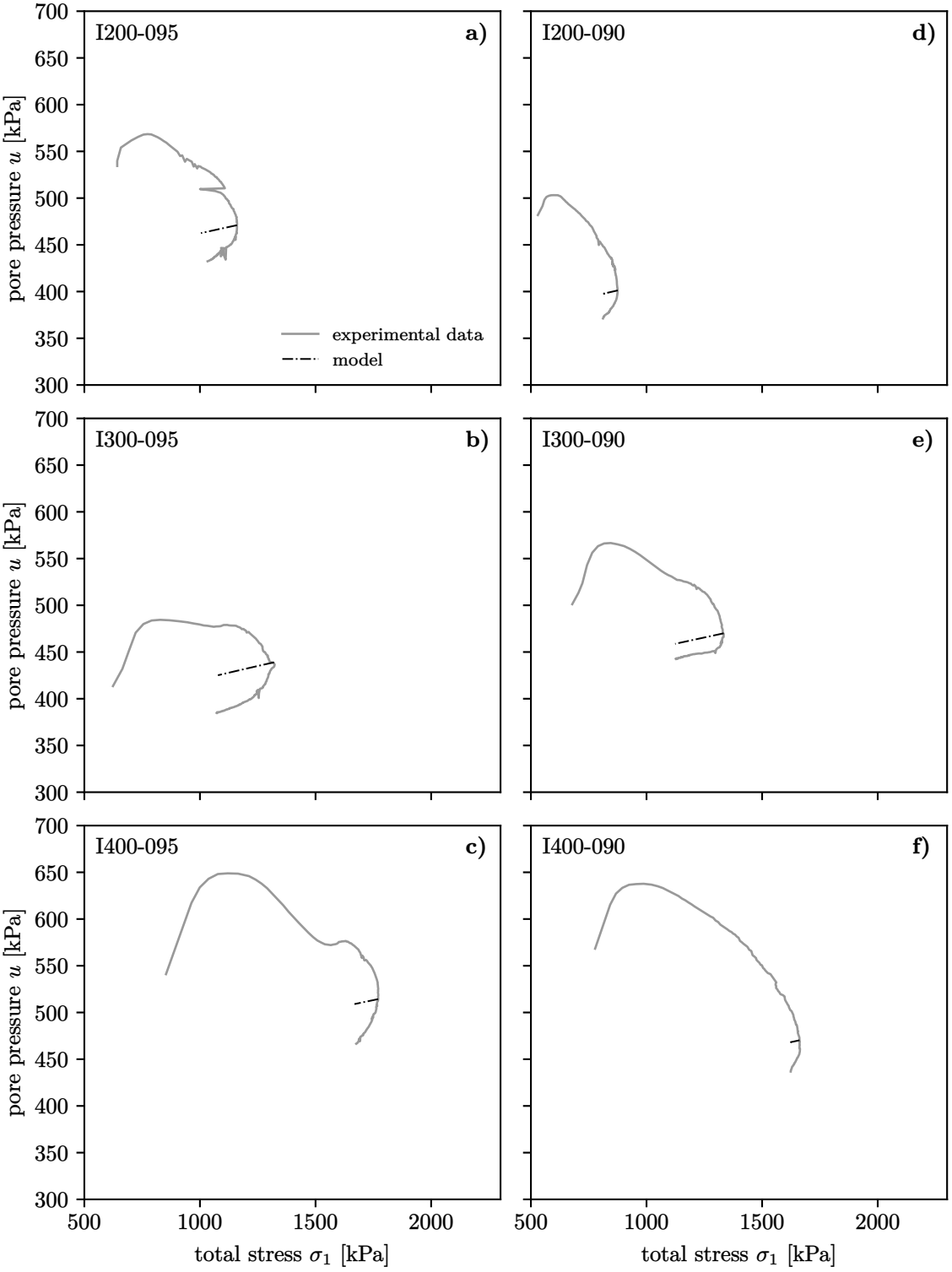

Figure 7.6: application of the unloading model by Sobkowicz and Morgenstern (1984) to the experimental data from the triaxial test series on ISS0 sand

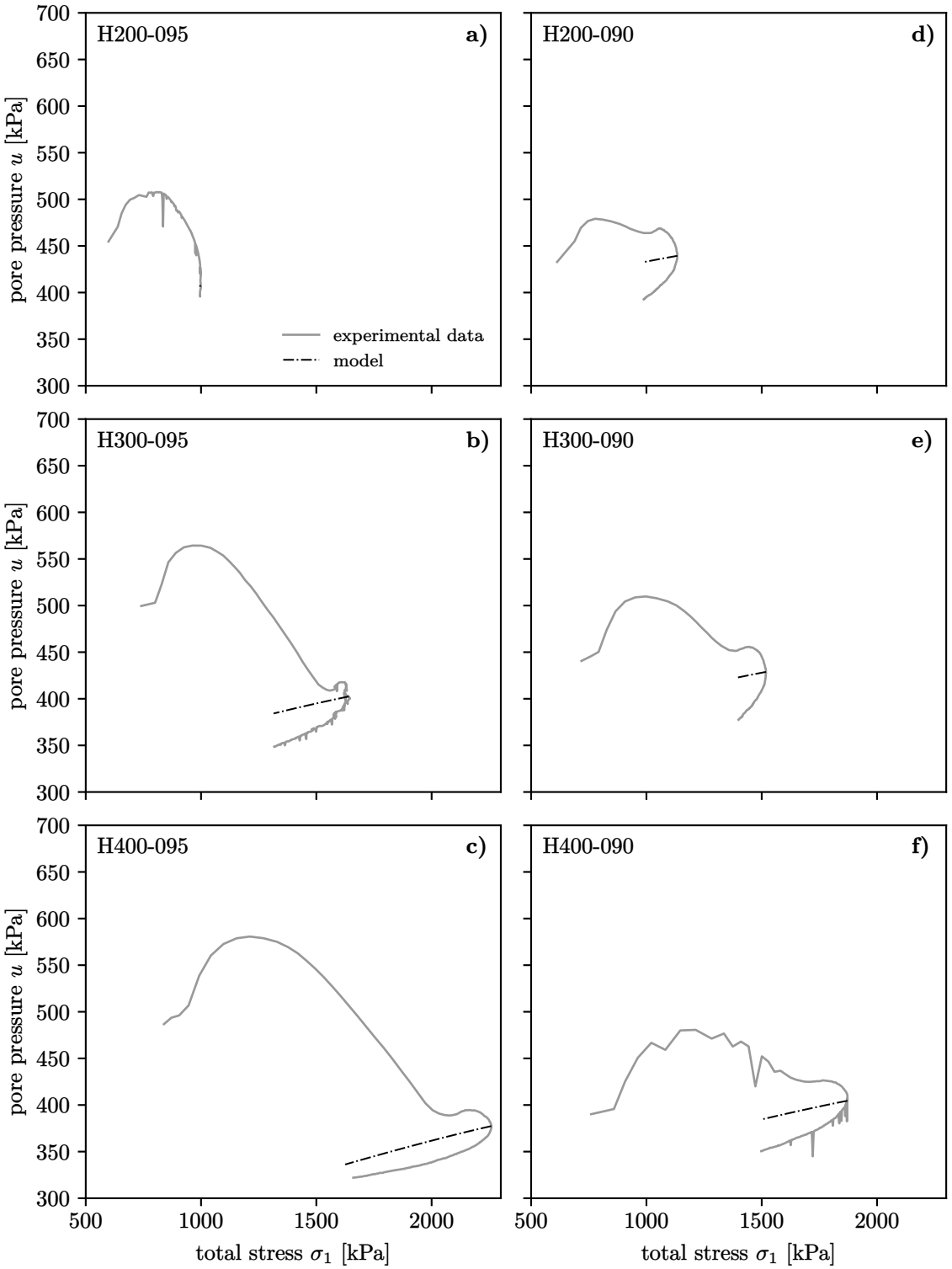

Figure 7.7: application of the unloading model by Sobkowicz and Morgenstern (1984) to the experimental data from the triaxial test series on Hamburg sand

8 Conclusion

Partially saturated soils can be encountered under many circumstances and with different characteristics, amongst gassy soils in the offshore domain which exhibit a discontinuous gas phase. The stress-strain behaviour of these soils is of relevance to understand the systemical processes at the continental slopes that involve naturally formed and anthropogenically produced gas deposits. With an enhanced understanding of the gas-soil-interaction, the integrity of offshore infrastructure can be optimised and the industrial use of marine space can be designed to preserve system functions. However, the current state of knowledge does not allow for definite conclusions to be drawn regarding the mechanical characteristics of gassy soils. Therefore, this thesis investigated the micromechanical controls of the macroscopic stress-strain behaviour in order to forward a holistic understanding of gassy soil mechanics.
The methodology chosen for this analysis is a micro-to-macro approach, which combines experimental methods acting on different scales in an overarching analysis. To this end, a sample preparation methodology applicable in different test set-ups was developed. A thorough review and assessment of previously applied methods described in the literature pointed towards an improvement and further development of the axis-translation method for gassy soils in order to fulfill the research objectives. The implemented advancement of the method creates repeatable and comparable gassy soil samples with characteristics as similar to the in-situ conditions as possible. On the macro-scale, the newly adapted sample preparation procedure was applied in a series of CU triaxial tests on both, a medium and a fine poorly-graded sand. In order to successfully conduct triaxial tests on gassy sand samples, the triaxial apparatus and procedure required adaptations that take the particularities of an additional gas phase into account. On the micro-scale, μCT scans of gassy sand samples with different gas contents were recorded and analysed with respect to the morphology of the gas phase created in the two model sands. To put the micro-scale experiments into practice, a new test set-up had to be developed. Finally, macro- and microscopic testing results were brought together in a joint interpretation to gain insights on the micromechanical processes governing the continuum behaviour.
The investigations performed yielded the following results and reveal these future research needs:

- The axis-translation method for gassy soils is suitable for a reliable experimental implementation under different boundary conditions while fulfilling all defined criteria (see page 18). Prospectively, the method can further be applied under more complex circumstances, e. g. with well-graded soils containing larger contents of fines.

- Two different gas morphologies can be identified in the medium and the fine sand, respectively: gas clusters that grow by capillary invasion within a stationary grain

skeleton and macrobubbles that grow by fracturing, thus displacement, of the surrounding saturated soil matrix. Neither of the observed gas phase characteristics is in line with the theoretical assumptions on gassy sands drawn from the literature. While gas clusters growing by capillary invasion share many implications with the traditional unsaturated sand, macropore formation and fracturing in fine sand is identified as a new scenario in the mechanical assessment of partially saturated soils. The governing factor for the two types of gas phase properties is the mean grain size of the host soil. In order to shed further light on a potential threshold grain size and other thresholding boundary conditions, a further development of the miniaturised test stand that, for instance, incorporates controlled axial loading or confinement of the soil sample to targeted effective stress states is conceivable in future research activities.

- The two different gas morphologies manifest themselves in a different mechanical behaviour on the macro-scale. With respect to the shear parameters, gas clusters and capillary invasion lead to a slightly elevated friction angle. Macropore formation and fracturing generates a substantial capillary cohesion during shearing. However, concluding from the shapes of the stress paths, capillary forces play a significant role in both investigated gradations. Especially the interaction between the gas phase and the formation of a shear band seems to be relevant for the effectiveness of the surface tension on the resulting shear parameters. In order to validate this hypothesis, the relevant processes governing the interaction between gas phase and soil skeleton during shearing have to be identified and assessed with respect to the operative effect of the gas-water interface. This can be achieved by applying imaging methods to a gassy soil sample subjected to shear loading within the scope of follow-up research. For this purpose, the experimental challenge of developing a minituarised triaxial set-up fit for gassy soil testing must be faced.

- As a consequence of identifying the importance of capillary forces in gassy sands, TERZAGHI's principle of effective stress is determined unfit for the application on gassy sands without compromising accuracy. Furthermore, other existing stress approaches, like BISHOP's effective stress or the operative stress concept, likewise bear significant shortcomings and can therefore not be considered valid alternatives. Further information on the controlling parameters for the gas phase morphology as well as on the processes governing the effectiveness of the surface tension, as described in the previous points, is necessary to develop a novel stress concept for gassy sands.

- The bearable shear stresses are significantly reduced in gassy soils due to the entrainment of an equilibrium condition between degree of saturation and pore pressure. This equilibrium is enabled by grain rearrangement and local drainage processes that lead to a quasi-drained soil behaviour. In this context, the invalidity of the unloading model by Sobkowicz and Morgenstern (1984) can be established if a non-stationary grain skeleton is present. The overall lower shear stress has no impact on the derivable shear parameters but must be considered in application cases.

- The evaluation of the state of research on gassy soil mechanics and multi-phase flow in porous media shows a discrepancy between the disciplines. Recent results have

not found their way into soil mechanical considerations and investigations. Greater interdisciplinary collaboration is required in the future if a holistic assessment of the processes is to succeed. The results obtained within the scope of this study support this observation.

In summary, this thesis introduces novel insights into the stress-strain behaviour of gassy sands. For the first time, the micromechanical processes governing the continuum behaviour are analysed and so far unknown interactive processes between gas phase and grain skeleton are detected. Moreover, the impact of the host soil's grain size distribution is assessed on the micro- as well as the macro-scale and the relevance of different modes of effect of acting capillary forces is identified. The investigations conducted within the scope of this study further reveal important future research needs in the field of gassy soil mechanics and represents a crucial step on the way to a holistic understanding of mechanical processes in multi-phase granular media.

Literature

Amaratunga, A. and J. L. Grozic (2009). "On the undrained unloading behaviour of gassy sands". In: *Canadian Geotechnical Journal* 46 (11), pp. 1267–1276. DOI: 10.1139/T09-056.

Ambrose, J. (1973). "Computerized transverse axial scanning (tomography): Part 2. Clinical application". In: *British Journal of Radiology* 46 (552), pp. 1015–1088. DOI: 10.1259/0007-1285-46-552-1023.

Archer, D. (2007). "Methane hydrate stability and anthropogenic climate change". In: *Biogeosciences* 4 (4), pp. 521–544. DOI: 10.5194/bg-4-521-2007.

ASTM D2487-17e1 (2020). *Standard Practice for Classification of Soils for Engineering Purposes (Unified Soil Classification System, USCS)*. West Conshohocken, USA: ASTM International. DOI: 10.1520/D2487-17E01.

ASTM D4767-11 (2020). *Standard Test Method for Consolidated Undrained Triaxial Compression Test for Cohesive Soils*. West Conshohocken, USA: ASTM International. DOI: 10.1520/D4767-11R20.

ASTM D8295-19 (2019). *Standard Test Method for Determination of Shear Wave Velocity and Initial Shear Modulus in Soil Specimens using Bender Elements*. West Conshohocken, USA: ASTM International. DOI: 10.1520/D8295-19.

Astuto, G., F. Molina-Gómez, E. Bilotta, A. V. da Fonseca, and A. Flora (2023). "Some remarks on the assessment of P-wave velocity in laboratory tests for evaluating the degree of saturation". In: *Acta Geotechnica* 18, pp. 777–790. DOI: 10.1007/s11440-022-01610-9.

Atkins, P. W., J. de Paula, and J. J. Keeler (2018). *Atkins' physical chemistry*. Oxford, UK & New York, USA: Oxford University Press.

Ben-Noah, I., S. P. Friedman, and B. Berkowitz (2023). "Dynamics of Air Flow in Partially Water-Saturated Porous Media". In: *Reviews of Geophysics* 61.e2022RG000798 (2). DOI: 10.1029/2022RG000798.

Berndt, C., S. Costa, M. Canals, A. Camerlenghi, B. de Mol, and M. Saunders (2012). "Repeated slope failure linked to fluid migration: The Ana submarine landslide complex, Eivissa Channel, Western Mediterranean Sea". In: *Earth and Planetary Science Letters* 319-320, pp. 65–74. DOI: 10.1016/j.epsl.2011.11.045.

Beucher, S. and F. Meyer (1992). "The Morphological Approach to Segmentation: The Watershed Transformation". In: *Mathematical Morphology in Image Processing*. Ed. by E. Dougherty. Boca Raton, USA: CRC Press, pp. 433–481. DOI: 10.1201/9781482277234.

Bindoff, N. L., W. W. L. Cheung, J. G. Kairo, J. Arístegui, V. A. Guinder, R. Hallberg, N. Hilmi, N. Jiao, M. S. Karim, L. Levin, S. O'Donoghue, S. R. Purca Cuicapusa, B. Rinkevich, T. Suga, A. Tagliabue, P. Williamson, S. Acar, J. J. Alava, E. Allison, B. Arbic, T. Bambridge, I. Bartsch, L. Bopp, P. W. Boyd, T. Browning, J. Bruggemann, M. Butenschön, F. P. Chávez, L. Cheng, M. Cinar, D. Costa, O. Defeo, S. Djoundourian,

C. Domingues, T. Eddy, S. Endres, A. Fox, C. Free, T. Fröhlicher, J.-P. Gattuso, G. Gerber, C. Greene, N. Gruber, G. Hallegraef, M. Harrison, S. Hennige, M. Hindell, A. Hogg, T. Ito, T.-A. Kenny, K. Kroeker, L. Kwiatkowski, V. W. Y. Lam, C. Laüfkotter, P. LeBillon, N. Le Bris, H. Lotze, J. MacKinnon, A. de Marffy-Mantuano, P. Martel, N. Marshall, K. McInnes, J. Garcia Molinos, S. Moseman-Valtierra, A. Matau, S. Mulsow, K. Mutombo, A. Oschlies, M. Oyinlola, E. S. Poloczanska, N. Pascal, M. Philip, S. Purkey, S. Rathore, X. Rebelo, G. Reygondeau, J. Rice, A. Richardson, U. Riebesell, C. Roach, J. Rocklöv, M. Roberts, A. Safa, S. Schmidtko, G. Singh, B. Sloyan, K. von Schuckmann, M. Shehabi, M. Smith, A. Shurety, F. Tuya, C. Vargas, C. Wabnitz, and C. Whalen (2019). "Changing Ocean, Marine Ecosystems, and Dependent Communities". In: *IPCC Special Report on the Ocean and Cryosphere in a Changing Climate*. Ed. by H.-O. Pörtner, D. C. Roberts, V. Masson-Delmotte, P. Zhai, M. Tignor, E. Poloczanska, M. Mintenbeck, A. Alegría, M. Nicolai, A. Okem, J. Petzold, B. Rama, and N. M. Weyer. Cambridge, UK & New York, USA: Cambridge University Press, pp. 447–588. DOI: 10.1017/9781009157964.007.

Bishop, A. W. and G. E. Green (1965). "The influence of end restraint on the compression strength of a cohesionless soil". In: *Géotechnique* 15 (3), pp. 243–266. DOI: 10.1680/geot.1965.15.3.243.

Blackford, J., J. M. Bull, M. Cevatoglu, D. Connelly, C. Hauton, R. H. James, A. Lichtschlag, H. Stahl, S. Widdicombe, and I. C. Wright (2015). "Marine baseline monitoring strategies for carbon dioxide capture and storage (CCS)". In: *International Journal of Greenhouse Gas Control* 38, pp. 221–229. DOI: 10.1016/j.ijggc.2014.10.004.

Blouin, A., N. Sultan, J.-P. Callot, and P. Imbert (2019). "Sediment damage caused by gas exsolution: A key mechanism for mud volcano formation". In: *Engineering Geology* 263.105313. DOI: 10.1016/j.enggeo.2019.105313.

Bosch, T., F. Colijn, R. Ebinghaus, A. Körtzinger, M. Latif, B. Matthiessen, F. Melzner, A. Oschlies, S. Petersen, A. Proelß, M. Quaas, T. Requate, T. Reusch, P. Rosenstiel, K. Schrottke, H. Sichelschmidt, U. Siebert, R. Soltwedel, U. Sommer, K. Stattegger, H. Sterr, R. Sturm, T. Treude, A. Vafeidis, C. van Bernem, J. van Beusekom, M. Visbek, M. Wahl, K. Wallmann, and F. Weinberger (2010). *world ocean review – Mit den Meeren leben*. Vol. 1. Hamburg, Germany: maribus gGmbH.

Böttner, C., M. Haeckel, M. Schmidt, C. Berndt, L. Vielstädte, J. A. Kutsch, J. Karstens, and T. Weiß (2020). "Greenhouse gas emissions from marine decommissioned hydrocarbon wells: leakage detection, monitoring and mitigation strategies". In: *International Journal for Greenhouse Gas Control* 100.103119. DOI: 10.1016/j.ijggc.2020.103119.

Boudreau, B. P., C. Algar, B. D. Johnson, I. Croudace, A. Reed, Y. Furukawa, K. M. Dorgan, P. A. Jumars, A. S. Grader, and B. S. Gardiner (2005). "Bubble growth and rise in soft sediments". In: *Geology* 33 (6), pp. 517–520. DOI: 10.1130/G21259.1.

Bridgeman, P. W. (1964). "The compression of 39 substances to 100,000 kg/cm^2". In: *Collected Experimental Papers*. Vol. VI. Cambridge, USA & London, UK: Harvard University Press, pp. 3819–3834. DOI: 10.4159/harvard.9780674287839.c39.

Buades, A., B. Coll, and J. M. Morel (2005). "A review of image denoising algorithms, with a new one". In: *Multiscale Modeling & Simulation* 4 (2), pp. 490–530. DOI: 10.1137/040616024.

Bui, M., C. S. Adjiman, A. Bardow, E. J. Anthony, A. Boston, S. Brown, P. S. Fennell, S. Fuss, A. Galindo, L. A. Hackett, J. P. Hallett, H. J. Herzog, G. Jackson, J. Kemper, S. Krevor, G. C. Maitland, M. Matuszewski, I. S. Metcalfe, C. Petit, G. Puxty, J. Reimer, D. M. Reiner, E. S. Rubin, S. A. Scott, N. Shah, B. Smit, J. P. M. Trusler, P. Webley, J. Wilcox, and N. Mac Dowell (2018). "Carbon capture and storage (CCS): the way forward". In: *Energy & Environmental Science* 11 (5), pp. 1062–1176. DOI: 10.1039/c7ee02342a.

Bünz, S., J. Mienert, P. Bryn, and K. Berg (2005). "Fluid flow impact on slope failure from 3D seismic data: a case study in the Storegga Slide". In: *Basin Research* 17 (1), pp. 109–122. DOI: 10.1111/j.1365-2117.2005.00256.x.

Buzug, T. M. (2008). *Computed Tomography – From Photon Statistics to Modern Cone-Beam CT*. Berlin & Heidelberg, Germany: Springer-Verlag. DOI: 10.1007/978-3-540-39408-2.

Cahill, A. G., C. M. Steelman, O. Forde, O. Kuloyo, S. E. Ruff, B. Mayer, K. U. Mayer, M. Strous, M. C. Ryan, J. A. Cherry, and B. L. Parker (2017). "Mobility and persistance of methane in groundwater in a controlled-release field experiment". In: *Nature Geoscience* 10, pp. 289–294. DOI: 10.1038/ngeo2919.

Carroll, J. J., J. D. Slupsky, and A. E. Mather (1991). "The Solubility of Carbon Dioide in Water at Low Pressures". In: *Journal of Physical and Chemical Reference Data* 20 (6), pp. 1201–1209. DOI: /10.1063/1.555900.

Cekerevac, C. and L. Laloui (2004). "Experimental study of thermal effects on the mechanical behaviour of a clay". In: *International Journal for Numerical and Analytical Methods in Geomechanics* 28 (3), pp. 209–228. DOI: 10.1002/nag.332.

Chillarige, A. V., N. R. Morgenstern, P. K. Robertson, and H. A. Christian (1997). "Seabed instability due to flow liquefaction in the Fraser River delta". In: *Canadian Geotechnical Journal* 34 (4), pp. 520–533. DOI: 10.1139/T97-019.

Clare, M. A., J. E. Hughes Clarke, P. J. Talling, M. J. B. Cartigny, and D. G. Pratomo (2016). "Preconditioning and triggering of offshore slope failures and turbidity currents revealed by most detailed monitoring yet at a fjord-head delta". In: *Earth and Planetary Science Letters* 450, pp. 208–220. DOI: 10.1016/j.epsl.2016.06.021.

Clayton, C. R. I. and S. A. Khatrush (1986). "A new device for measuring local axial strains on triaxial specimens". In: *Géotechnique* 36 (4), pp. 593–597. DOI: 10.1680/geot.1986.36.4.593.

Cnudde, V. and M. N. Boone (2013). "High-resolution X-ray computed tomography in geosciences: A review of the current technology and applications". In: *Earth-Science Reviews* 123, pp. 1–17. DOI: 10.1016/j.earscirev.2013.04.003.

Connelly, D. P., J. M. Bull, A. Flohr, A. Schaap, D. Koopmans, J. C. Blackford, P. R. White, R. H. James, C. Pearce, A. Lichtschlag, E. P. Achterberg, D. de Beer, B. Roche, J. Li, K. Saw, G. Alendal, H. Avlesen, R. Brown, S. M. Borisov, C. Böttner, P. W. Cazenave, B. Chen, A. W. Dale, M. Dean, M. Dewar, M. Esposito, J. Gros, R. Hanz, M. Haeckel, B. Hosking, V. Huvenne, J. Karstens, T. Le Bas, T. G. Leighton, P. Linke, S. Loucaides, J. M. Matter, S. Monk, M. C. Mowlem, A. Oleynik, A. M. Omar, K. Peel, G. Provenzano, U. Saleem, M. Schmidt, B. Schramm, S. Sommer, J. Strong, I. Falcon Suarez, B. Ungerboeck, S. Widdicombe, H. Wright, and E. Yakushev (2022). "Assuring

the integrity of offshore carbon dioxide storage". In: *Renewable and Sustainable Energy Reviews* 166.112670. DOI: 10.1016/j.rser.2022.112670.

Daigle, H., A. Cook, Y. Fang, A. Bihani, W. Song, and P. B. Flemings (2020). "Gas-Driven Tensile Fracturing in Shallow Marine Sediments". In: *Journal of Geophysical Research: Solid Earth* 125.e2020JB020835 (12). DOI: 10.1029/2020JB020835.

DeJong, J. T., K. Soga, E. Kavazanjian, S. Burns, L. A. van Paassen, A. Al Qabany, A. Aydilek, S. S. Bang, M. Burbank, L. F. CasLake, C. Y. Chen, X. Cheng, J. Chu, S. Ciurli, A. Esnault-Filet, S. Fauriel, N. Hamdan, T. Hata, Y. Inagaki, S. Jefferies, M. Kuo, L. Laloui, J. Larrahondo, D. A. C. Manning, B. Martinez, B. M. Montoya, D. C. Nelson, A. Palomino, P. Renforth, J. C. Santamarina, E. A. Seagren, B. Tanyu, M. Tsesarsky, and T. Weaver (2013). "Biogeochemical processes and geotechnical applications: progress, opportunities and challenges". In: *Géotechnique* 63 (4), pp. 287–301. DOI: 10.1680/geot.SIP13.P.017.

Desrues, J., R. Chambin, M. Mokni, and F. Mazerolle (1996). "Void ratio evolution inside shear bands in triaxial sand specimens studied by computed tomography". In: *Géotechnique* 46 (3), pp. 529–546. DOI: 10.1680/geot.1996.46.3.529.

Deutscher, R. L. and S. Fletcher (1990). "Nucleation on active sites – Part V. The theory of nucleation rate dispersion". In: *Journal of Electroanalytical Chemistry and Interfacial Electrochemistry* 277 (1-2), pp. 1–18. DOI: 10.1016/0022-0728(90)85088-M.

Diamond, L. W. and N. N. Akinfiev (2003). "Solubility of CO_2 in water from -1.5 to 100°C and from 0.1 to 100 MPa: evaluation of literature data and thermodynamic modelling". In: *Fluid Phase Equilibria* 208 (1-2), pp. 265–290. DOI: 10.1016/S0378-3812(03)00041-4.

DIN EN ISO 17892-9 (2018). *Geotechnical investigation and testing – Laboratory testing of soil – Part 9: Consolidated triaxial compression tests on water saturated soils; German version.* Beuth Verlag, Berlin, Germany: DIN Deutsches Institut für Normung e. V. DOI: 10.31030/2791792.

Duan, Z., N. Moller, J. Greenberg, and J. H. Weare (1992). "The Prediction of Methane Solubility in Natural Waters to High Ionic Strength from 0 to 250°C and from 0 to 1600 Bar". In: *Geochimica et Cosmochimica Acta* 56 (4), pp. 1451–1460. DOI: 10.1016/0016-7037(92)90215-5.

Dusseault, M. and R. Jackson (2014). "Seepage pathway assessment for natural gas to shallow groundwater during well stimulation, in production, and after abandonment". In: *Environmental Geosciences* 21 (3), pp. 107–126. DOI: 10.1306/eg.04231414004.

Elger, J., C. Berndt, L. Rüpke, S. Krastel, F. Gross, and W. H. Geissler (2018). "Submarine slope failure due to pipe structure formation". In: *Nature Communications* 9.715. DOI: 10.1038/s41467-018-03176-1.

Eseller-Bayat, E. E. (2009). "Seismic response and prevention of liquefaction failure of sands partially saturated through introduction of gas bubbles". PhD thesis. Northeastern University. DOI: 10.17760/d20000133.

Espinoza, D. N. and J. C. Santamarina (2010). "Water-CO_2-mineral systems: Interfacial tension, contact angle, and diffusion – Implications to CO_2 geological storage". In: *Water Resources Research* 46.W07537 (7). DOI: 10.1029/2009WR008634.

Fahed Qureshi, M., V. Dhamu, A. Usadi, T. A. Brackholtz, A. B. Mhadeshwar, and P. Linga (2022). "CO_2 Hydrate Formation Kinetics and Morphology Observations Us-

ing High-Pressure Liquid CO_2 Applicable to Seqestration". In: *Energy Fuels* 36 (18), pp. 10627–10641. DOI: 10.1021/acs.energyfuels.1c03840.

Falcon-Suarez, I. H., A. Lichtschlag, H. Martin-Moreno, G. Papageorgiou, S. K. Sahoo, B. Roche, B. Callow, R. A. S. Gehrmann, M. Chapman, and L. North (2021). "Core-scale geophysical and hydromechanical analysis of seabed sediments affected by CO_2 venting". In: *International Journal of Greenhouse Gas Control* 108.103332. DOI: 10.1016/j.ijggc.2021.103332.

Fauria, K. E. and A. W. Rempel (2011). "Gas invasion into water-saturated, unconsolidated porous media: Implications for gas hydrate reservoirs". In: *Earth and Planetary Science Letters* 312 (1-2), pp. 188–193. DOI: 10.1016/j.epsl.2011.09.042.

Ferreira, C., F. Díaz-Durán, A. V da Fonseca, and G. Cascante (2021). "New Approach to Concurrent V_S and V_P Measurements Using Bender Elements". In: *Geotechnical Testing Journal* 44 (6), pp. 1801–1820. DOI: 10.1520/GTJ20200207.

Finno, R. J., Y. Zhang, and G. Buscarnera (2017). "Experimental Validation of Terzaghi's Effective Stress Principle for Gassy Sand". In: *Journal of Geotechnical and Geoenvironmental Engineering* 143 (12), p. 04017092. DOI: 10.1061/(ASCE)GT.1943-5606.0001797.

Fleischer, P., T. H. Orsi, M. D. Richardson, and A. L. Anderson (2001). "Distribution of free gas in marine sediment: a global overview". In: *Geo-Marine Letters* 21, pp. 103–122. DOI: 10.1007/s003670100072.

Fredlund, D. G. and H. Rahardjo (1993). *Soil Mechanics for Unsaturated Soils*. New York, USA: Wiley. DOI: 10.1002/9780470172759.

Fredlund, D. G., H. Rahardjo, and M. D. Fredlund (2012). *Unsaturated Soil Mechanics in Engineering Practice*. New York, USA: Wiley. DOI: 10.1002/9781118280492.

Gardner, T. N. (1988). "The Acoustic Properties of Gassy Soil". PhD thesis. University of Oxford.

Garga, V. K. and H. Zhang (1997). "Volume changes in undrained triaxial tests on sands". In: *Canadian Geotechnical Journal* 34 (5), pp. 762–772. DOI: 10.1139/t97-038.

Garing, C., J. A. de Chalendar, M. Voltolini, J. B. Ajo-Franklin, and S. M. Benson (2017). "Pore-scale capillary pressure analysis using multi-scale X-ray microtomography". In: *Advances in Water Resources* 104, pp. 223–241. DOI: 10.1016/j.advwatres.2017.04.006.

Geistlinger, H., G. Krauss, D. Lazik, and L. Luckner (2006). "Direct gas injection into saturated glass beads: Transition from incoherent to coherent gas flow pattern". In: *Water Resources Research* 42.W07403 (7). DOI: 10.1029/2005WR004451.

Gilfillan, S. M. V., B. Sheerwood Lollar, G. Holland, D. Blagburn, S. Stevens, M. Schoell, M. Cassidy, Z. Ding, Z. Zhou, G. Lacrampe-Couloume, and C. J. Ballentine (2009). "Solubility trapping in formation water as dominant CO_2 sink in natural gas fields". In: *Nature* 458, pp. 614–618. DOI: 10.1038/nature07852.

Gilfillan, S. M. V., M. Wilkinson, R. S. Haszeldine, Z. K. Shipton, S. T. Nelson, and R. J. Poreda (2011). "He and Ne as tracers of natural CO_2 migration up a fault from a deep reservoir". In: *International Journal of Greenhouse Gas Control* 5 (6), pp. 1507–1516. DOI: 10.1016/j.ijggc.2011.08.008.

Gitman, I. M., H. Askes, and L. J. Sluys (2007). "Representative volume: Existance and size determination". In: *Engineering Fracture Mechanics* 74 (16), pp. 2518–2534. DOI: 10.1016/j.engfracmech.2006.12.021.

GPG Gase Partner GmbH (2023). *500g / 0,5 kg CO2 Flasche Aquaristik Kohlensäure E290 Made in Germany SV653 – 200806 Produktspezifikation Kohlensäure Getränke*. https://gase-kaufen.de/index.php?controller=attachment&id_attachment=102. last accessed: January 10, 2024.

Greenspan, H., B. van Ginneken, and R. M. Summers (2016). "Guest Editorial Deep Learning in Medical Imaging: Overview and Future Promise of an Exciting New Technique". In: *IEEE Transactions on Medical Imaging* 35 (5), pp. 1153–1159. DOI: 10.1109/TMI.2016.2553401.

Gross, D. and T. Seelig (2018). *Fracture mechanics – With an Introduction to Micromechanics*. Cham, Switzerland: Springer International Publishing AG. DOI: 10.1007/978-3-642-19240-1.

Grozic, J. L., S. M. R. Imam, P. K. Robertson, and N. R. Morgenstern (2005). "Constitutive modeling of gassy sand behaviour". In: *Canadian Geotechnical Journal* 42 (3), pp. 812–829. DOI: 10.1139/t05-015.

Grozic, J. L., P. K. Robertson, and N. R. Morgenstern (1999). "The behaviour of loose gassy sand". In: *Canadian Geotechnical Journal* 36 (3), pp. 482–492. DOI: 10.1139/t99-007.

Haflidason, H., H. P. Sejrup, A. Nygård, J. Mienert, P. Bryn, R. Lien, C. F. Forsberg, K. Berg, and D. Masson (2004). "The Storegga Slide: architecture, geometry and slide development". In: *Marine Geology* 213 (1-4), pp. 201–234. DOI: 10.1016/j.margeo.2004.10.007.

He, J., J. Chu, and V. Ivanov (2013). "Mitigation of liquefaction of saturated sand using biogas". In: *Géotechnique* 63 (4), pp. 267–275. DOI: 10.1680/geot.SIP13.P.004.

Hong, Y., L. Z. Wang, and B. Yang (2018). "Undrained Shear Behaviour of Gassy Clay with Varying Initial Pore Water Pressures". In: *Proceedings of China-Europe Conference on Geotechnical Engineering*. Ed. by W. Wu and H.-S. Yu. Vol. 1. Springer Series in Geomechanics and Geoengineering (SSGG). Cham, Switzerland: Springer Nature, pp. 524–528. DOI: 10.1007/978-3-319-97112-4_117.

Hou, S.-X., G. C. Maitland, and J. M. P. Trusler (2012). "Measurement and Modeling of the Phase Behaviour of the (Carbon Dioxide + Water) Mixture at Temperatures from 298.15 K to 448.15 K". In: *The Journal of Supercritical Fluids* 73, pp. 87–96. DOI: 10.1016/j.supflu.2012.11.011.

Hounsfield, G. N. (1973). "Computerized transverse axial scanning (tomography): Part 1. Description of system". In: *British Journal of Radiology* 46 (552), pp. 1015–1088. DOI: 10.1259/0007-1285-46-552-1016.

Hsu, S.-H., J. Kuo, C.-L. Lo, C.-H. Tsai, W.-B. Doo, C.-Y. Ku, and J.-C. Sibuet (2008). "Turbidity Currents, Submarine Landslides and the 2006 Pingtung Earthquake off SW Taiwan". In: *Terrestrial, Atmospheric and Oceanic Sciences Journal* 19 (6), pp. 767–772. DOI: 10.3319/TAO.2008.19.6.767(PT).

Hu, Y., Y. She, A. Patmonoaji, C. Zhang, and T. Suekane (2020). "Effect of capillary number on morphological characterizations of trapped gas bubbles: Study by using

micro-tomography". In: *International Journal of Heat and Mass Transfer* 163.120508. DOI: 10.1016/j.ijheatmasstransfer.2020.120508.

Hühnerbach, V. and D. G. Masson (2004). "Landslides in the North Atlantic and its adjacent seas: an analysis of their morphology, setting and behaviour". In: *Marine Geology* 213 (1-4), pp. 343–362. DOI: 10.1016/j.margeo.2004.10.013.

Iassonov, P., T. Gebrenegus, and M. Tuller (2009). "Segmentation of X-ray computed tomogrpahy images of porous materials: A crucial step for characterization and quantitative analysis of pore structures". In: *Water Resources Research* 45.W09415 (9). DOI: 10.1029/2009WR008087.

Jommi, C., S. Murano, E. Trivellato, and C. Zwanenburg (2019). "Experimental results on the influence of gas on the mechanical response of peats". In: *Géotechnique* 69 (9), pp. 753–766. DOI: 10.1680/jgeot.17.P.148.

Jones, S. F., G. M. Evans, and K. P. Galvin (1999). "Bubble nucleation from gas cavities – a review". In: *Advances in Colloid and Interface Science* 80 (1), pp. 27–50. DOI: 10.1016/S0001-8686(98)00074-8.

Judd, A. and M. Hovland (2009). *Seabed fluid flow: the impact on geology, biology and the marine environment*. Cambridge, UK: Cambridge University Press. DOI: 10.1017/CBO9780511535918.

Kaminski, P. and J. Grabe (2023a). "Triaxial set-up and procedure to investigate the shear strength of gassy sediment". In: *Proceedings of the 9th International Offshore Site Investigation and Geotechnics Conference: Innovative Geotechnologies for Energy Transition, 12 - 14 September 2023*. Society for Underwater Technology (SUT). London, UK.

Kaminski, P. and J. Grabe (2023b). "Triaxial Testing Methodology for Gassy Soils". In: *Geotechnical Testing Journal* 46 (6), pp. 1027–1045. DOI: 10.1520/GTJ20230296.

Kaminski, P., J. Grabe, and Z. Fatima (2023). "Miniaturised testing device for the qualitative analysis of gas exsolution in soil". In: *Proceedings of the ASME 2023 42nd International Conference on Ocean, Offshore and Arctic Engineering OMAE2023, 11 - 16 June 2023*. OMAE2023-101605. The American Society of Mechanical Engineers (ASME). Melbourne, Australia.

Kaminski, P., T. Sager, J. Grabe, and M. Urlaub (2021). "A new methodology to assess the potential of conjectural trigger mechanisms of submarine landslides exemplified by marine gas occurrence on the Balearic Promontory". In: *Engineering Geology* 295.106446. DOI: 10.1016/j.enggeo.2021.106446.

Kaminski, P., M. Urlaub, J. Grabe, and C. Berndt (2020). "Geomechanical behaviour of gassy soil and implications for submarine slope stability - a literature analysis". In: *Subaqueous Mass Movements and their Consequences: Advances in Process Understanding, Monitoring and Hazard Assessment*. Ed. by A. Georgiopoulou, L. A. Amy, S. Benetti, J. D. Chaytor, M. A. Clare, D. Gamboa, P. D. W. Haughton, J. Moernaut, and J. J. Mountjoy. Vol. 500. Special Publications. London, UK: Geological Society of London, pp. 277–288. DOI: 10.1144/SP500-2019-149.

Ketcham, R. A. and W. D. Carlson (2001). "Acquisition, optimization and interpretation of X-ray computed tomography imagery: applications to the geosciences". In: *Computers & Geosciences* 27 (4), pp. 381–400. DOI: 10.1016/S0098-3004(00)00116-3.

Khaddour, G. (2015). "Multi-scale characterisation of the hydro-mechecanical behaviour of unsaturated sand: water retention and triaxial responses". PhD thesis. Université Grenoble Alpes.

Kong, L.-W., A.-G. Guo, J.-B. Chen, and G.-S. Liu (2005). "On strength property of gassy fine sand and model tests of pile foundation". In: *Proceedings of the 16th International Conference on Soil Mechanics and Geotechnical Engineering: Geotechnology in Harmony with the Global Environment.* IOS Press BV. Amsterdam, Netherlands, pp. 2009–2012. DOI: 10.3233/978-1-61499-656-9-2009.

Kumar, J. and B. N. Madhusudhan (2012). "Dynamic properties of sand from dry to fully saturated states". In: *Géotechnique* 62 (1), pp. 45–54. DOI: 10.1680/geot.10.P.042.

Kvenvolden, K. A. (1993). "Gas Hydrates – Geological Perspective and Global Change". In: *Reviews of Geophysics* 31 (2), pp. 173–187. DOI: 10.1029/93RG00268.

Lagioia, R., A. Sanzeni, and F. Colleselli (2006). "Air, water and vacuum pluviation of sand specimens for the triaxial apparatus". In: *Soils and Foundation* 46 (1), pp. 61–67. DOI: 10.3208/sandf.46.61.

Langeheinecke, K., P. Jany, G. Thieleke, K. Langeheinecke, and A. Kaufmann (2013). *Thermodynamik für Ingenieure – Ein Lehr- und Arbeitsbuch für das Studium.* Wiesbaden, Germany: Springer Fachmedien. DOI: 10.1007/978-3-658-03169-5.

Li, X. and Y. C. Yortsos (1995). "Theory of multiple bubble growth in porous media by solute diffusion". In: *Chemical Engineering Science* 50 (8), pp. 1247–1271. DOI: 10.1016/0009-2509(95)98839-7.

Liu, L., T. de Kock, J. Wilkinson, V. Cudde, S. Xiao, C. Buchmann, D. Uteau, S. Peth, and A. Lorke (2018). "Methane Bubble Growth and Migration in Aquatic Sediments Observed by X-ray μCT". In: *Environmental Science & Technology* 52 (4), pp. 2007–2015. DOI: 10.1021/acs.est.7b06061.

Liu, L., J. Wilkinson, K. Koca, C. Buchmann, and A. Lorke (2016). "The role of sediment structure in gas bubble storage and release". In: *Journal of Geophysical Research: Biogeosciences* 121 (7), pp. 1992–2005. DOI: 10.1002/2016JG003456.

Liu, T., X. Yang, and Y. Zhang (2022). "A Review of Gassy Sediments: Mechanical Property, Disaster Simulation and In-Situ Test". In: *Frontiers in Earth Science* 10.915735. DOI: 10.3389/feart.2022.915735.

Locat, J. and H. J. Lee (2002). "Submarine landslides: advances and challenges". In: *Canadian Geotechnical Journal* 39 (1), pp. 193–212. DOI: 10.1139/t01-089.

Lu, N., J. W. Godt, and D. T. Wu (2010). "A closed-form equation for effective stress in unsaturated soil". In: *Water Resources Research* 46.W05515 (5). DOI: 10.1029/2009WR008646.

Mabrouk, A. and R. K. Rowe (2011). "Effect of sand lenses on a deep excavation in a clayey soil". In: *Engineering Geology* 122 (3-4), pp. 292–302. DOI: 10.1016/j.enggeo.2011.06.009.

Masson, D. G., C. B. Harbitz, R. B. Wynn, G. Pedersen, and F. Løvholt (2006). "Submarine landslides: processes, triggers and hazard prediction". In: *Philosophical Transactions of the Royal Society* 364 (1845), pp. 2009–2039. DOI: 10.1098/rsta.2006.1810.

Mehmani, Y. and K. Xu (2022). "Pore-network modeling of Ostwald ripening in porous media: How do trapped bubbles equilibrate?" In: *Journal of Computational Physics* 457.111041. DOI: 10.1016/j.jcp.2022.111041.

Milatz, M. (2023). "Investigation of capillary effects on the grain scale by means of in situ experiments, imaging and numerical simulations". Habilitation thesis. Hamburg University of Technology. DOI: 10.15480/882.4803.

Milatz, M., E. Andò, G. Viggiani, and S. Mora (2022). "In situ X-ray CT imaging of transient water retention experiments with cyclic drainage and imbibition". In: *Open Geomechanics* 3.5, p. 33. DOI: 10.5802/ogeo.13.

Milatz, M., N. Hüsener, E. Andò, G. Viggiani, and J. Grabe (2021). "Quantitative 3D imaging of partially saturated granular materials under uniaxial compression". In: *Acta Geotechnica* 16, pp. 3573–3600. DOI: 10.1007/s11440-021-01315-5.

Molina-Gómez, F., A. V. da Fonseca, C. Ferreira, and B. Caicedo (2023). "Improvement of cyclic liquefaction resistance induced by partial saturation: An interpretation using wave-based approaches". In: *Soil Dynamics and Earthquake Engineering* 167.107819. DOI: 10.1016/j.soildyn.2023.107819.

Mountjoy, J. J., A. Georgiopoulou, J. Chaytor, M. A. Clare, D. Gamboa, and J. Moernaut (2020). "Subaqueous mass movements in the context of observations of contemporary slope failure". In: *Subaqueous Mass Movements and their Consequences: Advances in Process Understanding, Monitoring and Hazard Assessment*. Ed. by A. Georgiopoulou, L. A. Amy, S. Benetti, J. D. Chaytor, M. A. Clare, D. Gamboa, P. D. W. Haughton, J. Moernaut, and J. J. Mountjoy. Vol. 500. Special Publications. London, UK: Geological Society of London, pp. 1–12. DOI: 10.1144/SP500-2019-237.

Nageswaran, S. (1983). "Effect of gas bubbles on the sea bed behaviour". PhD thesis. St. Catherines College of Oxford.

Nicholson, P. G., R. B. Seed, and H. A. Anwar (1993). "Elimination of membrane compliance in undrained triaxial testing. I. Measurement and evaluation". In: *Canadian Geotechnical Journal* 30 (5), pp. 727–738. DOI: 10.1139/t93-065.

Omar, T. and A. Sadrekarimi (2014). "Effects of multiple corrections on triaxial compression testing of sands". In: *Journal of GeoEngineering* 9 (2), pp. 75–83. DOI: 10.6310/jog.2014.9(2).3.

Ommaya, A. K., G. Murray, J. Ambrose, A. Richardson, and G. N. Hounsfield (1976). "Computerized Axial Tomography: Estimation Of Spatial And Density Resolution Capability". In: *British Journal of Radiology* 49 (583), pp. 577–656. DOI: 10.1259/0007-1285-49-583-604.

Ortiz, L., G. Volckaert, and D. Mallants (2002). "Gas generation and migration in Boom Clay, a potential host rock formation for nuclear waste storage". In: *Engineering Geology* 64 (2-3), pp. 287–296. DOI: 10.1016/S0013-7952(01)00107-7.

Pal, N. R. and S. K. Pal (1993). "A review on image segmentation techniques". In: *Pattern Recognition* 26 (9), pp. 1277–1294. DOI: 10.1016/0031-3203(93)90135-J.

Plampin, M. R., R. N. Lassen, T. Sakaki, M. L. Porter, R. J. Pawar K. H. Jensen, and T. H. Illangasekare (2014). "Heterogeneity-enhanced gas phase formation in shallow aquifers during leakage of CO_2-saturated water from geological sequestration sites". In: *Water Resources Research* 50 (12), pp. 9251–9266. DOI: 10.1002/2014WR015715.

Puzrin, A. M., J. Tront, A. Schmid, and J. B. Hughes (2011). "Engineered use of microbial gas production to decrease primary consolidation settlement in clayey soils". In: *Géotechnique* 61 (9), pp. 785–794. DOI: 10.1680/geot.9.T.023.

Rad, N. S., A. J. D. Vianna, and T. Berre (1994). "Gas in Soils II: Effect of Gas on Undrained Static and Cyclic Strength of Sand". In: *Journal of Geotechnical Engineering* 120 (4), pp. 716–736. DOI: 10.1061/(ASCE)0733-9410(1994)120:4(716).

Ramirez-Llodra, E., P. A. Tyler, M. C. Baker, O. A. Bergstad, M. R. Clark, E. Escobar, L. A. Levin, L. Menot, A. A. Rowden, C. R. Smith, and C. L. Van Dover (2011). "Man and the Last Great Wilderness: Human Impact on the Deep Sea". In: *PLoS ONE* 6.e22588 (8). DOI: 10.1371/journal.pone.0022588.

Al-Raoush, R. and A. Papadopoulos (2010). "Representative elementary volume analysis of porous media using X-ray computed tomography". In: *Powder Technology* 200 (1-2), pp. 69–77. DOI: 10.1016/j.powtec.2010.02.011.

Rebata-Landa, V. and J. C. Santamarina (2012). "Mechanical Effects of Biogenic Nitrogen Gas Bubbles in Soils". In: *Journal of Geotechnical and Geoenvironmental Engineering* 138 (2), pp. 128–137. DOI: 10.1061/(ASCE)GT.1943-5606.0000571.

Ringrose, P. S. and T. A. Meckel (2019). "Maturing global CO_2 storage resources on offshore continental margins to achieve 2DS emissions reductions". In: *Scientific Reports* 9.17944. DOI: 10.1038/s41598-019-54363-z.

Rist, D. (1996). *Dynamik realer Gase: Grundlagen, Berechnungen und Daten für Thermogasdynamik, Strömungsmechanik und Gastechnik*. Berlin & Heidelberg, Germany: Springer-Verlag. DOI: 10.1007/978-3-642-61402-6.

Rodríguez-Rodríguez, J., A. Casado-Chacón, and D. Fuster (2014). "Physics of Beer Tapping". In: *Physical Review Letters* 113.214501 (21). DOI: 10.1103/PhysRevLett.113.214501.

Roerdink, J. B. T. M. and A. Meijster (2000). "The Watershed Transform: Definitions, Algorithms and Parallelization Strategies". In: *Fundamenta Informaticae* 41 (1-2), pp. 187–228. DOI: 10.3233/FI-2000-411207.

Rogelj, J., G. Luderer, R. C. Pietzcker, E. Kriegler, M. Schaeffer, V. Krey, and K. Riahi (2015). "Energy system transformations for limiting end-of-century warming to below 1.5°C". In: *Nature Climate Change* 5, pp. 519–527. DOI: 10.1038/nclimate2572.

Ruppel, C. D. and J. D. Kessler (2016). "The interaction of climate change and methane hydrates". In: *Reviews of Geophysics* 55 (1), pp. 126–168. DOI: 10.1002/2016RG000534.

Schafer, S. and J. H. Siewerdsen (2020). "Technology and applications in interventional imaging: 2D X-ray radiography/fluoroscopy and 3D cone-beam CT". In: *Handbook of Medical Image Computing and Computer Assisted Intervention*. Ed. by S. K. Zhou, D. Rueckert, and G. Fichtinger. The Elsevier and MICCAI Society Book Series. London, UK: Elsevier Academic Press, pp. 625–671. DOI: 10.1016/B978-0-12-816176-0.00031-4.

Schmidt, S., M. Wiebicke, and I. Herle (2022). "On the determination and evolution of fabric in representative elementary volumes for a sand specimen in triaxial compression". In: *Granular Matter* 24.97. DOI: 10.1007/s10035-022-01262-2.

Sezgin, M. and B. Sankur (2004). "Survey over image thresholding techniques and quantitative performance evaluation". In: *Journal of Electronic Imaging* 31 (1), pp. 146–165. DOI: 10.1117/1.1631315.

Sills, G. C. and R. Gonzalez (2001). "Consolidation of naturally gassy soft soil". In: *Géotechnique* 51 (7), pp. 629–639. DOI: 10.1680/geot.2001.51.7.629.

Sills, G. C. and S. J. Wheeler (1992). "The significance of gas for offshore operations". In: *Continental Shelf Research* 12 (10), pp. 1239–1250. DOI: 10.1016/0278-4343(92)90083-V.

Sills, G. C., S. J. Wheeler, S. D. Thomas, and J. N. Gardner (1991). "Behaviour of offshore soils containing gas bubbles". In: *Géotechnique* 41 (2), pp. 227–241. DOI: 10.1680/geot.1991.41.2.227.

Singh, K., B. Bijeljic, and M. J. Blunt (2016). "Imaging of oil layers, curvature and contact angle in a mixed-wet and a water-wet carbonate rock". In: *Water Resources Research* 52 (3), pp. 1716–1728. DOI: 10.1002/2015WR018072.

Skarke, A., C. Ruppel, M. Kodis, D. Brothers, and E. Lobecker (2014). "Widespread methane leakage from the sea floor on the northern US Atlantic margin". In: *Nature Geoscience* 7, pp. 657–661. DOI: 10.1038/ngeo2232.

Soares, J. V., C. Chopra, C. J. C. Van De Ven, A. G. Cahill, R. D. Beckie, T. A. Black, B. Ladd, and K. U. Mayer (2021). "Towards quantifying methane emissions from energy wells with integrity failure". In: *Atmospheric Pollution Research* 12.101223 (12). DOI: 10.1016/j.apr.2021.101223.

Sobkowicz, J. C. and N. R. Morgenstern (1984). "The undrained equilibrium behaviour of gassy sediments". In: *Canadian Geotechnical Journal* 21 (3), pp. 439–448. DOI: 10.1139/t84-048.

Steelman, C. M., D. R. Klazinga, A. G. Cahill, A. L. Endres, and B. L. Parker (2017). "Monitoring the evolution and migration of a methane gas plume in an unconfined sandy aquifer using time-lapse GPR and ERT". In: *Journal of Contaminant Hydrology* 205, pp. 12–24. DOI: 10.1016/j.jconhyd.2017.08.011.

Stranne, C., M. O'Regan, G. R. Dickens, P. Crill, C. Miller, P. Preto, and M. Jakobsson (2016). "Dynamic simulations of potential methane release from East Siberian continental slope sediments". In: *Geochemistry, Geophysics, Geosystems* 17 (3), pp. 872–886. DOI: 10.1002/2015GC006119.

Sultan, N., V. de Gennaro, and A. Puech (2012). "Mechanical behaviour of gas-charged marine plastic sediments". In: *Géotechnique* 62 (9), pp. 751–766. DOI: 10.1680/geot.12.OG.002.

Sultan, N. and S. Garziglia (2014). "Mechanical behaviour of gas-charged fine sediments: model formulation and calibration". In: *Géotechnique* 64 (11), pp. 851–864. DOI: 10.1680/geot.13.P.125.

Sun, C.-Y., G.-J. Chen, and L.Y. Yang (2004). "Interfacial Tension of Methane + Water with Surfactant near the Hydrate Formation Conditions". In: *Journal of Chemical Engineering Data* 49 (4), pp. 1023–1025. DOI: 10.1021/je049948p.

Tamura, S., K. Tokimatsu, A. Abe, and M. Sato (2002). "Effects of air bubbles on B-value and P-wave velocity of a partly saturated sand". In: *Soils and Foundations* 42 (1), pp. 121–129. DOI: 10.3208/sandf.42.121.

Tengattini, A., N. Lenoir, E. Andò, and G. Viggiani (2021). "Neutron imaging for geomechanics: A review". In: *Geomechanics for Energy and the Environment* 27.100206. DOI: 10.1016/j.gete.2020.100206.

Terzariol, M., N. Sultan, R. Apprioual, and S. Garziglia (2021). "Pore Habit of Gas in Gassy Sediments". In: *Journal of Geophysical Research: Solid Earth* 126.e2020JB021511 (5). DOI: 10.1029/2020JB021511.

Thomas, S. D. (1987). "The consolidation behaviour of gassy soil". PhD thesis. University of Oxford.

Tjelta, T. I., G. Svanø, J. M. Strout, C. F. Forsberg, H. Johansen, and S. Planke (2007). "Shallow Gas and Its Multiple Impact on a North Sea Production Platform". In: *Proceedings of the 6th International Offshore Site Investigation and Geotechnics Conference: Confronting New Challenges and Sharing Knowledge, 11 - 13 September 2007*. Society for Underwater Technology (SUT). London, UK.

Twichell, D. C., J. D. Chaytor, U. S. ten Brink, and B. Buczkowski (2009). "Morphology of late Quarternary submarine landslides along the U.S. Atlantic continental margin". In: *Marine Geology* 264 (1-2), pp. 4–15. DOI: 10.1016/j.margeo.2009.01.009.

Valtz, A., A. Chapoy, C. Coquelet, P. Paricaud, and D. Richon (2004). "Vapour-liquid Equilibria in the Carbon Dioxide-water System, Measurement and Modelling from 278.2 to 318.2 K". In: *Fluid Phase Equilibria* 226, pp. 333–344. DOI: 10.1016/j.fluid.2004.10.013.

Van De Ven, C. J. C. and K. G. Mumford (2020a). "Intermediate-Scale Laboratory Investigation of Stray Gas Migration Impacts: Methane Source Architecture and Dissolution". In: *Environmental Science & Technology* 54 (10), pp. 6299–6307. DOI: 10.1021/acs.est.0c00456.

Van De Ven, C. J. C. and K. G. Mumford (2020b). "Intermediate-Scale Laboratory Investigation of Stray Gas Migration Impacts: Transient Gas Flow and Surface Expression". In: *Environmental Science & Technology* 54 (19), pp. 12493–12501. DOI: 10.1021/acs.est.0c03530.

Vega-Posada, C. A., R. J. Finno, and D. G. Zapata-Medina (2014). "Effect of Gas on the Mechanical Behavior of Medium-Dense Sands". In: *Journal of Geotechnical and Geoenvironmental Engineering* 140 (11), p. 04014063. DOI: 10.1061/(ASCE)GT.1943-5606.0001163.

Wagner, W. and A. Pruß (2002). "The IAPWS Formulation 1995 for the Thermodynamic Properties of Ordinary Water Substance for General and Scientific Use". In: *Journal of Physical and Chemical Reference Data* 31 (2), pp. 387–535. DOI: 10.1063/1.1461829.

Wang, C., Y. Mehmani, and K. Xu (2021). "Capillary equilibrium of bubbles in porous media". In: *Proceedings of the National Academy of Sciences* 118.e2024069118 (17). DOI: 10.1073/pnas.2024069118.

Wang, Y., L. Kong, M. Wang, Y. Wang, and P. Cheng (2021). "An improved specimen preparation method for marine shallow gas-bearing sediments and its validation". In: *Journal of Rock Mechanics and Geotechnical Engineering* 13 (3), pp. 682–693. DOI: 10.1016/j.jrmge.2020.11.010.

Watson, T. L. and S. Bachu (2009). "Evaluation of the Potential for Gas and CO_2 Leakage Along Wellbores". In: *SPE Drilling & Completion* 24 (1), pp. 115–126. DOI: 10.2118/106817-PA.

Wendlinger, B., R. Schulting, M. Bradtmöller, L. Clare, M. Collard, K. Edinborough, J. Hilpert, O. Jöris, M. Niekus, E. J. Rohling, and B. Wagner (2008). "The catastrophic final flooding of Doggerland by the Storegga Slide tsunami". In: *Documenta Praehistorica* XXXV, pp. 1–24. DOI: 10.4312/dp.35.1.

Wheeler, S. J. (1986). "The stress-strain behaviour of soils containing gas bubbles". PhD thesis. University of Oxford.

Wheeler, S. J. (1988a). "A conceptual model for soils containing large gas bubbles". In: *Géotechnique* 38 (3), pp. 389–397. DOI: 10.1680/geot.1988.38.3.389.

Wheeler, S. J. (1988b). "The undrained shear strength of soils containing large gas bubbles". In: *Géotechnique* 38 (3), pp. 399–413. DOI: 10.1680/geot.1988.38.3.399.

Wheeler, S. J., W. Sham, and S. D. Thomas (1990). "Gas pressure in unsaturated offshore soils". In: *Canadian Geotechnical Journal* 27 (1), pp. 79–89. DOI: 10.1139/t90-008.

Wiącek, J. and M. Molenda (2016). "Representative elementary volume analysis of polydisperse granular packings using discrete element method". In: *Particuology* 27, pp. 88–94. DOI: 10.1016/j.partic.2015.08.004.

Wichtmann, T., A. Niemunis, and T. Triantafyllidis (2010). "On the „elastic" stiffness in a high-cycle accumulation model for sand: a comparison of drained and undrained cyclic triaxial tests". In: *Canadian Geotechnical Journal* 47 (7), pp. 791–805. DOI: 10.1139/T09-142.

Wildenschild, D. and A. P. Sheppard (2013). "X-ray imaging and analysis techniques for quantifying pore-scale structure and processes in subsurface porous medium systems". In: *Advances in Water Resources* 51, pp. 217–246. DOI: 10.1016/j.advwatres.2012.07.018.

Will, D., N. Gebhardt, R. Nollau, D. Herschel, and H. Ströh (2011). "Druckflüssigkeiten". In: *Hydraulik – Grundlagen, Komponenten, Schaltungen.* Ed. by D. Will and N. Gebhardt. Vol. 5. Berlin & Heidelberg, Germany: Springer-Verlag, pp. 13–40. DOI: 10.1007/978-3-642-17243-4_3.

Wood, D. M. (2012). "Heterogeneity and soil element testing". In: *Géotechnique Letters* 2 (3), pp. 101–106. DOI: 10.1680/geolett.12.00019.

Yegian, M. K., E. Eseller-Bayat, A. Alshawabkeh, and S. Ali (2007). "Induced-Partial Saturation for Liquefaction Mitigation: Experimental Investigation". In: *Journal of Geotechnical and Geoenvironmental Engineering* 133 (4), pp. 372–380. DOI: 10.1061/(ASCE)1090-0241(2007)133:4(372).

Zhang, H. and V. K. Garga (1997). "Quasi-steady state: a real behaviour?" In: *Canadian Geotechnical Journal* 34 (5), pp. 749–761. DOI: 10.1139/t97-046.

Zhao, B., J. Wang, M. R. Coop, G. Viggiani, and M. Jiang (2015). "An investigation of single sand particle fracture using X-ray micro-tomography". In: *Géotechnique* 65 (8), pp. 625–641. DOI: 10.1680/geot.4.P.157.

Appendix A Notation

This list describes the symbols and abbreviations used within the body of the document. If not indicated otherwise in the list below, the prefix Δ designates a difference between two states of the respective variable. Furthermore, the indices *max* and *min* generally refer to maxima and minima of the respective variable. Other descriptive indices are either self-exlanatory and/or indicated at relevant positions in the body of the text.

Abbreviations

μCT micro-CT

2D two-dimensional

3D three-dimensional

CCD charge-coupled-device

CCS carbon capture and storage

CT X-ray computed tomography

CU consolidated undrained

FTV fluid transfer vessel

HH Hamburg

I^2C inter-integrated circuit

LEFM linear elastic fracture mechanics

LVDT linear variable differential transformer

P-wave pressure wave

PCR point of capillary relevance

PVC polyvinyl chloride

REV representative elementary volume

USCS Unified Soil Classification System

Latin Symbols

A	cross-sectional area of sample
A_{if}	interfacial area between two phases
B	B value measured in the B-check during triaxial tests
c	cohesion
c'	effective cohesion
C_c	coefficient of curvature (page 26)
C_c	oedometric compression index (within the Sobkowicz and Morgenstern (1984)-model)
c_g	gas concentration in water
C_u	coefficient of uniformity
D	sample diameter
d	grain diameter
D_0	initial sample diameter
D_m	sample diameter averaged over the middle half of the sample
d_{10}	grain diameter at 10 % sieve passage
d_{50}	mean grain diameter
D_{max}	maximum sample diameter
e	void ratio
e_{prep}	void ratio after sample preparation
E_m	Young's modulus of membrane
e_{max}	maximum void ratio
e_{min}	minimum void ratio
F	force
f	volume fraction of gas
f_s	flow force
f_{REV}	volume fraction of gas in the REV
H	sample height

H_0 initial sample height

H_s HENRY's constant

H_{rel} relative sample height

I attenuated radiation intensity

I_0 initial radiation intensity

$I_{\mathrm{D,prep}}$ specific density after sample preparation

$I_{D,0}$ initial specific density

K compression or bulk modulus

k intercept of the failure plane with the ordinate axis in the t-s-diagram

k_f permeability

$m_{\mathrm{H_2O}}$ mass of water

n amount of gas

n_{free} amount of free gas

n_{dis} amount of dissolved gas

n_{tot} total amount of gas in a sample

p pressure

P_0 absolute initial pressure (within the Sobkowicz and Morgenstern (1984)-model)

r particle radius

R_s specific gas constant

s shear parameter for the stress path evaluation in triaxial tests

S_r^* target degree of saturation

$S_{\mathrm{r,equ}}$ degree of saturation at equilibrium

$S_{\mathrm{r,REV}}$ degree of saturation in the REV

S_r degree of saturation

T temperature

t shear parameter for the stress path evaluation in triaxial tests

T_{mean} averaged mean temperature

$T_{s,air}$ surface tension at the air-water interface

T_{s,CH_4} surface tension at the CH_4-water interface

T_{s,CO_2} surface tension at the CO_2-water interface

t_m thickness of membrane

T_s surface tension at a gas-water interface

u pore pressure

u_0 initial pore pressure

u_g pore gas pressure

u_w pore water pressure

V sample volume

V_0 initial sample volume

V_g gas volume

V_l liquid volume

V_p pore volume

v_p P-wave velocity

V_s solid volume

$V_{g,c}$ gas volume per gas cluster

V_{tot} total sample volume

x thickness of scanned object

Greek Symbols

α parameter for the Sobkowicz and Morgenstern (1984)-model

α' gradient of the failure plane in the t-s-diagram

β parameter for the Sobkowicz and Morgenstern (1984)-model

χ saturation parameter by Bishop

χ^2 criterion to evaluate statistical scatter (only on page 76)

Δu induced pore pressure

δ parameter for the Sobkowicz and Morgenstern (1984)-model

$\Delta(\sigma_1 - \sigma_3)_m$ membrane correction in triaxial tests

γ_d dry unit weight

$(\sigma_1 - \sigma_3)_c$ corrected principle stress difference in triaxial tests

μ_a linear attenuation coefficient

ρ_l density of liquid

ρ_s grain density

σ total stress

σ' effective stress

σ'' operative stress

σ'_1 vertical/major effective principal stress

σ'_3 horizontal/minor effective principal stress

σ_1 vertical/major principal stress

σ_3 horizontal/minor principal stress

σ'_c isotropic effective stress after consolidation

σ'_v vertical effective stress

ε_1 axial strain

ε_{rad} radial strain

ε_{vol} volumetric strain

φ friction angle

φ' effective friction angle

Chemical Notations

CH_4 methane

CO_2 carbon dioxide

H_2 hydrogen

H_2O water

N_2 nitrogen

O_2 oxygen

Appendix B Supplementary Data on the Triaxial Tests

The information compiled in the following is intended to supplement the outline of the macroscopic test series, i. e. the triaxial shear tests, given in chapter 5 of this thesis.

B.1 Calibration of Hall Effect Displacement Transducers

The HALL effect displacement transducers implemented in the triaxial apparatus to monitor the sample's deformation behaviour exhibit a linear measurement range of $\pm 3\,\mathrm{mm}$. Since the radial strain expected during shear is larger than this linear range, the entire length, i. e. the non-linear regime, of the semiconductor plate is utilised in the macroscopic experiments. For this purpose, calibration tests are conducted to link the measurement data to the imposed displacement. This link is established by means of calibration curves which can be consulted to translate the measured data from triaxial tests back to relevant displacements.
The developed test set-up for calibration testing consists of two mounting blocks for the two sensor parts, respectively. One mounting block is fixed to a base, the other moves along a guide rail. The movement is induced manually by means of a standardised M16 screw which exhibits a thread pitch of $2\,\mathrm{mm}/360°$ rotation. Thereby, the displacement can be applied by a controlled turn of the screw. The measurement data of the sensor is recorded by means of the triaxial testing software. The test stand is presented in fig. B.1. In the calibration tests, the data was acquired in displacement steps of $0.5\,\mathrm{mm}$, i. e. $90°$ rotations.
In order to calibrate the radial HALL effect sensor, five calibration tests were conducted. The measurement data is depicted in fig. B.2 in conjunction with the derived calibration curve for the diameter D in mm:

$$\begin{aligned} y = &- 3.228 \cdot D^7 - 93.038 \cdot D^6 + 1.134 \cdot 10^4 \cdot D^5 - 3.476 \cdot 10^5 \cdot D^4 \\ &+ 3.732 \cdot 10^6 \cdot D^3 + 0.093 \cdot D^2 - 9.333 \cdot 10^{-4} \cdot D + 3.445 \cdot 10^{-6}\,. \end{aligned} \tag{B.1}$$

The calibration testing for the axial HALL effect sensors involved three and four tests for sensor #1 and sensor #2, respectively. The resulting calibration curve for axial strain sensor #1 is given by

$$\begin{aligned} y = &- 0.002 \cdot x^7 + 0.048 \cdot x^6 - 0.279 \cdot x^5 + 0.111 \cdot x^4 \\ &- 2.358 \cdot x^3 - 7.266 \cdot 10^{-5} \cdot x^2 + 5.421 \cdot 10^{-6} \cdot x - 8.435 \cdot 10^{-8} \end{aligned} \tag{B.2}$$

and presented in fig. B.3a together with the measured data points. x is given in mm. Fig. B.3b shows the data and calibration curve for axial strain sensor #2 which is given

by

$$y = -0.007 \cdot x^7 + 0.087 \cdot x^6 - 0.352 \cdot x^5 + 0.007 \cdot x^4 - 2.333 \cdot x^3 + 2.625 \cdot 10^{-4} \cdot x^2 - 4.181 \cdot 10^{-6} \cdot x + 2.073 \cdot 10^{-8} \,. \tag{B.3}$$

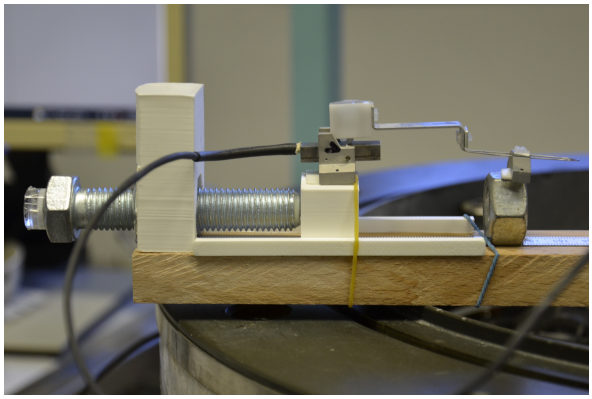

(a) calibration set-up for axial strain sensors

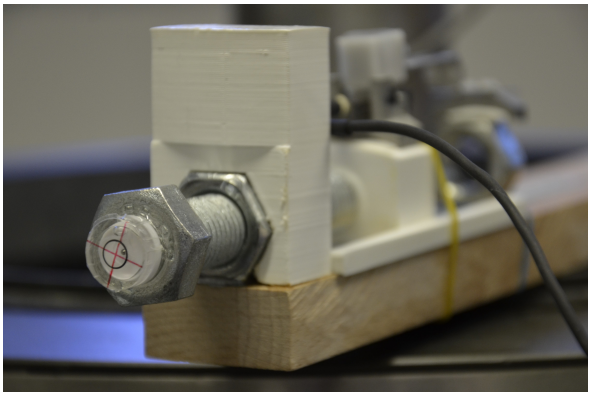

(b) M16 screw for controlled displacement

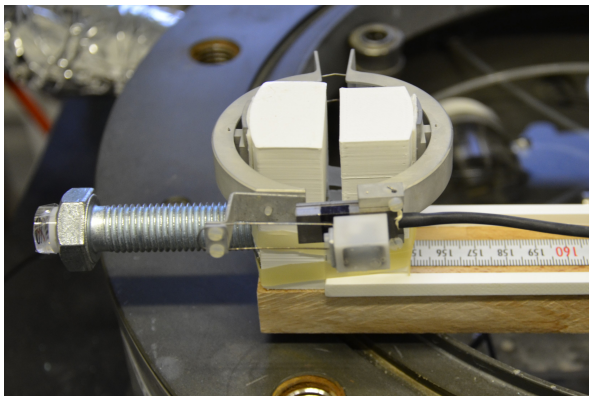

(c) calibration set-up for the radial strain sensor (side view)

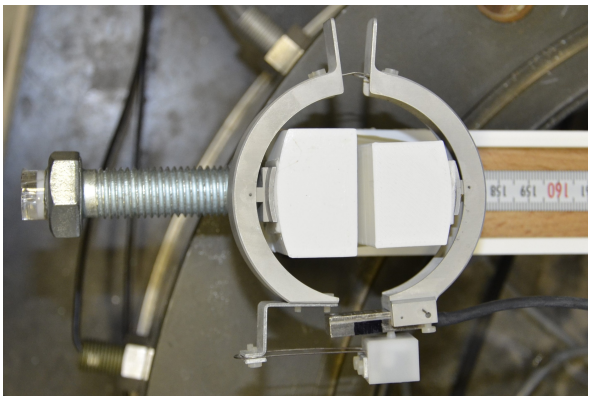

(d) calibration set-up for the radial strain sensor (top view)

Figure B.1: calibration test stand for the local strain measurement equipment

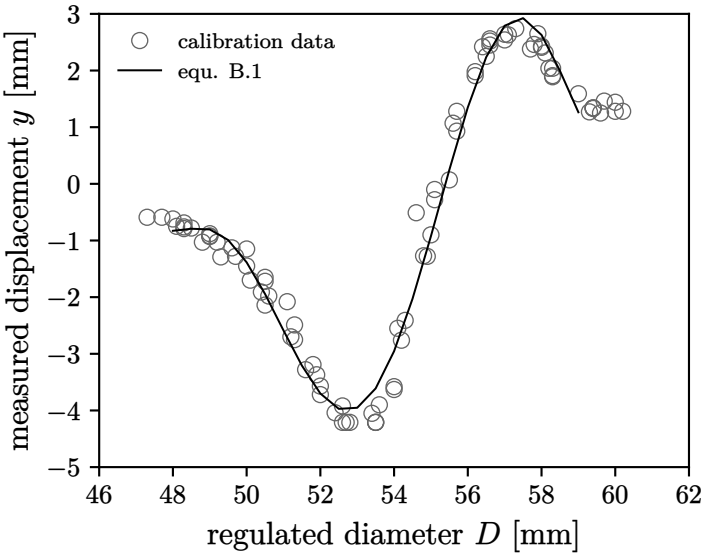

Figure B.2: calibration curve and test data for the local radial strain sensor

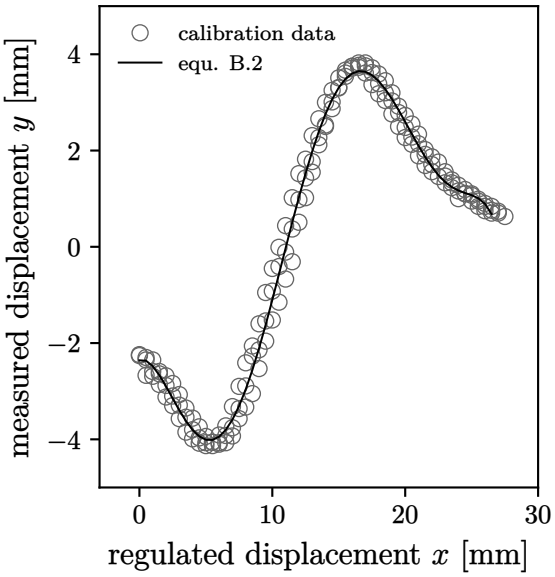

(a) local axial strain sensor #1

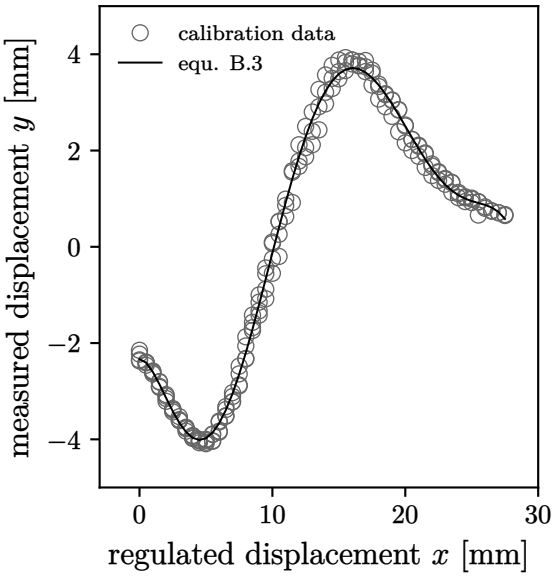

(b) local axial strain sensor #2

Figure B.3: calibration curve and test data for the local axial strain sensors

B.2 Temperature Data

The development of the temperature in the triaxial cell over the course of the shear phase of each experiment is depicted in fig. B.4 for ISS0 sand as well as for Hamburg sand.

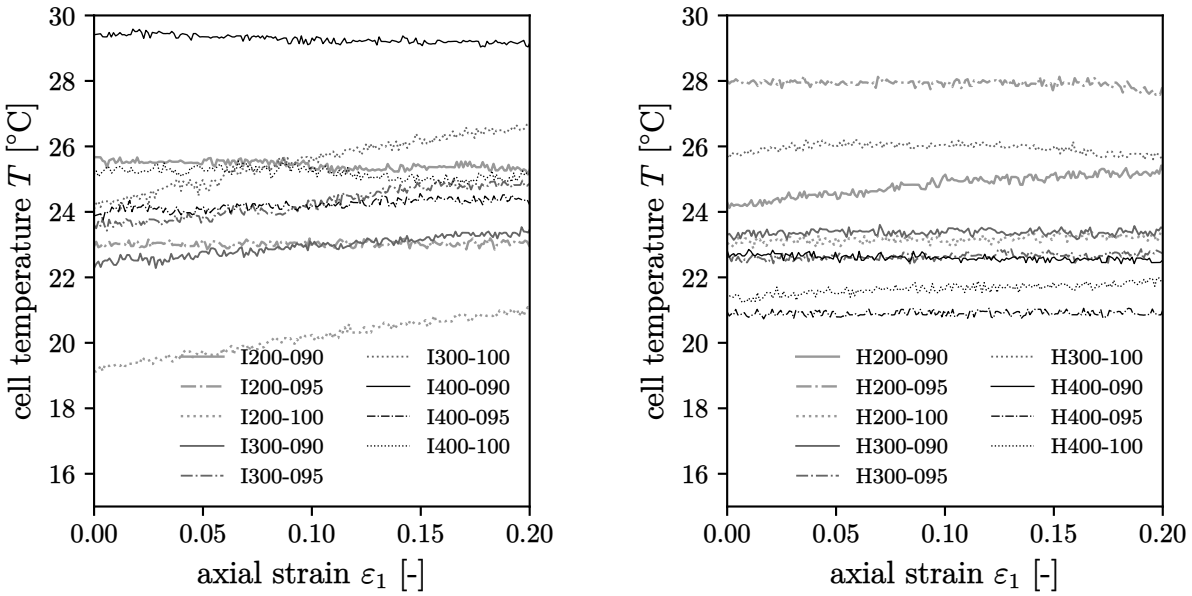

(a) experiments on ISS0 sand

(b) experiments on Hamburg sand

Figure B.4: temperature in the triaxial cell

Appendix C Supplementary Data on the μCT-Experiments

The information presented as follows is an addition to the elaborations on the microscopic experiments given in chapter 6.

C.1 Set-Up of the Differential Pore Pressure Sensor

The test tube containing the soil sample during the scanning procedure is equipped with a differential, gauge, analogue pore pressure sensor (Honeywell Low Pressure Sensor, type 24PCFFM6G) in order to be able to monitor the development of the pore pressure during the CT scans. Differential pressure sensors measure the relative difference in pressure at two points in a system. Precisely, a gauge pressure sensor measures the pressure at its port with respect to the local atmospheric pressure. To do so, it relies on the changing of resistance to measure the change in pressure. Specifically for the Honeywell 24PCFFM6G, an input voltage ranging from 2.5 to 12 V is supplied to the sensor, which then goes through the resistors and comes out the two output ports. Both output ports are connected to membranes fitted with resistors that change resistance when flexed. One of the output ports indicates the change in resistance due to atmospheric pressure, while the other indicates the change in resistance from the externally applied pressure. The exact location of the sensor, at which the two pressures are measured, is illustrated in the experimental set-up of the test tube given in fig. C.1. The sensor is fixed in the outlet pipe by means of a M3x0.5-6H thread and is additionally sealed with PVC glue.
The sensor itself has four SIP pins. Following the circuit schematic in fig. C.2, pin 1 is connected to the 5 V power supply. Pin 2 is connected to the channel 1 (CH1) of an ADS1115 analogue to digital converter (ADC). The two sets of analogue output signals go to the ADC in a WHEATSTONE bridge circuit. For this specific set-up, the ADC's I^2C protocol is used. The I^2C protocol is a master-slave protocol consisting of two ports of communication: SCL (serial clock) and SDA (serial data). Furthermore, a voltage shifter is used in this set-up. The main purpose of the shifter is to prevent the Raspberry Pi's GPI0 pins from being damaged during the communications with the ADC. The ADC's SDA and SCL ports are connected to the higher voltage side of the shifter (H), while the respective Raspberry Pi ports are connected to the lower voltage side of the shifter (L). Pin 3 and 4 of the pore pressure sensor are connected to ground (GND).

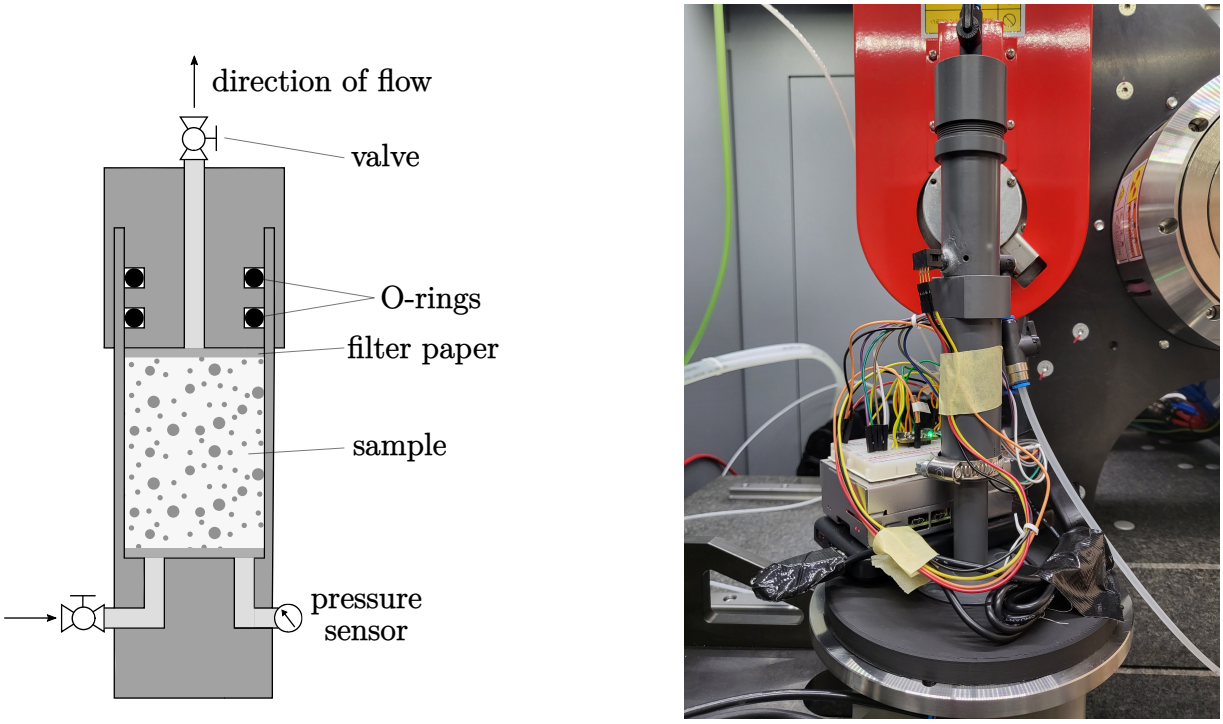

(a) schematic illustration (b) photo of implementation

Figure C.1: experimental set-up of the test tube for CT scanning

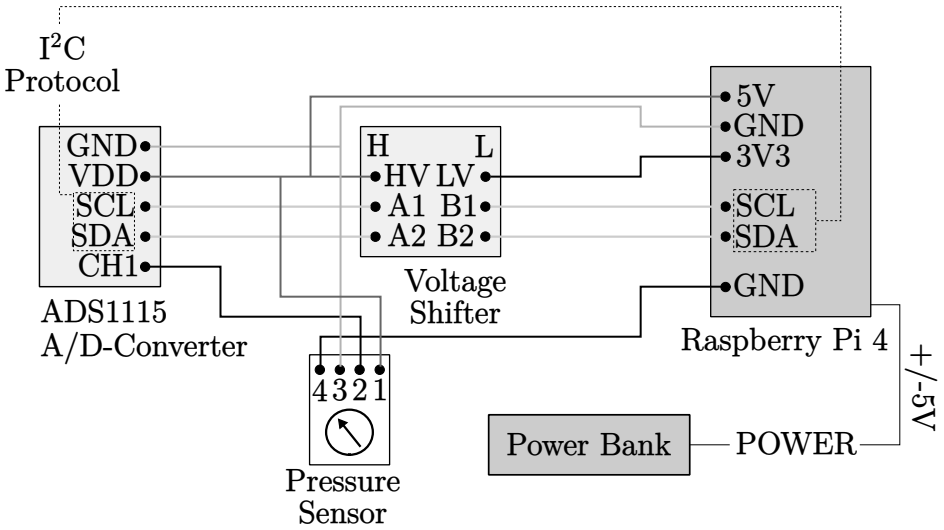

Figure C.2: circuit schematic of the pressure sensor set-up

C.2 Visualisation of Further CT Image Data

Fig. C.3 to C.9 illustrated in the following, visualise additional image data to complement the data presented in chapter 6. The depicted subvolumes correspond to the defined REV, i. e. exhibit an edge length of 600 px or 9.654 mm.

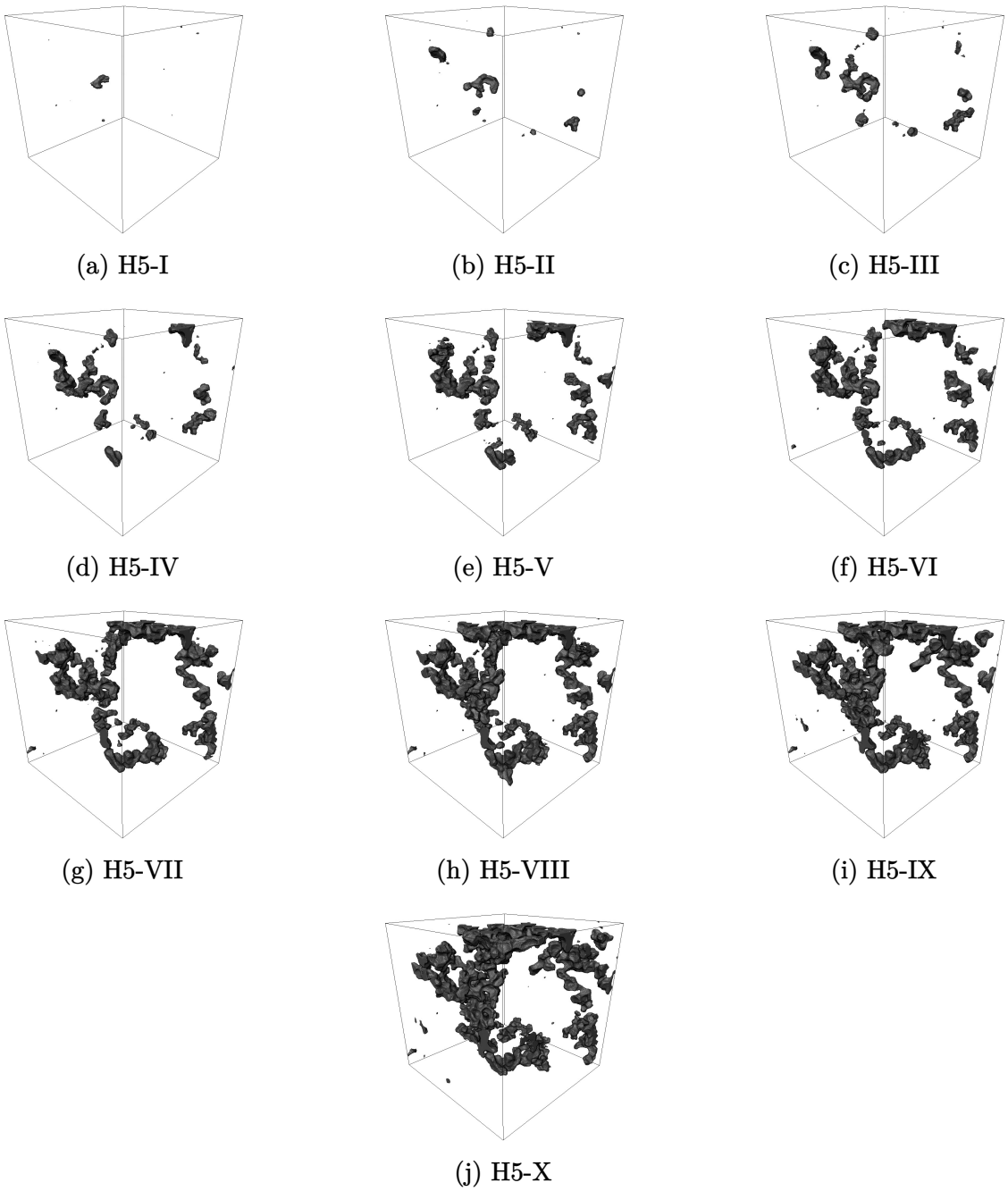

(a) H5-I (b) H5-II (c) H5-III

(d) H5-IV (e) H5-V (f) H5-VI

(g) H5-VII (h) H5-VIII (i) H5-IX

(j) H5-X

Figure C.3: gas phase in Hamburg sand ($\Delta p = 5\,\mathrm{kPa}$) – entire scanning sequence

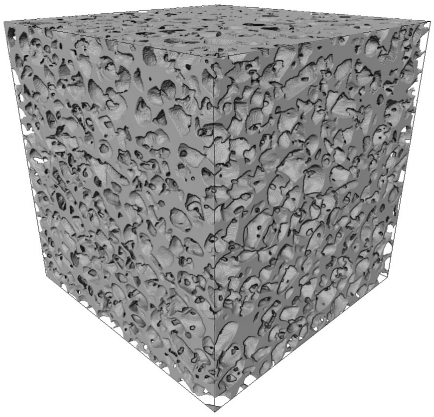

(a) H10-I

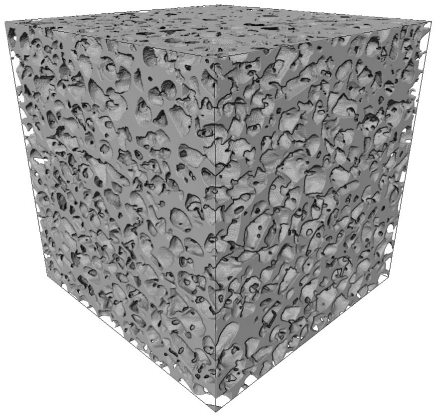

(b) H10-II

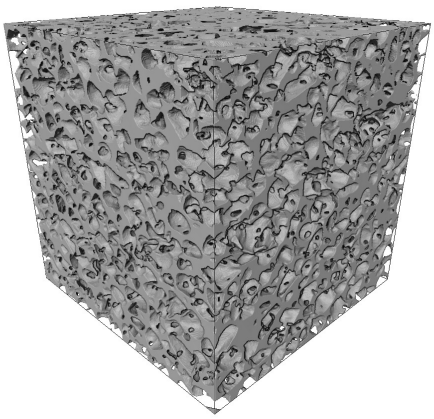

(c) H10-III

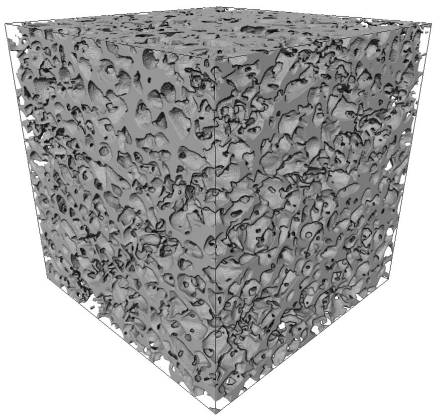

(d) H10-IV

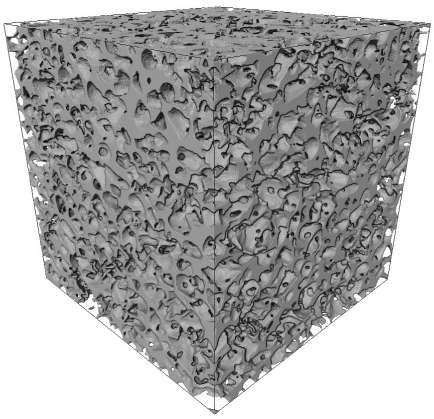

(e) H10-V

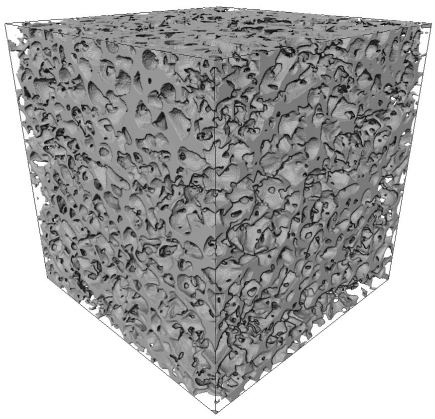

(f) H10-VI

Figure C.4: water phase in Hamburg sand ($\Delta p = 10\,\mathrm{kPa}$)

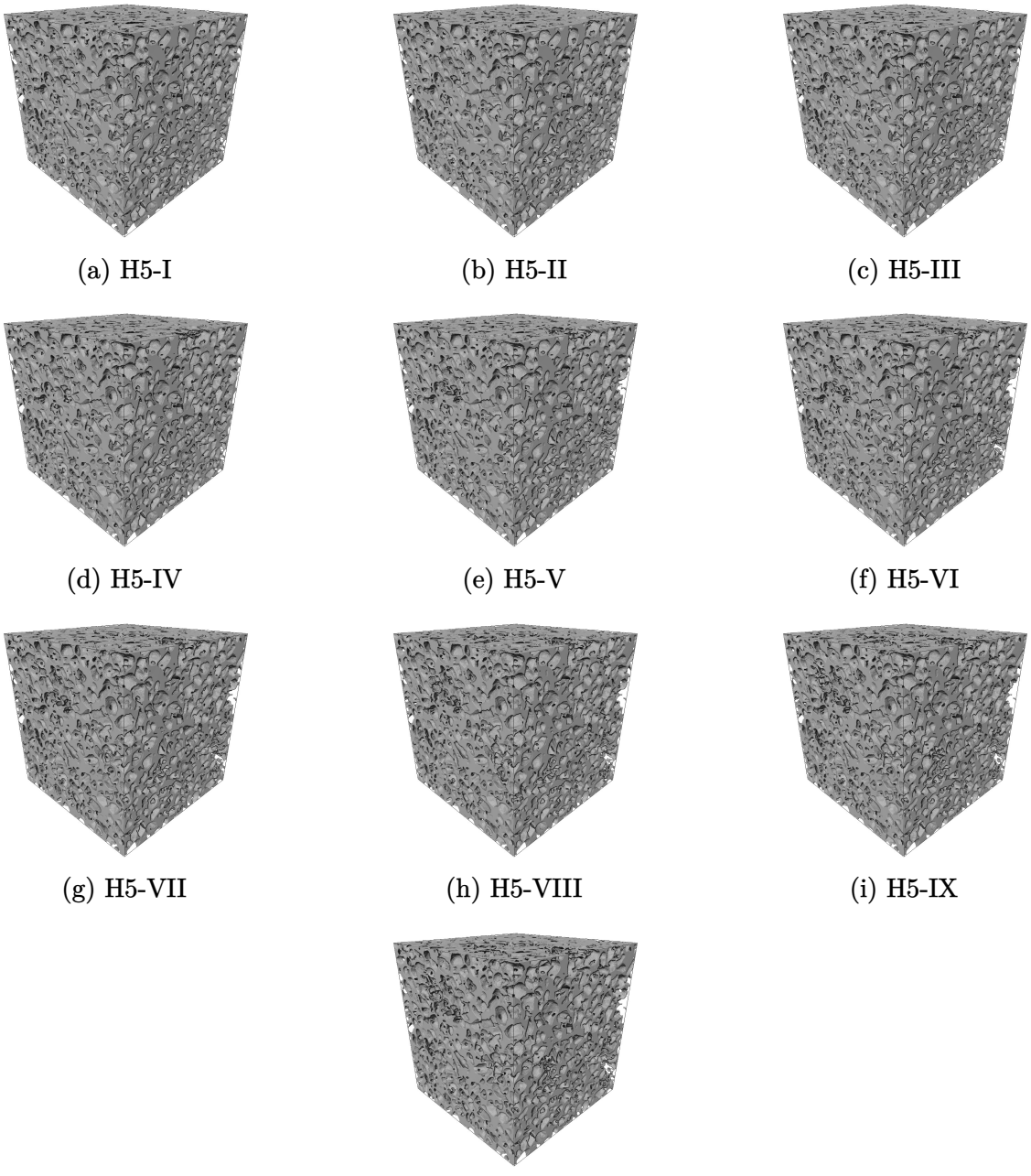

(a) H5-I (b) H5-II (c) H5-III

(d) H5-IV (e) H5-V (f) H5-VI

(g) H5-VII (h) H5-VIII (i) H5-IX

(j) H5-X

Figure C.5: water phase in Hamburg sand ($\Delta p = 5\,\mathrm{kPa}$)

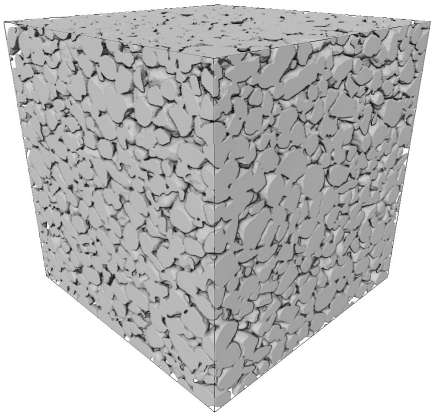

(a) H10-I

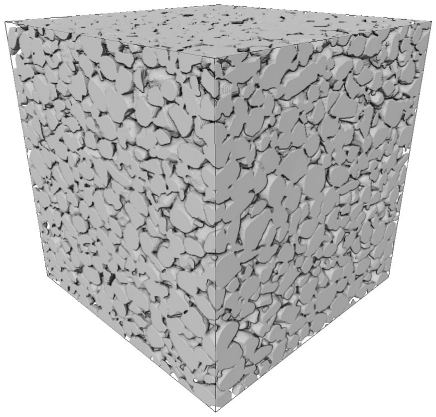

(b) H10-II

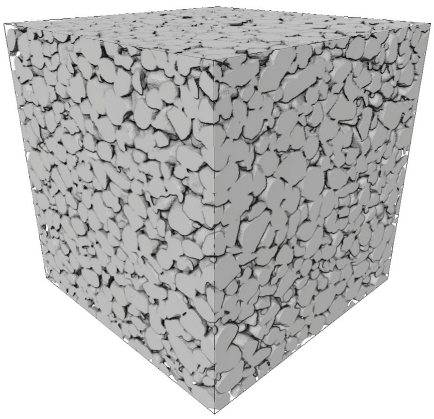

(c) H10-III

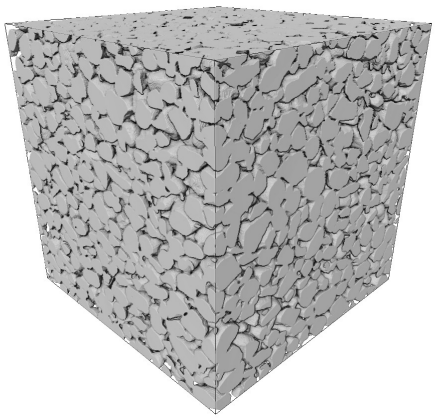

(d) H10-IV

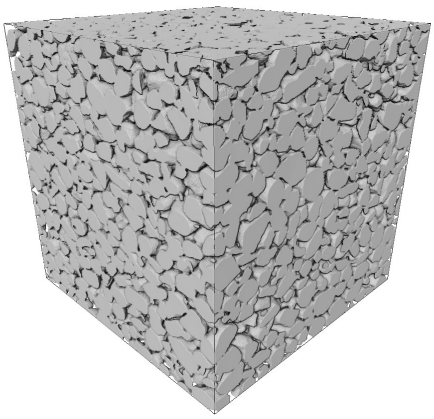

(e) H10-V

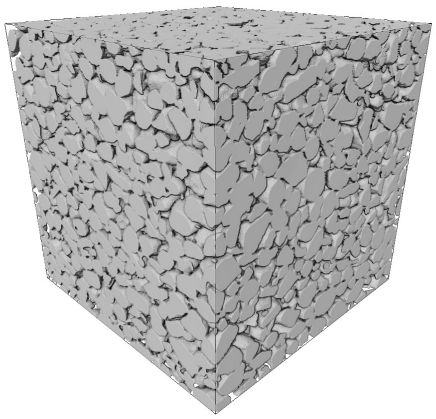

(f) H10-VI

Figure C.6: solid phase in Hamburg sand ($\Delta p = 10\,\mathrm{kPa}$)

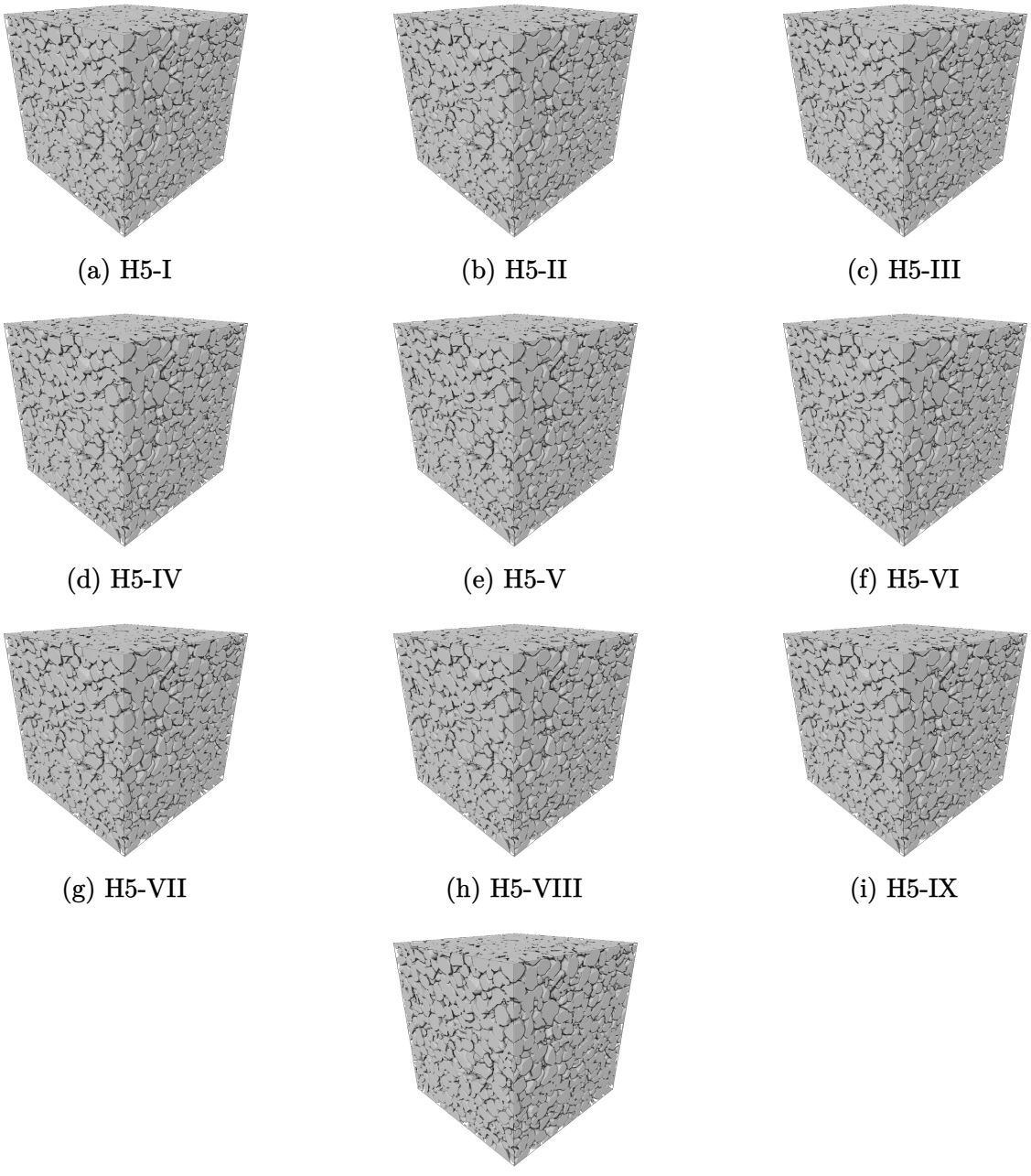

(a) H5-I (b) H5-II (c) H5-III

(d) H5-IV (e) H5-V (f) H5-VI

(g) H5-VII (h) H5-VIII (i) H5-IX

(j) H5-X

Figure C.7: solid phase in Hamburg sand ($\Delta p = 5\,\mathrm{kPa}$)

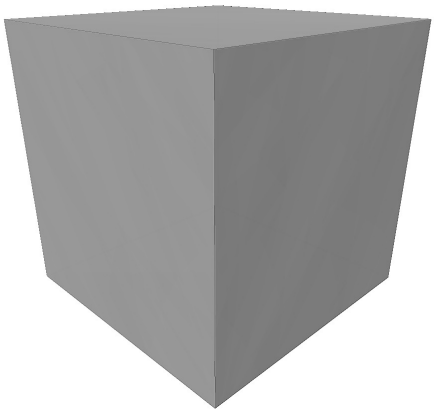

(a) I10-I

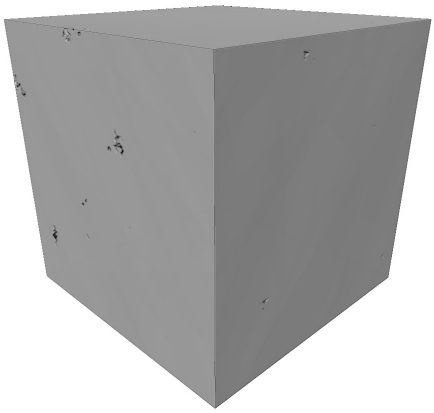

(b) I10-II

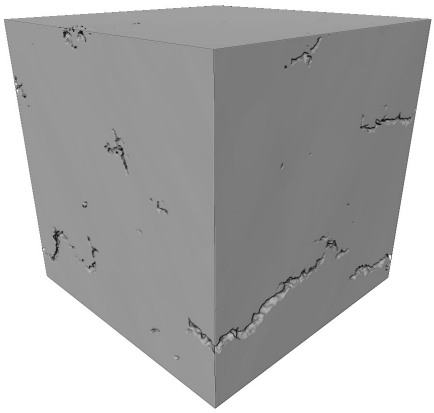

(c) I10-III

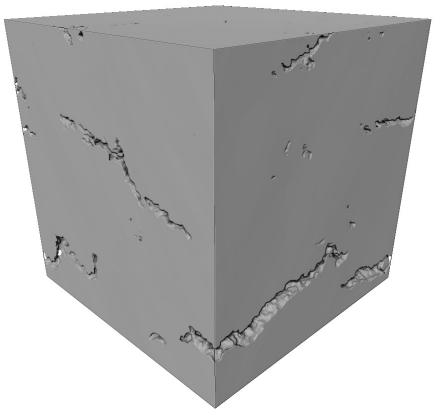

(d) I10-IV

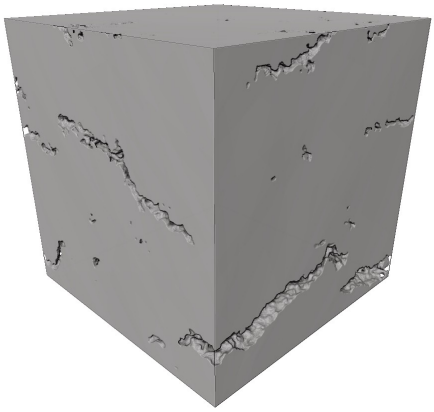

(e) I10-V

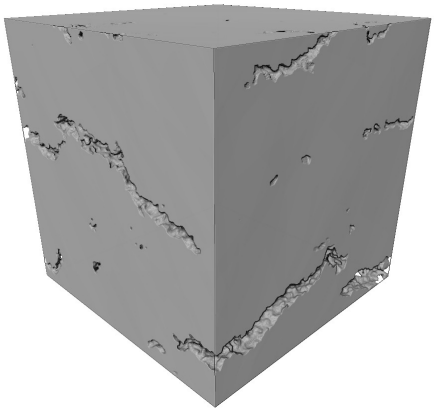

(f) I10-VI

Figure C.8: saturated soil matrix in ISS0 sand ($\Delta p = 10\,\mathrm{kPa}$)

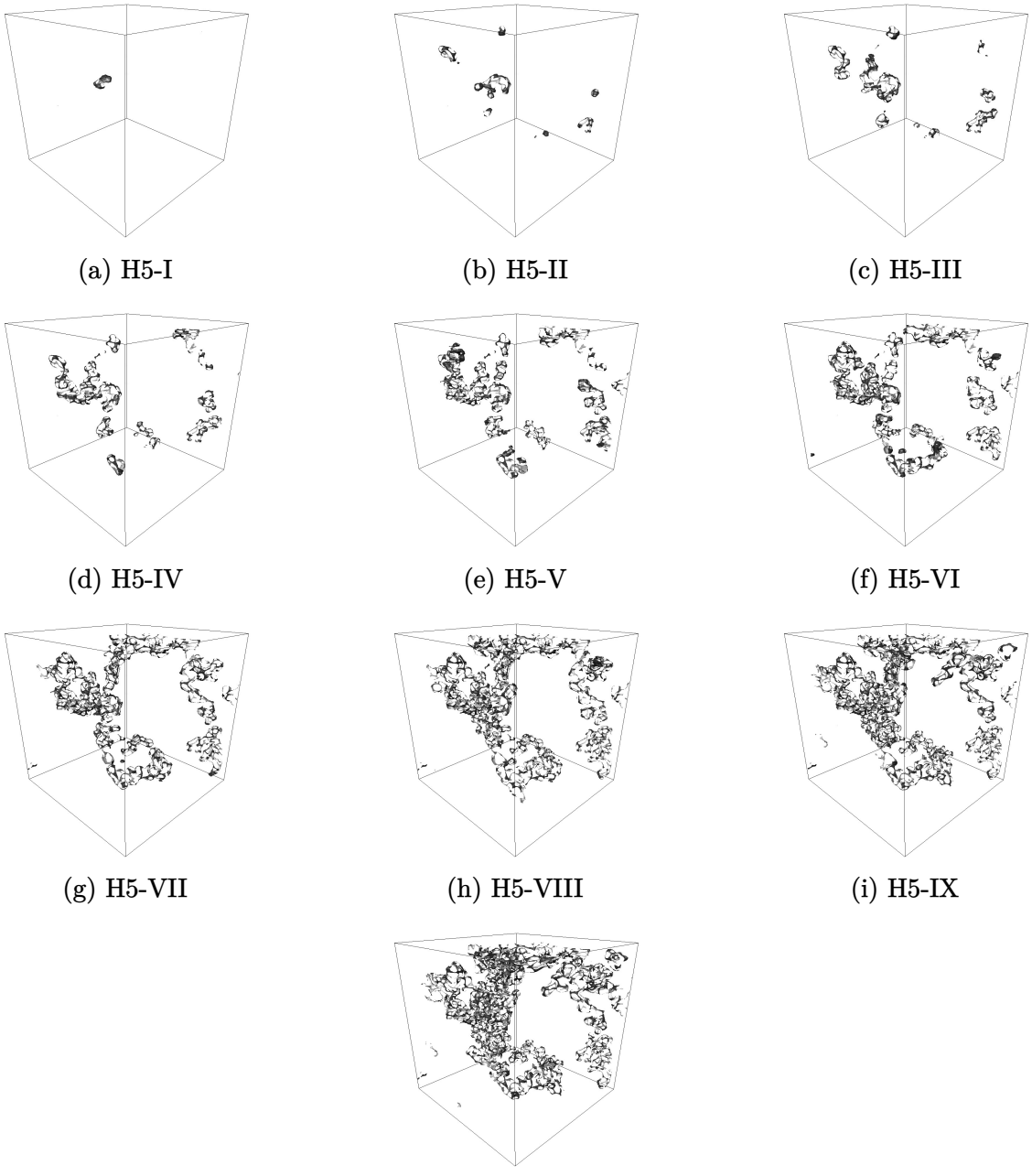

(a) H5-I (b) H5-II (c) H5-III

(d) H5-IV (e) H5-V (f) H5-VI

(g) H5-VII (h) H5-VIII (i) H5-IX

(j) H5-X

Figure C.9: gas-water interface in Hamburg sand ($\Delta p = 5\,\mathrm{kPa}$) – entire scanning sequence

C.3 Temperature Data

The development of the temperature in the scanning chamber over the course of each scan is depicted in fig. C.10 for ISS0 sand as well as for Hamburg sand. One scan consists of 1440 images per 360° rotation; see tab. 6.1. Thus, the image number is equivalent to the progression of the scan.

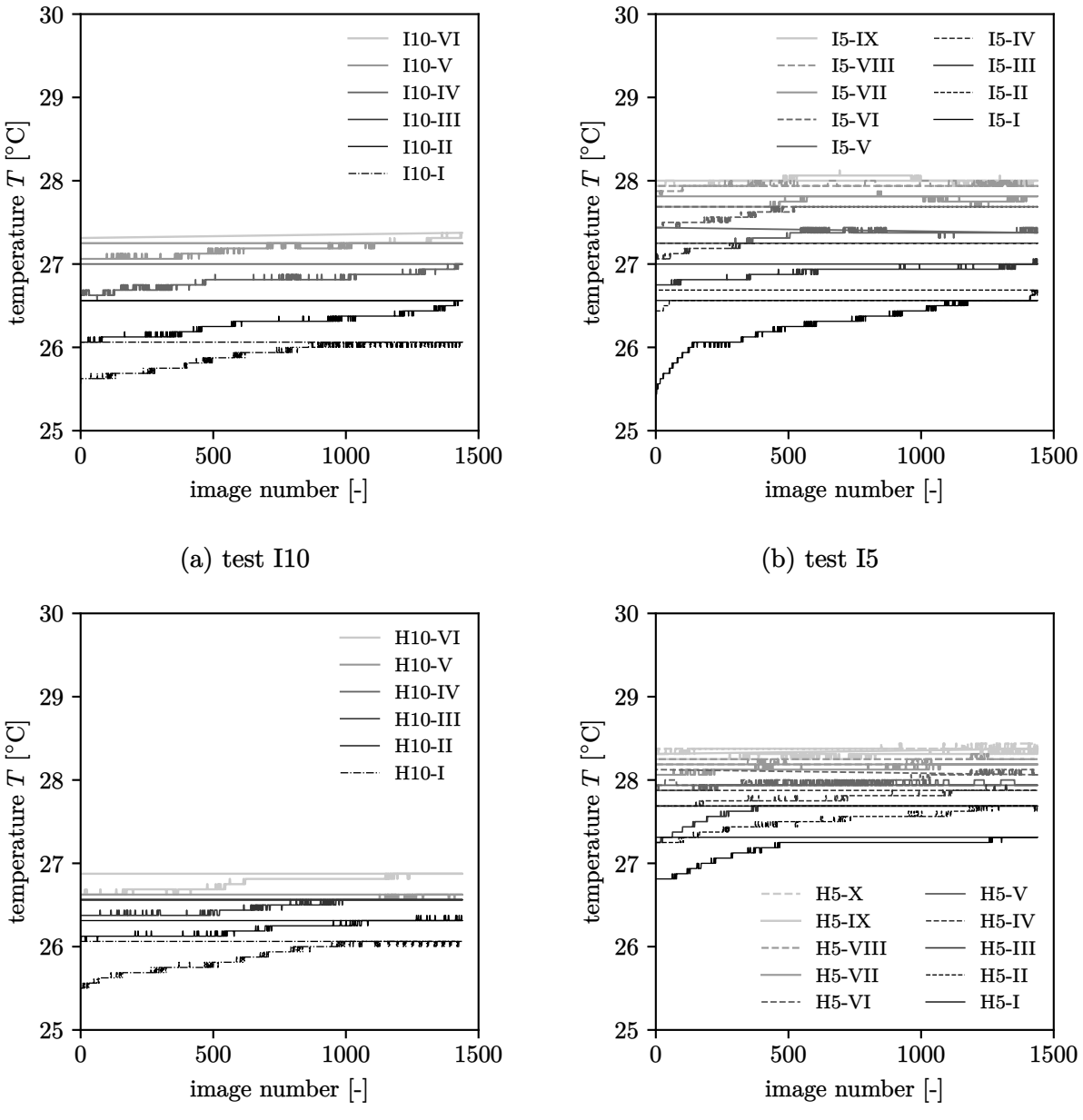

(a) test I10

(b) test I5

(c) test H10

(d) test H5

Figure C.10: temperature in the scanning chamber during image acquisition